EULERIAN AND LAGRANGIAN STUDIES OF CIRCULATION ON THE SCOTIAN SHELF AND ADJACENT DEEP WATERS OF THE NORTH ATLANTIC WITH BIOLOGICAL IMPLICATIONS

by

Shiliang Shan

Submitted in partial fulfillment of the requirements
for the degree of Doctor of Philosophy

at

Dalhousie University
Halifax, Nova Scotia
August 2016

TABLE OF CONTENTS

LIST OF TABLES

LIST OF FIGURES

ABSTRACT

A thorough understanding of circulation and hydrography over the eastern Canadian Shelf remains a major challenge within the field of physical oceanography. Reliable predictions of physical oceanic conditions are of great importance to studies of marine animal distribution and migration in the region. This thesis examines the circulation, hydrography, and associated variabilities on the Scotian Shelf and adjacent deep waters. An Eulerian perspective is taken and extensive use is made of a newly developed state-of-the-art multi-nested ocean circulation modelling system. The model performance is assessed extensively against various observations. Model results are used to quantify the tide-topography interaction, wind-driven circulation, shelfbreak jet, cross-shelf transport, upstream/downstream areas, and residence time in the Sable Gully Marine Protected Area. A process study is conducted to investigate the contributions of tidal mixing and wind-driven coastal upwelling to the formation of cold surface water along the Nova Scotia's coast in summer. The important influence on coastal upwelling of small-scale irregularities in the coastline and nearshore bathymetry near the Halifax Harbour is identified and explained through model sensitivity studies.

This thesis also investigates how the distribution and migration of marine animals respond to changes in the physical marine environment. A Lagrangian perspective is taken and a new biophysical particle tracking model is developed by adding the migratory behaviors to the passive drift. An in-depth numerical study of the spawning migration of American and European eels is conducted to examine the influence of the North Atlantic circulation on their migration from the coastal ocean (e.g., Scotian Shelf) to the Sargasso Sea. The model results suggest that orientated swimming behavior is required for eels to reach their spawning areas within the expected time window. The presence of ocean currents increases the duration of migration and travelled distances, particularly for American eel migrating at low swimming speed. In addition, the implications of circulation for the northern bottlenose whale in the Gully and Atlantic salmon transiting the Scotian Shelf are briefly discussed. The expertise gathered in the present work can be used to develop similar models for other regions and species.

List of Abbreviations and Symbols Used

Abbreviation	Definition
2D	two-dimensional
3D	three-dimensional
AC	Azores Current
ADCP	Acoustic Doppler Current Profiler
AMSRE	Advanced Microwave Scanning Radiometer-EOS
AVISO	Archiving, Validation and Interpretation of Satellite Oceanographic data
AZMP	Atlantic Zone Monitoring Program
BB	Banquereau Bank
BoF	Bay of Fundy
CANDIE	CANadian version of DIEcast (Dietrich Center for Air Sea Technology) model
CC	Canaries Current
CFSv2	Climate Forecast System Version 2
CIL	cold intermediate layer
CNES	Centre National d'Etudes Spatiales, France
CODAR	Coastal Ocean Dynamics Applications Radar
CORE	Common Ocean-ice Reference Experiments
COSEWIC	Committee on the Status of Endangered Wildlife in Canada
CS	Cabot Strait
CTD	conductivity, temperature, and depth
DVM	diel vertical migration
EB	Emerald Basin
EGC	East Greenland Current
EK	Emerald Bank
GB	Georges Bank
GEBCO	General Bathymetric Chart of the Oceans

Abbreviation	Definition
GEM	Global Environmental Multiscale
GHRSST	Group for High Resolution Sea Surface Temperature
GOAPP	Global Ocean-Atmosphere Prediction and Predictability
GoM	Gulf of Maine
GS	Gulf Stream
GSL	Gulf of St. Lawrence
HYCOM	HYbrid Coordinate Ocean Model
IC	Irminger Current
IQR	interquartile range
IUCN	International Union for Conservation of Nature
KPP	K profile parameterization
LB	LaHave Basin
LC	Laurentian Channel or Labrador Current
LIM2	Louvain-la-Neuve sea Ice Model version 2
LK	LaHave Bank
LM	coarse-resolution larger domain submodel
MATLAB	MATrix LABoratory
MEOPAR	Marine Environmental Observation Prediction and Response Network
MODIS	Moderate Resolution Imaging Spectroradiometer
MPA	Marine Protected Area
MSC	Meteorological Service of Canada
MUR	Multiscale Ultrahigh Resolution
NAC	North Atlantic Current
NARR	North American Regional Reanalysis
NASA	National Aeronautics and Space Administration
NC	Northeast Channel
NCEP	National Centers for Environmental Prediction
NEC	North Equatorial Current
NEMO	Nucleus for European Models of the Ocean
NSC	Nova Scotia Current

Abbreviation	Definition
OPA	Océan PArallélisé
OSU	Oregon State University
OTN	Ocean Tracking Network
PEI	Prince Edward Island
PHC	Polar science center Hydrographic Climatology
POM	Princeton Ocean Model
SA	spawning area
SB	Sable Bank
SG	Scotian Gulf
SI	Sable Island
SJR	Saint John River
SLP	sea level pressure
SLR	St. Lawrence River
SM	fine-resolution smaller domain submodel
SS	Scotian Shelf
SSS	sea surface salinity
SST	sea surface temperature
WGC	West Greenland Current
WIL	warm intermediate layer

Symbol	Description	Units
$\vec{u}$	velocity vector	$\mathrm{m\,s^{-1}}$
t	time	s
Δt	time-step	s
$\vec{x}$	position vector	
$\vec{\delta}$	random displacement	m
ξ	Gaussian random variable	
x, y, z	spatial coordinates	m
$\mathbf{K}(K_x, K_y, K_z)$	eddy diffusivity coefficient	$\mathrm{m^2\,s^{-1}}$

Symbol	Description	Units
K_h	horizontal eddy diffusivity coefficient	$\mathrm{m^2\,s^{-1}}$
$P(s, \mathbf{X}; t, \mathbf{Y})$	transition probability density from the positions of particles with a distribution of $\mathbf{X}$ at a time s to a distribution of $\mathbf{Y}$ at a later time t , where $t > s$	
γ^2	measure of fit	
O	observed variables	
M	simulated variables	
E_{rms}	root-mean-square error estimate	
n	number of data points	
D	the root-mean-square difference over a tidal cycle between observed and simulated velocities in each direction	
(A, ϕ)	amplitude and phase for a given tidal current constituent, respectively	
$(\phi_{CR},$ $\phi_{NT},$ $\phi_{NW})$	model results in the experiments *CR* (Control Run), *NT* (No Tides) and *NW* (No Wind), respectively	
$(\Delta\phi_{tide},$ $\Delta\phi_{wind},$ $\Delta\phi_{other})$	roles of tides, local wind forcing and other processes in the model results, respectively	
$< \cdot >$	annual mean	
U_e	eastward component of horizontal velocity	$\mathrm{m\,s^{-1}}$
V_n	northward component of horizontal velocity	$\mathrm{m\,s^{-1}}$
M_e	vertical integrated eastward component of horizontal velocity	$\mathrm{m^2\,s^{-1}}$
M_n	vertical integrated northward component of horizontal velocity	$\mathrm{m^2\,s^{-1}}$
J	volume transport	$\mathrm{m^3\,s^{-1}}$
s	along-transect direction	
(u, w)	tangential and vertical velocity components along the transect and in the vertical, respectively	$\mathrm{m\,s^{-1}}$

Symbol	Description	Units
P	percentage of the total number of particles inside the core protected area of the Gully	
T_e	e-folding residence time	
I	wind impulse	Pa s or N m^{-2} s
τ_a	along-shore wind stress	Pa or N m^{-2}
T	wind duration	day
$\vec{u}_P$	the horizontal velocity associated with passive drift by ocean currents	m s^{-1}
$\vec{u}_B$	the horizontal velocity associated with active migratory swimming	m s^{-1}
$p(\vec{u}_B)$	probability density of the swimming velocity	
α_i	weighting factor of the i^{th} behavior	
θ_0	preferred swimming direction	
$\Delta\theta$	spread around the preferred swimming direction	
BL	body length of eel	cm
ΔE_t	energy expenditure of eel from time t to $t + \Delta t$	J g^{-1}
V_t	swimming speed of eel	BL s^{-1}
MR_t	remaining body mass of eel	g
C_T	coefficient that takes into account the effect of water temperature on the oxygen consumption rate	
u_e	modelled normal flow at the eastern open boundary	m s^{-1}
η_e	modelled surface elevation at the eastern open boundary	m
η_w	wind-driven surface elevation	m
η_t	tidal sea surface elevation	m
u_w	depth-averaged wind-driven current	m s^{-1}
u_t	depth-averaged tidal current	m s^{-1}
u_c	depth-averaged climatological baroclinic current	m s^{-1}
c	phase speed of the external gravity wave	m s^{-1}
h	water depth	m

ACKNOWLEDGEMENTS

This thesis would not have been accomplished without the help and encouragement of a large number of people to whom I am very grateful.

Firstly, I would like to thank my supervisor, Dr. Jinyu Sheng for his guidance, support, inspiration and encouragement. I am sincerely thankful for the countless hours he spent with me, patiently debugging model codes and teaching me disciplined scientific research and writing. I would also like to thank him for graciously supporting me to visit the University of Southampton and University of Bergen.

Secondly, I would like to thank other members of my committee, Drs. Keith Thompson, Blair Greenan and Katja Fennel, who provided very valuable comments and guidance throughout my PhD studies. Their insightful suggestions and careful corrections greatly improved the science and presentation of my thesis. I would also like to thank Blair for bringing the Sable Gully project to me and for providing a research cruise opportunity to fulfill one of my PhD program requirements. Thanks to Keith for being the go-to person for a source of knowledge and experience, and for initiating the particle tracking project. The research collaboration with Drs. Mélanie Beguer, Martin Castonguay and Julian Dodson on tracking the eel migration in the North Atlantic ocean was very enjoyable to me. I would also like to thank my external examiner, Dr. Ruoying He for taking the time to read my thesis and for his insightful comments.

Thirdly, I would like to thank the Canadian Hydrographic Service for providing me the high resolution multibeam bathymetry for the Sable Gully. Thanks to Mathieu Dever for providing me the observations from the OTN project. Thanks to Dr. Simon Higginson for providing me the geodetic data. Thanks to Drs. Chris Jones and Emmanuel Devred for their help in obtaining the satellite observations. Thanks also to Drs. Kyoko Ohashi, Bo Yang, Jorge Urrego-Blanco, Yuehua Lin and Vasily Korabel for their contributions to my research work.

Many other people have helped me during the course of my study. I would like to thank Drs. Corinna Schrum and Ute Daewel for being my host at the University of Bergen, and professors and staff at the University of Southampton for an inspiring and enjoyable summer. To our computer system administrator, Daniel Morrison, for ensuring computer

systems are up and running. Thank you to fellow graduate students, to the staff and Faculty of the Department of Oceanography. The sweets and bitters of PhD life shared with Dr. Hongyang Lin at Dalhousie were unforgettable. I have also benefited from the very useful discussions with members of Jinyu's regional ocean modelling group.

I would like to acknowledge the financial support from the Killam Predoctoral Fellowship, MEOPAR, OTN, NSERC, and Lloyd's Register Foundation.

Finally, I would like to thank my family members for their continuing support. Thanks to Ying Lu for her patience, understanding and companionship throughout.

CHAPTER 1

INTRODUCTION

1.1 Background

Thorough understanding of the circulation and hydrography on the Scotian Shelf and adjacent North Atlantic is still an intriguing research topic in the field of physical oceanography, due to the complex topography, highly variable forcing functions, and strong nonlinear dynamics in the region. Reliable knowledge of physical oceanic conditions is also of great importance to studies concerning marine animal distribution and migration in the region.

The Scotian Shelf is a rugged continental shelf lying off Nova Scotia over the northwest Atlantic. The Shelf is about 700 km long and between 125 and 250 km wide, and bounded between the Laurentian Channel on the northeast and the Northeast Channel on the southwest (Fig. 1.1). There are several large shallow banks on the outer part of the Shelf, and basins and smaller banks in the middle and inner Shelf. There are several deep channels along the shelf break, especially the Sable Gully and Scotian Gulf, which extends further onto the Shelf.

The Sable Gully and the central Scotian Shelf adjacent to Halifax are two of several physically and ecologically significant areas on the Scotian Shelf. The Gully is a hotspot of marine biodiversity (*Rutherford et al.*, 2002) and is home to many marine organisms, such as the northern bottlenose whale, dolphins, squid, shrimp and deep-water coral. The central Scotian Shelf is dynamically and biologically complicated due to the effects of such oceanic processes as tides, the Nova Scotia Current, coastal upwelling (*Petrie et al.*, 1987), slope water intrusion (*McLellan et al.*, 1953; *Hachey*, 1953) and plankton blooms (*Greenan et al.*, 2008). The Sable Gully and the central Scotian Shelf are two study regions selected in this study.

Significant efforts have been made in monitoring oceanographic conditions on the Scotian Shelf and adjacent waters. There are three ongoing comprehensive research programs with observational components and some of their observations will be used in this study. The first research program is the Atlantic Zone Monitoring Program (AZMP) of the Department of Fisheries and Oceans Canada (*Therriault et al.*, 1998). The AZMP was implemented in 1998 with the aim of collecting and analyzing the biological, chemical, and physical field data in the Canadian Northwest Atlantic shelf region. Three of the 14 AZMP sections running from the coast to the shelf break are located on the eastern (Louisbourg Line), central (Halifax Line) and western (Browns Bank Line) Scotian Shelf, respectively. Seasonal and opportunistic hydrographic sampling along these sections are made to detect and quantify the interannual oceanographic variability. A fixed station (Station 2) on the Halifax Line is sampled at approximately biweekly frequency to monitor the shorter time scale dynamics. The second research program is the Ocean Tracking Network (OTN) (`http://oceantrackingnetwork.org`). The Halifax Line was also selected by OTN for monitoring the oceanic condition and migration of marine animals on the Scotian Shelf by deploying acoustic receivers, current-meters and other ocean-sensing instruments since 2008. As a part of the OTN, autonomous underwater gliders have been used to observe the oceanic conditions across the Halifax Line since 2011. Recently, a CODAR (Coastal Ocean Dynamics Applications Radar) system was constructed and came into operation as a part of the third research program known as the MEOPAR project (Marine Environmental Observation Prediction and Response Network, `http://meopar.ca`). The CODAR system is centred to the shelf waters off Halifax and provides real-time surface ocean currents up to 200 km off the coast.

Previous observational studies demonstrated that the circulation and hydrography on the Scotian Shelf and adjacent waters have significant temporal and spatial variability and are influenced by many forcing functions such as surface fluxes of heat, freshwater and momentum, low-salinity estuarine outflow from the Gulf of St. Lawrence, the advection of the Labrador Current, and the Slope Water intrusion. *Smith and Schwing* (1991) reviewed the circulation and variability on the eastern Canadian shelf including mean, seasonal and wind-driven variabilities based on historical observations made before 1990. *Loder et al.* (2003) studied the hydrographic and transport variability on the Halifax Line using archived current and hydrographic observations and found strong seasonal variations in

baroclinic transport of the Nova Scotia Current on the inner shelf and of the shelfbreak current at the shelf edge. The sea surface temperature (SST) on the Scotian Shelf has a strong seasonal cycle, with a mean range of about 16°C (*Thompson et al.*, 1988). Satellite images of SST presented in *Petrie et al.* (1987) demonstrated the development of a band of cool water over the inner Scotian Shelf during a month-long period of upwelling-favorable winds in 1984. The wavelike front associated with the upwelling is primarily due to baroclinic instability. The seasonal variability of sea surface salinity on the Scotian Shelf is influenced by the freshwater discharge from the St. Lawrence River (*Sutcliffe et al.*, 1976; *Smith*, 1989). The interannual and decadal variability of temperature and salinity on the Scotian Shelf is affected significantly by variations of the equatorward transport of the Labrador Current through the shelf-slope exchange (*Petrie and Drinkwater*, 1993).

Along with the observational studies, many numerical circulation models of different complexity have been developed for the Scotian Shelf and adjacent deep waters. Diagnostic models were used to study the seasonal circulation on the Scotian Shelf (e.g., *Han et al.* 1997; *Hannah et al.* 2001). Barotropic models were employed to study the wind-driven circulation on the Scotian Shelf (e.g., *Schwing* 1992; *Greenberg et al.* 1997; *Thompson and Sheng* 1997). Several prognostic three-dimensional (3D) circulation models have been developed over the past decade. A 3D circulation modelling system known as DalCoast was developed (*Bobanovic*, 1997; *Thompson et al.*, 2007) to simulate the storm surge and circulation over the eastern Canadian coast, particularly for the Scotian Shelf region. *Ohashi and Sheng* (2013) further upgraded the DalCoast with an enlarged model domain and better atmospheric forcing. *Wu et al.* (2012) developed a coupled ice-ocean circulation model whose domain includes the entire east coast of Canada to study the connection of the circulation over the Scotian Shelf to currents in other regions (e.g., the Labrador Current). *Urrego-Blanco and Sheng* (2014) recently examined the subtidal circulation in the Gulf of St. Lawrence, the Scotian Shelf and the Gulf of Maine using a nested-grid circulation model for the northwest Atlantic. *Brennan et al.* (2016) assessed the sensitivity of a northwest North Atlantic model to surface and boundary forcing and found that although all surface forcing datasets are capable of producing model sea surface temperature close to observed, the different datasets result in significant differences in modelled sea surface salinity. It should be noted that tides are not included in the models developed by *Wu et al.*, *Urrego-Blanco and Sheng*, and *Brennan et al.*. Recently, *Katavouta* (2015) developed a

high resolution regional model (1/36°) of the Gulf of Maine, Scotian Shelf and adjacent deep ocean. The regional model is then used to investigate the impact of seasonal changes in stratification on tides. It should be noted that the Gulf of St. Lawrence is not included in *Katavouta*'s model and the associated upstream lateral open boundary is specified using a coarse resolution (1/12°) global model.

Despite the above observational and numerical studies on the circulation and hydrography of Scotian Shelf, the literature on the circulation over several important regions such as the Sable Gully is very limited. *Petrie et al.* (1998) reviewed the general physical oceanographic conditions in the Sable Gully, primarily based on the sparse historical observations and coarse shelf-scale numerical modelling results. *Sandstrom and Elliott* (1984, 2011) discussed internal tides and their associated enhance mixing along the edge of the Scotian Shelf, particularly in the Sable Gully. In addition, a multi-disciplinary field program was carried out in 2006-07 over the Sable Gully (*Greenan et al.*, 2014), in which the physical oceanographic component consisting of the deployment and recovery of four current-meter moorings and CTD (conductivity, temperature, and depth) surveys was included. *Swart et al.* (2011) studied the tidal currents based on mooring observations and employed a simple idealized 1.5-layer, linear model to examine the amplification of tidal currents in the Gully. *Greenan et al.* (2014) recently discussed the mean circulation, bottom-intensified tidal current, overtides and compounded tides and enhanced vertical mixing in the Gully.

Beside the field observations mentioned above, only one published paper (*Han et al.*, 2001) was found in the literature focusing on the circulation in the Gully by employing numerical circulation model. It should be noted that *Han et al.*'s diagnostic model was not specifically developed for the Gully but for the Scotian Shelf and adjacent waters. The model had a horizontal resolution of $\sim$2 km for the Gully and 61 vertical levels, and was integrated only for 6-8 M_2 cycles. *Han et al.* (2001) then examined the modelled 3D tidal currents and seasonal mean circulation and found a cyclonic partial gyre along the Gully flanks with southwestward flows along the continental slope.

Although the aforementioned observational and numerical studies have been very useful in revealing the basic features of tidal and subtidal circulations and hydrographic distributions on the Scotian Shelf, the horizontal resolutions of previous numerical models are too coarse to resolve the Nova Scotia Current, coastal upwelling and their associated frontal

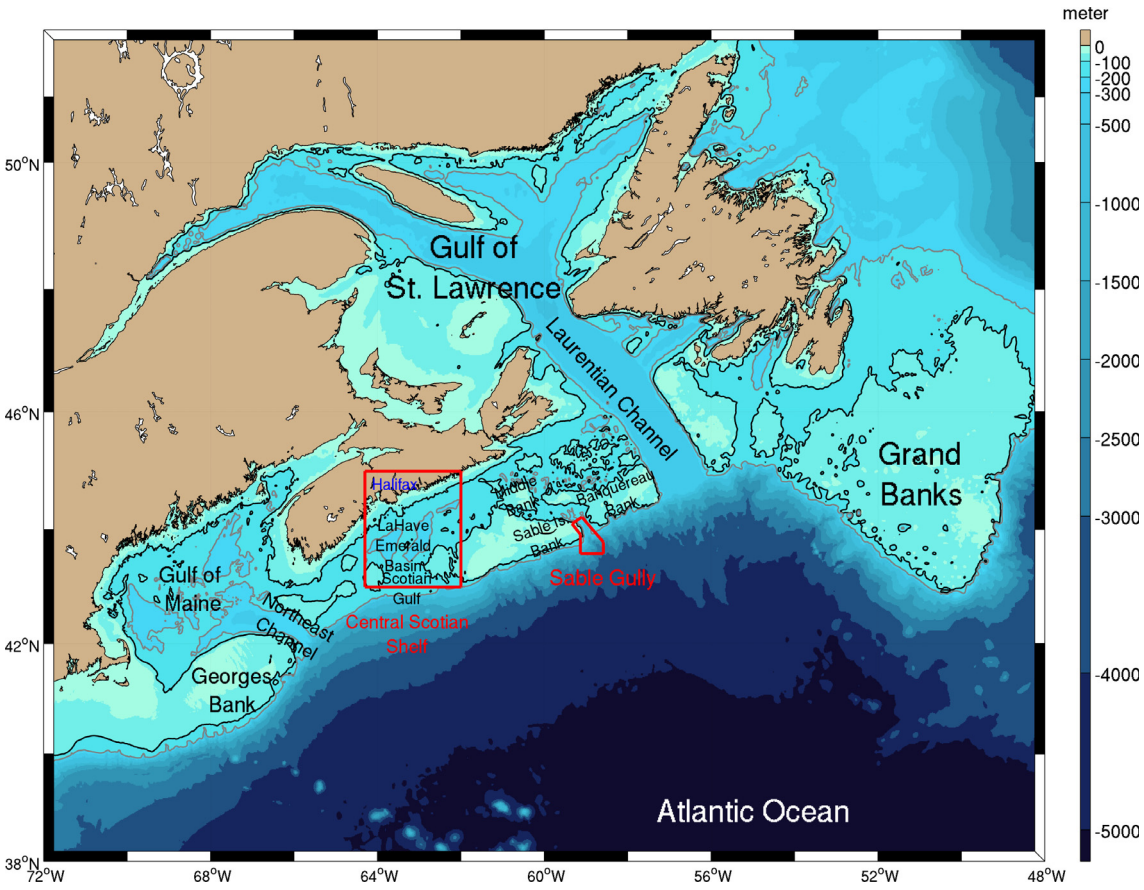

Figure 1.1: Major topographic features over the Gulf of St. Lawrence, Grand Banks, Scotian Shelf, Gulf of Maine and Georges Bank. The red polygon outlines the Gully Marine Protected Area. The red rectangle outlines the central Scotian Shelf adjacent to Halifax. The 100 m and 200 m isobaths are shown in black and gray contours, respectively.

instabilities. For the Sable Gully region, although some current and hydrographic measurements have been made, main physical processes affecting circulation in the Gully and many important hydrodynamic properties (e.g., residence time, source and sink regions) of the Gully Marine Protected Area have not been investigated. Thus, a better understanding and quantification of the 3D circulation and hydrography, and their temporal and spatial variability on the central Scotian Shelf adjacent to Halifax is required. In addition, a high-resolution numerical circulation modelling study is needed in order to have better knowledge of the circulation in the Gully.

The oceanic environmental conditions of the Scotian Shelf play an important role in the life cycle of many marine species, some of which are categorized as threatened or endangered species. My doctoral research focuses on physical processes that affect the

habitat and life cycle of three species: whale, salmon and eel. These species all have complex life cycles and are capable of migrating long distances. Many aspects of their life cycles are still not well understood [1].

The endangered northern bottlenose whale is a species of beaked whale that is endemic to the North Atlantic. One population has been found in the Sable Gully, Shortland Canyon (50 km east of the Gully), and Haldimand Canyon (100 km east of the Gully) (*Wimmer and Whitehead*, 2004). However, good knowledge of the 3D time-varying circulation and its linkage to whale distribution and migration in the Gully and adjacent canyons requires more study.

Atlantic salmon is widely distributed along the North Atlantic coast. The salmon is an anadromous species, living in the sea and migrating to fresh water to spawn. Most Atlantic salmon populations, particularly those in the southern range of their distribution, have declined throughout the last century (*Parrish et al.*, 1998). The OTN project has deployed acoustic receivers on the Halifax Line to monitor the seaward migration of Atlantic salmon on the Scotian Shelf. The circulation and hydrography on the central Scotian Shelf, which has significant temporal and spatial variability, may affect the Atlantic salmon migration and also requires further study.

American and European eels are widely distributed along the eastern coast of North America and the coast of Europe, respectively. The eel is a catadromous species, living in the fresh water and migrating to the open ocean to spawn. The American eel has been designated as threatened species by COSEWIC (Committee on the Status of Endangered Wildlife in Canada) since May 2012 and the European eel has been included as critically endangered species on the IUCN (International Union for Conservation of Nature) Red List of Threatened Species™ since 2010. In 1922, the Danish scientist Johannes *Schmidt* first deduced the Sargasso Sea as the spawning ground of the European eel, based on the location where the smallest eel larvae were found. However, the exact spawning area of the European and American eels in the Sargasso Sea remains a mystery. In addition to the migration routes eels take, the navigation cues they use and the environmental conditions they experience are not well understood.

The above discussions suggest that better knowledge of the circulation and hydrography

[1] Both whale and eel are two of the 11 things along with for example black holes highlighted in a cover story entitled "We know they're out there: 11 things we're sure exist - but have never seen" published in the issue of March 19-25 of "New Scientist" magazine in 2016.

on the Scotian Shelf, particularly over the Sable Gully and the central Scotian Shelf adjacent to Halifax, is needed in order to realistically predict the 3D time-varying physical, chemical and biological ocean state variables. In addition, detailed information on the physical environmental condition of the Scotian Shelf and adjacent deep waters of the North Atlantic is also required in order to explore marine animal migration corridors and behaviors in these regions. It should be noted that the migration routes of Atlantic salmon and American eel cover an extended area beyond the Scotian Shelf to include the subtropical and subpolar gyres of the North Atlantic. Thus, knowledge of the basin-scale circulation and hydrography of the North Atlantic, particularly the Gulf Stream and the Labrador Current, is also required.

The oceanic environmental condition and its linkage to marine animal migration, can be studied by two approaches: the Eulerian approach[2] and the Lagrangian approach[3]. These two approaches are often mentioned in textbooks of geophysical fluid dynamics (e.g., *Batchelor* 2000; *Marshall and Plumb* 2008).

The Eulerian approach is to investigate the evolution of flow properties at specific locations in space as time varies. By comparison, the Lagrangian approach is to examine the fluid motion by following an individual fluid parcel as it moves through space and time. Mathematically, two derivatives are named after Euler and Lagrange as:

Eulerian derivative

$$\left(\frac{\partial}{\partial t}\right)_{\substack{\text{fixed}\\ \text{point}}} \tag{1.1}$$

Lagrangian derivative

$$\frac{D}{Dt} = \left(\frac{\partial}{\partial t}\right)_{\substack{\text{fixed}\\ \text{point}}} + \vec{u}\cdot\nabla \tag{1.2}$$

where $\frac{\partial}{\partial t}$ represents the time rate of change at a fixed position, $\vec{u}$ is the velocity vector, and $\nabla \equiv \left(\frac{\partial}{\partial x}, \frac{\partial}{\partial y}, \frac{\partial}{\partial z}\right)$ is the spatial gradient operator at the same position. In Eq. (1.2), $\frac{D}{Dt}$ is called the Lagrangian derivative, which is also known as the substantial, the total, or the material derivative. Physically, this term represents the time rate of change of some characteristic of particular element of fluid (which in general is changing its position). In comparison with Lagrangian derivative, the Eulerian derivative $\frac{\partial}{\partial t}$ represents the rate of

[2] named after the Swiss mathematician Leonhard Euler (1707-1783) who first formulated the equations for fluid motion in a fixed frame of reference, considered one of the greatest mathematicians ever.

[3] named after the French mathematician Joseph Lagrange (1736-1813), who noted for his early work on fluid dynamics and tides. His academic advisor was Euler.

change of some characteristic at a fixed point in space (but with constantly changing fluid elements because the fluid is moving).

The most commonly used ocean circulation models are Eulerian and they usually define the time-varying flow fields using spatial structured/unstructured grids. At a fixed grid in space, the time rate of change of ocean state variables (e.g., current, temperature, and salinity) is updated numerically. Ocean circulation modelling has experienced explosive growth in the past few decades, due to theoretical and numerical advances converging with expanded computational power.

Particle tracking models are Lagrangian and they track the movement of a particle through space and time. Particle tracking models have increasingly been used to investigate the transport pathways, mixing, residence time and hydrodynamic connectivity in the ocean (e.g., *Awaji* 1982; *Ridderinkhof and Zimmerman* 1990; *Bilgili et al.* 2005; *Shan and Sheng* 2012. See *Lynch et al.* 2015 for a comprehensive review.). For the purpose of fisheries and coastal management, it is important to know where marine animals are located at specific times of the year and how they may be responding to oceanic conditions. The particle tracking models, in combination with ocean circulation models and animal swimming behavior, allow us to fill in some of the knowledge gaps left by observational studies and test basic assumptions regarding animals' movement and behavior. In these models, virtual marine animals are simulated in the 3D oceanic environment, which is normally generated by ocean circulation models.

1.2 Objectives of the Thesis

The main objectives of my doctoral research are twofold. The first objective is to examine the circulation and hydrography on the Scotian Shelf and adjacent deep waters of the North Atlantic. The second objective is to investigate how the distribution and migration of marine animals are influenced by changes in the physical environment.

My thesis work is carried out over the following three specific ocean waters and three representative species: (1) Sable Gully and northern bottlenose whale, (2) central Scotian Shelf adjacent to Halifax and Atlantic salmon, and (3) North Atlantic and American and European eels. For the study of circulation and associated variability, my thesis work focuses on the Sable Gully and central Scotian Shelf from an Eulerian perspective by using ocean circulation models. For the study of marine animal migration, my thesis work

explores the influence of circulation on the migration of American and European eels in the North Atlantic from a Lagrangian perspective by employing a biophysical particle tracking model. The following scientific questions related to the above research are addressed in this thesis:

a. Sable Gully and northern bottlenose whale

- How are the three-dimensional circulation and associated variability in the Sable Gully and adjacent waters affected by tides, wind forcing and large-scale oceanic circulation?
- To what extent is the Gully hydrodynamically connected to the adjacent regions? What is the role of the circulation on the movement of passive particles in the Gully? What is the residence time in the Gully?
- What are the implications of the circulation in the Gully for the northern bottlenose whale?

b. Central Scotian Shelf adjacent to Halifax and Atlantic salmon

- What is the temporal and spatial variability of circulation and hydrography on the central Scotian Shelf? What are the physical processes controlling the formation of cold surface waters along the coast of Nova Scotia in summer?
- How does the nested-grid model perform in simulating the circulation and hydrography over the central Scotian Shelf in comparison with satellite and *in-situ* observations?
- What is the spatial structure of the observed and simulated coastal upwelling plume on the central Scotian Shelf and how does the plume evolve in time? What is the role of irregular coastline and topography in the coastal upwelling?
- What are implications of the circulation and hydrography of the central Scotian Shelf for the Atlantic salmon?

c. North Atlantic and American and European eels

- What are the effects of large scale ocean circulation on the seaward migration of American and European eels in the North Atlantic?

- Is orientated swimming behavior required for the seaward migration of American and European eels from the coast to the Sargasso Sea?

To address the above questions, several numerical models have been developed as part of my thesis work, which includes a nested-grid circulation model for Sable Gully (DalCoast-Gully), a nested-grid circulation model for the central Scotian Shelf (DalCoast-CSS) and a biophysical particle tracking model for simulating the seaward migration of American and European eels.

1.3 Outline of the Thesis

This thesis is based on four peer-reviewed scientific papers and one manuscript in preparation. The rest of this thesis is structured as follows.

Chapter 2 presents the general oceanic conditions on the Scotian Shelf and relevant *in-situ* and satellite remote sensing observations.

Chapter 3 examines the 3D circulation, tide-topography interaction, wind-driven circulation, shelfbreak jet and cross shelf transport in the Sable Gully. The 3D circulation in the Gully in 2006 is reconstructed using a multi-nested 3D ocean circulation model (DalCoast-Gully) with realistic topography. The performance of the DalCoast-Gully in simulating the circulation, hydrography and their associated horizontal and vertical variations in the Sable Gully is assessed by comparing model results with various types of independent oceanographic observations including current-meter observations, data-assimilative tidal model outputs and CTD (conductivity, temperature, and depth) casts. A particle tracking study is then used to examine the role of physical environments on the movement of passive particles in the Gully Marine Protected Area (MPA). The residence time of the Gully is quantified based on the particle trajectories. In addition, the implications of circulation on the distribution and migration of northern bottlenose whale in the Gully are examined.

Chapter 4 investigates the temporal and spatial evolution of the circulation and hydrography on the central Scotian Shelf adjacent to Halifax. A multi-nested circulation model (DalCoast-CSS) is used in this chapter to simulate tides, the Nova Scotia Current and coastal upwelling on the central Scotian Shelf adjacent to Halifax. The DalCoast-CSS has the similar modelling framework to the DalCoast-Gully except that the innermost submodel covers the central Scotian Shelf adjacent to Halifax. The model results are validated

against observations, including satellite remote sensing data from GHRSST (Group for High Resolution Sea Surface Temperature) and Aquarius, and *in-situ* measurements taken by tide gauges, a marine buoy, ADCPs (Acoustic Doppler Current Profiler) and CTDs. Secondly, model results are used in a process study designed to examine the effect of tidal mixing and wind-driven coastal upwelling on the formation of cold surface waters along the coast of Nova Scotia. Thirdly, the observed and simulated coastal upwelling plumes on the central Scotia Shelf are presented in this chapter. In addition, the role of irregular coastline and topography in coastal upwelling is investigated by contrasting the results from a suite of model runs differing only in the specification of coastline and topography. Lastly, the implications of oceanic conditions, the surface temperature in particular on the salmon migration on the Scotian Shelf are discussed.

Chapter 5 quantifies the effect of the general oceanic circulation on the seaward migration of American and European eels from the coast to the Sargasso Sea. A biophysical particle tracking model is used in this chapter to include background ocean currents and various swimming behaviors. Ocean currents are simulated using a realistic, eddy-permitting model of the North Atlantic. Several swimming behaviors are considered including: passive drift, random swimming, true navigation to specific spawning sites and innate compass orientation towards the spawning area in the Sargasso Sea. Several combinations of swimming speeds and depths are also examined.

Chapter 6 gives an overall summary and conclusion.

Chapters 3 to 5 are mostly based on a collection of five 'stand-alone' manuscripts in different stages of publication. These manuscripts are listed in Appendix B. During the course of thesis writing, integration efforts have been made to prevent redundancy. Chapter 3 is modified from two published papers, in which I was the lead author. Chapter 4 is also modified from two manuscripts. One is published and the other one will be submitted for publication soon. I was also the lead author for the above two manuscripts. Chapter 5 is modified from a published paper. In this collaborative publication, I was the second author and the principal contributor for the model implementation and simulation, and associated description and discussion in this paper.

CHAPTER 2

GENERAL OCEANIC CONDITIONS ON THE SCOTIAN SHELF AND RELEVANT OBSERVATIONS

2.1 Introduction

Marine environment conditions on the Scotian Shelf have significant spatial and temporal variability. Many observational and numerical studies have been made in the past to improve our understanding of circulation and hydrography, and their associated variabilities. This chapter provides a brief description of the general oceanic conditions on the Scotian Shelf and presents the latest and relevant *in-situ* and satellite remote sensing observations for the region.

2.2 Circulation

The general circulation on the Scotian Shelf (SS) and adjacent waters is characterized by southwestward (equatorward) currents with inshore and offshore branches (See *Loder et al.* (1998) for a detailed review). The inshore branch is the Nova Scotia Current, which originates in the Gulf of St. Lawrence (GSL). This Current turns onto the SS at Cabot Strait and drifts southwestward along the coast of Nova Scotia and enters the Gulf of Maine (GoM) at Cape Sable. The offshore branch represents a downstream extension of the Labrador Current, which is the subpolar western boundary current in the northwest Atlantic. The offshore branch of the Labrador Current reduces its transport while flowing along the shelf break of the SS and entering the GoM through the Northeast Channel

(*Hannah et al.*, 2001; *Han and Loder*, 2003). The climatological flow over the SS outlined above generally persists year-round, but with strong seasonal variations in the transport on the inner shelf and at the shelf break. Both the Nova Scotia Current and the shelfbreak current are thought to be strongest in winter and weakest in summer (*Loder et al.*, 2003). In addition to the alongshore currents, the onshore flow of the nutrient-rich Slope Water occurs in several major cross-shelf channels (*Smith et al.*, 2001), including Laurentian Channel, Sable Gully, Scotian Gulf and Northeast Channel (see Fig. 1.1).

In addition to the Nova Scotia Current and the shelfbreak current mentioned above, the salinity and sea level on the Scotian Shelf are also influenced by the St. Lawrence River discharge, which peaks in May due mainly to the melting of sea ice and snow. The freshwater discharge generates an estuarine plume and a density-driven coastal current that propagates out of the Gulf of St. Lawrence and influences the salinity and circulation on the Scotian Shelf. A salinity variation associated with the spring-discharge plume takes about 6 months (*Sutcliffe et al.*, 1976) and 8-9 months (*Smith*, 1989) to reach the Halifax Line and Cape Sable, respectively. In addition, large sea level variations associated with the spring-discharge plume appear in the tide gauge observations along the coast. To demonstrate these variations, daily sea level observations from 1981 to 2010 at 10 tide gauges in the Gulf of St. Lawrence and along the south shore of Nova Scotia are averaged to generate the monthly mean sea levels (Fig. 2.1). At the head of the St. Lawrence Estuary (stations 1-4, Fig. 2.1), the monthly mean sea levels show an eastward reduction of the amplitude and phase propagation of the annual sea level maximum from April to July. The further downstream propagation of the spring-discharge plume signature in the monthly mean sea level is outweighed by other processes (e.g., wind stress and inverse barometer effect) along the western side of the Gulf of St. Lawrence and along the south shore of Nova Scotia.

Wind forcing is another forcing function affecting the circulation and hydrography on the Scotian Shelf, particularly in the upper water column. Figure 2.2 shows the annual and seasonal mean windroses calculated from hourly wind observations made by the weather station at Sable Island in 2006. The large seasonal variability in the hourly wind speed and direction is evident from these windroses with the predominant wind changing from southwesterly in summer to northwesterly in winter. The dominant southwesterly wind is favorable for coastal upwelling on the inner Scotian Shelf (*Petrie et al.*, 1987).

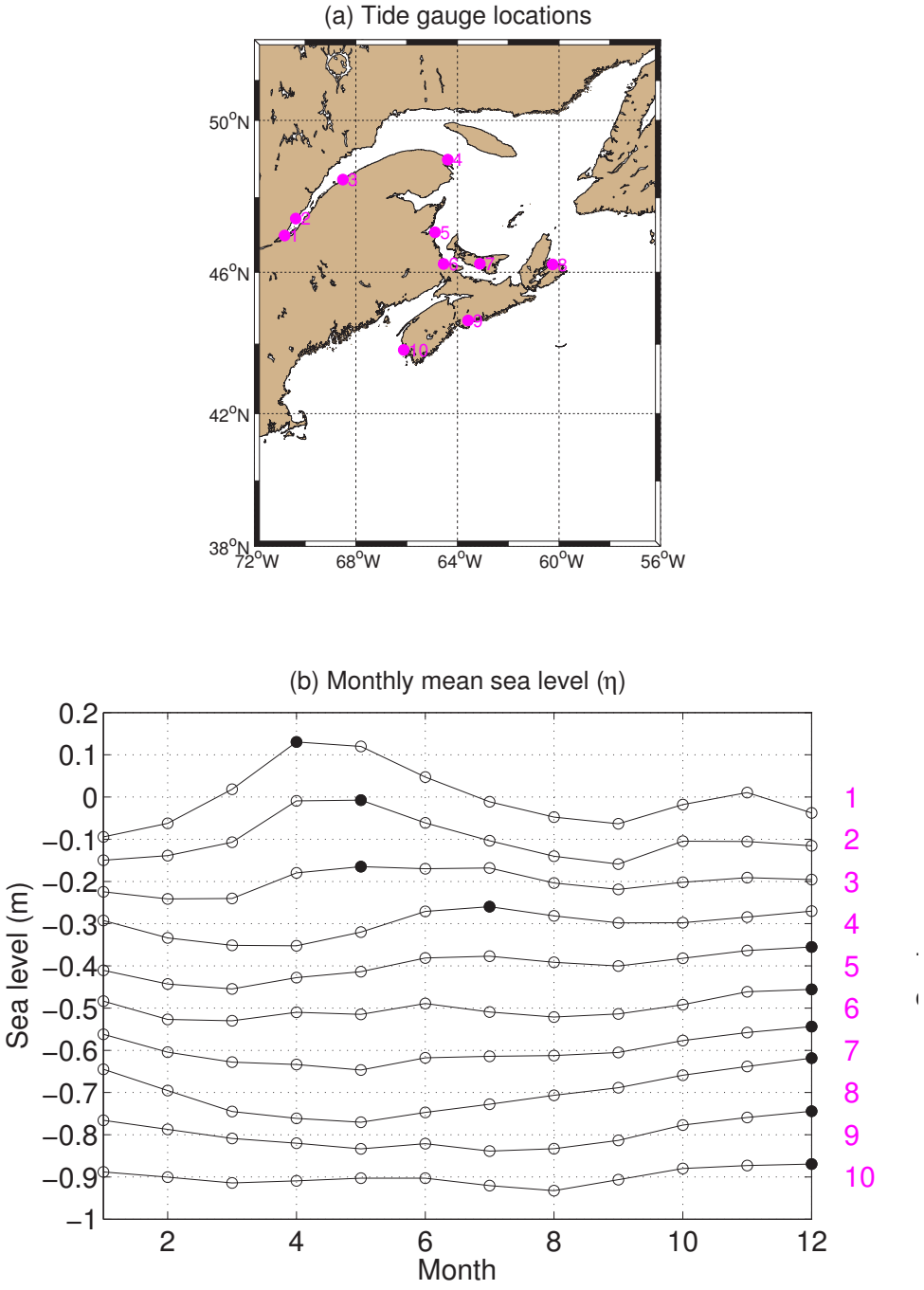

Figure 2.1: Monthly mean sea level at 10 selected tide gauges in the Gulf of St. Lawrence and along the coast of Nova Scotia. Positions of the 10 tide gauges are marked by magenta circles in (a). The black solid circles in (b) indicate the monthly mean sea level maxima. The lower series have been offset by 0.1 m from the one directly above. The observed sea level data are downloaded from `http://www.meds-sdmm.dfo-mpo.gc.ca`. The observations from 1981 to 2010 at each station are used to calculate the monthly sea level.

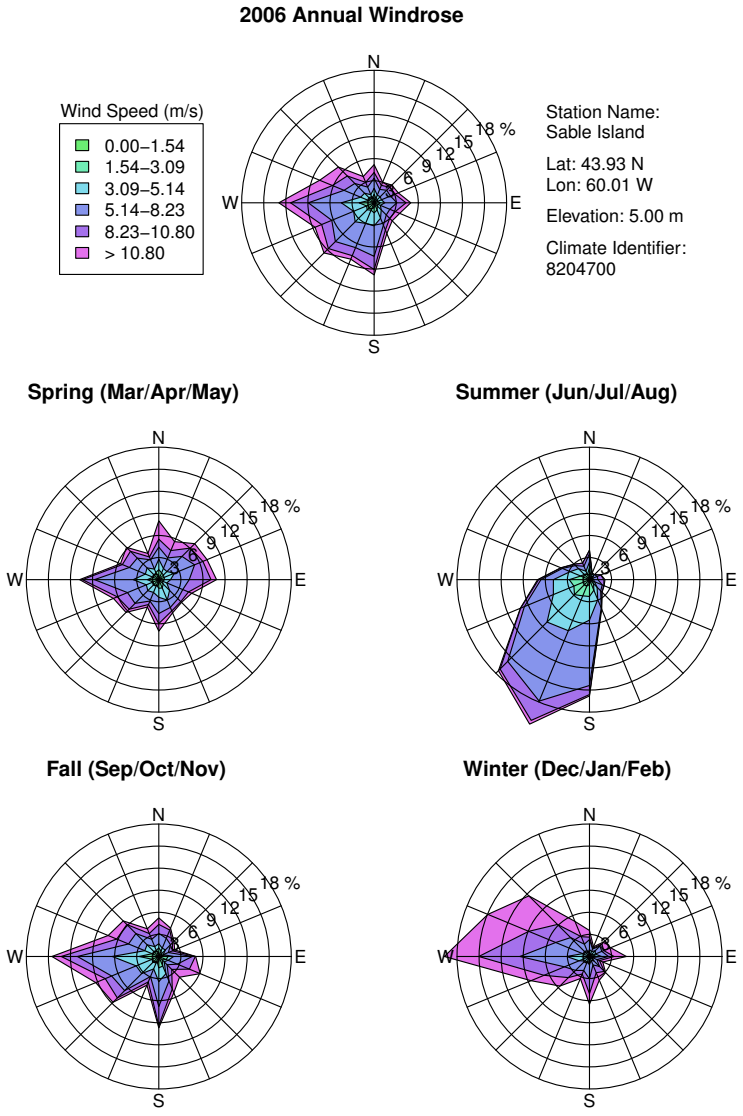

Figure 2.2: Annual and seasonal mean windroses at Sable Island based on the hourly weather station records in 2006. Each concentric circle represents a different frequency, emanating from zero at the center to increasing frequencies at the outer circles. Each arm is broken down into discrete frequency categories that show the percentage of time that winds blow from a particular direction and at certain speed ranges. Data were extracted from the National Climate Data and Information Archive of Canada (`http://climate.weather.gc.ca`).

2.3 Sea Surface Temperature Observed by Satellite and Buoy

Sea surface temperature (SST) observations made by the Moderate Resolution Imaging Spectroradiometer (MODIS) were obtained from the Ocean Color Website (`http://oceancolor.gsfc.nasa.gov`). It should be noted that the MODIS SST observations were often limited by the unfavorable atmospheric conditions such at high cloud coverage and storms over the Scotian Shelf. Two snapshots of MODIS SST observations on April 12 and October 9, 2006 presented in Fig. 2.3 are used to illustrate typical distributions of SSTs over the Scotian Shelf and adjacent waters in spring and fall of 2006. On April 12, cold surface waters occurred over the eastern Scotian Shelf, Laurentian Channel, Gulf of St. Lawrence and northwestern Grand Banks. Relatively warmer waters appeared in the Gulf Stream to the south of 40°N. Over the Slope Water region, a sharp thermal front with backward breaking waves were evident. On October 9, the SSTs were relatively uniform on the continental shelf. The sharp thermal front with meanders, filaments and backward breaking waves were also evident between the shelf waters and Gulf Stream waters. The SSTs in the Sable Gully on these two days (Fig. 2.3) were relatively uniform.

Two snapshots of MODIS sea surface temperature (SST) observations shown in Fig. 2.4 are also selected to illustrate the Nova Scotia Current and coastal upwelling in the central Scotian Shelf. The MODIS SST on March 10, 2012 (Fig. 2.4a) demonstrates the cold water plume associated with the Nova Scotia Current over the inner Scotian Shelf. The SST on September 1, 2012 (Fig. 2.4b) indicates an ongoing upwelling event near the coast. The relatively cold filaments extended $\sim$100 km offshore and advected to the southwest by the Nova Scotia Current.

The hourly time series of observed sea surface temperatures recorded by a marine buoy outside Halifax Harbour for the past 14 years (March 2000-March 2014, Fig. 2.5a) demonstrates that the SST has significant temporal variability on various timescales with the seasonal cycle being the dominant. The monthly mean climatological SST calculated from the 14-year hourly observations features a minimum of about 0.9°C in March and a maximum of about 15.8°C in September. The SST also has significant interannual variability around the monthly mean. For example, the monthly mean SST in March 2003 was about 1.5°C colder than the climatology and the monthly SST in August 2012 was about 2.7°C warmer than the climatology. In addition, the monthly mean SSTs in other

months of 2012 were all warmer than the climatology as shown in Fig. 2.5b. In fact, warm temperature anomalies in 2012 were also observed at various locations from surface to bottom over the SS and GoM as reported by *Hebert et al.* (2013) (Fig. 2.6, last column represents year 2012 and is shaded in red and purple.) The seasonal anomaly of SST in 2012 calculated by subtracting the seasonal cycle from the observed SST is presented in Fig. 2.5b. The seasonal anomaly of SST in 2012 was relatively small in winter and relatively large in summer (magenta line in Fig. 2.5b). A rapid SST cooling of $\sim$10°C at the end of August is associated with the upwelling event captured by the MODIS (Fig. 2.4b).

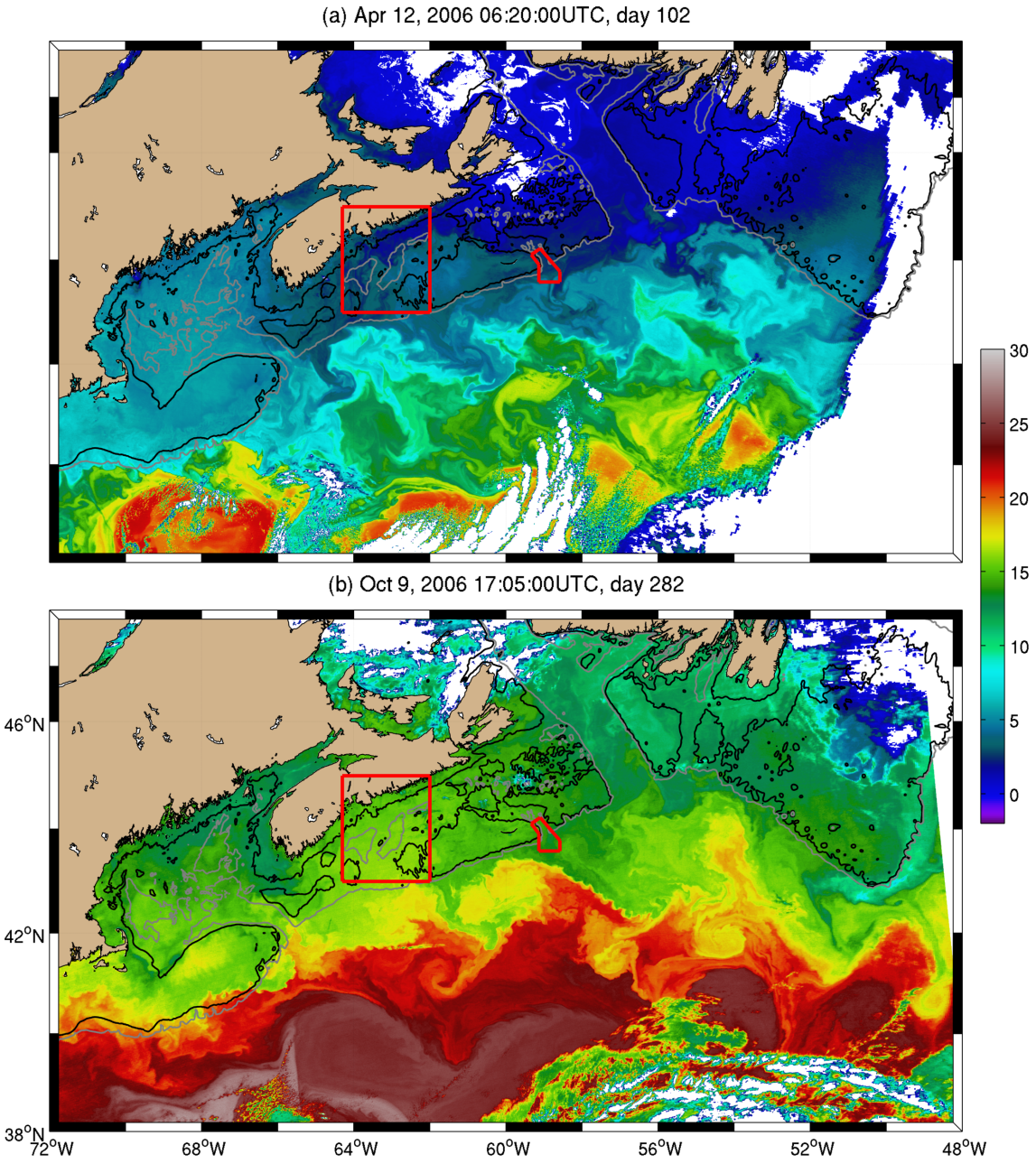

Figure 2.3: MODIS satellite remote sensing data of sea surface temperature (SST) over the Scotia Shelf and adjacent waters on (a) April 12 and (b) October 9, 2006. Data were extracted from the Ocean Color Website (`http://oceancolor.gsfc.nasa.gov`). The red polygon outlines the Gully Marine Protected Area. The red rectangle outlines the central Scotian Shelf adjacent to Halifax. The 100 m and 200 m isobaths are shown in black and gray contours, respectively.

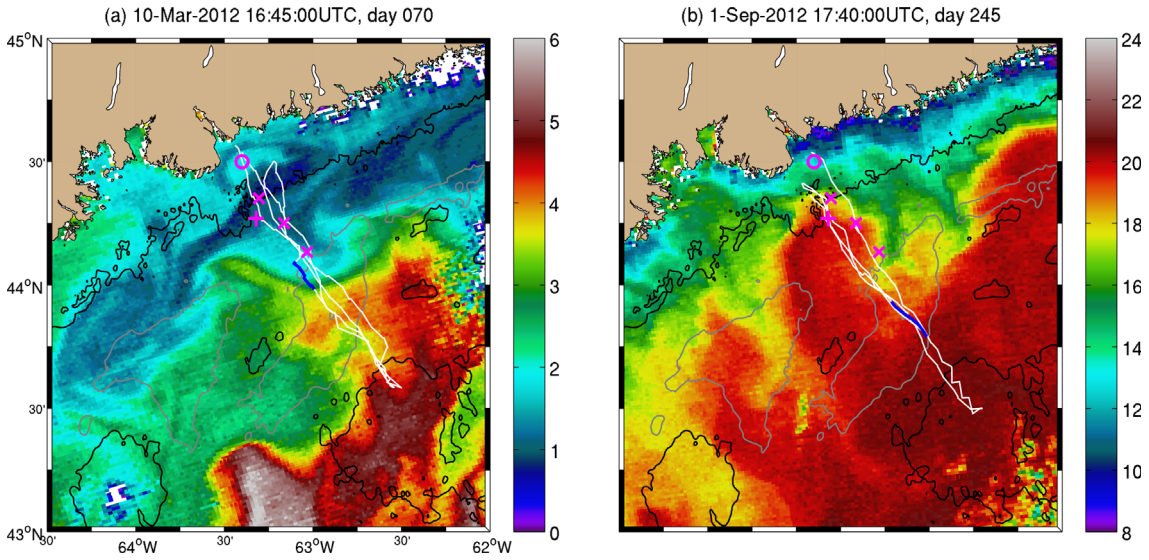

Figure 2.4: MODIS satellite remote sensing sea surface temperature (SST) over the central Scotian Shelf adjacent to Halifax on (a) March 10 and (b) September 1, 2012. Data were extracted from the Ocean Color Website (`http://oceancolor.gsfc.nasa.gov`). In each panel, the white line indicates the glider track during the corresponding month. The blue portion on the glider track highlights the path during the corresponding day. The "$\circ$" ,"$+$","$\times$" indicate the positions of the marine buoy outside Halifax Harbour, Station 2 of Halifax Line, and three moorings of OTN project, respectively. The 100 (black) and 200 (gray) isobaths are shown.

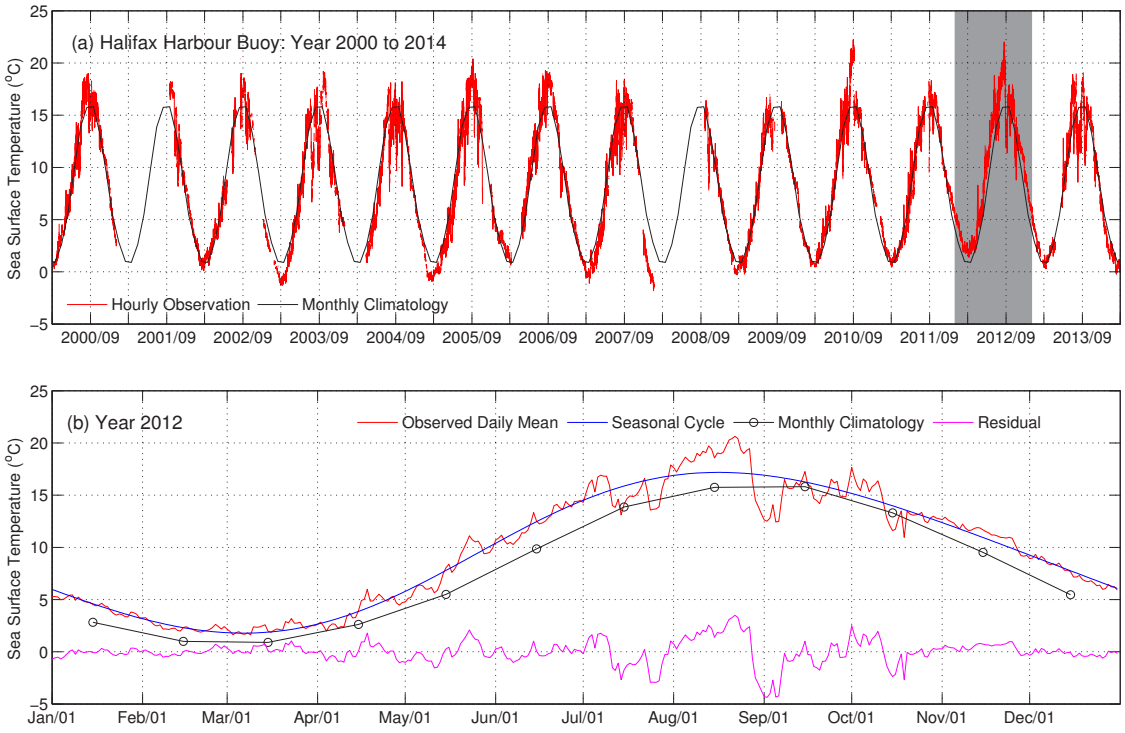

Figure 2.5: (a) Hourly time series of observed sea surface temperatures (red) between March 2000 and March 2014 and the monthly mean climatology (black) at the Halifax Harbour Buoy. The monthly mean climatology was calculated from the 14-year hourly observations. (b) Daily mean (red) sea surface temperature of 2012 calculated from the hourly observations. The daily mean is separated into the annual and semiannual harmonics (blue) and seasonal anomaly (magenta). The black line with open circles in (b) represents the monthly mean climatology shown in (a). Note an upwelling event occurred at the end of August 2012.

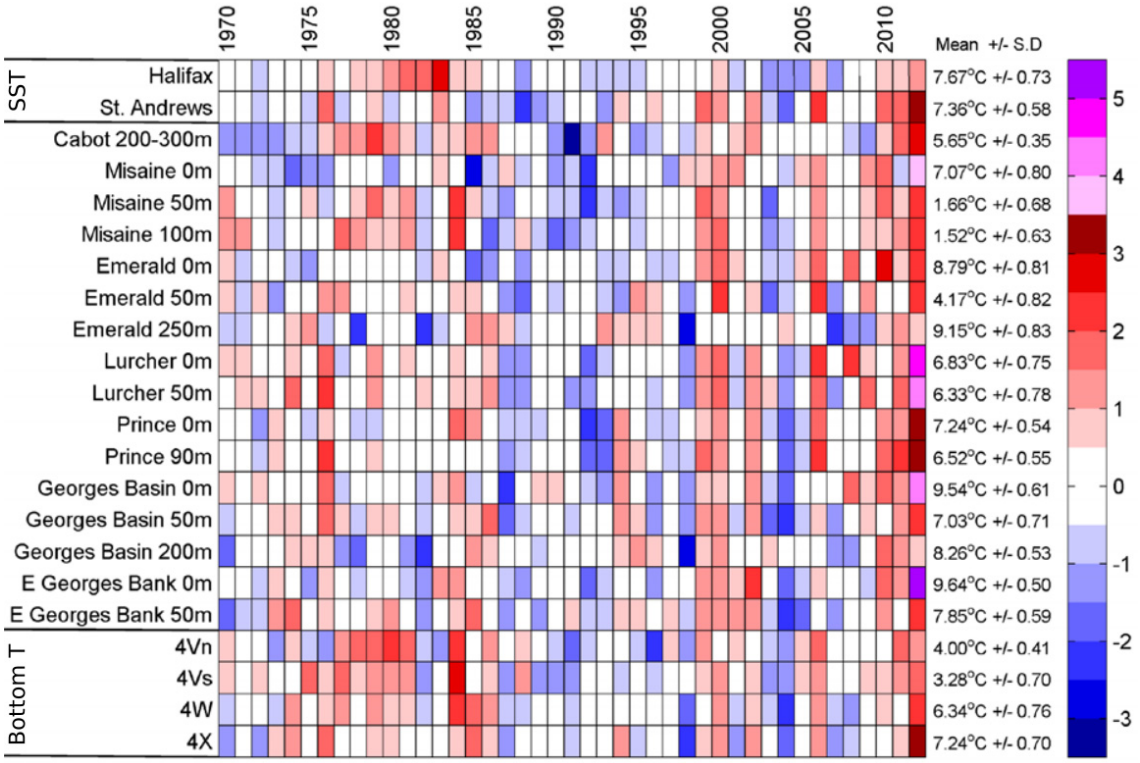

Figure 2.6: Normalized annual anomalies of temperatures at the bottom and discrete depths for the Scotian Shelf-Gulf of Maine region. These anomalies are based on the 1981-2010 means, divided by the standard deviation. Blue colors indicate below normal anomalies, red colors above normal anomalies. (For 2012, the color scale had to be increased above +3.5 SD and is shaded in purple.) 4Vn, 4Vs, 4W and 4X represent Northwest Atlantic Fisheries Organization area over the Scotian Shelf and adjacent waters. (Adapted from *Hebert et al.* 2013)

2.4 Temperature Transects Observed by Glider

Autonomous underwater gliders are valuable platforms for ocean observations. An underwater glider is able to move vertically and horizontally in a saw-tooth trajectory in the ocean by using an active buoyancy regulating unit combined with a set of fixed wings. With this special movement, a glider loaded with a suite of sensors can provide sustained observations at high spatiotemporal resolution of the ocean interior. The glider has been used to observe the ocean processes at various time and length scales including the eastern and western boundary currents, fronts and eddies, and internal waves and turbulent dissipation (see *Rudnick* (2016) for a review). The glider observations are also useful to validate numerical ocean circulation models and improve model skill through data assimilation.

Underwater gliders have been used to observe the oceanic conditions on the Scotian Shelf since 2011. Figure 2.7 presents time-depth distributions of glider observed temperatures on the Halifax Line in March and August-September 2012. The glider tracks are shown with MODIS SSTs in Fig. 2.4. In March, the glider observations show the cold water plume ($<4°C$) associated with the Nova Scotia Current centred at the 100 m isobath and relatively warm waters in the deep layer of the Emerald Basin (Fig. 2.7a). In August-September, the glider observations demonstrate the typical three layer distribution in the vertical on the Scotian Shelf (Fig. 2.7b). The surface layer was relatively warm ($>15°C$) at this time due to the positive heat flux from the atmosphere to the ocean. This warm surface layer traps a cold intermediate water layer between the seasonal thermocline and warmer but saltier bottom waters that intrude from beyond the shelf break, thus creating three distinct water types in the vertical on the Scotian Shelf. Figure 2.7b also illustrates that the temperatures in the top 20 m on September 2 and 5 were relatively cold as the glider flying through the upwelling plume towards the coast .

The *in-situ* and satellite remote sensing data discussed in this chapter together with other oceanographic observations will be used in later chapters to assess the performance of nested-grid ocean circulation models.

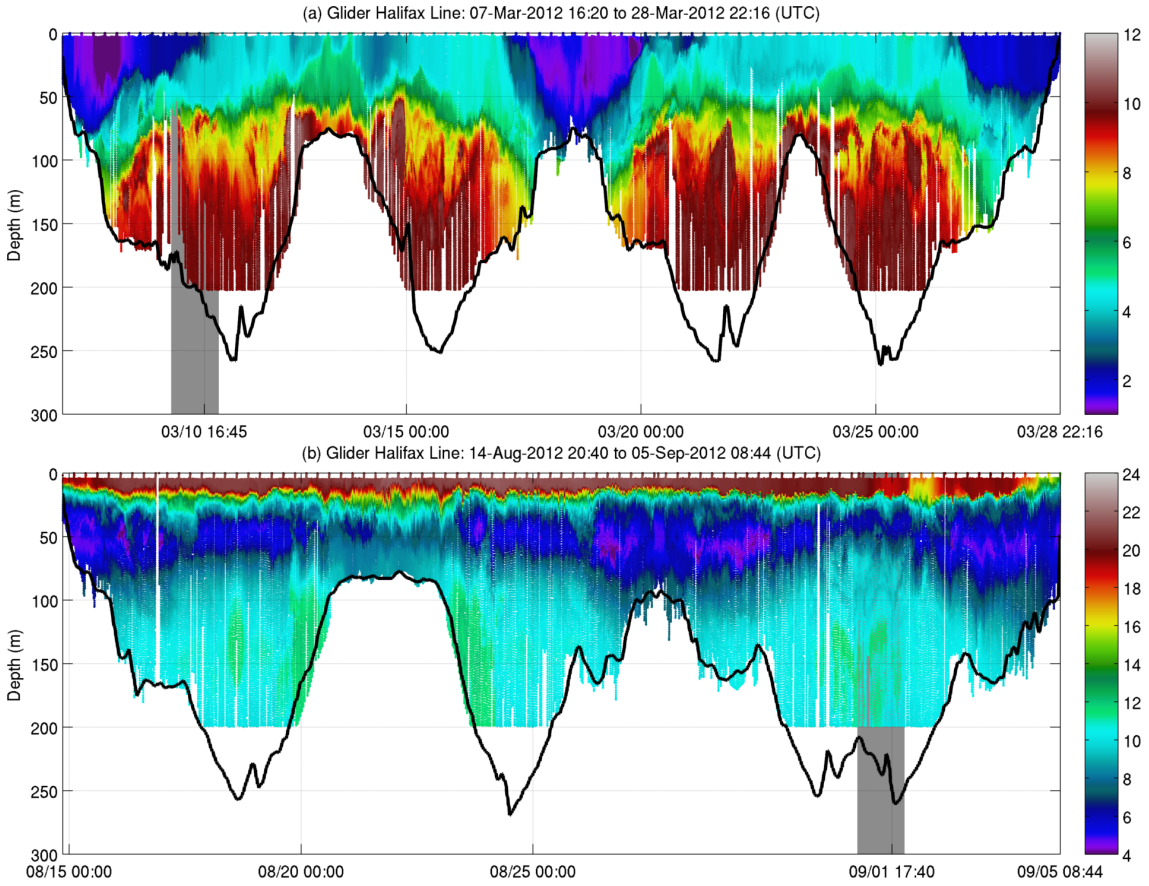

Figure 2.7: Underwater glider observations of temperature in (a) March 2012 and (b) in August-September 2012. The gray areas highlight glider observations on (a) March 10 and (b) September 1, and the corresponding MODIS SSTs on the these two days are presented in Fig. 2.4. The glider tracks are also shown in Fig. 2.4. The glider observations were provided by the glider research group from Dalhousie University (`http://gliders.oceantrack.org`).

CHAPTER 3

SABLE GULLY AND ADJACENT WATERS [1]

3.1 Introduction

The continental slope of the global ocean plays an important role in many physical, geological, biological and chemical oceanic processes. Submarine canyons are steep-sided valleys cut into the continental slope, and sometimes extend further onto the continental shelf. As a unique geographic feature along the continental margin, there are at least 660 submarine canyons worldwide (*De Leo et al.*, 2010). Submarine canyons are often recognized as hotspots of biological activity, fueled by strong and localized currents and upwellings that help transport food into canyons. Observations show that species diversity and abundance are greater in canyons than in noncanyon areas at comparable depths, indicating the importance of submarine canyons to the vibrant and complex marine ecosystem (*De Leo et al.*, 2010). Canyon ecosystems, and the physical processes that support them, have been the main focus of some recent research projects (e.g., HERMES from 2002 to 2009 and its successor HERMIONE, `www.eu-hermione.net`).

The Sable Gully is a large submarine canyon on the eastern seaboard of North America, which is located approximately 40 km east of Sable Island on the edge of the eastern Scotian Shelf and separates Banquereau Bank and Sable Island Bank (Fig. 1.1). Banquereau Bank is located on the eastern flank of the Gully which is about 150 km west of the Laurentian

[1] This chapter was modified from two peer-reviewed papers entitled: (1)"Physical processes affecting circulation and hydrography in the Sable Gully of Nova Scotia" by Shan, S., J. Sheng, and B. J. W. Greenan published in *Deep Sea Research Part II: Topical Studies in Oceanography* in 2014; and (2)"Modelling study of three-dimensional circulation and particle movement over the Sable Gully of Nova Scotia" by Shan, S., J. Sheng, and B. J. W. Greenan published in *Ocean Dynamics* in 2014.

Channel. The Laurentian Channel is a trough of 300–400 m depth, spanning the Gulf of St. Lawrence (GSL) from the northwest to southeast and through the Cabot Strait to the continental slope. Sable Island Bank is located on the western flank of the Sable Gully, featuring a narrow and crescent-shaped sandbar — Sable Island. As a broad, deep submarine canyon, the Sable Gully is 10 km wide and 40 km long running from northwest (head) to southeast (mouth), reaching depths of over 2000 m near its mouth and narrowing significantly along its sinuous axis toward the head (Fig. 1.1). The Sable Gully is unique among canyons on the eastern Canadian continental shelf because of its depth, steep slopes and extension far onto the shelf.

The circulation and its variability in the Gully and adjacent waters are influenced by the Labrador Current, the outflow from the GSL, and warm-core eddies pinched from the Gulf Stream. Part of the Labrador Current that flows around the tail of Grand Banks reaches the eastern Scotian Shelf by crossing the Laurentian Channel. Part of the low-salinity estuarine water emanated from the GSL moves onto the eastern Scotian Shelf after passing western Cabot Strait. The rest of the estuarine water continuously flows southeastward along the Laurentian Channel and joins the Labrador Current at the shelf break of the Scotian Shelf to form a southwestern shelfbreak jet outside the mouth of the Gully. To the south of the Scotian Shelf break, the warm and salty Slope Water Jet flows northeastward (*Csanady and Hamilton*, 1988).

The circulation and hydrography in the Sable Gully and adjacent waters can have important implications for the nutrient supply to the ecosystem, commercial fishery and natural gas industry operations of the region (Sable Offshore Energy Project, `www.soep.com`). The Sable Gully is a hotspot of marine biodiversity (*Rutherford et al.*, 2002), which is home to a variety of marine organisms, such as northern bottlenose whale, dolphins, squid, shrimp and deep-water coral. The Gully appears to be a prime habitat for whales and offers an important source of food. It was suggested that whales feed year-round on deep-water squid that is concentrated in the Gully, and their distribution and movement patterns are related to foraging and access to food resources (*Rutherford et al.*, 2002). Relatively little is known, however, about the foraging behavior and distribution of these whales. High concentrations of organic carbon at the head, and along the sinuous deep channel of the Gully (thalweg), also suggest that the canyon may act as a conduit for the production and export of organic matter to the deep ocean (*Kepkay et al.*, 2002). The Gully's unique

physical attributes, its ecological significance and increasing human pressures, generated a major conservation interest during the mid-1990s. In 2004, Canada designated the Sable Gully as a Marine Protected Area (*Gully Marine Protected Area Regulations*, 2004) with the intent of securing long-term protection for the core of the deep-water canyon ecosystem, although the physical mechanism responsible for the nutrient transport required to sustain the enhanced productivity in the Gully remains to be addressed.

The general circulation and hydrographic distributions over submarine canyons have been studied using observational, theoretical and numerical methods. Submarine canyons along the east and west coasts of North America are some of the most studied sites (*Shepard and Dill*, 1969), including Baltimore Canyon (*Hunkins*, 1988), Carson Canyon (*Kinsella et al.*, 1987), Monterey Canyon (*Hall and Carter*, 2010 and references therein) and Astoria Canyon (*Hickey*, 1997). *Shepard et al.* (1974) conducted one of the early comprehensive observation studies on the circulation of submarine canyons. *Hickey* (1995) provided a review of progress on understanding the interaction of the submarine canyon with stratified coastal circulation. The progress was due to the availability of measurements over canyon flanks and to the development of circulation models with realistic topography. *Klinck* (1996) examined the effect of stratification (weakly or strongly) and direction of alongshore flow (upwelling or downwelling) on the circulation near idealized submarine canyons. *Allen and Durrieu De Madron* (2009) reviewed the state of the science describing the dynamics of flows in submarine canyons and pointed out that accurate numerical simulations over canyons are challenging.

Efforts have also been made to understand the physical processes of the Sable Gully through observations and numerical modelling. *Petrie et al.* (1998) reviewed the general physical oceanographic conditions in the Gully, primarily based on the sparse historical observations and coarse shelf-scale numerical modelling results, to provide an initial indication of the key resources and related conservation issues in the Gully. *Sandstrom and Elliott* (1984, 2011) observed and discussed internal tides and their associated enhanced mixing along the edge of the Scotian Shelf, particularly in the Sable Gully. A multi-disciplinary field program was carried out in 2006-07 over the Sable Gully (*Greenan et al.*, 2014), of which the physical oceanographic component consisted of the deployment and recovery of four current-meter moorings and conductivity, temperature, and depth (CTD) (conductivity, temperature, and depth) surveys. *Swart et al.* (2011) studied the

tidal currents based on mooring observations and employed a simple idealized 1.5-layer, linear model to examine the amplification of tidal currents in the Gully. *Greenan et al.* (2014) further discussed the mean circulation, bottom-intensified tidal current, overtides and compounded tides and enhanced vertical mixing in the Gully. *de Margerie and Lank* (1986) found relatively strong tidal currents over shallow banks and relatively weak tidal currents in deep waters of the Gully using a two-dimensional (2D) tidal model. *Han et al.* (2001) developed a diagnostic numerical model for the eastern Scotian Shelf to examine the three-dimensional (3D) tidal currents and seasonal mean circulation. Their diagnostic model had a horizontal resolution of $\sim$2 km for the Gully and 61 vertical levels, and the model was integrated only for 6-8 M_2 cycles.

Particle tracking models are widely used to investigate the transport pathways, mixing, residence time and hydrodynamic connectivity in the ocean as mentioned in Chapter 1. Based on our literature review, the only particle tracking study over the Sable Gully was conducted by *Cong et al.* (1996). In their study, passive particles were tracked on the Scotian Shelf at a fixed depth of 30 m using a non-tidal flow field driven mainly by the wind forcing with a horizontal resolution of $\sim$5 km. They found that particles are retained over some offshore areas on the Scotian Shelf, including the Gully and Banquereau Bank.

The Sable Gully's complex topography and unique physical attributes pose a great challenge for accurate numerical simulations of circulation and hydrography over the Gully and adjacent waters. The main objectives of this study are, therefore, to simulate the 3D circulation and hydrography and examine the main physical processes over the Sable Gully using a multi-nested ocean circulation model with realistic topography and a suite of forcing functions. The innermost submodel of the multi-nested circulation model has a horizontal resolution of $\sim$500 m over the Gully, which allows us to resolve small-scale circulation features in the region. The simulated time-dependent 3D flow fields are then used by a particle tracking model to examine the role of physical environments on the movements of passive particles in the Gully.

This chapter is organized as follows. A multi-nested ocean circulation model for the Sable Gully is described in Section 2. The model performance is assessed in Section 3 by comparing model results with oceanographic observations. The major physical processes affecting the circulation and hydrography in the Gully and adjacent waters are discussed in Section 4 based on model results in different experiments. A series of particle

tracking experiments are presented in Section 5. Based on the particle movements, the upstream/downstream area and residence time in the Gully are discussed and quantified. The implications for the distribution and migration of northern bottlenose whale in the Gully and adjacent canyons are discussed in section 6. The results of this study are summarized in the final section.

3.2 Numerical Modelling System

The numerical modelling system used in this study has two components: a 3D circulation model and a particle tracking model. The former is the multi-nested circulation model developed for the Sable Gully and adjacent waters (DalCoast-Gully). The latter is based on the fourth-order Runge-Kutta method to track the movements of passive particles carried by the time-dependent 3D flow fields produced by DalCoast-Gully.

3.2.1 Multi-Nested Circulation Model

The ocean circulation model used in this study was modified from the circulation modelling system developed previously for two coastal waters along the Nova Scotia coast: Lunenburg Bay (DalCoast-LB, *Yang and Sheng*, 2008) and Halifax Harbour (DalCoast-HFX, *Shan et al.*, 2011). Both DalCoast-LB and DalCoast-HFX were extensively validated against observations. In this study, the three innermost submodels of DalCoast-HFX are relocated to the Sable Gully and adjacent waters for covering the core of the Gully Marine Protected Area. The innermost submodel of the Gully is modified to have a finer resolution in the vertical to accommodate the steep bathymetry and unique attributes of the Sable Gully at the shelf break. As a result, the latest model setup is named as DalCoast-Gully. The main advantage of the multi-nested model is that fine-scale circulation features in the Gully can be resolved by the finest-resolution submodel driven by dynamically consistent open boundary conditions provided by larger domain, coarser resolution submodels.

The DalCoast-Gully has five submodels with progressively smaller model domains and finer horizontal resolutions covering from the northwest Atlantic to the Sable Gully (Fig. 3.1). The two outermost submodels, L1 and L2, are based on DalCoast (*Thompson et al.*, 2007) and constructed from the Princeton Ocean Model (POM, *Mellor*, 2004). Submodels L3 to L5 are based on the free-surface version of CANDIE (*Sheng et al.*, 1998), which is a 3D, primitive equation ocean circulation model that uses an A-grid, z-level

and fourth-order advection scheme. The outermost submodel L1 is a 2D barotropic storm surge model covering the eastern Canadian shelf from the Labrador Shelf to the Gulf of Maine with a horizontal resolution of 1/12°. Submodel L2 is a 3D prognostic model with horizontal resolutions of 1/16° and 30 σ-levels in the vertical. Submodels L3 to L5 are also 3D and prognostic with horizontal resolutions of $\sim$2 km, $\sim$1 km and $\sim$500 m, respectively.

The bathymetry varies significantly in the Gully. A fine resolution topography (100 m) for the Sable Gully region was constructed based on multibeam observations provided by the Canadian Hydrographic Service. This newly constructed topography for the Gully was used in submodels L4 and L5. To better resolve the steep topography in the model, particularly along the shelf break, 80 unevenly-spaced z-levels in the vertical are used in L3 to L5 with relatively fine vertical resolutions of 4 m in the top 100 m, and 8 m between 100 m and 250 m, and 100 m in the deep water. A detailed description of the nested-grid modelling system is presented in appendix A. The DalCoast-Gully was integrated for 13 months from December 2005 to December 2006. The model results of year 2006 are used in the validation, discussion and particle tracking experiments in this study.

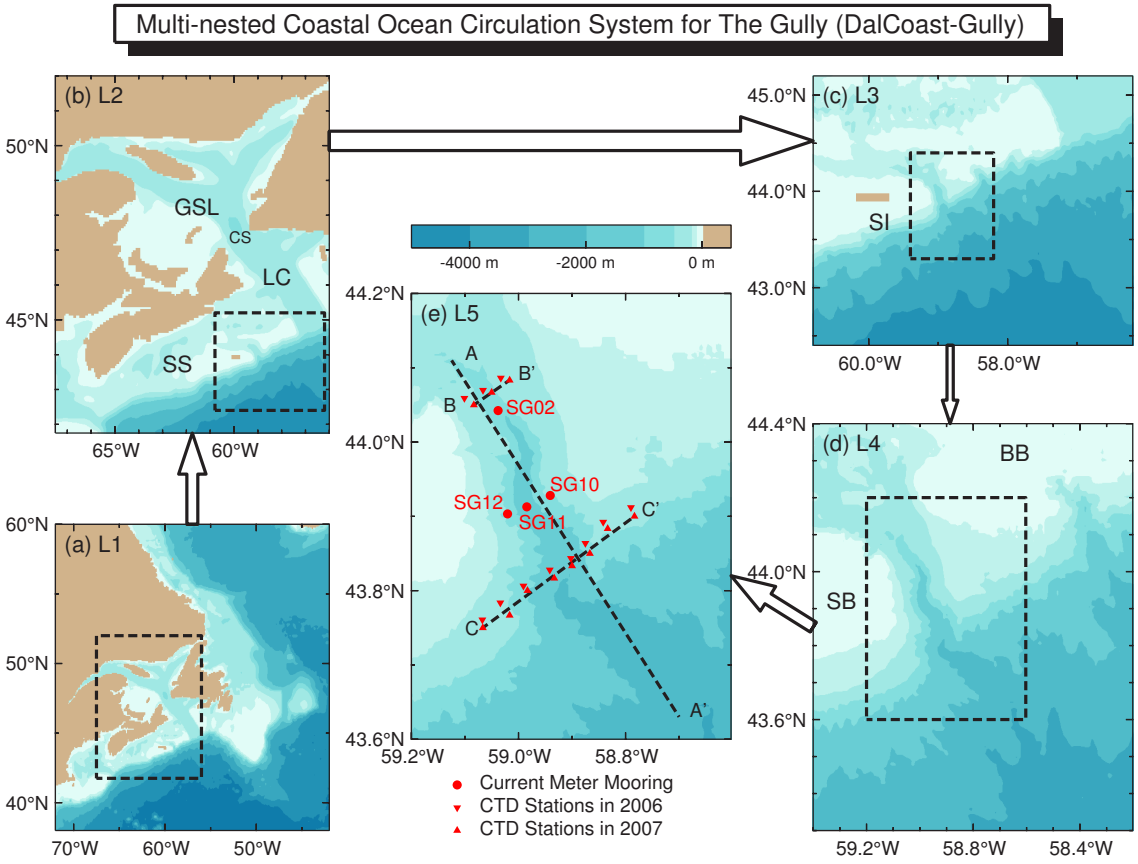

Figure 3.1: Major topographic features and domains of the five-level multi-nested modelling system for the Sable Gully and adjacent waters. Submodel (a) L1 and (b) L2 are based on DalCoast (*Thompson et al.*, 2007), with horizontal resolutions of 1/12° and 1/16°, respectively. Submodels (c) L3, (d) L4 and (e) L5 are based on CANDIE (*Sheng et al.*, 1998), with horizontal resolutions of ∼2 km, ∼1 km and ∼500 m, respectively. The one arc-minute global relief dataset (ETOPO1, `http://www.ngdc.noaa.gov/mgg/global/global.html`) was used for the bathymetry of L3. Bathymetry of Submodels L4 and L5 is based on the multibeam observations. Red dots in (e), indicate positions of four current moorings: SG02, SG10, SG11 and SG12; the dashed lines represents three transects along the longitudinal axis of the Sable Gully (AA'); and across the head (BB') and mouth (CC') of the Gully. Triangles in (e) denote CTD stations on the transects. Land is masked in tan color. Scotian Shelf (SS), Gulf of St. Lawrence (GSL), Laurentian Channel (LC) and Cabot Strait (CS) are marked in (b). Sable Island (SI) is marked in (c). Sable Bank (SB) and Banquereau Bank (BB) are marked in (d).

3.2.2 Particle Tracking Model

The movement of a particle in the water can be described by advection due to the currents and random walk associated with the subgrid-scale diffusion:

$$\vec{x}^{t+\Delta t} = \vec{x}^{t} + \int_{t}^{t+\Delta t} \vec{u}(\vec{x}, t)\, dt + \vec{\delta}^{t} \tag{3.1}$$

where $\vec{x}^{t+\Delta t}$ and $\vec{x}^{t}$ are respectively the 3D position vectors of a passive particle at time $t + \Delta t$ and previous time t, $\vec{u}(\vec{x}, t)$ is the 3D velocity vector of model currents, and $\vec{\delta}^{t}$ is a random displacement from t to $t + \Delta t$ to account for particle movement associated with subgrid-scale turbulence and other local processes which are not resolved by the model. The random walk $\vec{\delta}(\delta_x, \delta_y, \delta_z)$ is expressed as (*Taylor*, 1922):

$$\delta_x = \xi\sqrt{2K_x\Delta t}, \qquad \delta_y = \xi\sqrt{2K_y\Delta t}, \qquad \delta_z = \xi\sqrt{2K_z\Delta t} \tag{3.2}$$

where ξ is a Gaussian random variable with zero mean and unit variance, and are different in the three directions. K_x, K_y and K_z are respectively eddy diffusivity coefficients for the random walk in the x, y and z directions, and Δt is the same time-step used in the integration of Eq. (3.1). The fourth-order Runge-Kutta scheme (*Press et al.*, 1992) is used to calculate the part that depends on $\vec{u}$ in Eq. (3.1) numerically.

The above particle tracking model can be used to answer where the particles go and where the particles come through forward and backward in time tracking, respectively. Considering a patch of particles carried passively by the model flow field ($\vec{u}$) with the random walk ($\vec{\delta}$), the positions of particles have a distribution of $\mathbf{X}$ at a time s. At a later time t, where $t > s$, the positions of particles have a distribution of $\mathbf{Y}$. The transition probability density, $P(s, \mathbf{X}; t, \mathbf{Y})$, satisfies the following Kolmogorov forward equation (*Kolmogorov*, 2000):

$$\frac{\partial P(s, \mathbf{X}; t, \mathbf{Y})}{\partial t} + \nabla \cdot [\vec{u}(t, \mathbf{Y})P] = \mathbf{K}\nabla^2 P \tag{3.3}$$

where $\mathbf{K}(K_x, K_y, K_z)$ is the eddy diffusivity coefficient for the random walk with constant values horizontally and vertically. The Kolmogorov forward equation is also known as the advection-diffusion equation or Fokker-Planck equation. The Kolmogorov forward equation is physically intuitive and commonly used to describe "where will the particles go?". The complementary question: "where did the particles come from?" can be

addressed by the Kolmogorov backward equation (*Kolmogorov*, 2000), which is the adjoint of Eq. (3.3):

$$-\frac{\partial P(s,\mathbf{X};t,\mathbf{Y})}{\partial s}-\vec{u}(s,\mathbf{X})\cdot\nabla P=\mathbf{K}\nabla^2 P \tag{3.4}$$

The main difference in the forward and backward Kolmogorov equations is the advection term, which can be expanded into two components:

$$\nabla\cdot(\vec{u}P)=\vec{u}\cdot\nabla P+P\nabla\cdot\vec{u} \tag{3.5}$$

If the flow field is non-divergent: $\nabla\cdot\vec{u}=0$, the backward tracking can be achieved by reversing the flow field in time (*Thygesen*, 2011).

In this study, we set the vertical eddy diffusivity coefficient (K_z) for the random walk in the control case to be about 180 $\times 10^{-4}$ m^2 s^{-1} based on a correlation analysis for observed temperature time series from a mooring at two depths in the Gully (*Greenan et al.*, 2014). Previous field dye tracing experiments in coastal waters demonstrated that the observed horizontal eddy diffusivity coefficient is about 1000 times larger than the vertical eddy diffusivity coefficient (*Riddle and Lewis*, 2000). Thus, the horizontal diffusivity coefficient (K_h) for the random walk in the control case is set to be homogeneous and isotropic (K_x=K_y=K_h) with a characteristic value of 180 $\times 10^{-1}$ m^2 s^{-1}. The simulated 3D flow field produced by DalCoast-Gully is non-divergent since the ocean is assumed to be incompressible. It is justified, therefore, to use the reversed flow field produced by DalCoast-Gully for the 3D tracking backward in time.

3.3 Model Validation

The performance of DalCoast-Gully in simulating the circulation, hydrography and their associated horizontal and vertical variations in the Sable Gully and adjacent waters is assessed by comparing model results with various types of independent oceanographic observations including current-meter data, the OSU (Oregon State University) tidal dataset, and CTD casts.

Current-meter observations to be used in the validation were made at four moorings deployed in the Sable Gully (Fig. 3.1e) from late April 2006 to early August 2007. One of the moorings was located at the Gully head (SG02). The other three moorings were deployed on an across-canyon transect perpendicular to the longitudinal axis of the Gully marked as SG10, SG11 and SG12 (Fig. 3.1e), which were on the eastern, central and

western parts of the Gully, respectively. More discussion about this Gully observation project can be found in *Greenan et al.* (2014).

To assess the accuracy of submodel L5 in simulating the time-mean circulation in the Sable Gully, the instantaneous model currents in year 2006 are averaged to generate the annual mean currents. Figure 3.2 shows vertical profiles of the simulated annual mean currents at the four moorings in the Gully. The simulated annual mean currents are characterized by relatively intense surface currents and a very strong vertical shear at depths above the Gully rim ($\sim$200 m). The simulated annual mean current speeds decrease roughly linearly downward to near zero at the depth of the Gully rim. The simulated surface currents at the four moorings are southwestward and greater than 10 cm s^{-1}. At depths below the Gully rim, the simulated annual mean currents are much weaker with a northwestward mean flow along the longitudinal axis of the Gully (SG02 and SG11), suggesting a weak and on-shelf transport in the Gully. Figure 3.2 also demonstrates that the simulated currents have relatively large seasonal variability above the Gully rim and small seasonal variability below the rim.

The vertical profiles of the simulated annual mean currents are in fair agreement with the observed profiles at four moorings, particularly at SG10, SG11 and SG12 (Fig. 3.2). The fit between the simulated and observed currents can be quantified in terms of γ^2 defined as:

$$\gamma^2 = \frac{\sum (O - M)^2}{\sum O^2} \tag{3.6}$$

where O and M denote the observed and simulated variables respectively. Thus, γ^2 is smaller when there is better agreement between observed and simulated values. At SG10, SG11 and SG12, we found $\gamma^2 < 0.7$ for both the eastward and northward components of time-mean currents. These relatively low γ^2 values indicate that DalCoast-Gully reproduces reasonably well the vertical profile of observed currents in the Gully on the annual mean timescale. At SG11, the simulated annual mean currents are consistent with the observed values including the southwestward shear flow at depths above the Gully rim and northwestward on-shelf flow at depths below the rim. At SG10 and SG12, the observed currents and associated vertical variations above and below the Gully rim are also reconstructed reasonably well by the model. At the Gully Head (SG02), there are relatively large differences between the observed and simulated currents at depths below the Gully rim, with γ^2 values to be about 1.2 and 0.7 respectively for the eastward and northward components of the currents. The exact reason for these large differences is unknown.

It should be noted that current observations at SG02 were made only at depths greater than 125 m. It is also worthwhile to note that the moorings along the longitudinal axis of the Gully experienced significant knockdowns when the magnitude of the instantaneous currents reached as high as 100 cm s^{-1} (*Greenan et al.*, 2014). The large differences between the annual mean currents and instantaneous currents indicate that there are strong oscillating tidal components in the flow. These high velocities and knockdowns mean that the nominal depths of the instruments may not accurately reflect their positions all the time, which could explain some of large discrepancies between the observed and simulated results.

In addition to the assessment of the simulated annual mean currents, Figure 3.3 presents vertical profiles of simulated seasonal mean currents at the center of the Sable Gully where observations were collected by a mooring (SG11) from April 2006 to August 2007 (Fig. 3.1e). The simulated seasonal mean currents feature relatively intense surface currents with a very strong vertical shear at depths above the Gully rim ($\sim$200 m). The simulated seasonal mean surface currents in the Gully are southwestward throughout the year with relatively large magnitudes in the fall and winter. The current speeds decrease almost linearly downward to near zero at the depth of the Gully rim. At depths below the Gully rim, the seasonal mean currents are much weaker with a northwestern mean flow along the Gully thalweg, suggesting the weak and on-shelf transport in the Gully. The vertical profiles of the simulated seasonal mean currents are in good agreement with the observed profiles at SG11, including the southwestern shear flow at depths above the Gully rim and northwestern on-shelf flow at depths below the rim.

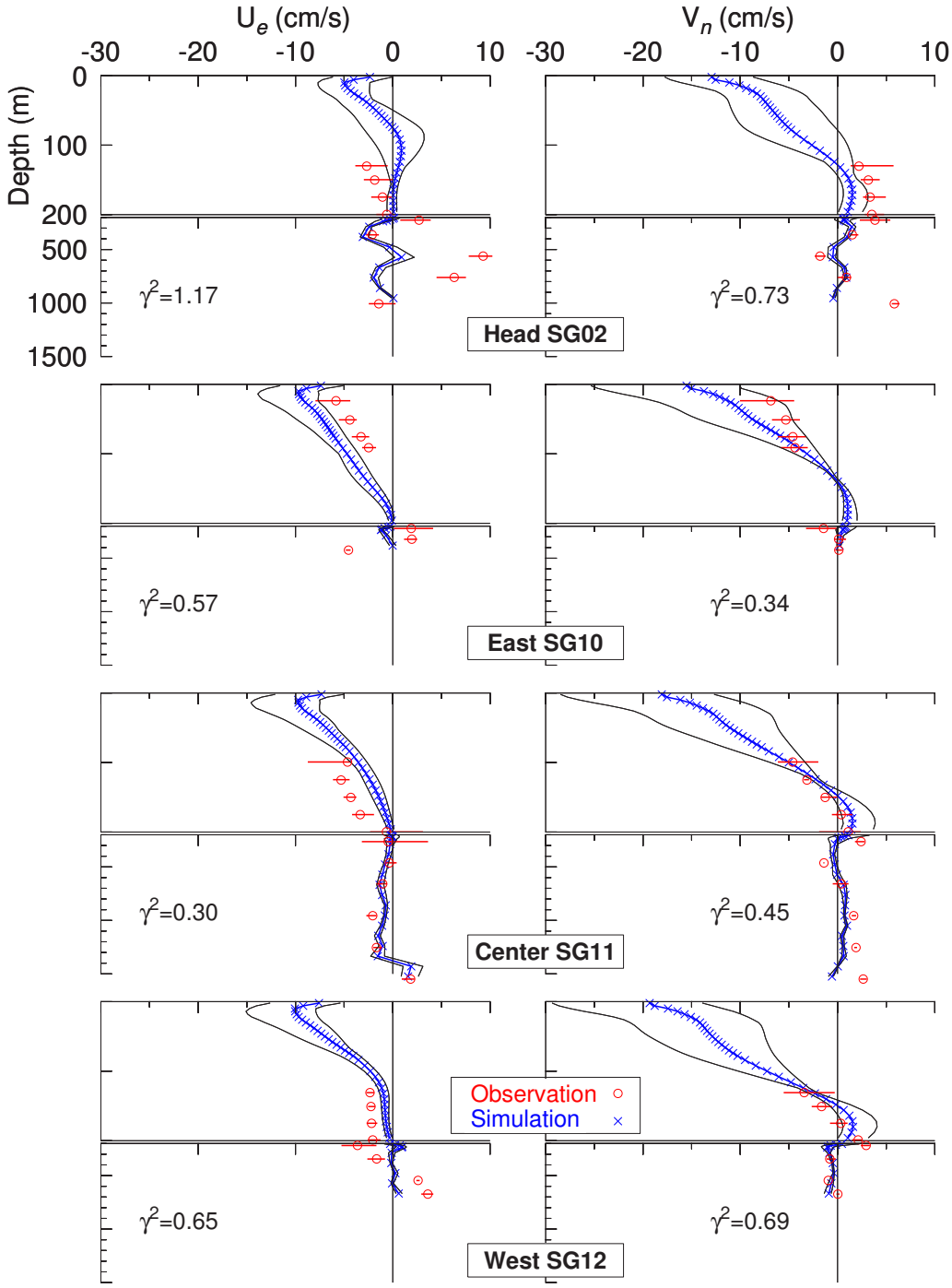

Figure 3.2: Vertical profiles of the horizontal components (U_e, V_n) of time-mean currents at four mooring stations: SG02, SG10, SG11 and SG12 in the Sable Gully. The positions of four moorings are marked in Fig. 3.1e. The blue solid curves with cross marks represent the annual mean currents in 2006 produced by submodel L5 of DalCoast-Gully. The two black curves represent the minima and maxima of simulated seasonal mean currents. The open red circles represent the mean currents computed from current-meter observations from April 2006 to August 2007. The endpoints of the red horizontal line segment on each red circle represent the observed minima and maxima of seasonal mean currents.

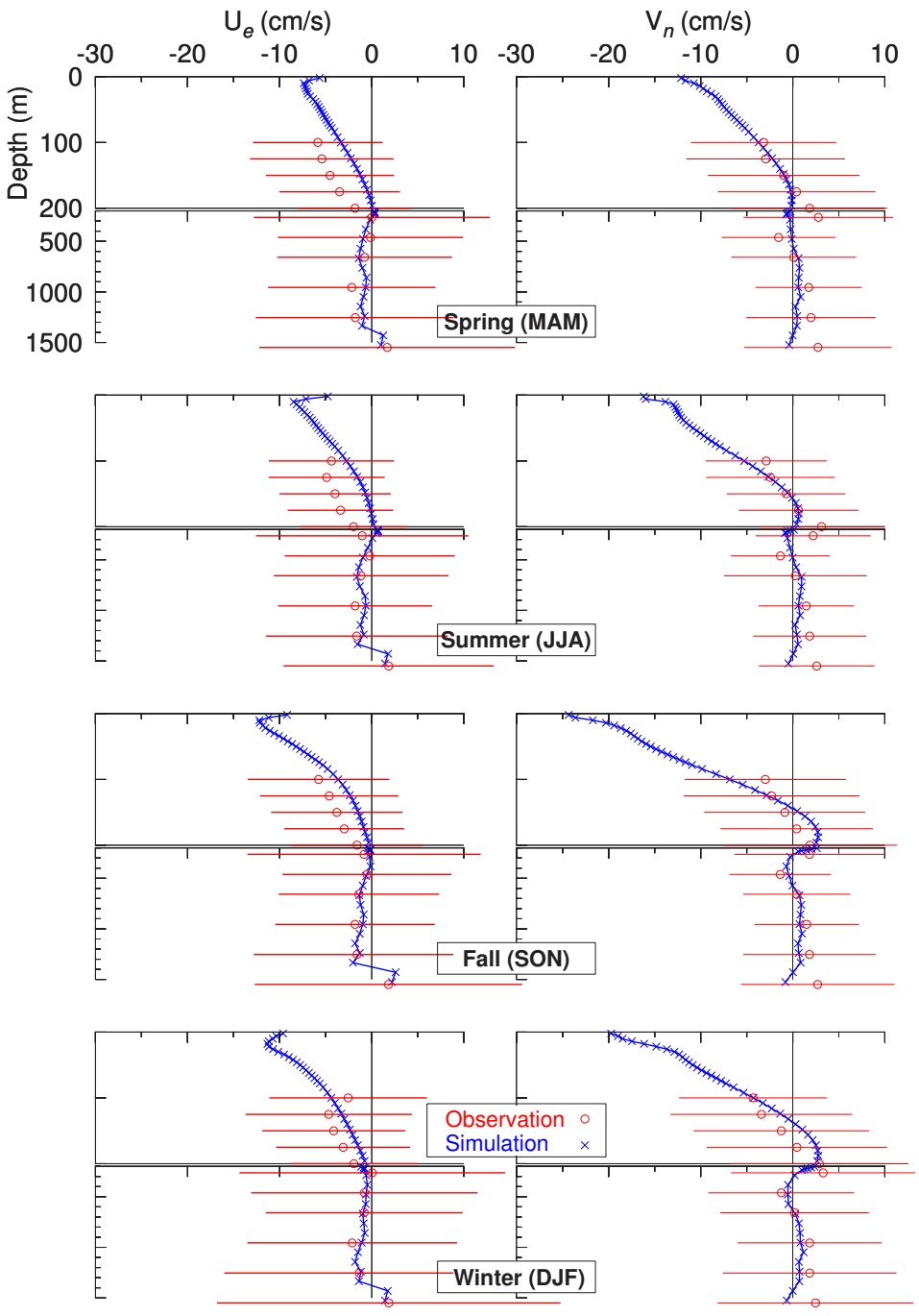

Figure 3.3: Vertical profiles of seasonal mean currents in the eastward (U_e) and northward (V_n) directions at the center of the Sable Gully (SG11). The position of this mooring is marked in Fig. 3.1e. The blue solid curves with crosses represent the seasonal mean currents in 2006 calculated from the non-tidal component in submodel L5. The open red circles represent the seasonal mean currents calculated from the non-tidal component of the current-meter observations from April 2006 to August 2007. The horizontal red lines indicate ± 1 standard deviation of the observed hourly non-tidal component.

The subtidal circulation in the Sable Gully has profound seasonal variability, especially in the subsurface. Figure 3.4 presents monthly mean currents in February and August 2006 at two selected depths (surface and 200 m) produced by submodel L5 of DalCoast-Gully. At the surface, the simulated February mean currents feature a southwestward flow over Banquereau Bank with magnitudes of $\sim$10 cm s^{-1}. Over the Gully and Sable Island Bank, the February mean surface currents turn cyclonically and run roughly southward. The February mean surface currents are southwestward and relatively strong in the deep waters off the Scotian Slope. It should be noted that the mean wind stress in February is northwesterly over the domain of submodel L5 (Figs. 3.4a and 2.2). Based on the steady *Ekman* (1963) theory, the steady-state surface currents forced directly by the wind stress are at 45° to the right of the wind direction. The simulated surface currents shown in Fig 3.4a have an angle of about 135° to the right of the wind stress vectors, indicating that other forcing functions (e.g., shelf-scale circulation) in addition to the wind forcing play an important role in driving the monthly mean circulation. At the subsurface (200 m) (Fig. 3.4b), the simulated February mean currents feature a strong southwestward flow with a typical magnitude of $\sim$10 cm s^{-1} along the shelf break outside the Gully. Inside the Gully, the northwestward currents are relatively weak and less than 5 cm s^{-1} flowing along the Gully thalweg. At the head of the Gully, the simulated February mean currents feature a partial cyclonic circulation. There is a very weak southeastward return flow along the western flank of the Gully. By comparison, the August mean surface currents have similar circulation patterns as in February, except that the surface currents are stronger over the Gully and weaker along the shelf break (Fig. 3.4a and c). At the subsurface (200 m), the southwestward flow along the shelf break is relatively weak in August in comparison with the flow in February. The monthly mean northwestward (on-shelf) subsurface currents along the Gully thalweg diminished significantly to nearly zero in August.

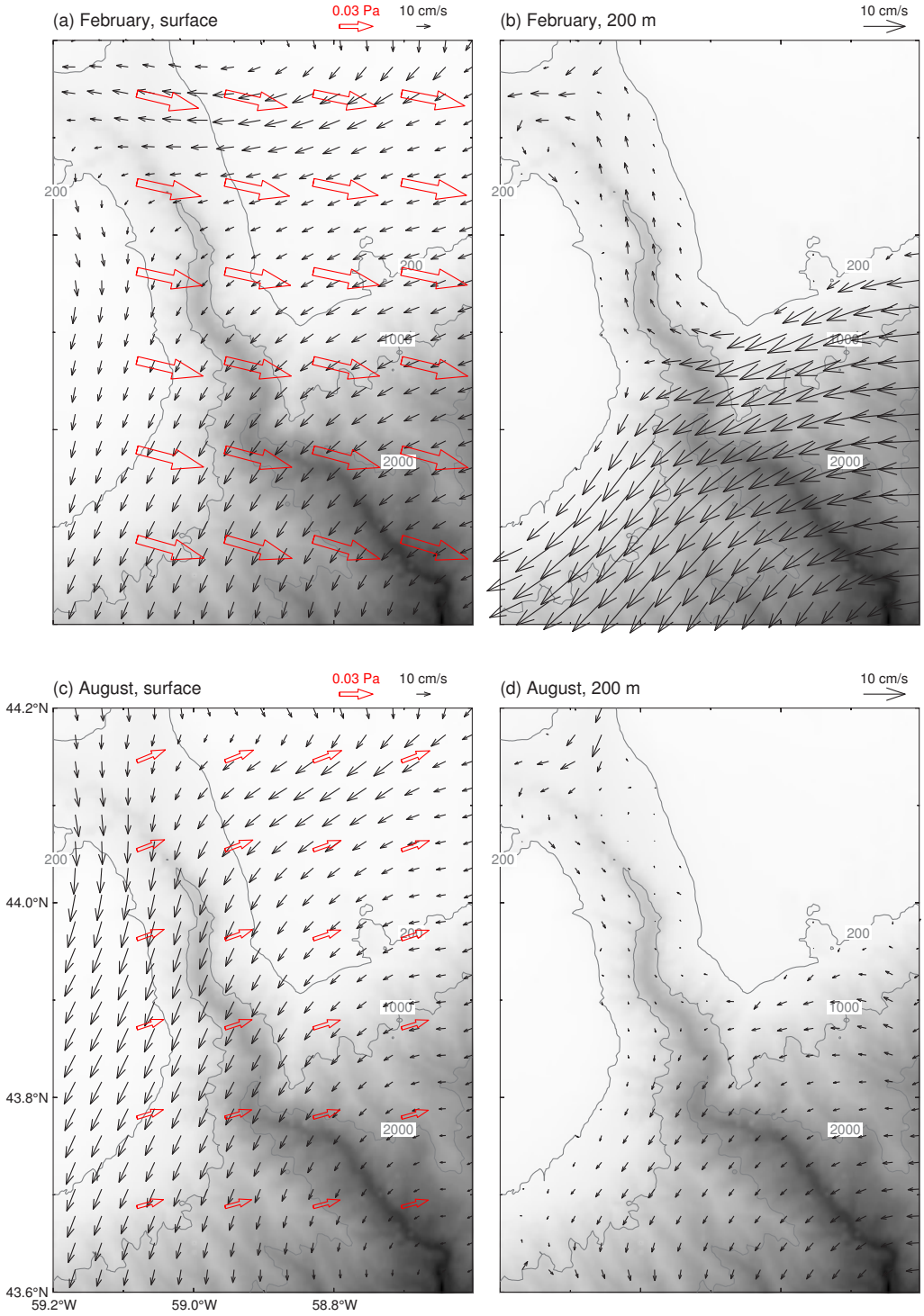

Figure 3.4: February (a and b) and August (c and d) mean surface and subsurface (200 m) currents in 2006 in the Sable Gully and adjacent waters produced by submodel L5 of DalCoast-Gully. Black arrows represent ocean currents. Open red arrows represent wind stress vectors. For clarity, ocean currents and wind stress vectors are plotted at every 6th and 20th model grid point, respectively. Selected isobaths in meters are shown by the gray contours.

Tidal currents are an important component of the total currents in the Sable Gully (*Swart et al.*, 2011). We next examine the distributions of major tidal currents of M_2 and K_1 computed from submodel L5 results in March 2006, when the near-surface water column was well mixed and the barotropic dynamics were dominant. It should be noted that tides on the outer Scotian Shelf are affected by stratification as shown in the studies made by *Ohashi et al.* (2009) and *Katavouta* (2015).

The simulated tidal currents during this period have significant spatial variations (Fig. 3.5). The simulated depth-averaged tidal currents of M_2 and K_1 in March (Fig. 3.5a and b) are relatively strong over shallow banks and relatively weak in the deep waters over the Gully and adjacent continental slope. The simulated tidal currents intensified from the mouth to head of the Gully (Fig. 3.5a and b) due to topographic funneling and amplification of tidal energy travelling toward the Gully head (*Swart et al.*, 2011).

The simulated depth-averaged tidal ellipses are in good visual agreement with the 2D tidal model results produced previously by *de Margerie and Lank* (1986). The simulated tidal currents of M_2 and K_1 are further compared with the OSU (Oregon State University) tidal dataset for the east coast of North America. (A detailed description of this dataset can be found at `http://volkov.oce.orst.edu/tides/EC.html`.) The OSU tidal dataset is the best tidal dataset available to this region and it was generated using a 1/30° horizontal resolution barotropic tidal circulation model with assimilation of various altimetric observations (*Egbert et al.*, 1994; *Egbert and Erofeeva*, 2002).

The tidal current ellipses of M_2 and K_1 produced by submodel L5 are in good agreement with the tidal current ellipses extracted from the OSU tidal dataset, especially in the Gully, over the Scotian Slope, and the shallow bank to the west of Gully (Fig. 3.5a and b). The model performance is quantitatively assessed by using a root-mean-square error estimate in each direction defined as $E_{rms} = n^{-1} \sum_n D$, where n is the number of data points and D is the root-mean-square difference over a tidal cycle between observed and simulated velocities in each direction (*Cummins and Oey*, 1997; *Carter*, 2010; *Hall et al.*, 2011):

$$D = \sqrt{\frac{1}{2}(A_o^2 + A_m^2) - A_o\, A_m \cos(\phi_o - \phi_m)} \tag{3.7}$$

where A and ϕ are amplitudes and phases for a given tidal current constituent, and subscripts $_o$ and $_m$ refer to observed and simulated values, respectively. The $E_{rms}(U_e, V_n)$ are about (1.4, 1.5) cm s^{-1} for M_2 and about (1.6, 1.7) cm s^{-1} for K_1, where U_e and V_n are eastward and northward components of depth-averaged tidal currents, respectively.

It should be noted that the simulated tidal current ellipses of M_2 and K_1 are smaller on the shallow bank to the east of the Gully in comparison with the OSU tidal dataset. The OSU dataset has a horizontal resolution of 1/30° over the Sable Gully region, which barely resolves the major topographic feature of the Gully (Fig. 3.5c and d). Therefore, the large differences between our model results and the OSU dataset are partially due to the coarse horizontal resolution in the OSU dataset. This is consistent with the previous finding by *Martin et al.* (2009), who demonstrated that the coarse model resolution and bathymetry are the major limiting factors affecting the accuracy of the OSU tidal dataset over certain regions.

The model performance in simulating the vertical variations of tidal currents of M_2 and K_1 are further examined by comparing observed and simulated M_2 and K_1 tidal currents at SG11 (Fig. 3.6), which was located at the center of the Sable Gully along its longitudinal axis. The $E_{rms}(U_e, V_n)$ are also calculated according to Eq. (3.7) for the eastward (U_e) and northward (V_n) components of tidal currents, which are about (2.5, 2.8) cm s^{-1} for M_2 and about (2.2, 2.8) cm s^{-1} for K_1. Both the observed and simulated tidal currents have significant vertical variability (Fig. 3.6). The observed tidal current ellipses are relatively elliptical with the semi-major axis of about 10 cm s^{-1} in the upper water column of less than 200 m. The tidal current ellipses change from elliptical shapes in the upper layer to rectilinear shapes which align with the longitudinal axis of the Gully below 400 m due to the topographic constraints. The observed tidal currents have large amplification towards bottom, particularly for the K_1. It was suggested that the observed tidal amplification is mainly due to internal waves and internal tides trapped at the bottom (*Gordon and Marshall*, 1976; *Swart et al.*, 2011). The simulated tidal current ellipses reasonably reproduce the observed tidal current ellipses including the complex tidal current ellipses variations around the depth of the Gully rim ($\sim$200 m) and the amplification in the middle layer. However, the simulated tidal currents decrease near bottom in contrast to the observations. It should be noted that submodel L5 uses staircase z-level grid with a relatively coarse resolution in the vertical near the bottom. Explicitly resolving internal waves and internal tides are challenging (*Carter et al.*, 2012) and beyond the scope of this study.

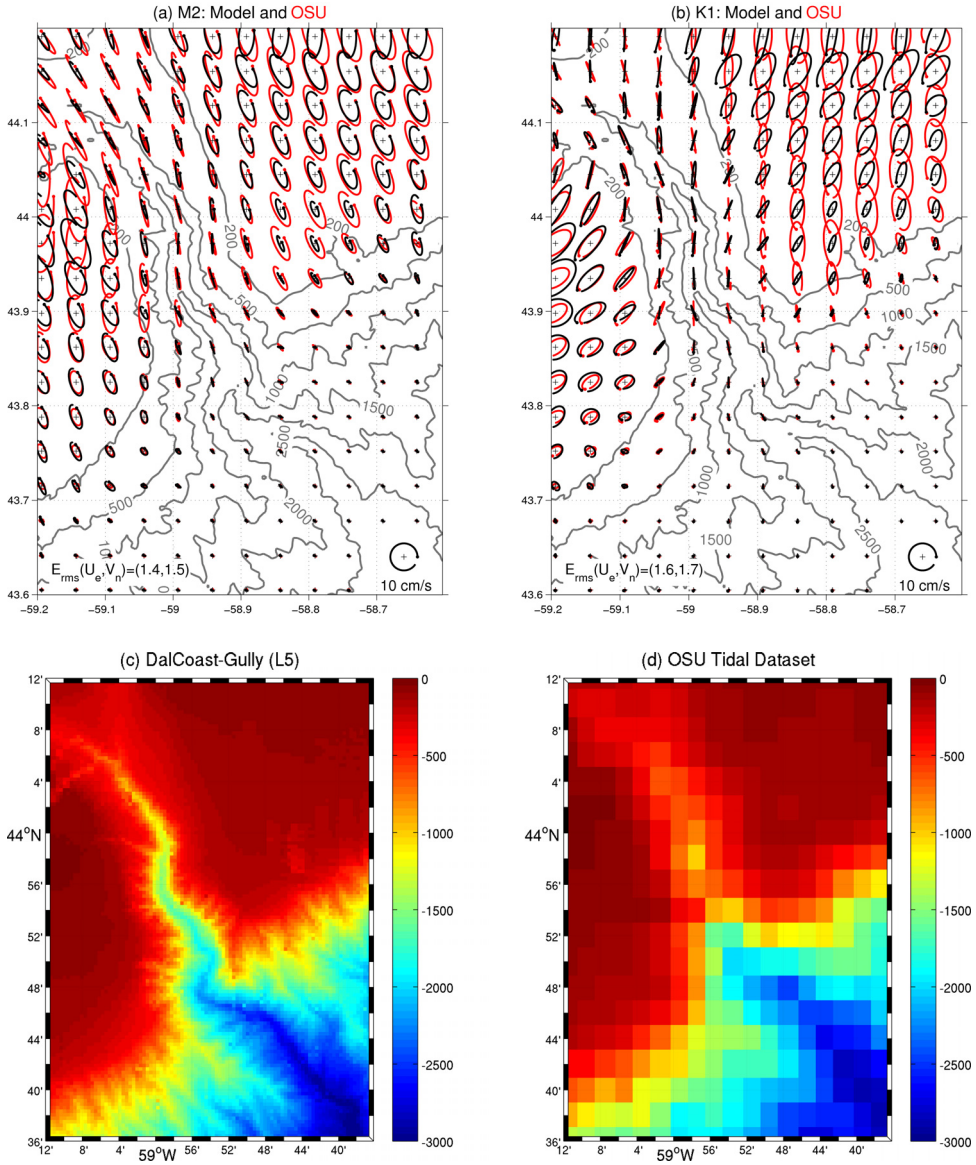

Figure 3.5: Tidal current ellipses of depth-averaged (a) M_2 and (b) K_1 calculated from the results produced by submodel L5 of DalCoast-Gully (in black) and OSU tidal dataset (in red). For the illustration purpose, the tidal current ellipses are shown at every 8th grid point of submodel L5 of DalCoast-Gully. Selected isobaths in meters are shown by the gray contours. The lower panels show the model bathymetry used in (c) submodel L5 of DalCoast-Gully and (d) OSU tidal dataset based on Global Topography Version 12.1 (*Smith and Sandwell*, 1997).

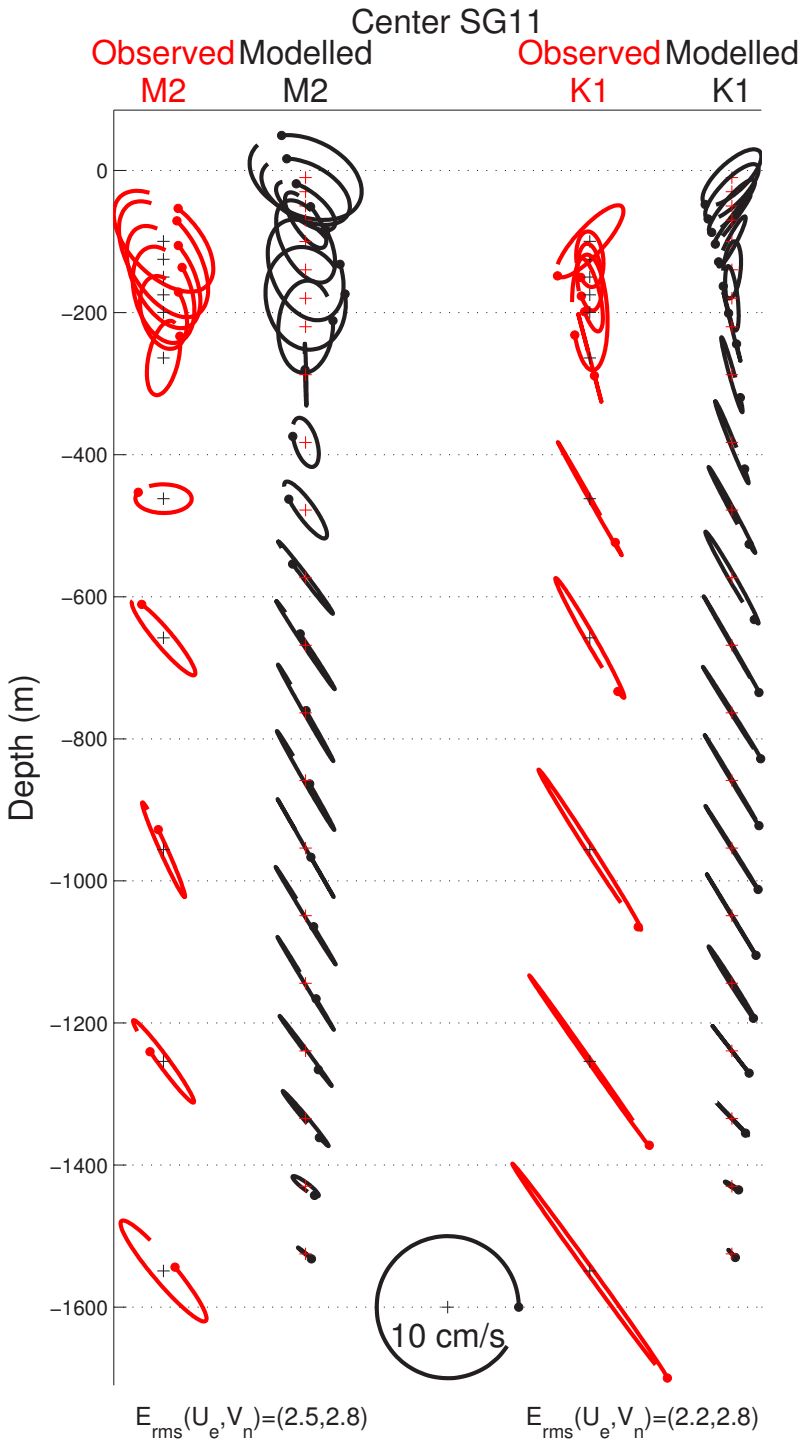

Figure 3.6: Vertical profiles of observed (in red) and simulated (in black) M_2 and K_1 tidal current ellipses at SG11. The "+" marks the center of each ellipse. The location of SG11 is marked in Fig. 3.1e. There are 80 unevenly-spaced z-levels in the vertical used in submodel L5 with relatively fine vertical resolutions of 4 m in the top 100 m, and 8 m between 100 m and 250 m, and 100 m in the deep water. For depth $<$ 250 m, the ellipses are plotted at every 5th z-level with the first level at 10 m. For depth $>$ 250 m, the ellipses are plotted at every z-level.

The model performance in simulating hydrography in the Sable Gully is assessed by comparing model results with the observed CTD temperature and salinity profiles made at the time of mooring deployment in late April 2006 and recovery in early August 2007, which allows us to examine the seasonal hydrographic variation in the Sable Gully. The model results in August 2006 are used for a qualitative comparison with the observations made in August 2007. Two across-canyon transects are selected for the comparison, one at the Gully head (BB') and the other at the Gully mouth (CC') (marked in Fig. 3.1e). The observed temperature and salinity fields were almost horizontally uniform along the two transects (not shown), therefore, vertical profile plots are used for the direct comparison between the observations and model results.

The observed hydrographic profiles in the Gully were characterized by large vertical variations in both temperature and salinity in the top 500 m, with a cold intermediate layer (CIL) centred at $\sim$50 m and warm intermediate layer (WIL) centred at $\sim$200 m (Figs. 3.7 and 3.8). The formation of the CIL is due mainly to the winter convection, wind-induced strong mixing in the previous winter and advection of cold water from northeast. Based on the warm and salty nature of the WIL, most likely the WIL water was originated over the Slope Water region (*Csanady and Hamilton*, 1988). The CIL was more pronounced in August in comparison with the CIL in April. The WIL was well-defined in April and had a sharp turning point in both temperature and salinity at about 100 m at the Gully mouth in August. The CIL and WIL alter the vertical stratification and may play an important role in the generation, propagation and dissipation of internal tides and internal waves (*Hall et al.*, 2014) and may also have significant biological implications to marine organisms in the Gully Marine Protected Area.

The hydrographic observations made in late April 2006 at the head and mouth of the Gully are presented in Fig. 3.7. At the Gully head, the observed surface temperature at this time was around 3°C (Fig. 3.7a). There was a CIL below the surface layer centred at about 50 m. Below the CIL, there was a WIL centred around 200 m. Below the WIL, the observed temperature in late April was about 5°C and decreased slowly with increasing depths. The observed salinity at this time was relatively low and about 32.5 in the upper water column of less than 50 m (Fig. 3.7b). The observed salinity increased significantly with depth and reached about 34.5 at a depth of $\sim$200 m. Below 200 m, the observed salinity increased gradually with increasing depths. At the Gully mouth (Fig. 3.7c and

d), the observed temperature and salinity had similar vertical distributions as at the Gully head, except that the CIL and WIL were relatively stronger. The observed temperature reached up to 10°C and the salinity was about 35 in the WIL.

The hydrographic observations made in early August 2007 at the head and mouth of the Gully are presented in Fig. 3.8. At the Gully head, the observed surface temperature was about 18°C due mainly to the positive surface heat fluxes from the overlying atmosphere (Fig. 3.8a). A CIL can be seen below the warm surface layer centred around 50 m. There was a WIL below the CIL with the highest temperature ($\sim$8°C) at depth of 200 m. At the Gully mouth (Fig. 3.8c and d), the observed temperature and salinity had the similar vertical structures in comparison with the observations at the Gully head except for the relatively stronger temperature and salinity gradients in the WIL.

The simulated temperature and salinity reproduce the general vertical variations in observations in late April and early August, particularly above the CIL and below the WIL (Figs. 3.7 and 3.8). The simulated temperature in the surface layer changes from cold well-mixed to warm stratified due to the the positive surface heat flux (i.e., the ocean gains heat from the atmosphere) in the model from April to August. It should be noted that the simulated CIL and WIL are too diffusive in comparison with the hydrographic observations. The simulated Slope Water intrusion is also too weak to propagate into the Gully head. The high salinity water associated with the WIL could not be seen between 100 to 500 m in the model results at the Gully mouth. There are three main factors limiting the accuracy of the DalCoast-Gully in simulating the CIL and WIL: (1) the coarse ($\sim$200 km) horizontal resolution NCEP reanalysis dataset used in calculating the net heat flux in the model, (2) the seasonal mean climatology used in submodel L2, and (3) the vertical mixing parameterization used in the model.

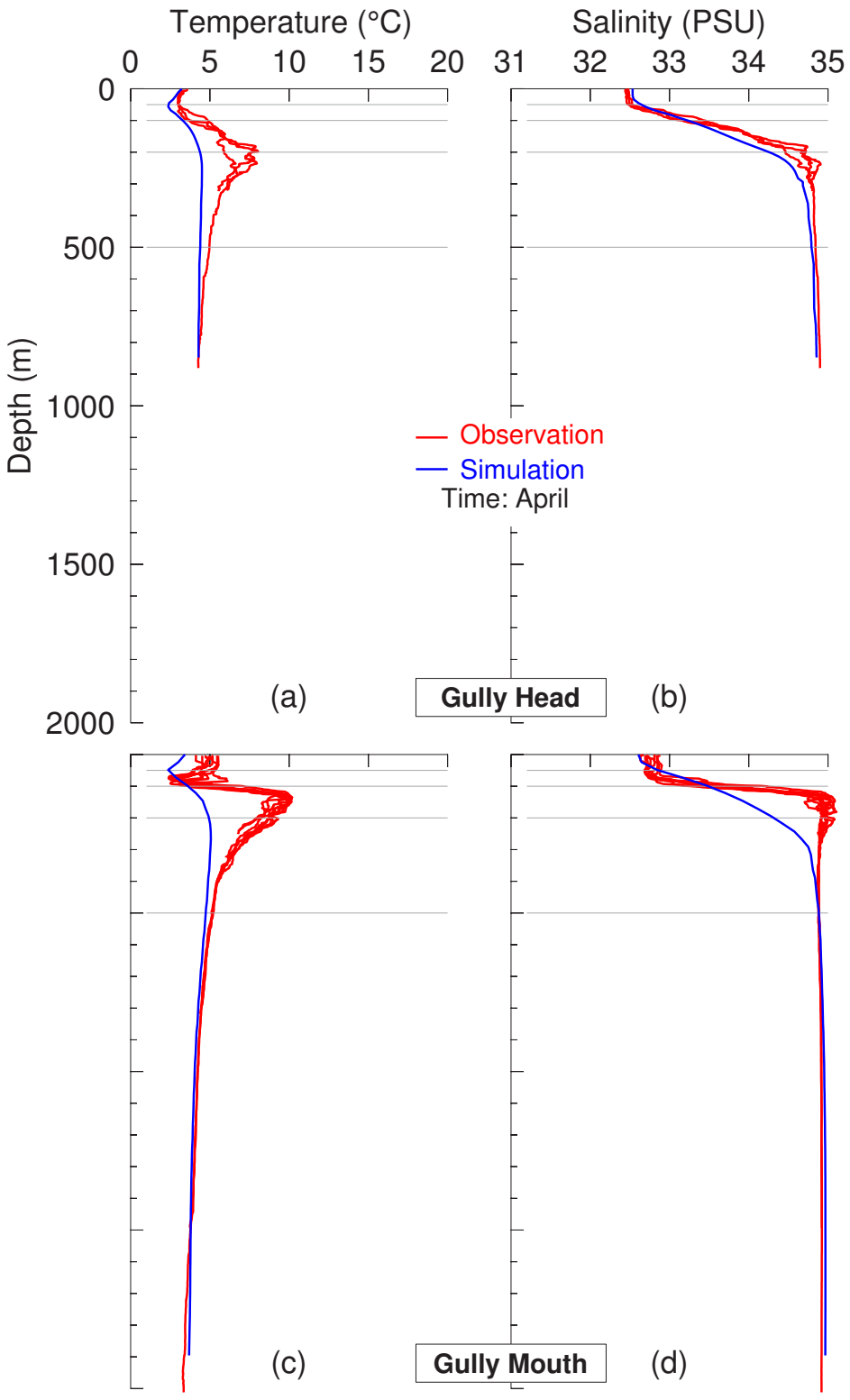

Figure 3.7: Vertical profiles of observed and simulated temperature and salinity in April along transect BB' (Gully Head) and CC' (Gully Mouth). The observed profiles (in red) were made on April 25 and 26, 2006. The measurement locations are marked by solid triangles in Fig. 3.1e. The simulated profiles (in blue) are based on transect-averaged model results on April 25 and 26, 2006. The depths of 50, 100, 200 and 500 m are shown by the horizontal gray lines.

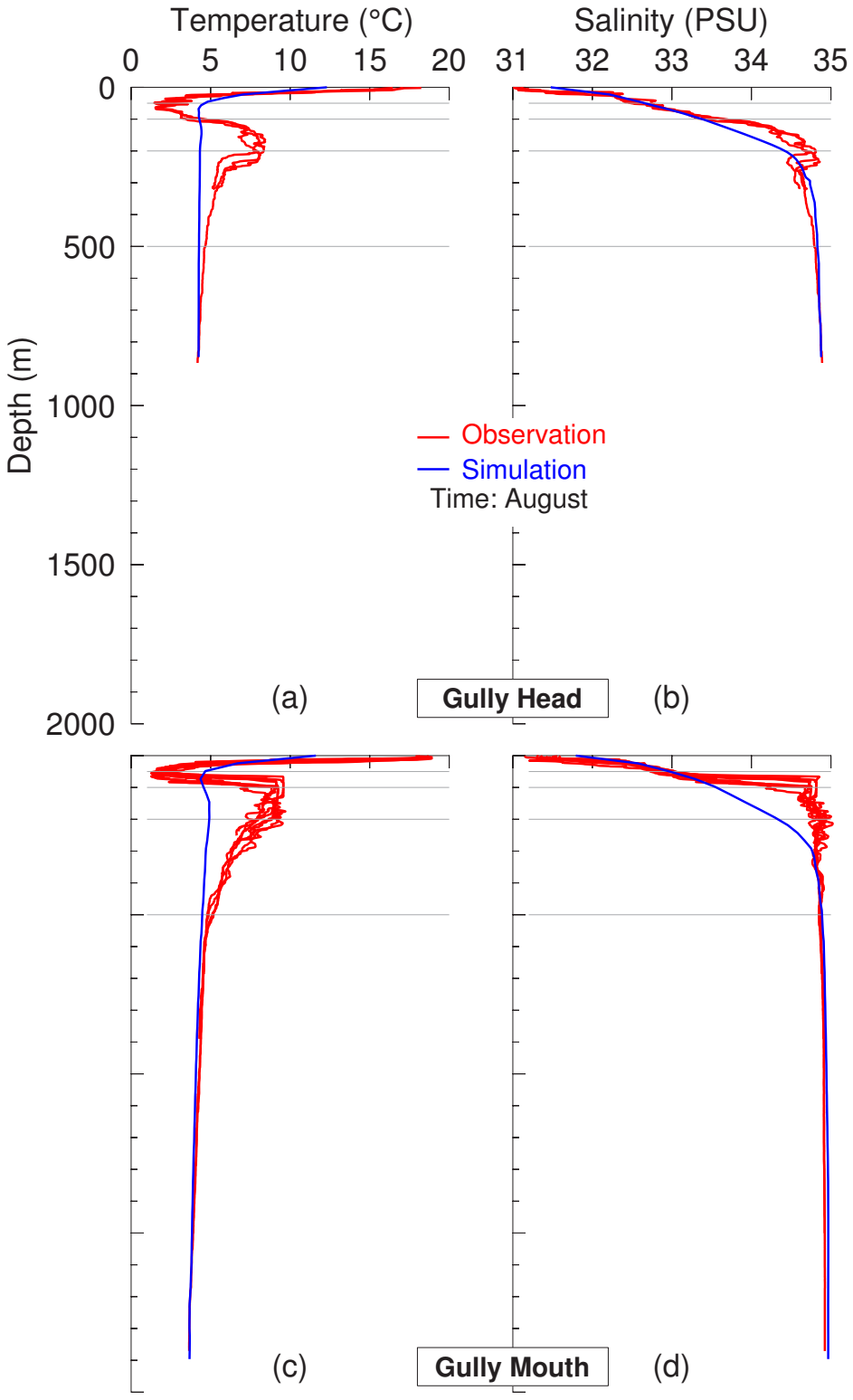

Figure 3.8: Vertical profiles of observed and simulated temperature and salinity in August along transect BB' (Gully Head) and CC' (Gully Mouth). The observed profiles (in red) were made on August 4 and 6, 2007. The measurement locations are marked by solid triangles in Fig. 3.1e. The simulated profiles (in blue) are based on transect-averaged model results on August 4 and 6, 2006. The depths of 50, 100, 200 and 500 m are shown by the horizontal gray lines.

3.4 Physical Processes Affecting Circulation and Hydrography

As shown in the previous section, the circulation and hydrography in the Sable Gully have significant temporal and spatial variability. To quantify the main physical processes affecting the circulation and hydrography in the Gully, the following three numerical experiments were conducted with different configurations of the multi-nested ocean circulation modelling system:

1. CONTROL RUN (*CR*): The DalCoast-Gully in this experiment is driven by the suite of forcing functions discussed in Section 2, which include tides, wind forcing, atmospheric pressure, sea surface heat/freshwater fluxes and open boundary forcing.

2. NO TIDES (*NT*): Same as the *CR*, except that the tides are turned off in this experiment. Specifically, the tidal elevations (η_t) and tidal currents (u_t) are set to zero along the open boundaries of submodel L2 (see Eq. (A.1)).

3. NO WIND (*NW*): Same as the *CR*, except that the local wind stress is set to zero in submodels L3, L4 and L5.

The model results from the above three experiments are used to quantify the role of the tides, local wind and other forcings in the Sable Gully and adjacent waters. Let ϕ_{CR}, ϕ_{NT} and ϕ_{NW} be model results in the experiments *CR*, *NT* and *NW*, respectively. The role of the tidal forcing can be estimated by

$$\Delta\phi_{tide} = \phi_{CR} - \phi_{NT} \tag{3.8}$$

Similarly, the role of the local wind forcing can be quantified approximately by

$$\Delta\phi_{wind} = \phi_{CR} - \phi_{NW} \tag{3.9}$$

In addition to the tides and local wind forcing, the other processes, such as the outflow from the Gulf of St. Lawrence, the equatorward Labrador Current, the Slope Water Jet and net surface heat/freshwater fluxes can also affect the circulation and hydrography in the Gully and adjacent waters. All of the processes other than the tides and local wind can be estimated by

$$\Delta\phi_{other} = \phi_{CR} - \Delta\phi_{tide} - \Delta\phi_{wind} \tag{3.10}$$

$$= \phi_{NT} + \phi_{NW} - \phi_{CR} \tag{3.11}$$

The roles of tides ($\Delta\phi_{tide}$), local wind forcing ($\Delta\phi_{wind}$) and other processes ($\Delta\phi_{other}$) in the Sable Gully will be discussed next at three different timescales: the synoptic, annual mean and seasonal mean timescales.

3.4.1 Circulation during a Storm Event

As mentioned above, local wind forcing plays an important role in affecting the circulation and hydrography in the upper water column, particularly during storm events. We examine the model results during tropical storm Alberto, which was the first tropical storm of the Atlantic hurricane season in 2006. Alberto deepened into a powerful post-tropical storm as it swept the Scotian Shelf on June 15 with maximum sustained winds of about 100 km h^{-1} (*Franklin and Brown*, 2008), resulting in large sea states over the Scotian Shelf.

The ocean response during the peak of the storm produced by DalCoast-Gully in control run (*CR*) is shown in Fig. 3.9. At 00:00 June 16, the simulated sea levels reach a maximum of about 0.4 m close to the storm centre near the Sable Island (Fig. 3.9a). The depth-averaged currents produced by submodel L1 are strongest on the Scotian Shelf. The surface circulation on the Scotian Shelf and the Gulf of St. Lawrence simulated by submodel L2 (Fig. 3.9b) at this time features strong well-defined storm-induced cyclonic circulation centred on the Scotian Shelf. Relatively low surface salinity waters can be seen over the western Gulf of St. Lawrence and the inner Scotian Shelf (Fig. 3.9b), due to the effect of freshwater discharge from the St. Lawrence River. The near surface salinity over the Gully is relatively high in the deep water to the south of the Gully (Fig. 3.9c). The simulated surface current over the Sable Gully at this time is roughly northeastward at about 50 cm s^{-1} (Fig. 3.9d and e) and is affected strongly by the wind.

Figure 3.10 presents the surface currents at the peak of the storm produced by submodel L5 in experiments *CR* and *NW*, which demonstrates that the wind-driven currents override the tidal currents at this time. The northeastward surface current in the deep water to the southeast of the Gully (Fig. 3.10a) is about 45° to the right of the wind stress direction, which can be explained by the classic Ekman theory (1963). The surface currents in experiment *NW* at this time are mainly tidal currents, which are significantly steered by the local topography of the Gully (Fig. 3.10b). The westward tidal currents are separated into two parts at the eastern flank of the Gully with one branch turning to the north, and the other following the isobaths of the shelf break to the south. A very weak flow region occurs to the west of the bifurcation point.

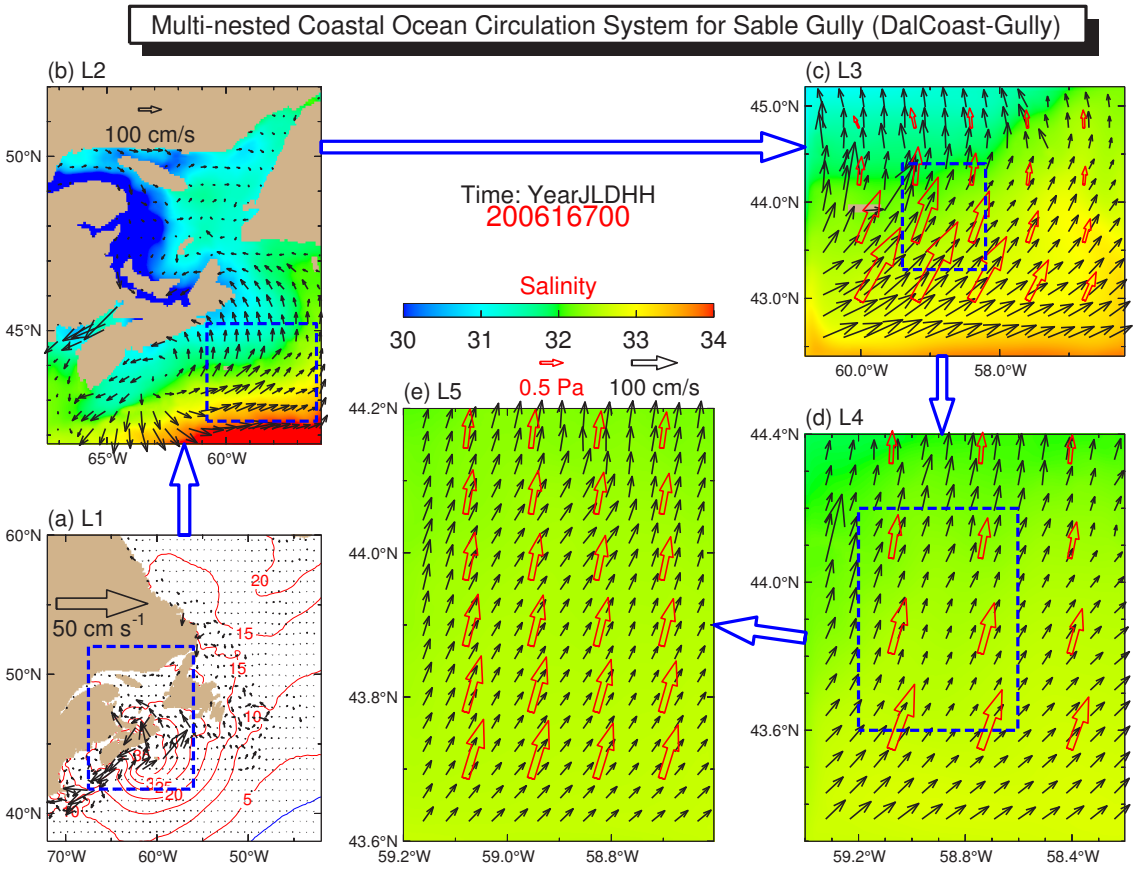

Figure 3.9: A snapshot of five-level multi-nested model results in control run (*CR*) at the peak of tropical storm Alberto at 00:00 UTC June 16, 2006 (day 167.0): (a) depth-averaged currents (black arrows) and sea surface elevations (red/blue contours for positive/negative values with a contour interval of 5 cm) produced by submodel L1; (b) surface currents (black arrows) and sea surface salinity (images) produced by submodel L2; and (c-e) near surface (2 m) currents and salinity produced by submodels L3-L5. Red open arrows are wind stress vectors. For clarity, velocity vectors are plotted at every (a) 9th, (b) 8th, (c) 8th, (d) 7th, and (e) 7th model grid point.

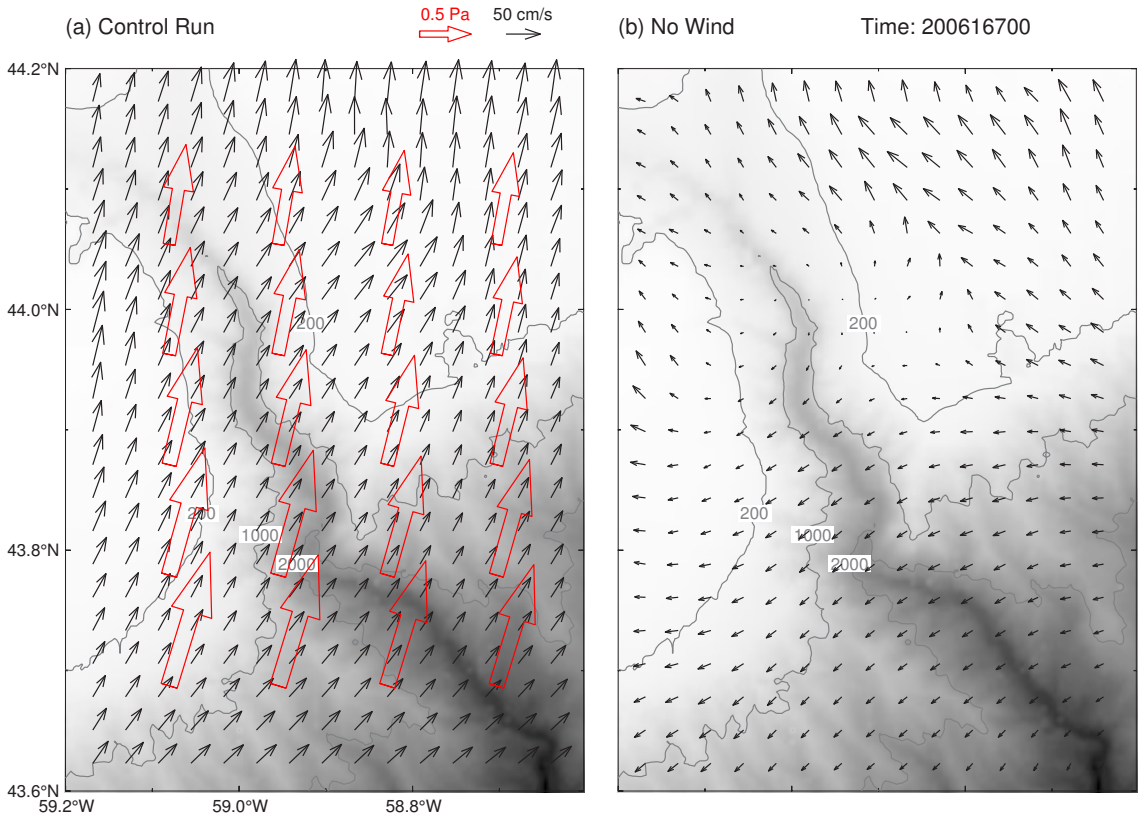

Figure 3.10: Surface currents produced by submodel L5 at 00:00 UTC June 16, 2006 (day 167.0) in experiments (a) *CR* and (b) *NW*. Red open arrows in (a) are wind stress vectors. For clarity, velocity vectors are plotted at every 6th model grid point. Selected isobaths in meters are shown by the gray contours.

We next examine the distributions of currents in $\Delta\phi_{tide}$, $\Delta\phi_{wind}$ and $\Delta\phi_{other}$ at two selected transects, AA' and CC' (marked in Fig. 3.1e). Transect AA' is along the longitudinal axis of the Gully. Transect CC' is located at the mouth of Gully and aligned roughly with the isobaths. A new coordinate system is used in depicting currents at the two transects. In this new coordinate system, the x-axis is along transect CC' pointing to northeast (from C to C'), and the y-axis is along transect AA' pointing to northwest (from A' to A). Thus, the corresponding velocity components in x- and y- direction can be used to represent the across-canyon (U) and along-canyon (V) velocities. The eastward and northward modelled velocities are transformed to the tangential and normal components of the currents at each transect. During the passing of storm Alberto, two snapshots with flood and ebb tide will be discussed. Here, the flood (ebb) tide refers to the period between low (high) and high (low) tidal sea surface elevations, during which the water in the Gully flows toward (away from) the shelf.

Figures 3.11 and 3.12 present snapshots of the along-canyon (V), vertical (W) and across-canyon (U) components of the 3D circulation during flood tide (03:00 June 16, 2006) at the transect AA' and CC', respectively. The tidal currents ($\Delta\phi_{tide}$) are on-shelf and reach up to 15 cm s^{-1} in the subsurface inside Gully (Fig. 3.11a-1). At the Gully mouth, a layer of weak flow at the depth of the Gully rim ($\sim$200 m) separates the on-shelf tidal currents (Fig. 3.12a-1). The strong on-shelf tidal currents are accompanied by strong upward vertical components of currents (Fig. 3.11a-2), which is required by the kinematic bottom boundary condition on the transect,

$$w|_{z=-h} = -u\frac{\partial h}{\partial s}|_{z=-h} \tag{3.12}$$

where (u, w) are the tangential and vertical velocity components along the transect (s) and in the vertical (z), respectively. h is the water depth.[2]

Wind-driven horizontal currents ($\Delta\phi_{wind}$) are only strong in the top surface mixed layer (Figs. 3.11b-1, b-3 and 3.12b-1, b-3). The subsurface currents due to the wind are relatively weak in comparison with those due to tides. The flow components driven by the processes

[2] The bottom frictional boundary layer is not resolved in the current configuration of the model. The slip boundary condition is used in the model, in which u in Eq. (3.12) represents the velocity above the bottom frictional layer. If the model vertical resolution is fine enough to resolve the bottom frictional layer, no-slip condition is required at the fluid-solid boundary and the water velocity is zero at the ocean floor. Equation (3.12) is derived from the kinematic bottom boundary condition ($\frac{D\,(z-(-h))}{D\,t} = 0$) and valid for both slip and no-slip boundary conditions.

other than tides and wind forcing ($\Delta\phi_{other}$) feature a strong jet ($\sim$10 cm s^{-1}) flowing to the southwest with a core centred at 500 m over the shelf slope (Fig. 3.11c-3).

Figures 3.13 and 3.14 presents snapshots of the along-canyon (V), vertical (W) and across-canyon (U) components of the 3D circulation during ebb tide (18:00 August 16, 2006) at the transect AA' and CC', respectively. The tidal currents ($\Delta\phi_{tide}$) at this time are off-shelf throughout the water column with magnitudes greater than 20 cm s^{-1} at the Gully head (Fig. 3.13a-1). At the Gully mouth, the off-shelf ebb tidal currents at this time (Fig. 3.14a-1) have a strong subsurface flow at the depth of the Gully rim. In order to satisfy the kinematic bottom boundary condition on the transect, the off-shelf ebb tidal currents are accompanied by strong downward vertical currents close to the bottom (Fig. 3.13a-2). Wind-driven horizontal currents ($\Delta\phi_{wind}$) are strong in the surface mixed layers (Figs. 3.13b-1, b-3 and 3.14b-1, b-3). The time-dependent wind-driven currents increase with time and can reach up to a few cm s^{-1} at subsurface (compare Figs. 3.13b-1, b-3 and 3.11b-1, b-3). The wind-driven time-dependent vertical currents also increase from 0.05 cm s^{-1} to 0.1 cm s^{-1} (compare Figs. 3.13b-2 and 3.11b-2). The flow components driven by other processes ($\Delta\phi_{other}$) also demonstrate a strong shelfbreak jet flows to the southwest with a core centred at 500 m, suggesting this shelfbreak jet is a persistent feature (Figs. 3.11c-3 and 3.13c-3).

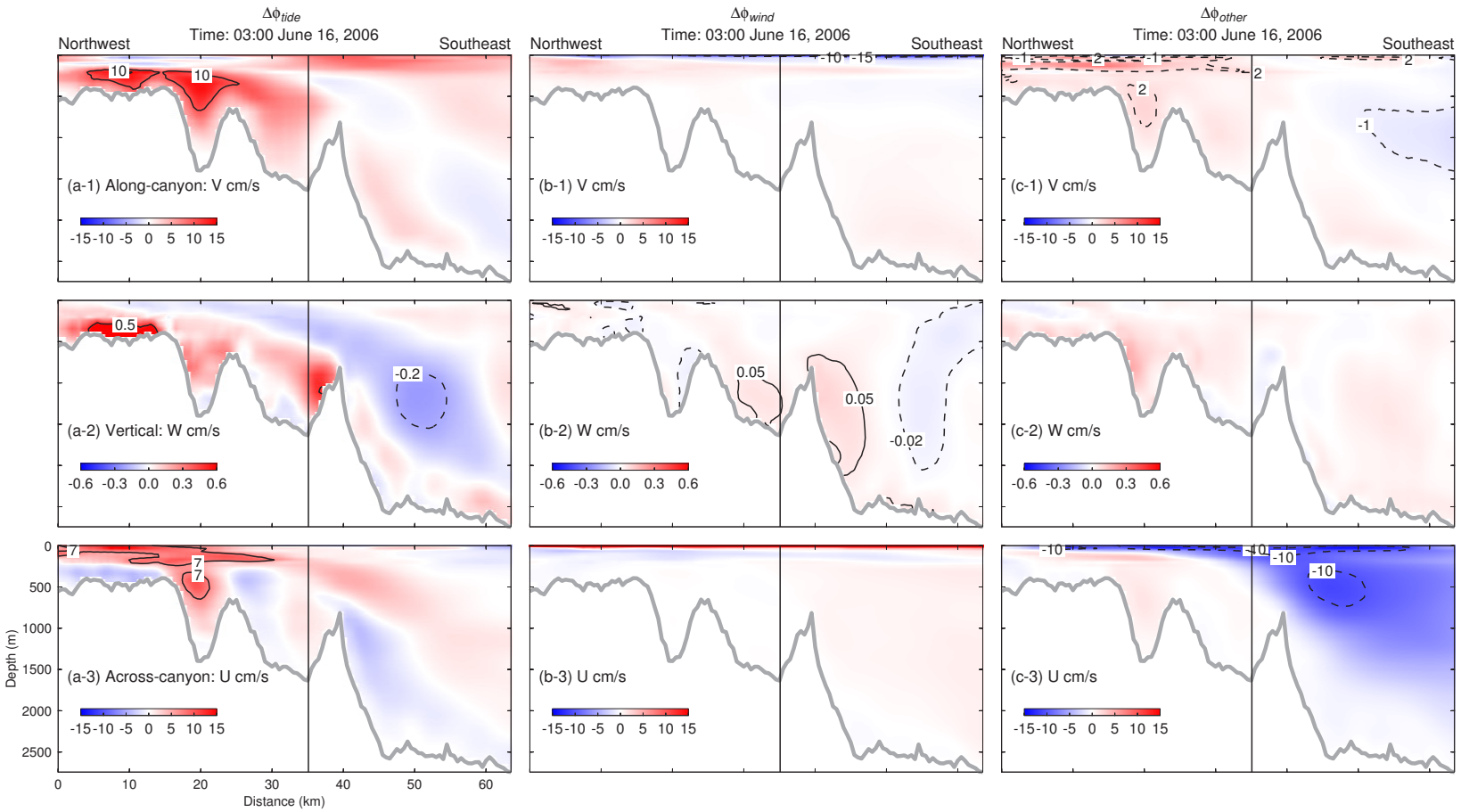

Figure 3.11: Vertical distributions of currents ($\Delta\phi_{tide}$, $\Delta\phi_{wind}$ and $\Delta\phi_{other}$) in the Sable Gully at along-canyon transect AA' (marked in Fig. 3.1e) on 03:00 UTC June 16, 2006. The upper, middle and lower panels are the along-canyon (V), vertical (W) and across-canyon (U) currents with positive values pointing to the northwest, upward and northeast, respectively. The vertical line indicates the position of across-canyon transect CC'. Note that the color scale for W is different from that of U and V.

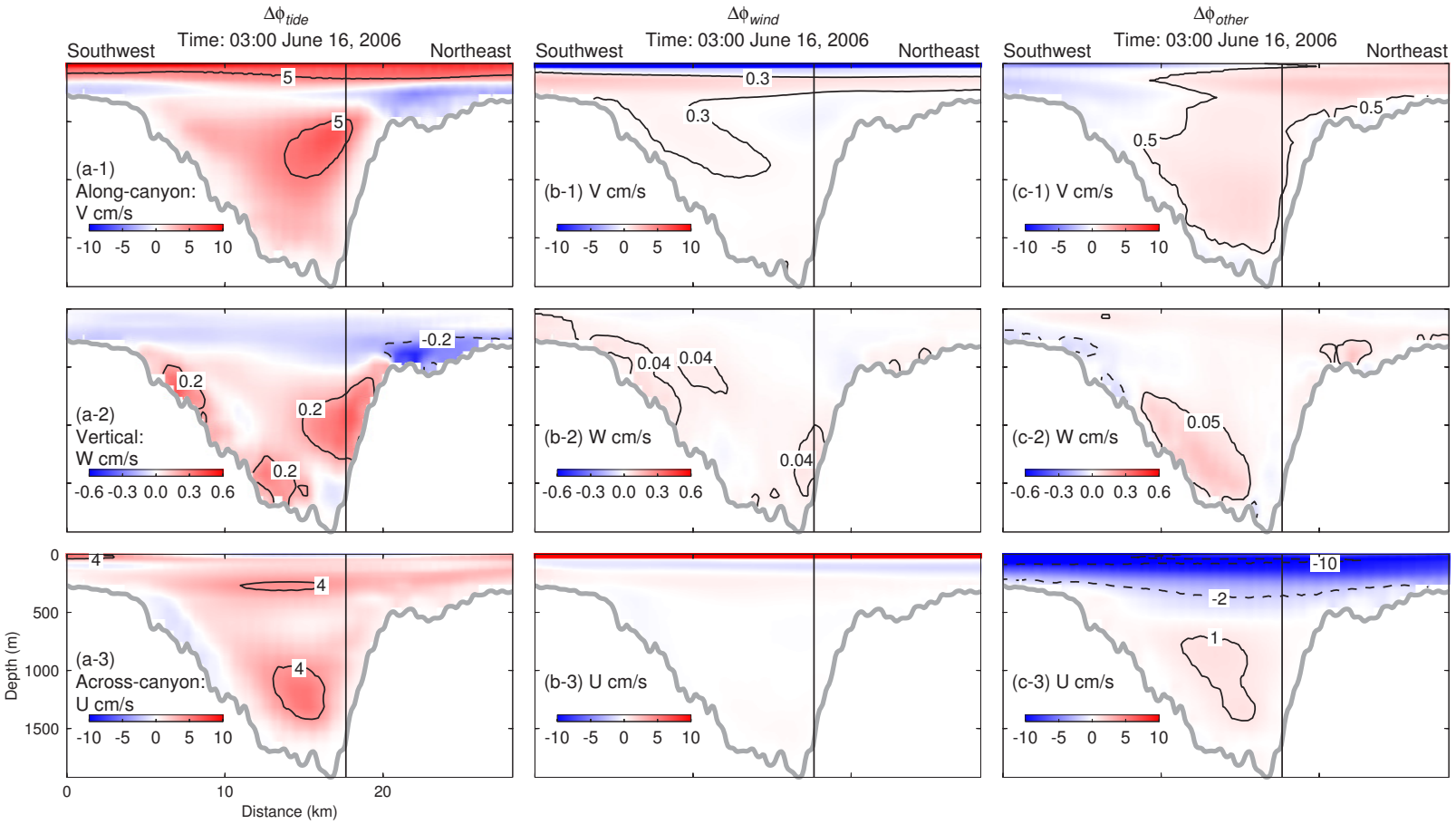

Figure 3.12: Vertical distributions of currents ($\Delta\phi_{tide}$, $\Delta\phi_{wind}$ and $\Delta\phi_{other}$) in the Sable Gully at across-canyon transect CC' (marked in Fig. 3.1e) on 03:00 UTC June 16, 2006. The upper, middle and lower panels are the along-canyon, vertical and across-canyon currents with positive values pointing to the northwest, upward and northeast, respectively. The vertical line indicates the position of along-canyon transect AA'.

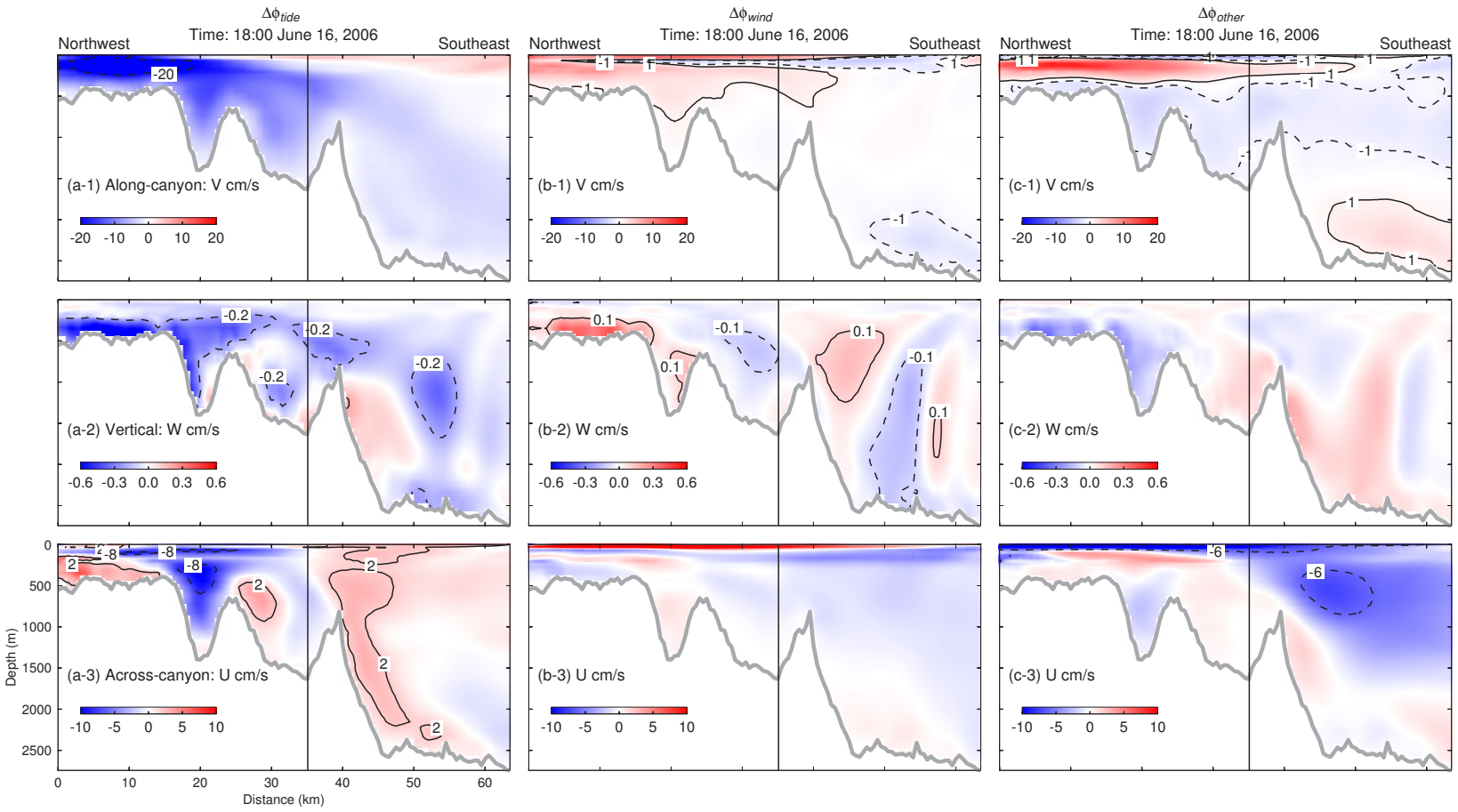

Figure 3.13: Vertical distributions of currents ($\Delta\phi_{tide}$, $\Delta\phi_{wind}$ and $\Delta\phi_{other}$) in the Sable Gully at along-canyon transect AA' (marked in Fig. 3.1e) on 18:00 UTC June 16, 2006. The upper, middle and lower panels are the along-canyon, vertical and across-canyon currents with positive values pointing to the northwest, upward and northeast, respectively. The vertical line indicates the position of across-canyon transect CC'.

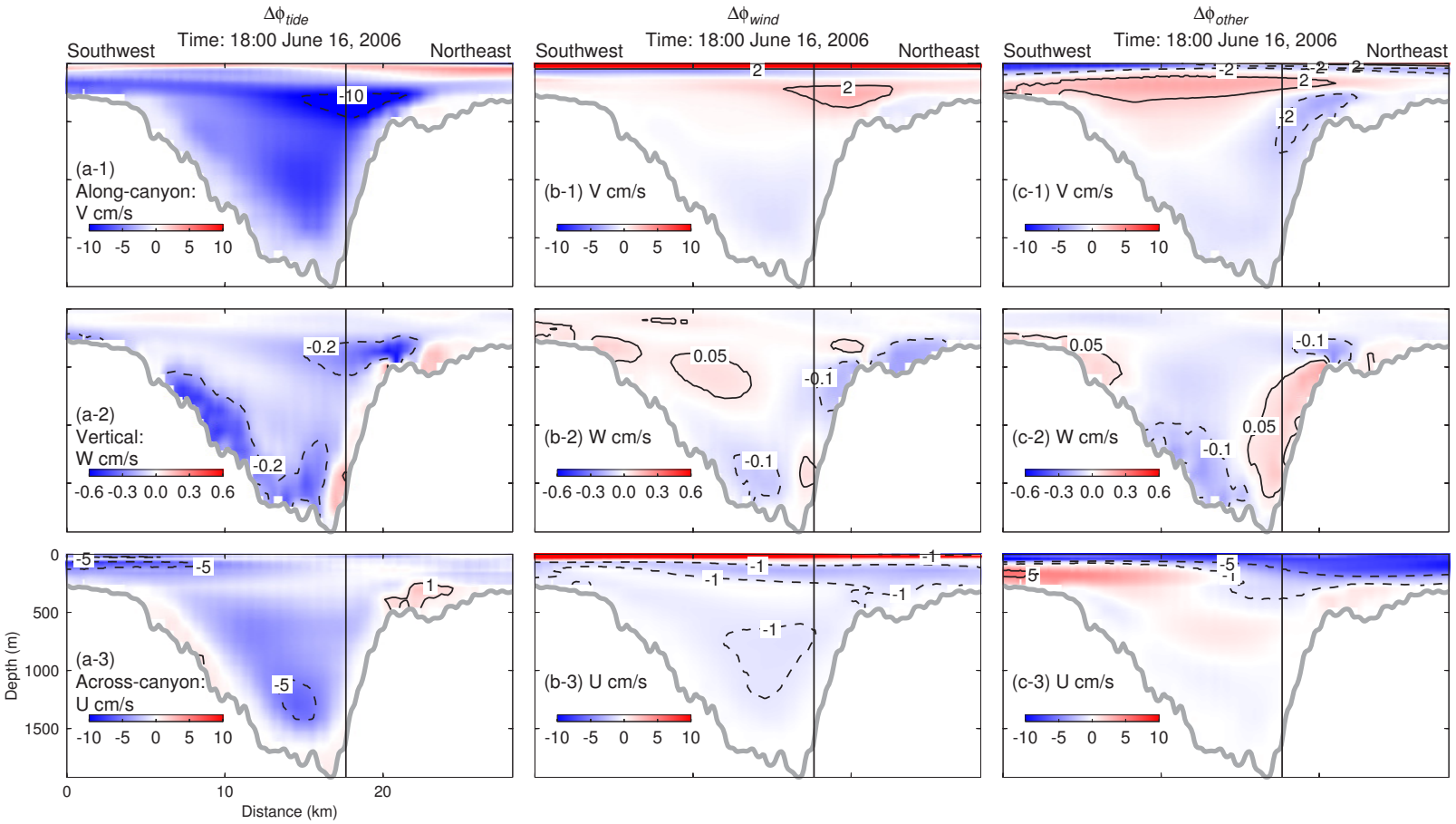

Figure 3.14: Vertical distributions of currents ($\Delta\phi_{tide}$, $\Delta\phi_{wind}$ and $\Delta\phi_{other}$) in the Sable Gully at across-canyon transect CC' (marked in Fig. 3.1e) on 18:00 UTC June 16, 2006. The upper, middle and lower panels are the along-canyon, vertical and across-canyon currents with positive values pointing to the northwest, upward and northeast, respectively. The vertical line indicates the position of along-canyon transect AA'.

3.4.2 Annual Mean Circulation

We next examine the main physical processes affecting the annual mean circulation in the Gully based on the model results in three experiments. As shown in Fig. 3.2, the annual mean circulation in the surface mixed layer of the Gully has a strong vertical shear. The annual mean surface currents produced by the model in *CR* are southwestward and relatively strong in comparison with subsurface currents (Fig. 3.15a-1 and a-3). There is an on-shelf subsurface current inside the Gully with a typical magnitude of 1 cm s^{-1}, indicating the transport of slope water into the Gully (Fig. 3.15a-1). The southwestward shelfbreak jet extends from the surface to 2000 m with a core centred at about 500 m (Fig. 3.15a-3). The subsurface currents are much weaker along the slope in comparison with the surface currents ($\sim$15 cm s^{-1}). At the mouth of the Gully (Fig. 3.15b-1), the annual mean surface currents are northwestward on the eastern and southeastward on western side of the Gully, respectively. The annual mean subsurface currents are characterized by an on-shelf flow with magnitude of 0.2 cm s^{-1} and relatively weak off-shelf flow along the sidewall of the Gully (Fig. 3.15b-1). The annual mean vertical currents are very weak in the surface mixed layer and relatively strong in the subsurface due mainly to the nonlinear interaction between the current and complex steep topography (Fig. 3.15a-2 and b-2).

A natural question arises about the roles of tides, wind forcing and other processes on the annual mean circulation in the Sable Gully. To address this question, we compare the annual mean model results in three numerical experiments *CR*, *NT* and *NW*:

$$< \Delta\phi_{tide} > \;=\; < \phi_{CR} > - < \phi_{NT} > \tag{3.13}$$

$$< \Delta\phi_{wind} > \;=\; < \phi_{CR} > - < \phi_{NW} > \tag{3.14}$$

$$< \Delta\phi_{other} > \;=\; < \phi_{NT} > + < \phi_{NW} > - < \phi_{CR} > \tag{3.15}$$

where "$< >$" denotes the annual mean. $< \Delta\phi_{tide} >$, $< \Delta\phi_{wind} >$ and $< \Delta\phi_{other} >$ are used to approximately represent the tidal residual currents, wind-driven currents and currents due to other processes (e.g., shelf-scale circulation), respectively, in the annual mean circulation of the Gully. We examine the three components at two selected transects, AA' and CC' (Figs. 3.16 and 3.17).

The annual mean tidal residual currents ($< \Delta\phi_{tide} >$) are relatively strong inside the Gully, particularly over steep topography, in comparison with tidal residual currents off the shelf slope. The surface tidal residual currents are strong and off-shelf inside the

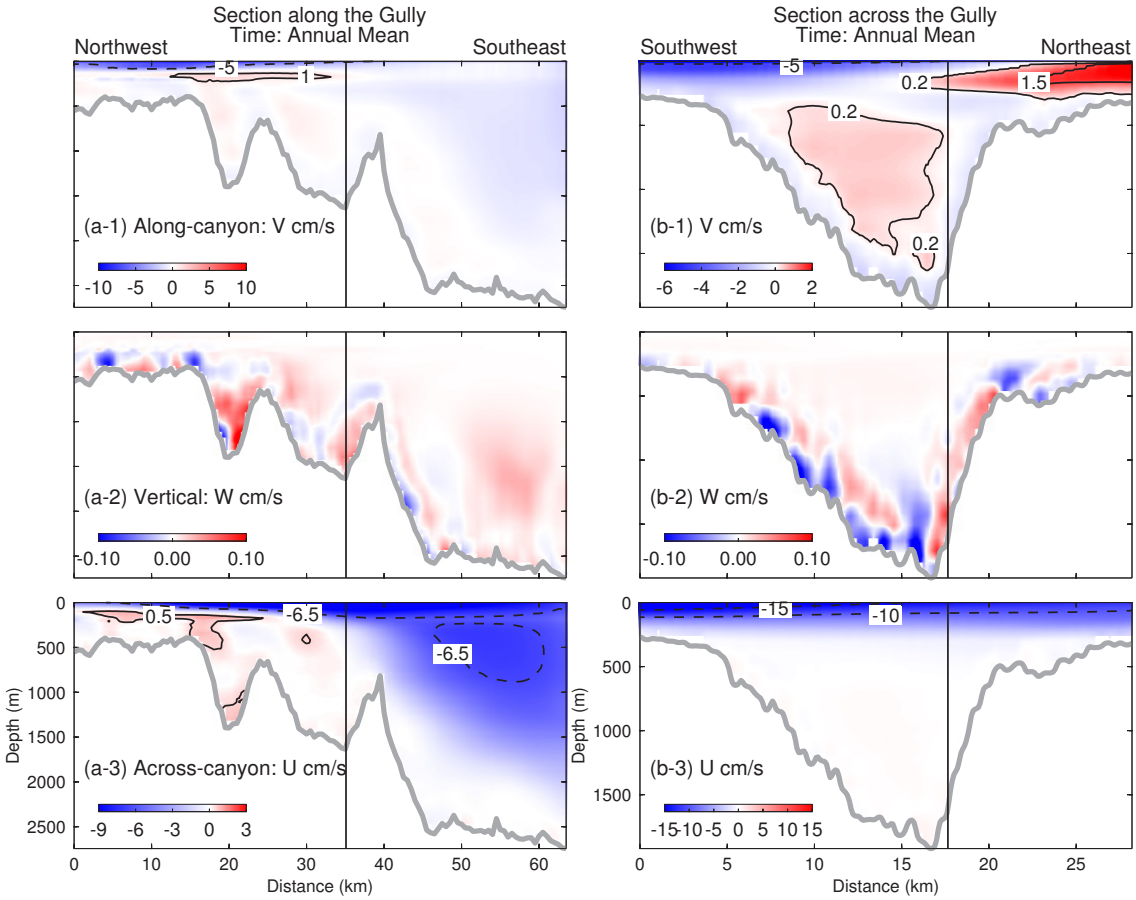

Figure 3.15: Vertical distributions of annual mean currents produced by submodel L5 of DalCoast-Gully in control run (*CR*) at along-canyon transect AA' (left panels) and across-canyon transect CC' (right panels). See Fig. 3.1e for the position of transects in the Gully. The upper, middle and lower panels are the along-canyon, vertical and across-canyon currents with positive values pointing to the northwest, upward and northeast, respectively. The vertical line on transect AA' (CC') indicates the position of transect CC' (AA').

Gully (Fig. 3.16a-1). The vertical components of the tidal residual currents are relatively strong along the sinuous axis in the Gully at subsurface (Fig. 3.16a-2). At the shelf break (Fig. 3.16a-3), the tidal residual currents are characterized by a northeastward subsurface flow at about 2 cm s^{-1} centred at 500 m. At the mouth of the Gully (Fig. 3.17a-1), the annual mean tidal residual currents are mainly on-shelf at depths below the Gully rim and off-shelf over the western side of the Gully. The relatively strong tidal residual currents inside the Gully indicate the strong nonlinear interaction between the tides and the steep topography of the Gully due mainly to three nonlinear terms in the governing equations: (1) the nonlinear term in the continuity equation, (2) the advection term in the momentum

equation, and (3) the nonlinear bottom friction term (*Parker*, 1991). In addition, the tidal residual currents in the Gully are also affected by the interaction between tides and stratification. Furthermore, tidal mixing modifies the density structure, which in turn modifies the baroclinic circulation in the region.

The annual mean wind-driven circulation ($< \Delta\phi_{wind} >$) is only significant in the surface mixed layer and relatively weak in the subsurface. The annual mean surface wind-driven currents (Figs. 3.16b-1, b-3 and 3.17b-1, b-3) are southwestward due mainly to the southwesterly and northwesterly wind in summer and winter. The annual mean vertical components of wind-driven currents are only significant inside the Gully along the steep topography.

The annual mean currents driven by other processes (e.g., shelf-scale circulation) ($< \Delta\phi_{other} >$) feature a strong shelfbreak jet along the slope. The shelfbreak jet is surface intensified ($>$10 cm s^{-1}) and has a subsurface core of 8 cm s^{-1} centred at about 500 m (Fig. 3.16c-3). The annual mean vertical components of currents forced by processes other than tides and wind (Figs. 3.16c-2 and 3.17c-2) are strong along the bottom due to the interaction between the mean flow and topography. At the mouth of the Gully (Fig. 3.17c-1), the annual mean currents driven by other processes are on-shelf and off-shelf on the eastern and western side of the Gully, respectively, and on-shelf at depths below the Gully rim. A close examination of Fig. 3.17a-1, b-1 and c-1 reveals that the contributions to the annual mean on-shelf currents at the Gully mouth are primarily from tidal residual currents and other processes (e.g., shelf-scale circulation).

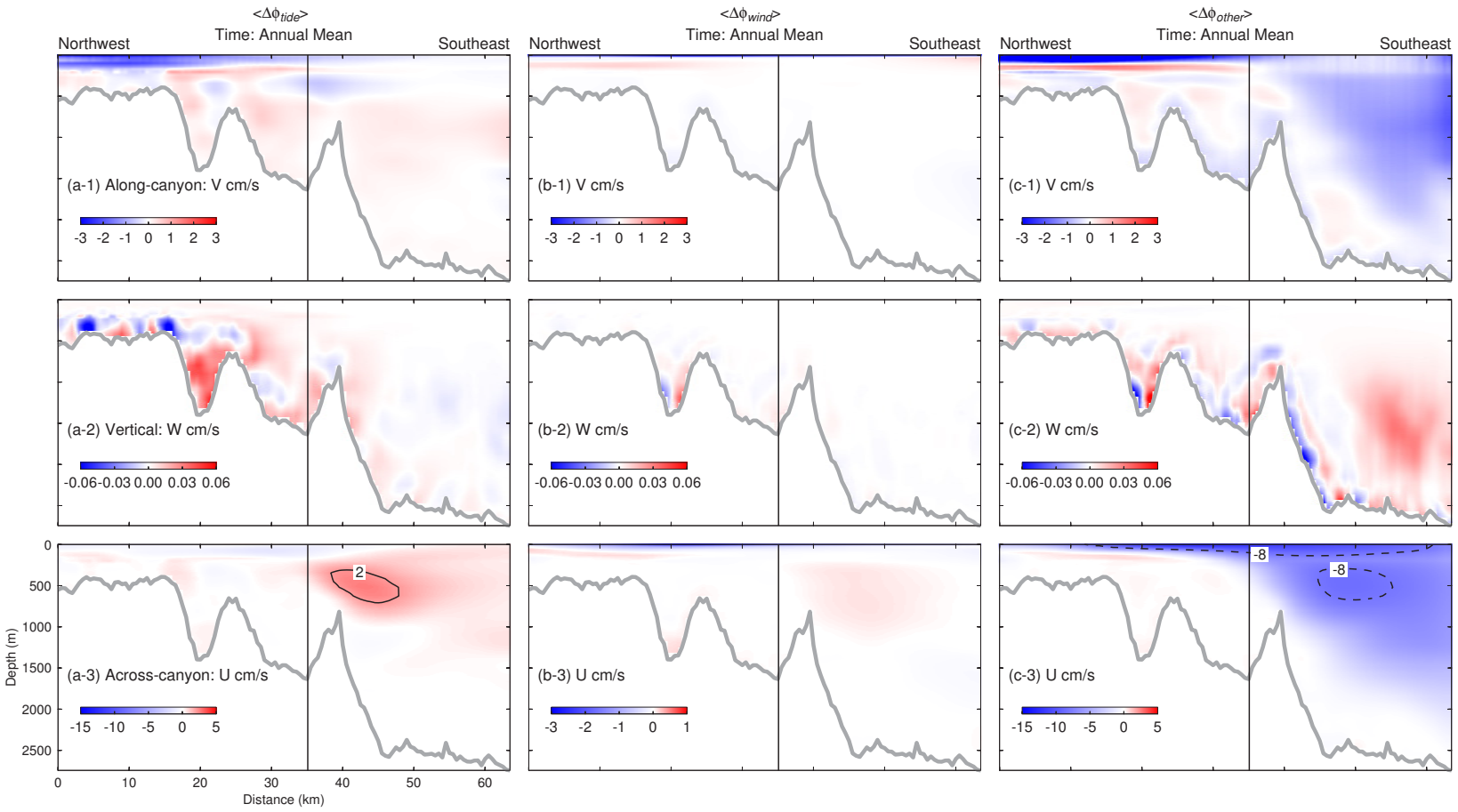

Figure 3.16: Vertical distributions of currents ($< \Delta\phi_{tide} >$, $< \Delta\phi_{wind} >$ and $< \Delta\phi_{other} >$) in the Sable Gully at along-canyon transect AA' (marked in Fig. 3.1e). "$< >$" denotes the annual mean. The upper, middle and lower panels are the along-canyon, vertical and across-canyon currents with positive values pointing to the northwest, upward and northeast, respectively. The vertical line indicates the position of across-canyon transect CC'.

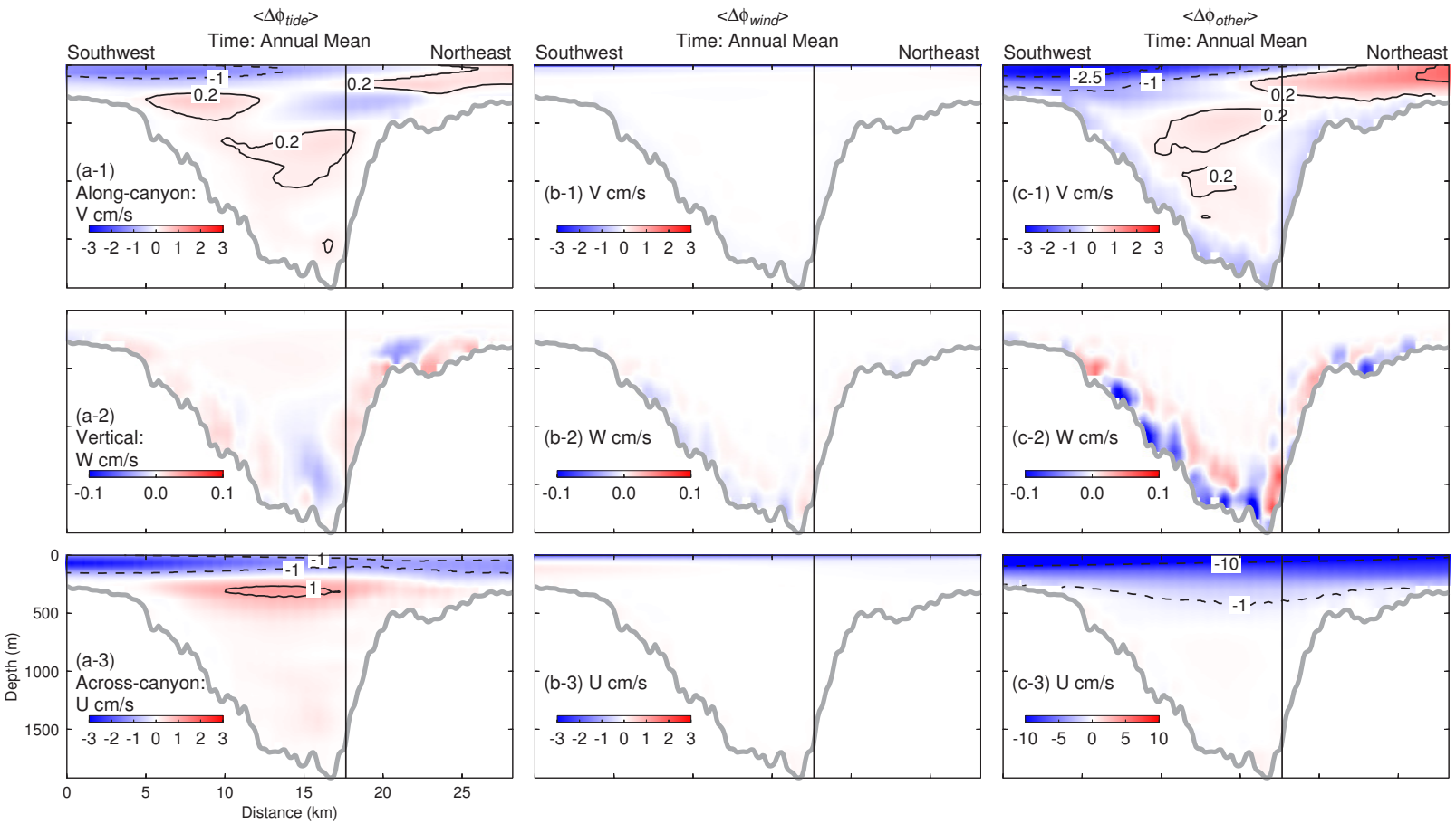

Figure 3.17: Vertical distributions of currents ($< \Delta\phi_{tide} >$, $< \Delta\phi_{wind} >$ and $< \Delta\phi_{other} >$) in the Sable Gully at across-canyon transect CC' (marked in Fig. 3.1e). "$< >$" denotes the annual mean. The upper, middle and lower panels are the along-canyon, vertical and across-canyon currents with positive values pointing to the northwest, upward and northeast, respectively. The vertical line indicates the position of along-canyon transect AA'.

To further quantify the across-shelf transport through the Gully due to model forcing functions, the volume transport (i.e., vertical integrated velocity) over a depth range from h_1 to h_2 is used, which is defined as:

$$(M_e, M_n) = \int_{h_1}^{h_2} (U_e, V_n)\, dz \tag{3.16}$$

where U_e and V_n are eastward and northward components of modelled horizontal velocities, respectively. Figure 3.18a-1 presents distributions of (M_e, M_n) in control run (*CR*) integrated from the depth of the Gully rim (h_1=$\sim$200 m) to the bottom (h_2=h). The (M_e, M_n) features a southwestward volume transport along the isobaths over the shelf slope with magnitudes of greater than 10 m^2 s^{-1}. A branch of the southwestward volume transport turns into the Gully and follows the sinuous longitudinal axis onto the shelf. To examine the roles of the major forcing functions in (M_e, M_n) shown in Fig. 3.18a-1, the model results in *CR* are separated into three components: tidal residual, wind forcing, and other processes (e.g., shelf-scale circulation). Figures 3.18b-1 to d-1 demonstrate that the volume transport are mainly due to tidal residual and other processes with relatively small contribution from the wind. Over the shelf slope, the southwestward volume transport is mainly due to other processes (e.g., shelf-scale circulation) and reduced by an opposite tidal residual transport. Inside the Gully, the on-shelf volume transport is mainly due to tidal residual and enhanced by other processes. An across-canyon transect (FF', marked in Fig. 3.18) is selected where the on-shelf transport is relatively well-defined near the Gully mouth. The currents in *CR* normal to the transect FF' have a strong shear above the Gully rim and a relatively weak on-shelf flow below the Gully rim (Fig. 3.18b-1). The currents due to tidal residual (Fig. 3.18b-2) and other processes (Fig. 3.18d-2) have similar vertical structures in comparison with the results in *CR*. The wind-driven component is weak below the surface Ekman layer (Fig. 3.18c-1). The total volume transport (J) through transect FF' is calculated according to Eq. (3.17) and listed in Table 3.1:

$$J = \int_{F}^{F'} \int_{h_1}^{h_2} V\, ds\, dz \tag{3.17}$$

where V is the along-canyon velocity normal to transect FF', and s and z are the directions along the transect and in the vertical, respectively. The total volume transport through transect FF' (h_1=0 m) is off-shelf and about 0.025 Sv (1 Sv = 10^6 m^3 s^{-1}), of which 42% and 34% are due to wind and tidal residual, respectively. The total volume transport below

Table 3.1: Total volume transport through transect FF' (see Fig. 3.18) calculated using annual mean results in experiment *CR*. Positive (Negative) numbers indicate on-shelf (off-shelf) transports.

Water depth range	Volume transport ($m^3\ s^{-1}$)			
	Control Run	Tide	Wind	Other
Surface to Bottom	-25452	-8758	-10702	-5992
200 m to Bottom	3498	6246	-1619	-1129

the Gully rim (h_1=200 m) through transect FF' is on-shelf and about 0.003 Sv. In this case, only the tidal residual transport is on-shelf, and both transports due wind and other processes are off-shelf. The on-shelf total volume transport through the Gully may play an important role in supporting the richness in biodiversity inside the Gully in comparison with the adjacent shelf slope.

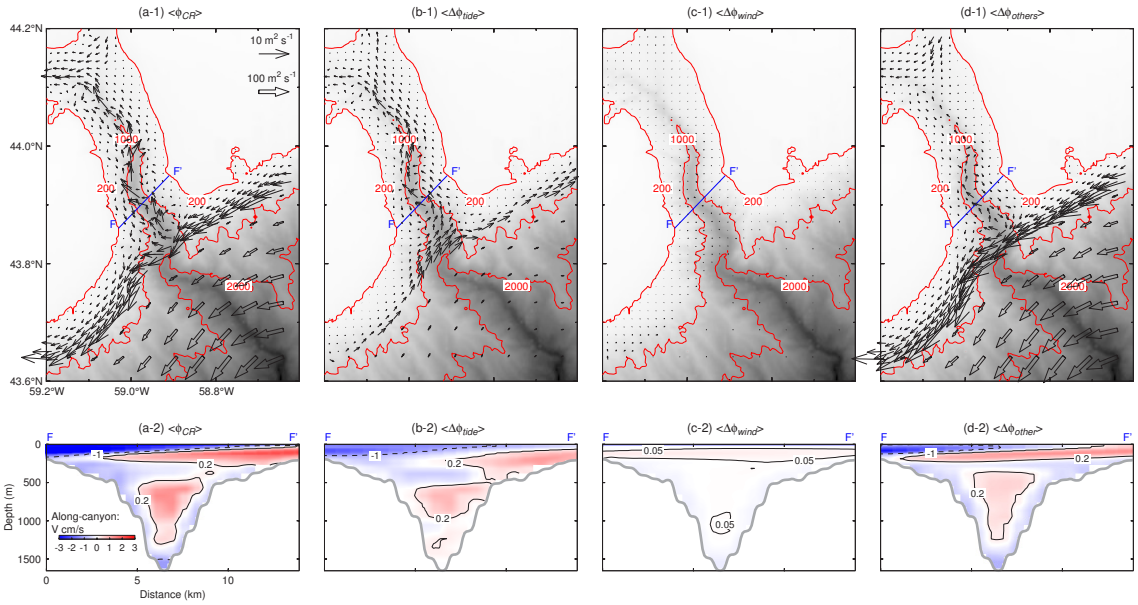

Figure 3.18: Horizontal distributions of volume transport in (a-1) $< \phi_{CR} >$, (b-1) $< \Delta\phi_{tide} >$, (c-1) $< \Delta\phi_{wind} >$, and (d-1) $< \Delta\phi_{other} >$ from a depth of 200 m to bottom in the Sable Gully. The values greater than 10 $m^2\ s^{-1}$ are plotted in open arrows. The corresponding currents normal to the transect FF' are plotted in (a-2) to (d-2). For clarity, volume transport vectors $\leq$ 10 $m^2\ s^{-1}$ and $>$ 10 $m^2\ s^{-1}$ are plotted at every 3rd and 10th model grid point, respectively. Selected isobaths in meters are shown by the red contours.

3.4.3 Seasonal Mean Circulation

To further quantify the seasonal variations of the subtidal circulation over the Gully and adjacent areas, the vertically integrated volume transport is calculated from model currents produced by submodel L5 of DalCoast-Gully, which is defined as an integral of velocity vectors from the depth of the Gully rim (200 m) to bottom. Figure 3.19 presents the simulated volume transports in February and August 2006. The February mean volume transport (Fig. 3.19a) is southwestward along the shelf break and northwestward along the Gully thalweg. There are off-shelf volume transports on the western side of the thalweg at the head and mouth of the Gully. The southwestward volume transport along the shelf break is relatively weak in August in comparison with the transport in February (Fig. 3.19b). The on-shelf (off-shelf) transport on the eastern (western) side of the thalweg is reduced (intensified) in August in comparison with the transport in February. Our finding of stronger transport in February (winter) and weaker transport in August (summer) along the shelf break is consistent with the finding of *Drinkwater et al.* (1979). Across the Gully mouth (FF', Fig. 3.19), the volume transports from the depth of the Gully rim to bottom are estimated to be on-shelf and about 9,890 m^3 s^{-1} and 2,357 m^3 s^{-1} in February and August, respectively. Our estimate is smaller than the estimate of about 35,500 m^3 s^{-1} made by *Greenan et al.* (2014) based on mooring observations. It should be noted that our estimate is based on the model results and dynamically consistent. In comparison, the accuracy of the estimate by *Greenan et al.* (2014) from observations depends on the spatial structure of the currents and the spatial coverage of the current observations.

The seasonal volume transports due to tidal residual, wind and other forcings (e.g., shelf-scale circulation) are also examined using the same approach for analyzing the annual mean volume transport. The analysis of modelled volume transports in February and August from the Gully rim ($\sim$200) to bottom (Fig. 3.20) suggests that the transports are mainly from tidal residual and other forcings (e.g., shelf-scale circulation), and the seasonal variations of transports are due primarily to the variations of other forcings (e.g., shelf-scale circulation). The monthly mean volume transport forced by the tides in February is slightly weaker than the counterpart in August due mainly to the relatively stronger interactions between tides and stratification in summer months. The monthly mean volume transport forced by the wind in February and August are both small. The monthly mean volume transport due to other forcings in February is on-shelf inside the

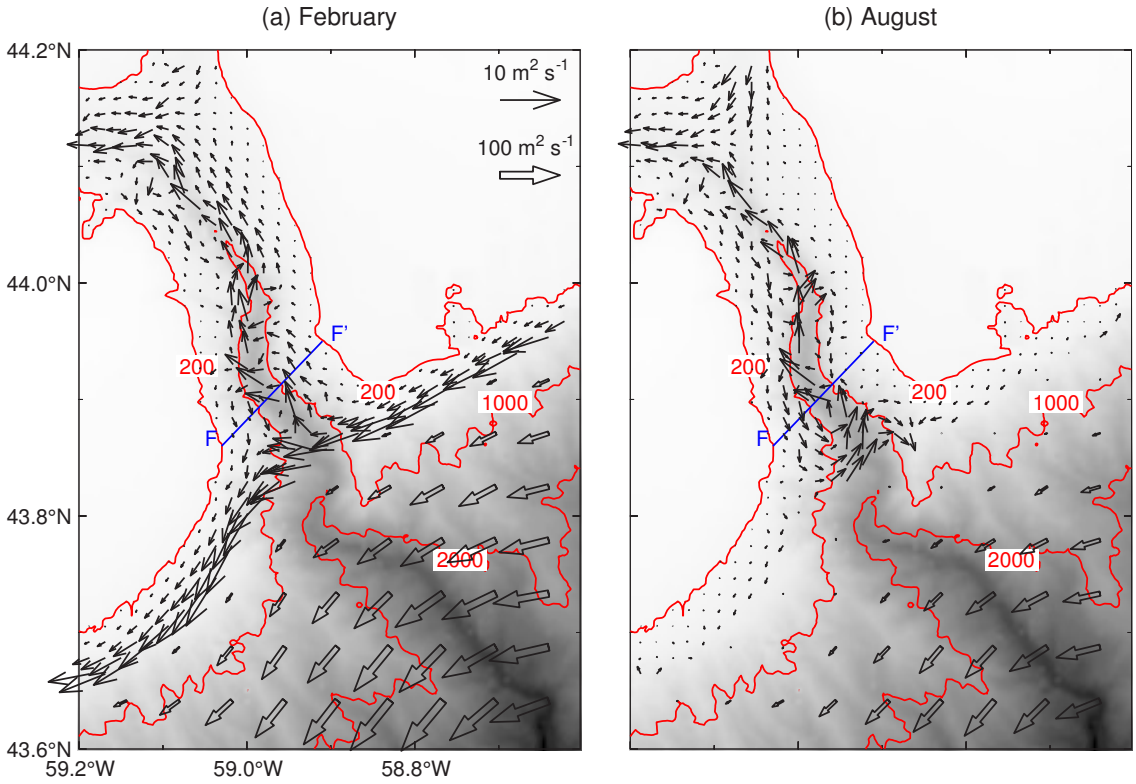

Figure 3.19: Horizontal distributions of simulated monthly mean volume transport in (a) February and (b) August 2006 from a depth of 200 m to bottom in the Sable Gully. The values greater than 10 m^2 s^{-1} are plotted in open arrows. For clarity, volume transport vectors $\leq$ 10 m^2 s^{-1} and $>$ 10 m^2 s^{-1} are plotted at every 3rd and 10th model grid point, respectively. Selected isobaths in meters are shown by the red contours.

Gully and southwestward outside the Gully. While in August, the monthly mean volume transport due to other forcings is off-shelf inside the Gully. The southwestward transport outside the Gully in August decreases significantly in comparison with the transport in February.

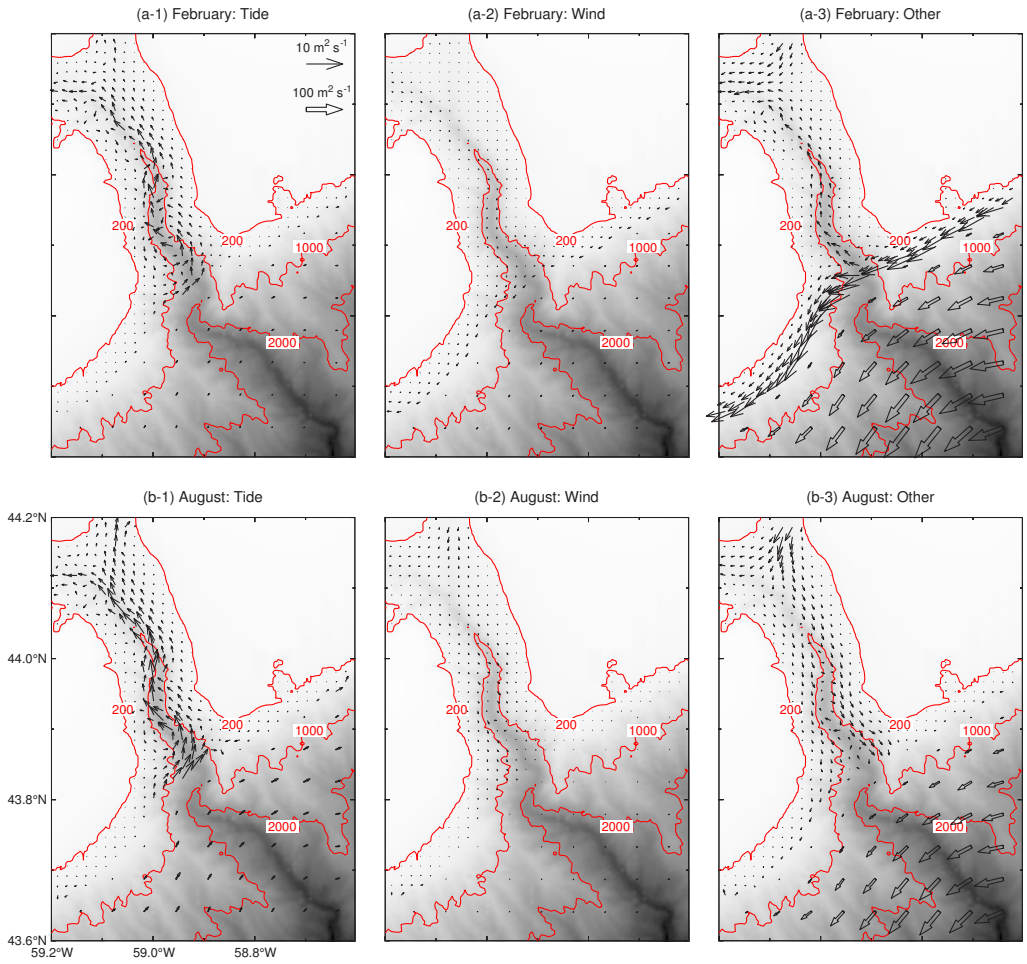

Figure 3.20: Horizontal distributions of the monthly mean volume transport forced by (a-1), (b-1) tides; (a-2), (b-2) wind; and (a-3), (b-3) other forcings. The top and bottom panels show the volume transports in February and August, respectively. The values greater than 10 m^2 s^{-1} are plotted in open arrows. For clarity, volume transport vectors $\leq$ 10 m^2 s^{-1} and $>$ 10 m^2 s^{-1} are plotted at every 3rd and 10th model grid point, respectively. Selected isobaths in meters are shown by the red contours.

3.5 Particle Movement in the Sable Gully

3.5.1 Design of Particle Tracking Experiments

The particle movements in the Gully and adjacent areas are calculated using the particle tracking model to examine the impact of circulation on the distribution of passive particles (e.g., nutrients, marine larvae, pollutants). The Gully Marine Protected Area (MPA) was divided into three management zones. Zone 1 (water depth $>$ 500 m) has the highest level of protection (*Gully Marine Protected Area Regulations*, 2004). A rectangular region covering the whole Zone 1 is used as the initial release area in this study (Fig. 3.21). Since the circulation above the depth of the Gully rim ($\sim$200 m) is weakly affected by the Gully bathymetry and the flow below the depth of the Gully rim are strongly constrained by the Gully thalweg (Figs. 3.2 and 3.4), the depth of the Gully rim was chosen as the initial release depth of particles in the control case (ExpCTL, Table 3.2) to investigate the connection between the upper and lower water columns (Fig. 3.21). The control case (ExpCTL) has two sets of particle tracking experiments covering February and August 2006 to examine the seasonal variations of the movement of particles (Fig. 3.22). Each set of experiments consists of about 30 pairs of runs forward and backward in time. Successive releases of a patch of particles are performed, at a time interval of one day, over a period of a month (Fig. 3.22). This suppresses the dependence of numerical results on the initial release time. Each run tracks a patch of particles for a 30-day period using the 3-hourly instantaneous 3D flow fields produced by submodel L5 (Fig. 3.4). Each patch of particles consists of 3,348 particles (Fig. 3.21). The initial distance between two adjacent particles is 500 m. Each particle is coded in a unique color (Fig. 3.21), which allows us to identify them through out the tracking experiments. The forward and backward tracking experiments allow us to estimate the downstream and upstream areas (*Tang et al.*, 2006) of the Gully. Physically, the downstream area represents a potential area to which the passive particles could be exported from the Gully within a given time. The upstream area is a potential area from which the passive particles could be imported to the Gully within a given time. The estimation of downstream and upstream areas is particularly useful for monitoring the Gully MPA.

The above describes the setup of particle tracking experiments for the control case (ExpCTL, Table 3.2). Since the particle tracking results are dependent on the time and location of initial release and also affected by the advection and diffusion processes (Eq.

(3.3)), three additional sensitivity studies are also conducted (Table 3.2). In the first additional study (ExpSUR and ExpBOT), the particles are released at the surface and at the depth of 1000 m to investigate how the movements of particles vary with different release depths. In the second additional study (ExpNT), the flow fields without tides are used to estimate the role of tidal currents in the movements of particles. In the third additional study (ExpLK and ExpHK), the random walk with different eddy diffusivity coefficients (**K**) is used to address the sensitivity of the residence time to the choice of **K**.

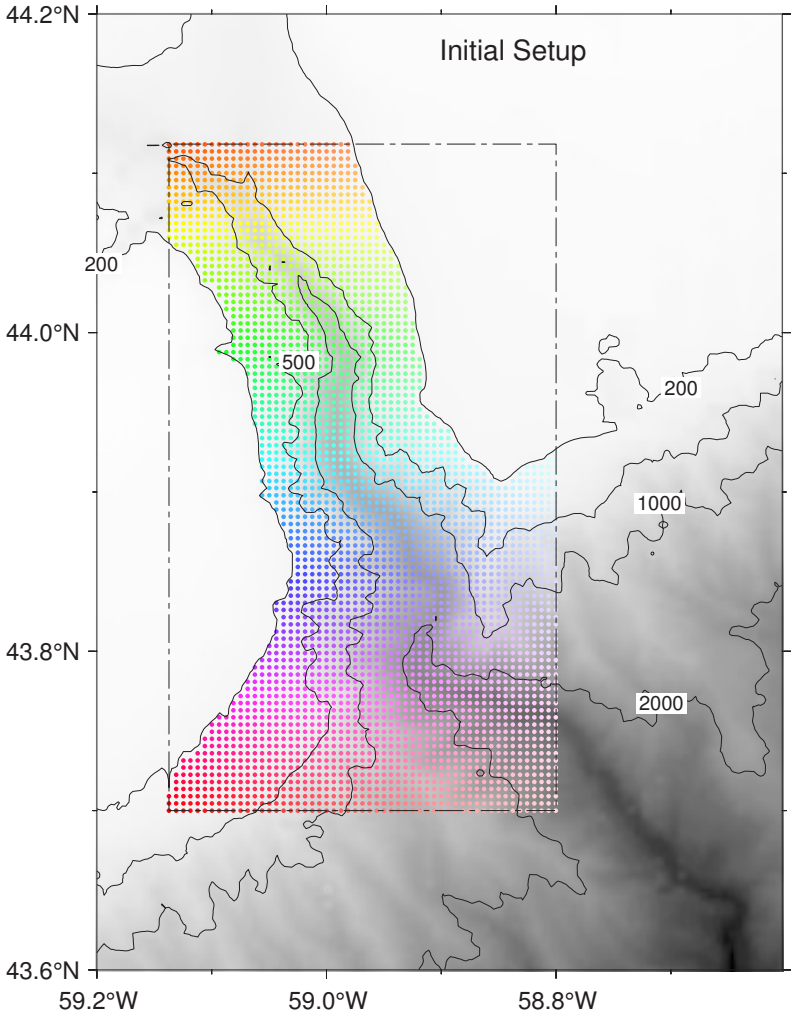

Figure 3.21: Initial positions of color-coded particles released at 200 m over Zone 1 of the Gully Marine Protected Area (dash-dotted box). The initial distance between two adjacent particles is 500 m. Selected isobaths in meters are shown by the gray contours.

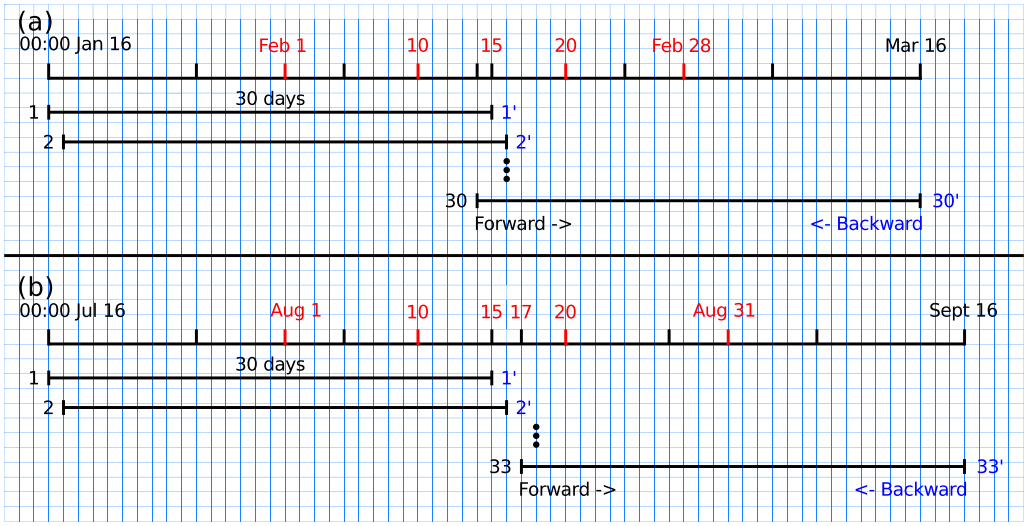

Figure 3.22: Schematics of two sets of tracking experiments in the Gully Marine Protected Area in: (a) February and (b) August 2006.

Table 3.2: List of particle tracking experiments using different model flow fields and different values of the eddy diffusivity coefficient for the random walk at different release depths.

Experiment	Release depth	Flow field	Random walk
ExpCTL	200 m	With tides	**K** (Observed)
ExpSUR	Surface	With tides	**K**
ExpBOT	1000 m	With tides	**K**
ExpNT	200 m	Without tides	**K**
ExpLK	200 m	With tides	0.1**K**
ExpHK	200 m	With tides	10**K**

3.5.2 Particle Movements Forward and Backward in Time

Figure 3.23 shows particle positions at day 3 and 6 in the case of forward in time tracking with the initial release time of February 11, 2006 in ExpCTL. Some particles initially released over the southern part of Zone 1 move southwestward associated with the flow along the shelf break during the first 3 days. Particles are also advected vertically by the vertical component of model currents, with 38% (9%) (Table 3.3) particles in depths greater (less) than the initial release depth at day 3. At day 6, about 47% of particles released inside Zone 1 are flushed out of the tracking domain with most of particles are advected from the mouth of the Gully southwestward along the shelf break. A significant number of particles are advected below (15%) and above (18%) the initial release depth. There are only a few particles that remained on the eastern side of the Gully (between 200 and 1000 m isobaths) in Zone 1 at day 6. Figure 3.24 shows particle positions at day 3 and 6 in the case of backward in time tracking with the initial release time of February 17, 2006 in ExpCTL. About 85% of particles are inside Zone 1 at day 3. Particles over the southern part of Zone 1 originate from the northeastern part. At day 6, about 46% of particles are outside of the tracking domain. Some of the particles at the head of the Gully originate from the southwestern part of the Gully. The forward and backward movements of particles indicate the downstream and upstream areas of the Gully. The southern part of Zone 1 is strongly connected to the Scotian Slope with particles moved into the Gully from northeast (upstream) and advected out of the Gully to southwest (downstream) along the Scotian Slope. The northern part of Zone 1 is weakly connected to the Scotian Slope with particles remain in the tracking domain at different water depths.

Figure 3.25 shows particle positions at day 3 and 6 in the case of forward in time tracking with the initial release time of August 12, 2006 in ExpCTL. Some particles initially released over the southern part of Zone 1 are advected southward/southwestward during the first 3 days. At day 6, about 11% of particles are flushed out of the tracking domain. There are also only a few particles that remained on the eastern side of the Gully (between 200 and 1000 m isobaths) in Zone 1. Figure 3.26 shows the particle positions at day 3 and 6 in the case of backward in time tracking with the initial release time of August 18, 2006 in ExpCTL. Nearly all particles remain inside Zone 1 at day 3. At day 6, almost all of the particles (99%) still remain inside the tracking domain. Particles over the southern part of Zone 1 also originate from the northeastern part. The forward

Table 3.3: Percentage of the total number of particles above/at/below the depth of the Gully rim (∼200 m) during selected tracking experiments in mid-February and mid-August 2006 in ExpCTL

Experiment	Percentage							
	Surface to 180 m		180 m to 220 m		220 m to bottom		Outside	
	Day 3	Day 6	Day 3	Day 6	Day 3	Day 6	Day 3	Day 6
Feb 11, forward	9	18	26	20	38	15	27	47
Feb 17, backward	22	34	40	14	23	6	15	46
Aug 12, forward	29	27	41	29	27	33	3	11
Aug 18, backward	31	49	45	32	24	18	0	1

and backward movements of particles in August also indicate the main downstream and upstream areas of the Gully are located along isobaths of the Scotian Slope, suggesting that the areas outside the Zone 1 of the Gully MPA along the slope may play an important role in sustaining the Gully ecosystem.

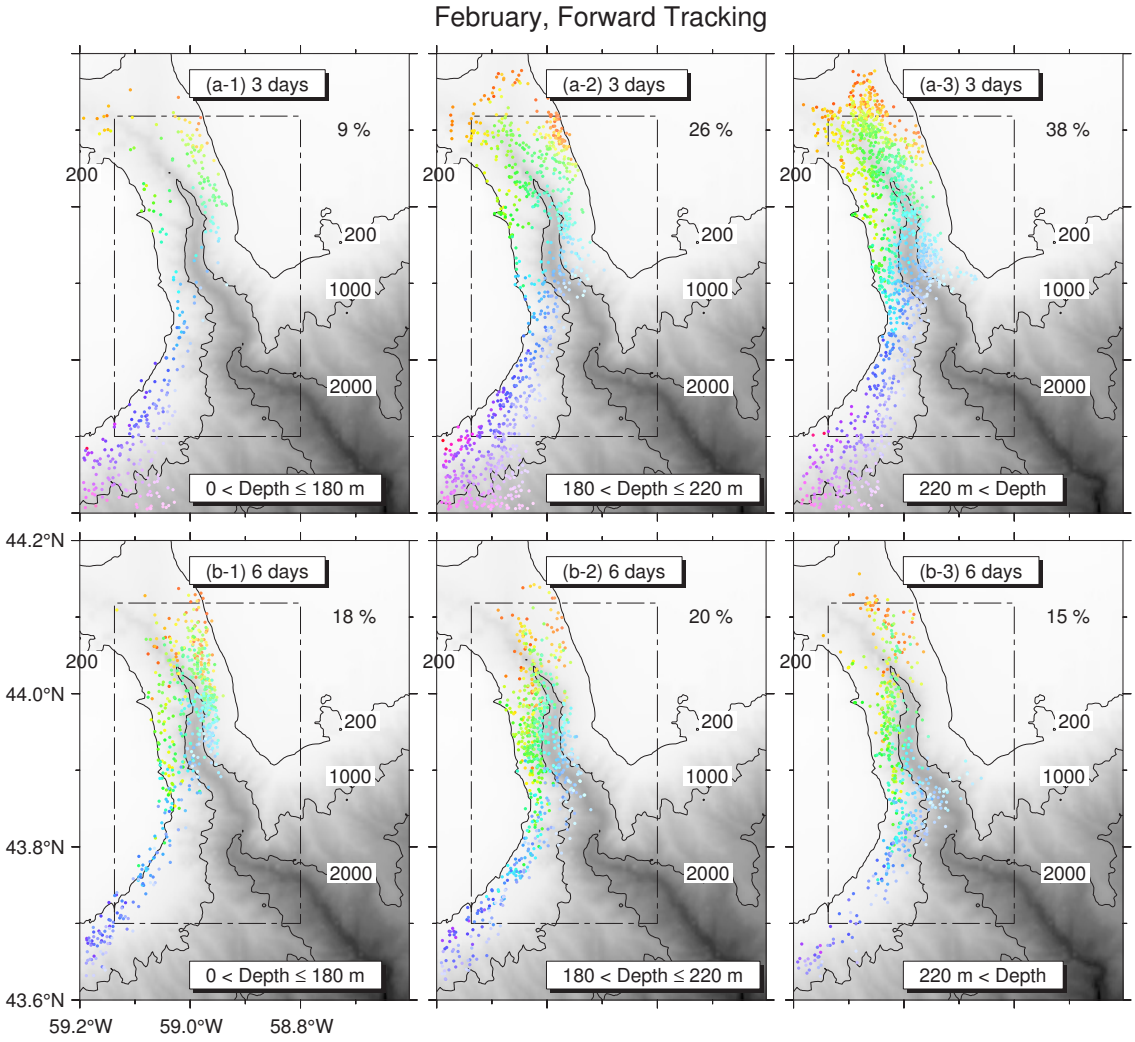

Figure 3.23: Particle positions in the top 180 m (left panels); between 180 to 220 m (middle panels); and below 220 m (right panels) at day 3 (upper panels) and day 6 (lower panels) in the case of forward in time tracking in ExpCTL using the 3-hourly instantaneous flow field produced by submodel L5 of DalCoast-Gully. All particles are released at 00:00 February 11, 2006. Selected isobaths in meters are shown by the gray contours.

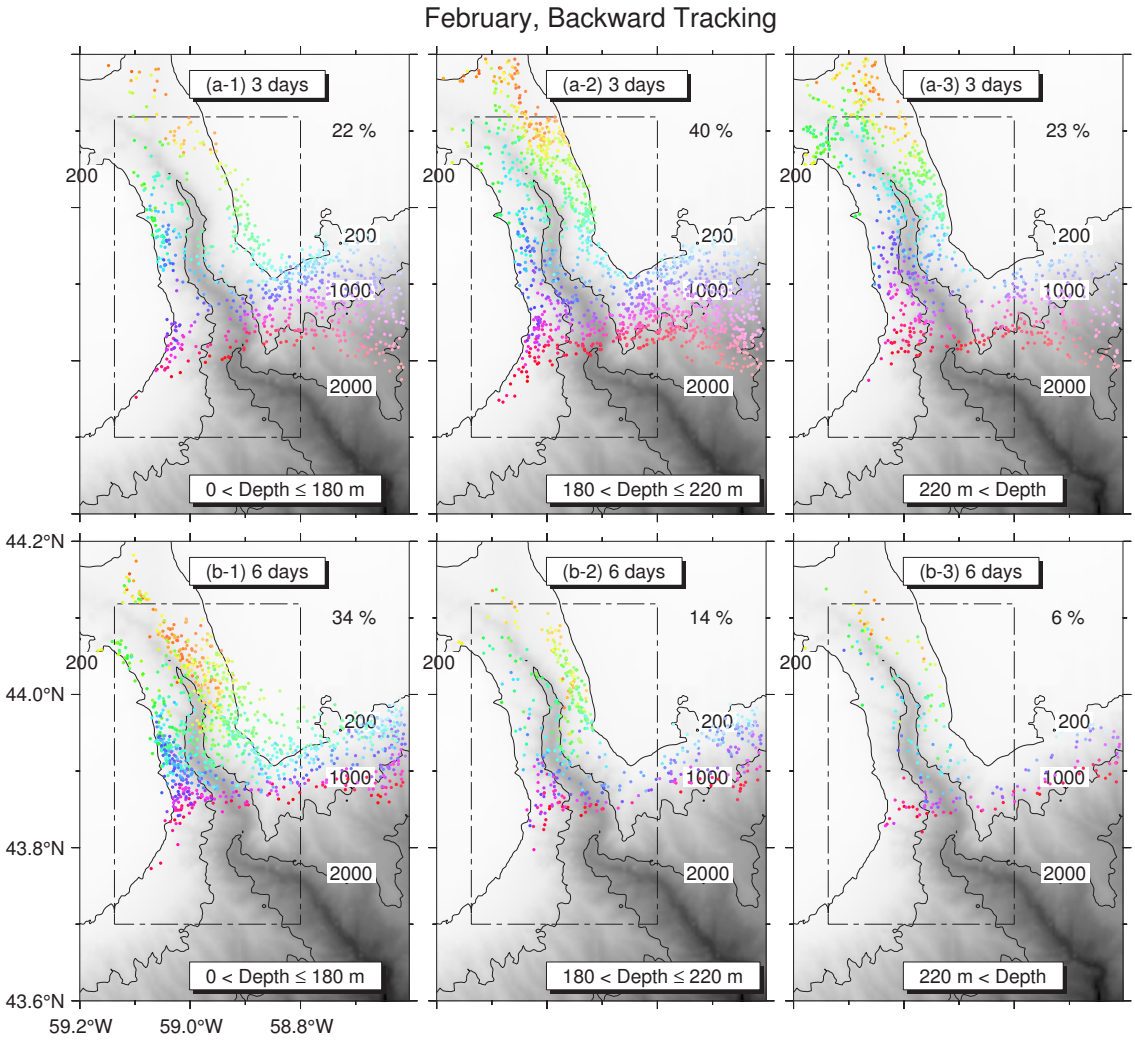

Figure 3.24: Same as Fig. 3.23, except that all particles are released at 00:00 February 17, 2006 and tracked backward in time in ExpCTL.

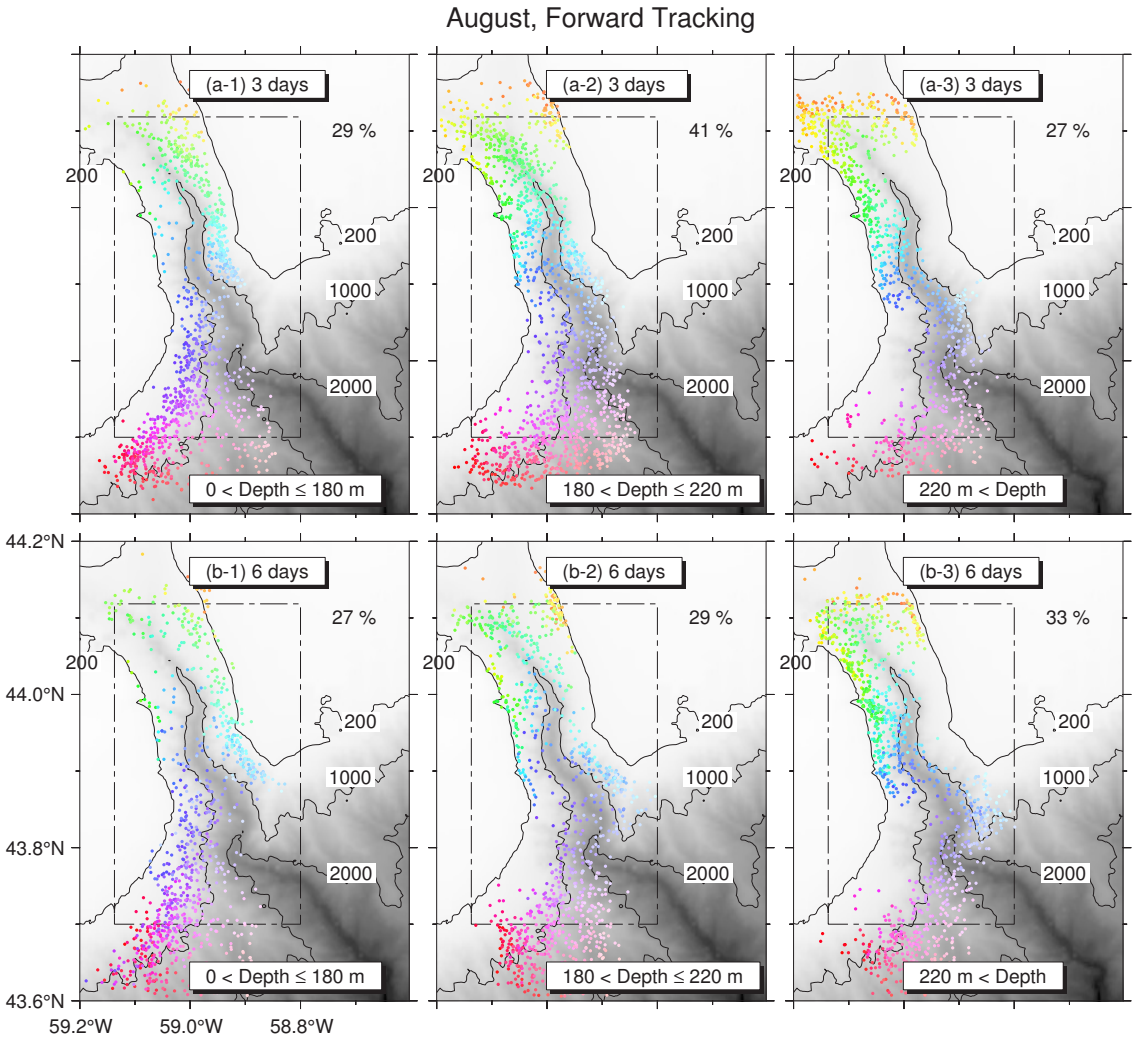

Figure 3.25: Same as Fig. 3.23, except that all particles are released at 00:00 August 12, 2006 and tracked forward in time in ExpCTL.

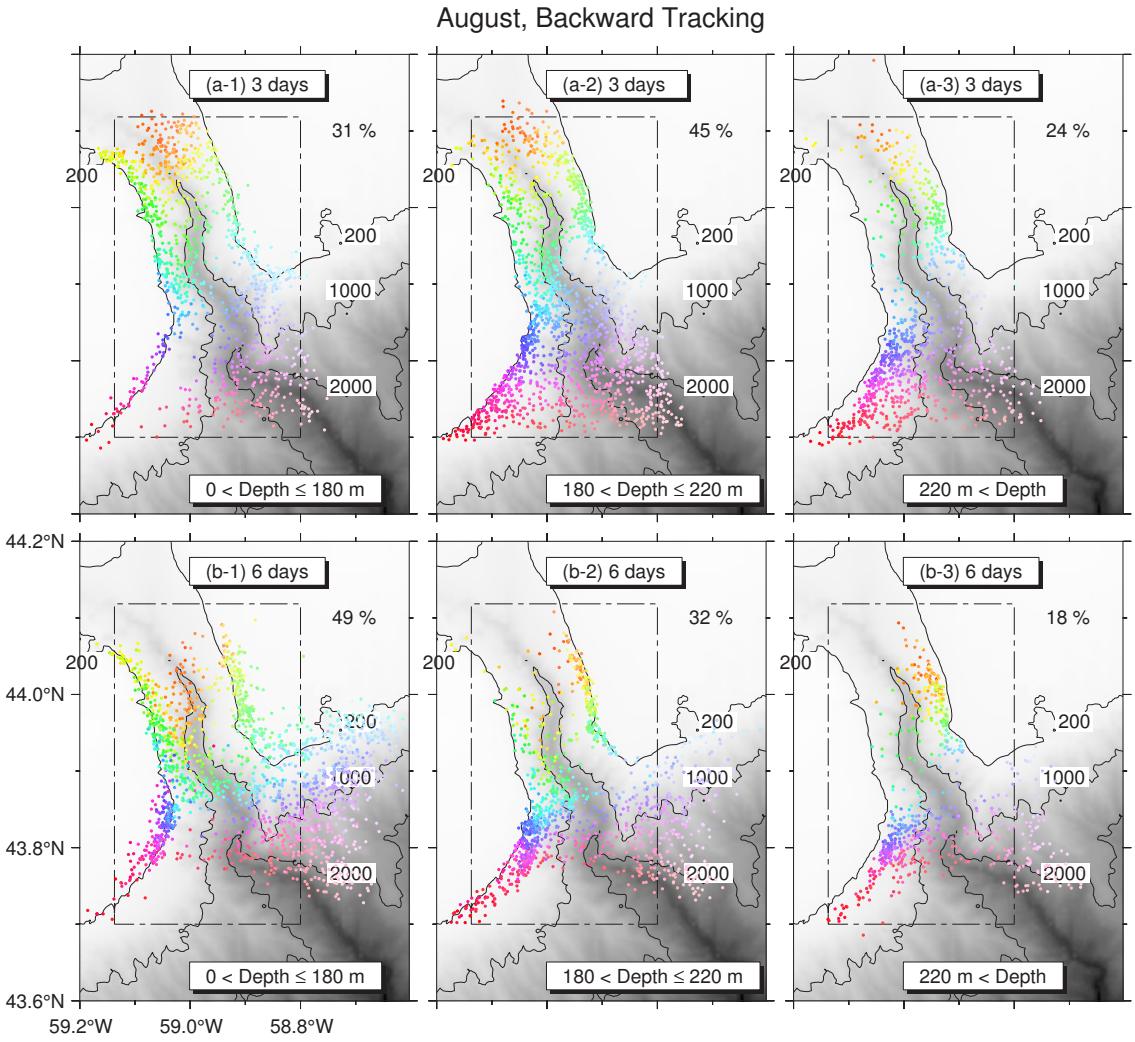

Figure 3.26: Same as Fig. 3.23, except that all particles are released at 00:00 August 18, 2006 and tracked backward in time in ExpCTL.

3.5.3 Residence Time

Residence time is one of important parameters in identifying the high retention and dispersion areas in ocean waters. Figure 3.27 shows the percentage of the total number of particles (P) inside the core protected area of the Gully (Zone 1) as a function of time (t) for each tracking experiment in the control runs (ExpCTL). The common feature in Fig. 3.27 is that P is characterized by a relatively rapid decay (local homogenization) followed by a slower "drain" out to the shelf break and deep ocean. The high frequency variations of typical semidiurnal and diurnal periods in the figure are due mainly to the number of particles moving in and out of Zone 1 caused by tides. The number of particles in a few tracking experiments decrease significantly by more than 80% in the first 5 days (Fig. 3.27a). The temporal decay of the percentage of the total number of particles (P) that remained inside a specific domain (Zone 1) can be approximated by (*Sheng et al.*, 2009; *Shan and Sheng*, 2012):

$$P = e^{-\frac{t}{T_e}} \tag{3.18}$$

where t is time, and T_e is the e-folding residence time. The exponential curve fitting based on the nonlinear least squares method in MATLAB® is used to estimate T_e for each tracking experiment. In the case of forward in time tracking, the estimated e-folding residence time is about 7 and 13 days in February and August 2006, respectively. The relatively short residence time in February is consistent with the strong monthly mean flow along the shelf break (Fig. 3.20). The residence time in the case of forward in time tracking is controlled mainly by the circulation in the downstream areas, while the residence time of backward in time tracking is controlled mainly by the circulation in the upstream areas. If the downstream and upstream circulations are symmetric, we can expect an identical residence time for the forward and backward tracking. In the Gully, the exponential decay of the percentage of the total number of particles (P) inside Zone 1 in the case of forward in time tracking is not symmetric to the decay of P in the case of backward in time tracking (Fig. 3.27a and b, c and d) due to the complex circulation over the Gully and adjacent waters. In the case of backward in time tracking, the estimated e-folding residence times are about 9 and 14 days in February and August 2006, respectively, which is longer than the estimates in the case of forward in time tracking.

Two additional sets of tracking experiments, ExpSUR and ExpBOT, were considered with initial release depths at surface and 1000 m respectively. The results of ExpSUR

Table 3.4: The residence time estimated from tracking experiments using different values of the eddy diffusivity coefficient, **K**(K_x,K_y,K_z), for the random walk. Here K_z = 180 $\times$ 10^{-4} m^2 s^{-1}. K_x=K_y=K_h is 1000 times larger than K_z. The low (0.1**K**) and high (10**K**) eddy diffusivity coefficients are considered

Experiment	Residence time in days		
	0.1**K**	**K**	10**K**
Feb, forward	8.0	7.0	5.3
Feb, backward	9.5	8.9	7.1
Aug, forward	14.7	12.9	9.7
Aug, backward	15.7	13.5	10.2

show nearly all the particles move out the Gully with the percentage of the total number of particles inside Zone 1 decreasing almost linearly to zero in the first few days. The results of ExpBOT show the most of the particles remain inside the Gully with the percentage of the total number of particles inside Zone 1 decaying exponentially to about 0.5 in the first 15 days and then slowly decreasing with time.

An additional set of tracking experiments (ExpNT) was calculated using the 3-hourly model flow fields without tides. The ensemble of $P(t)$ curves without tides are broader than the curves with tides (Figs. 3.27 and 3.28). The residence time without tides in the case of forward in time tracking is estimated to be about 8 and 20 days in February and August 2006, respectively, which is longer than the residence time with tides. This indicates that the tidal circulation increases the mixing and thus reduces the residence time of Zone 1.

The sensitivity of particle tracking results to the value of the eddy diffusivity coefficient (**K**) of the random walk is investigated through two additional sets of tracking experiments (ExpLK using low values of **K** and ExpHK using high values of **K**). The estimated residence times in ExpLK and ExpHK are comparable with the estimates in ExpCTL (Table 3.4). Our results demonstrate that the estimated residence time decreases with the increase of the eddy diffusivity coefficient.

Cong et al. (1996) conducted tracking experiments at a fixed depth of 30 m and found particles are likely to retain in the northern extension of the Gully which is surrounded by the Sable Island, Middle and Banquereau Banks (Fig. 1.1). Based on *Cong et al.* (1996)'s results, *Petrie et al.* (1998) estimated that the e-folding residence times of the northern

extension of the Gully are about 16 and 19 days for March and April, respectively, which are in the same order of magnitude as our estimates in the Gully. It should be noted that the flow field used in *Cong et al.* (1996) has a relatively coarse horizontal resolution (∼5 km) and does not include tidal currents.

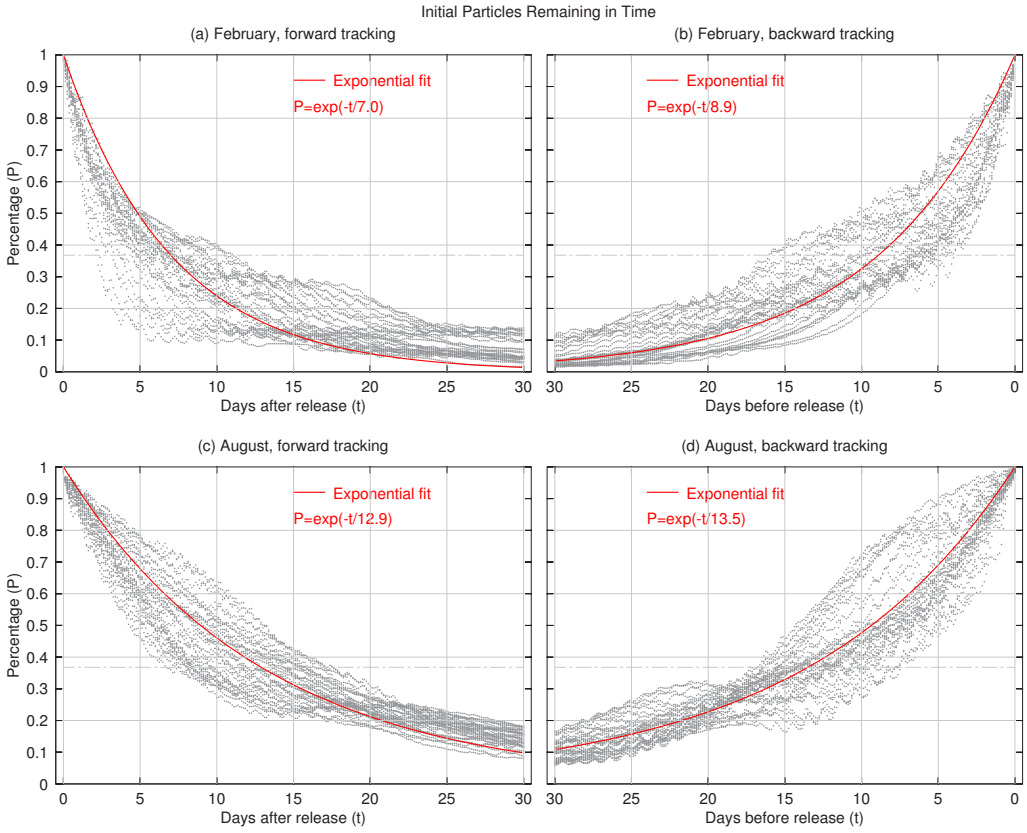

Figure 3.27: Time series of the percentage of the total number of particles ($P(t)$) remained in the initial release domain in ExpCTL. The gray dotted-lines are $P(t)$ curves for tracking experiments using (a) forward and (b) backward in time tracking in February and (c) forward and (d) backward in time tracking in August 2006. The red solid line is an exponential fit using the nonlinear least squares method.

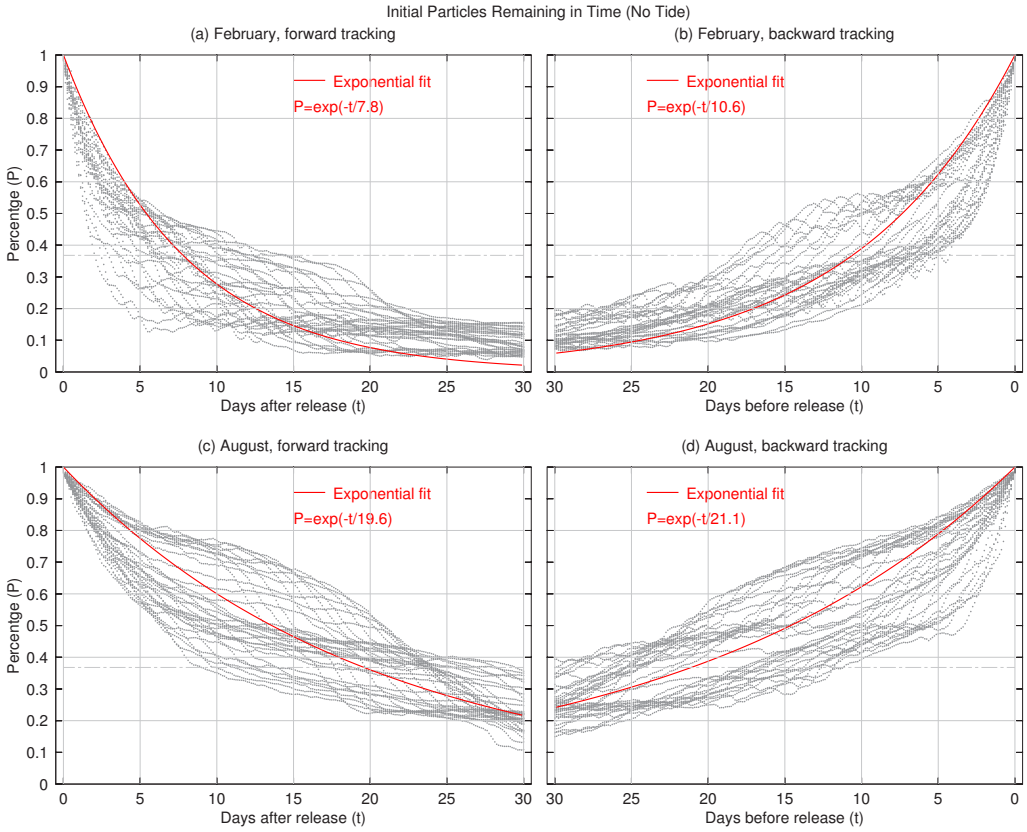

Figure 3.28: Same as Fig. 3.27, except that the particles are carried by the model flow fields without tides in ExpNT.

Maps showing the horizontal distribution of the residence time are also useful in identifying the high retention areas in the Gully. Figure 3.29 presents the distributions of the estimated residence time in February and August 2006 in ExpCTL. In the case of forward in time tracking, the residence time is about 2 days over the mouth and head of the Gully and about 10 days in the middle of the Gully in February (Fig. 3.29a). In August, the residence time has a similar spatial pattern as that in February, except for relatively higher values of residence time. The residence time is about 5 days over the mouth and head of the Gully and about 20 days in the middle of the Gully, particularly along the Gully flanks in August (Fig. 3.29c). In the case of backward in time tracking, the high residence time area occurs over a stripe extending from the western side of the Gully mouth to the eastern side of the middle of the Gully. The residence time along the stripe is about 15 and 25 days in February and August, respectively. It should be noted that the residence time discussed above is based on the movement of particles released in a rectangular region covering a management zone with the highest level of protection of the Gully MPA and the residence time, in general, depends on this initial release region.

Figure 3.30 presents distributions of the estimated residence time using the 3-hourly instantaneous model flow fields without tides in ExpNT. The high residence time area occurs along the Gully flanks with typical values of 20 and 30 days in February and August, respectively. The major differences between the residence maps with and without tides indicate that tidal circulation reduces the value of residence time in the Gully, particularly along the Gully flanks.

Distributions of the estimated residence time using different values of the eddy diffusivity coefficient (**K**) for the random walk are presented in Figs. 3.31 and 3.32. In the case of low **K** (ExpLK) the residence time is longer than that in the case of moderate **K** (ExpCTL) in the whole Gully. The residence time can reach up to 30 days in some localized areas in ExpLK. However, the spatial distribution of the residence time in the Gully in ExpLK is similar to that in ExpCTL, which suggests that the areas with relatively high values of residence time are not very sensitive to the value of **K**. In the case of high **K** (ExpHK), the residence time map is relatively uniform due to the enhanced diffusion in comparison with the residence map in ExpCTL. A comparison of the residence time maps at the low, moderate and high **K** indicates that the value of residence time decreases as the value of **K** increases in the Gully.

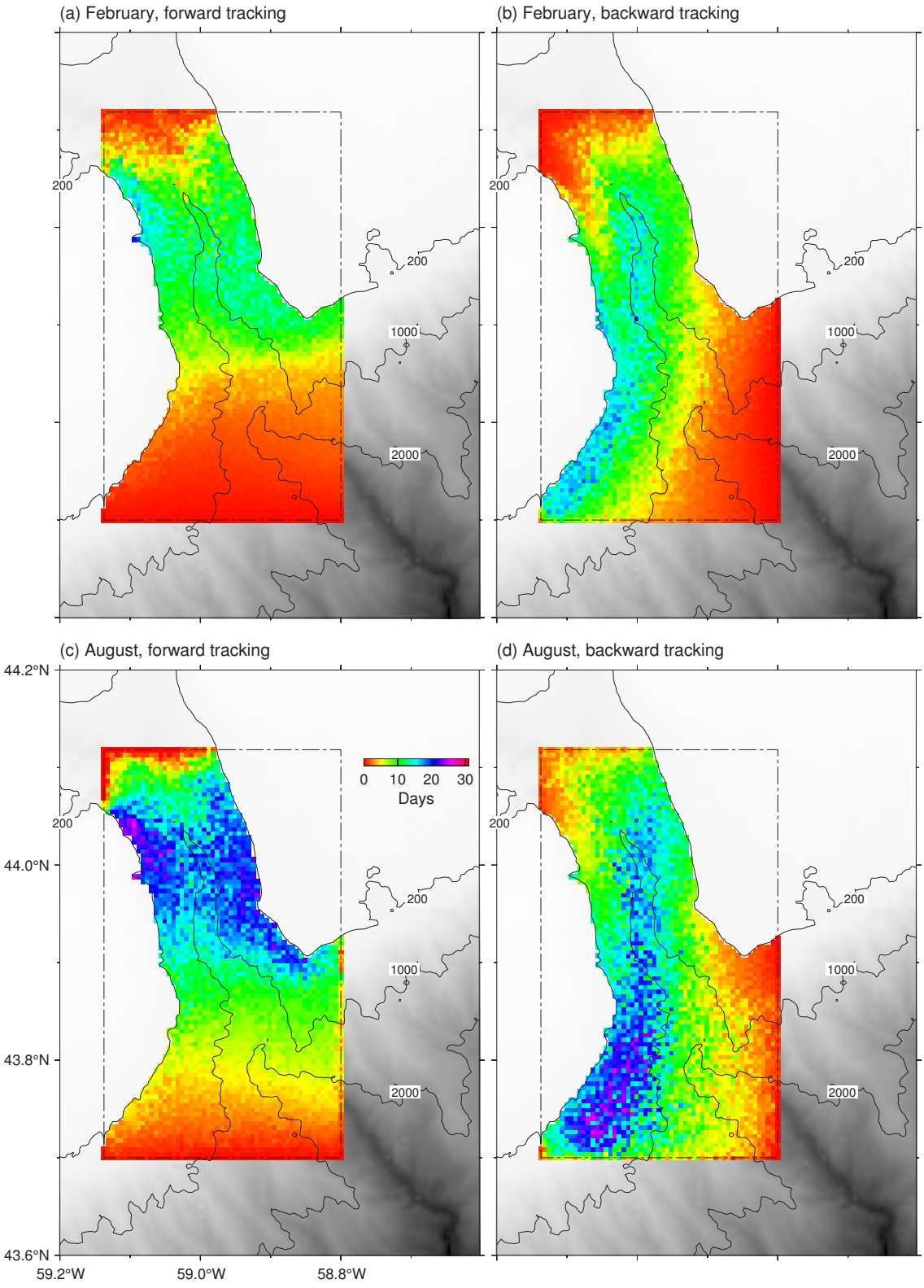

Figure 3.29: Distributions of the estimated residence time based on tracking experiments in ExpCTL using: (a) forward and (b) backward in time tracking in February and (c) forward and (d) backward in time tracking in August 2006. Color maps show the time particles spend in Zone 1 of the Gully Marine Protected Area (dash-dotted box).

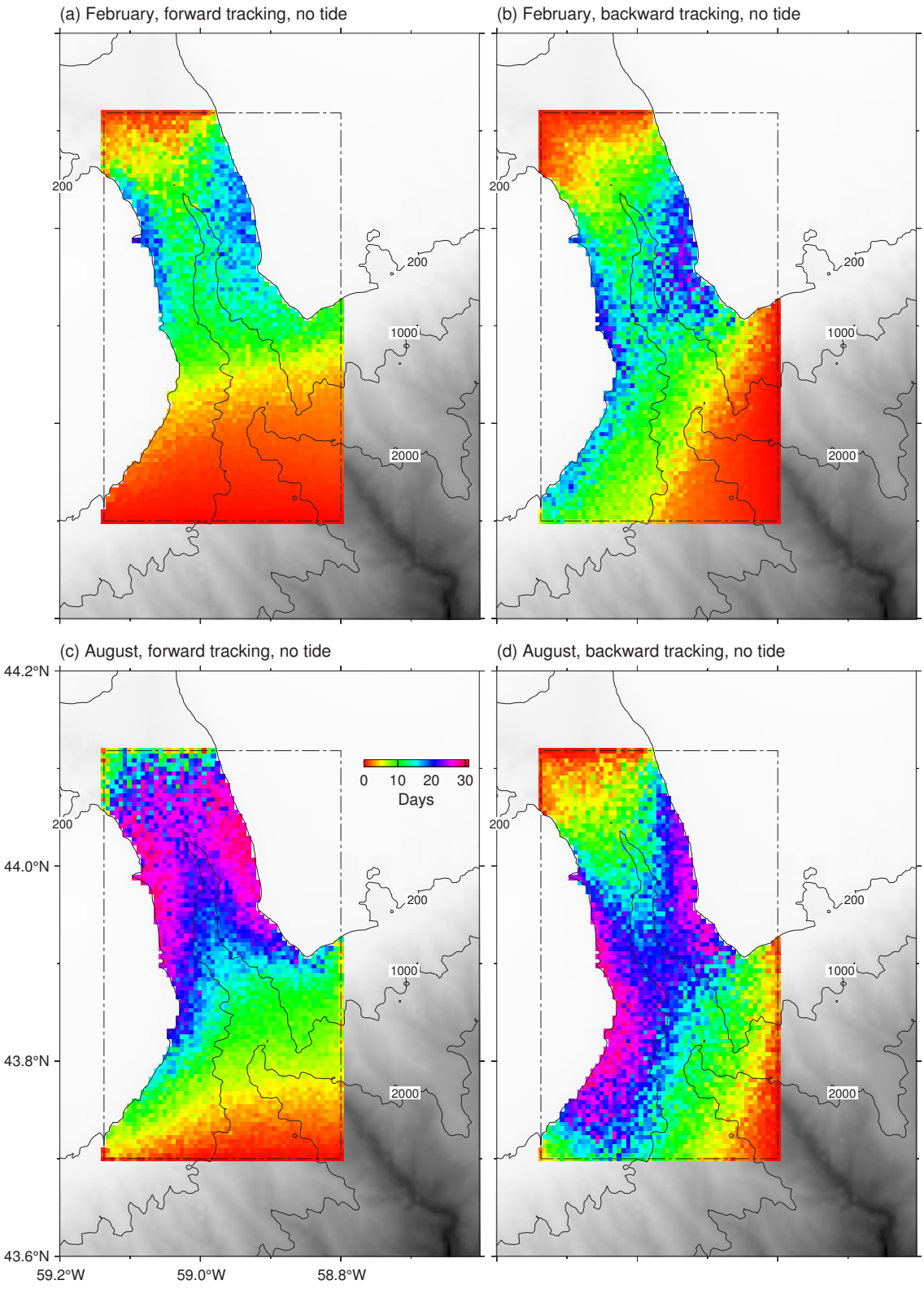

Figure 3.30: Same as Fig. 3.29, except that the particles were carried by the model flow fields without tides in ExpNT.

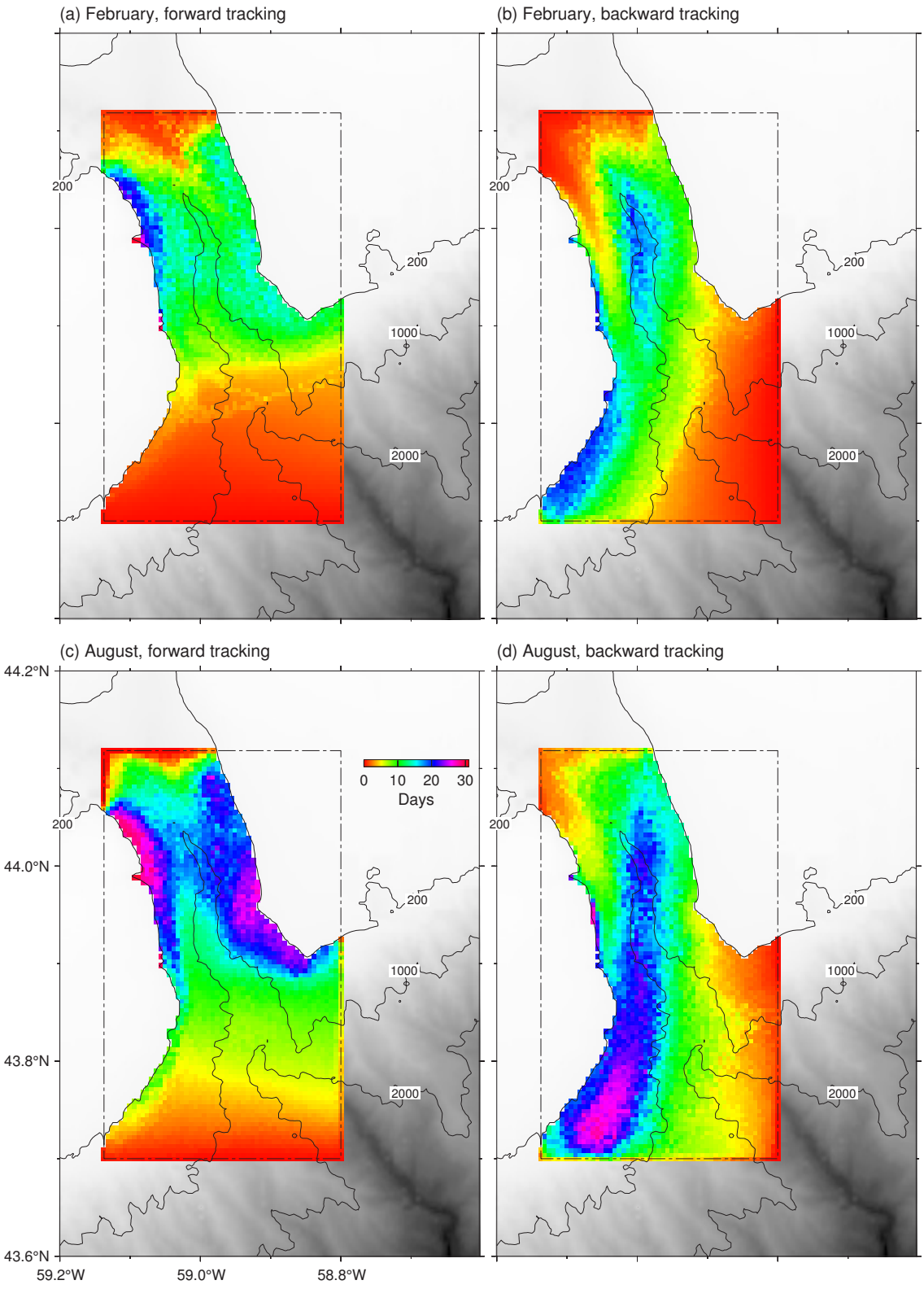

Figure 3.31: Same as Fig. 3.29, except that the eddy diffusivity coefficient **K** is 10 times smaller than the value used in ExpCTL.

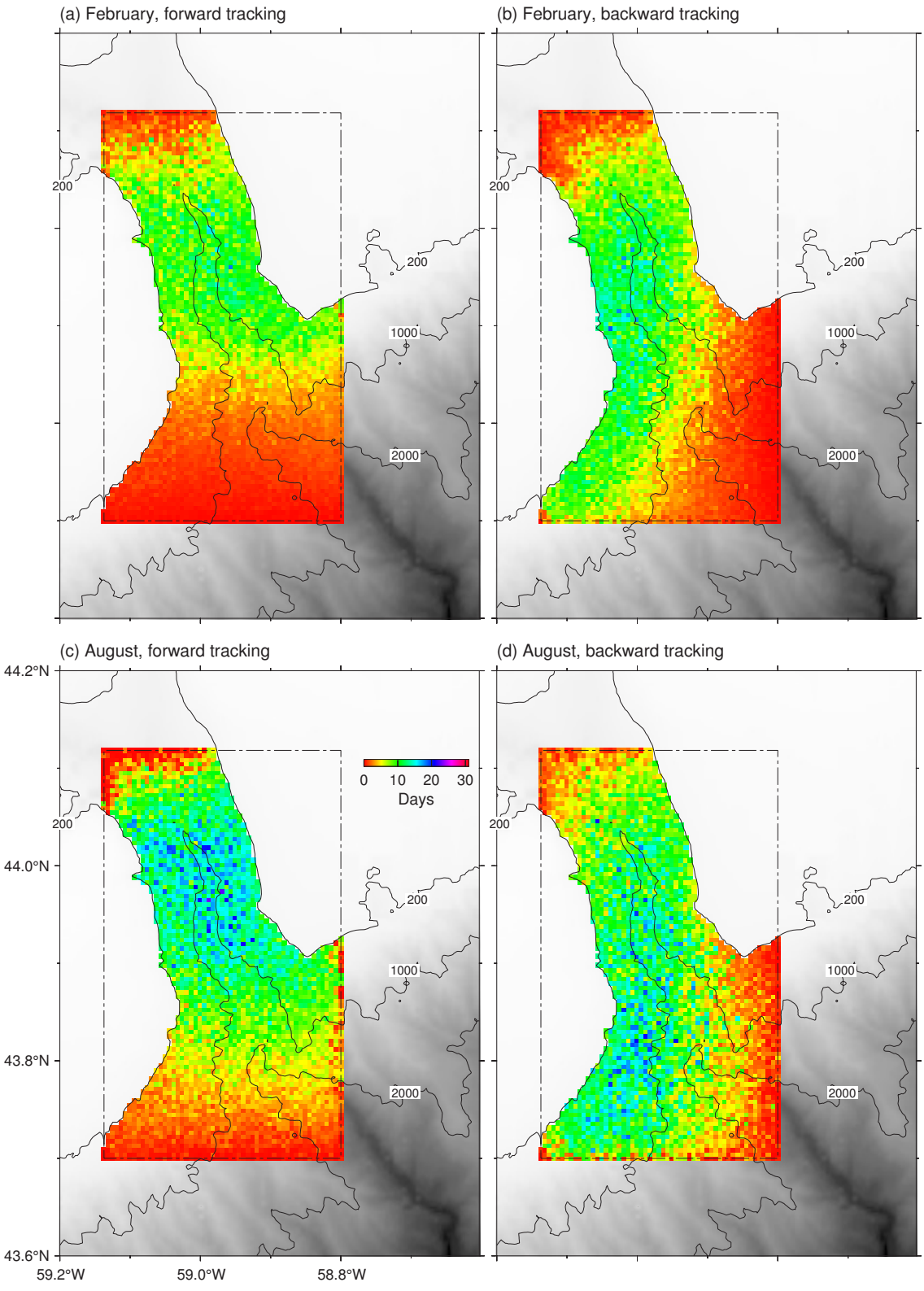

Figure 3.32: Same as Fig. 3.29, except that the eddy diffusivity coefficient **K** is 10 times larger than the value used in ExpCTL.

3.6 Implications for Whale Distribution and Migration

The Sable Gully is a particularly important habitat for northern bottlenose whales, which are known to occur along the canyon axis in the deep parts of the canyon (Fig. 3.33, *Moors-Murphy*, 2014). Northern bottlenose whales are also consistently observed in the nearby Shortland and Haldimand canyons located 50 km and 100 km to the east of the Gully, respectively (Fig. 3.33). Northern bottlenose whales are known to move regularly between these three canyons, though very few sightings have occurred in the adjacent shelf. It is thought that an abundant and reliable source of food, namely, Gonatus squid (the primary prey of northern bottlenose whales), must occur in the Gully in order to support the population (*Hooker et al.*, 2002).

Two implications of the oceanic circulation on the distribution and migration of northern bottlenose whale in the Gully and adjacent canyons can be made based on the above key observational results. First, the modelled circulation in the Gully shows relatively strong southwestward shelfbreak current. However the fact that the northern bottlenose whales are permanently resident in the Gully implies that the current has little direct impact on their migration and distribution. Second, the distribution and abundance of northern bottlenose whale's prey (e.g., squid) could be affected by the oceanic circulation, which could have indirectly impact on whale's migration and distribution. The particle tracking experiments conducted froward and backward in time identified that the source region of the Gully is to the northeast along the shelf break indicating that the Gully and the two canyons in the upstream along the shelf break are dynamically connected. Besides, the shelfbreak current may play an important role in advecting squid from northeast downstream into the Gully.

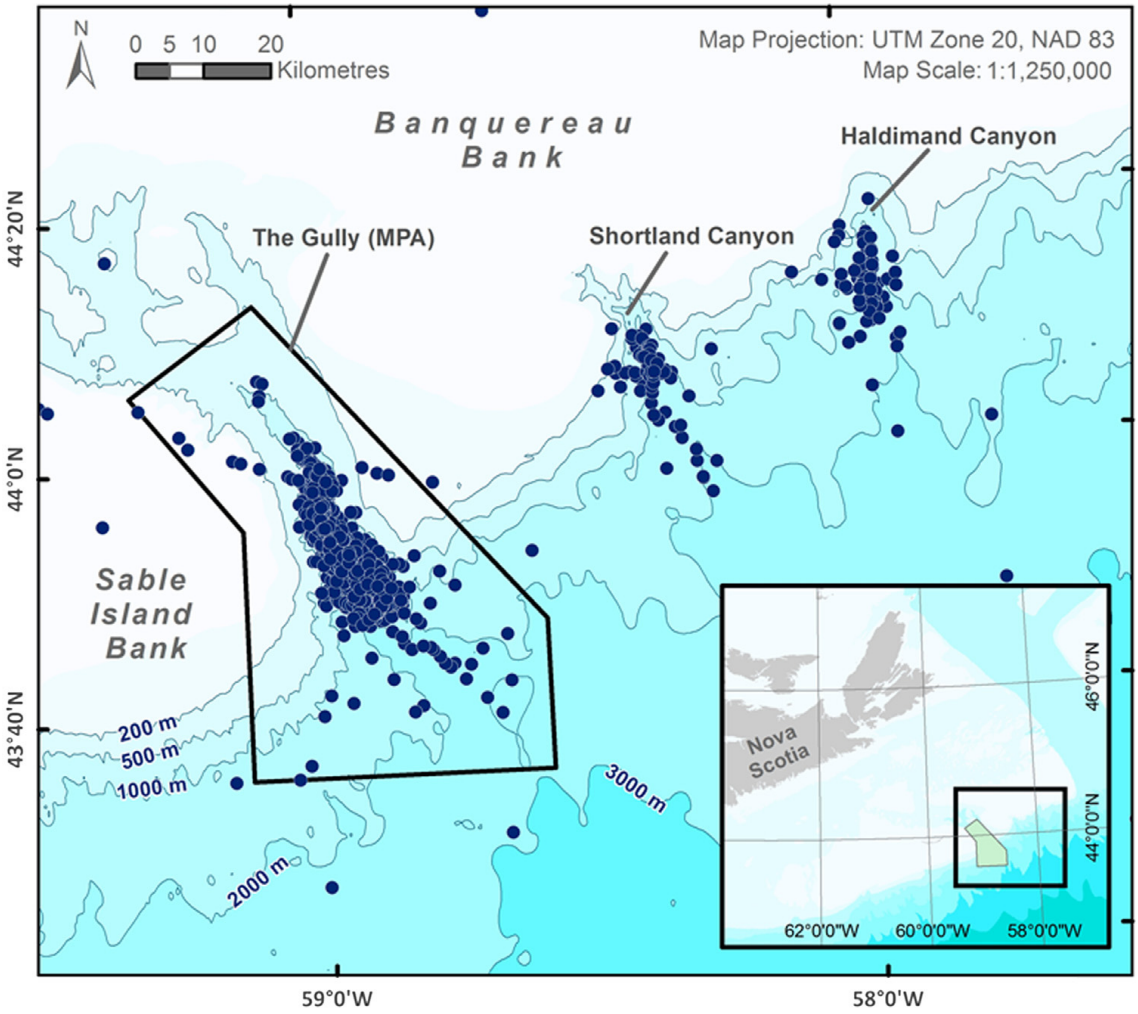

Figure 3.33: Documented northern bottlenose whale sightings (filled-in circles) around the canyons of the eastern Scotian Slope between 1967 and 2010. The outer boundary of the Gully MPA is shown. (Adapted from *Moors-Murphy*, 2014)

3.7 Summary

A five-level multi-nested, three-dimensional (3D), ocean circulation model was used to reconstruct the circulation and hydrography over the Sable Gully and adjacent waters in the year of 2006. The model performance was assessed by comparing the model simulations with current-meter observations, existing datasets and CTD measurements. The vertical profiles of the simulated annual mean currents in the Gully were in fair agreement with current-meter observations (*Greenan et al.*, 2014). The simulated depth-averaged tidal current ellipses agreed with the OSU tidal dataset. The model also captured the observed vertical variations of M_2 and K_1 tidal current ellipses from the surface to the deep water. The simulated temperature and salinity in the Gully were in fair agreement with the hydrographic observations made in April and August.

The circulation and hydrography in the Sable Gully and adjacent waters were shown to have significant temporal and spatial variability. A process study was conducted to quantify the main physical processes affecting the 3D circulation and hydrography in the Gully at the synoptic and annual mean timescales. On the synoptic timescale (storm events), the circulation in the surface mixed layer is affected significantly by the local wind forcing, particularly during the passing of storms. On a longer timescale (annual mean), the local wind forcing is only important in the surface Ekman layer. The tidal residual currents due to the nonlinear tide-topography interaction are strong inside and at the mouth of the Gully. A persistent strong southwestward shelfbreak jet exits along the slope with a core centred at about 500 m. An analysis of along-canyon volume transport suggested that on the annual mean timescale, tidal residual is the primary contributor to the on-shelf transport of the slope water into the Gully.

Based on the 3-hourly instantaneous currents produced by submodel L5 of DalCoast-Gully, particle tracking experiments were conducted both forward and backward in time to examine the particle pathway, upstream and downstream areas, and residence time of the Sable Gully. The downstream (upstream) area of the southern part of the Gully are located to the southwest (northeast) of the Gully mouth along the Scotian Slope. The e-folding residence time is about 7 and 13 days in February and August 2006, respectively, estimated from the movements of particles released at the depth of the Gully rim and tracked forward in time. The areas with a relatively high residence time are along the Gully flanks with typical values of 10 and 20 days in February and August 2006, respectively.

The particle movements from tracking experiments with and without tides suggested that tidal circulation reduces the value of residence time in the Gully, particularly along the Gully flanks. The 3D circulation and hydrography in the Gully discussed in this study may not have direct impact on the distribution and migration of northern bottlenose whale, but they could play an important role in advecting whale's prey (e.g., squid) into the Gully. The knowledge gained in this study can be used in developing an effective management plan for the Gully Marine Protected Area.

CHAPTER 4

CENTRAL SCOTIAN SHELF ADJACENT TO HALIFAX [1]

4.1 Introduction

Circulation and hydrography over coastal and shelf waters of Nova Scotia have significant temporal and spatial variability. For example, sharp sea surface temperature fronts were observed along the coast of Nova Scotia on September 1, 2012 by the Moderate Resolution Imaging Spectroradiometer (MODIS) instrument onboard the Aqua satellite (Fig. 4.1). The main physical processes that affect the circulation, hydrography and associated variability over the Scotian Shelf (SS) and adjacent waters include tides, wind forcing, net heat and freshwater fluxes at the sea surface, shelf-slope exchange, freshwater runoff, and other atmospheric forcing. The tides along the south shore of Nova Scotia are mainly semi-diurnal with amplitudes of the M_2 constituent increasing from $\sim$50 cm at the northeast tip to $\sim$100 cm at the southwest tip of Nova Scotia (*Dupont et al.*, 2002). In the Bay of Fundy (BoF), the tides resonate significantly with the local geometry (*Garrett*, 1972) to produce a large (up to $\sim$17 m) tidal range at the head of the BoF. Associated with large tides, strong tidal currents in the BoF provide an effective mechanism to vertically mix the water column (*Garrett et al.*, 1978).

[1] This chapter was modified from two manuscripts entitled: (1)"Assessing the performance of a multi-nested ocean circulation model using satellite remote sensing and *in-situ* observations" by Shan, S., J. Sheng, K. Ohashi and D. Mathieu published in *Satellite Oceanography and Meteorology* in 2016; and (2)"A modelling study of coastal upwelling on the Scotian Shelf" by Shan, S. and J. Sheng in preparation for submission to *Journal of Geophysical Research*.

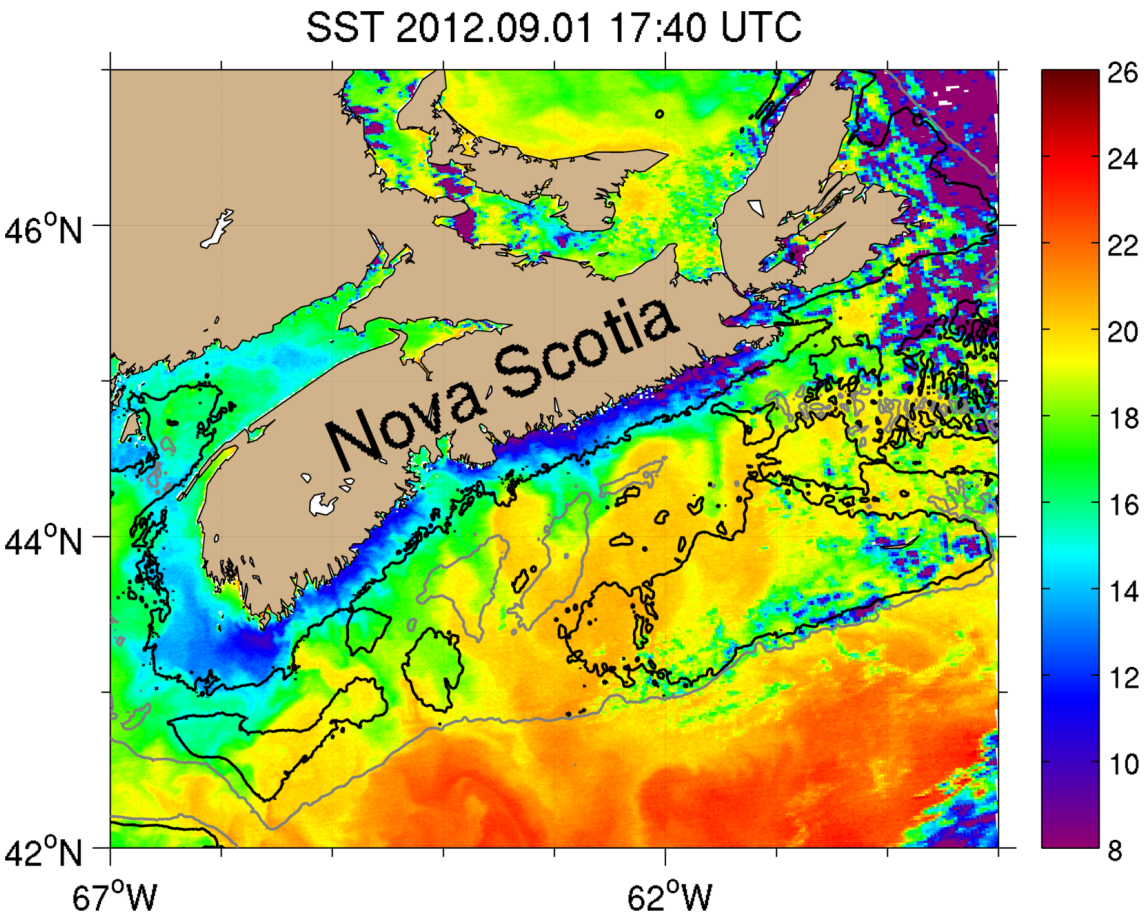

Figure 4.1: MODIS satellite remote sensing data of sea surface temperature (SST) on September 1, 2012. Data were extracted from the Ocean Color Website (`http://oceancolor.gsfc.nasa.gov`). The 100 m and 200 m isobaths are shown by the black and gray contours, respectively.

The SST over the study region has a strong seasonal cycle, with a mean range of about 16°C (*Thompson et al.*, 1988), largely due to the intense negative and positive heat fluxes at the sea surface from the atmosphere to the ocean in winter and summer, respectively. The interannual and decadal variability of temperature and salinity on the SS is affected significantly by variations of the equatorward transport of the Labrador Current through the shelf-slope exchange (*Petrie and Drinkwater*, 1993). The freshwater discharge from the St. Lawrence River (SLR) also plays an important role in affecting the salinity and circulation in the Gulf of St. Lawrence-Scotian Shelf-Gulf of Maine (GSL-SS-GoM). Previous studies suggested that the freshwater discharge signal of the SLR from Québec City reaches Halifax and Cape Sable in about 6 months (*Sutcliffe et al.*, 1976) and about 8-9 months (*Smith*, 1989), respectively.

Wind stress and associated variability also play an important role in driving the variation of circulation and hydrography of Nova Scotia's coastal and shelf waters. The dominant southwesterly wind in summer on the SS is favorable for coastal upwelling. Based on satellite images of SST, *Petrie et al.* (1987) demonstrated the development of a band of cool water over the inner SS during a month-long period of upwelling-favorable winds in 1984. In addition, tropical and winter storms can generate significant storm surges, shelf waves, and intense inertial currents on the SS and adjacent waters (*Sheng et al.*, 2006).

With the advent of computer technology and significant progress in numerical methods in the last 50 years, numerical ocean circulation models have increasingly been used in simulating three-dimensional (3D) circulation and hydrography in the ocean. Various numerical models were developed for simulating the circulation and hydrography of Nova Scotia's coastal and shelf waters (e.g., *Thompson et al.*, 2007; *Wu et al.*, 2012; *Urrego-Blanco and Sheng*, 2014; *Katavouta*, 2015; *Brennan et al.*, 2016). One of these numerical models is a 3D ocean circulation modelling system known as DalCoast. DalCoast has been developed over the past two decades to simulate the circulation and hydrography for the GSL-SS-GoM region. The earliest version of this model was used to simulate the storm surge and two-dimensional (2D) circulation over the eastern Canadian shelf, with a special emphasis of the SS and GSL region (*Bobanovic*, 1997). An improved version was then applied to simulate the 3D circulation and hydrography over the coastal and shelf waters of Nova Scotia (*Thompson et al.*, 2007), using a simple data assimilation method known as spectral nudging to suppress seasonal bias and drift in the model. The more recent version

was further developed with important modifications including an enlarged model domain and higher resolution atmospheric forcing (*Ohashi and Sheng*, 2013). A multi-nested version of DalCoast was developed by *Yang and Sheng* (2008) and later by *Shan et al.* (2011). DalCoast has been applied, using a one-way nesting technique, to simulate the circulation and hydrography over three scientifically and socio-economically important marine areas of Nova Scotia: Lunenburg Bay (DalCoast-LB, *Yang and Sheng* (2008)), Halifax Harbour (DalCoast-HFX, *Shan et al.* (2011)) and Sable Gully (DalCoast-Gully, *Shan et al.* (2014)). The circulation and hydrography simulated by the multi-nested version of DalCoast were extensively validated against observations (*Yang and Sheng*, 2008; *Shan et al.*, 2011, 2014).

It is a great challenge, however, for a numerical model to accurately reproduce the observed circulation and associated variability over the coastal and shelf waters of Nova Scotia, including the above-mentioned observed SST fronts and the Nova Scotia Current. This is mainly because important physical processes in operation are not fully understood in the region. For example, what are the variations in the strength and offshore extension of the SST front? What are the main physical factors affecting the interannual variability of the Nova Scotia Current? How is the circulation over the Scotian Shelf affected by Slope Water intrusions? An accurate circulation model for this region is a valuable tool in answering the above questions.

As a first step, the main objective of this study is to assess the performance of a nested-grid model for the coastal and shelf waters of Nova Scotia by using satellite remote sensing data and *in-situ* oceanographic observations. This chapter presents the latest version of DalCoast to date, in which the domain of the finest-resolution ($\sim$500 m) submodel covers the inshore part of the central SS region extending about 200 km seaward from Halifax Harbour and passing Emerald Basin to the shelf break (Fig. 4.2). The nesting approach provides a computationally efficient method to better resolve physical processes over the central SS, such as the Nova Scotia Current, coastal upwelling and shelf-slope exchange, within the upstream and downstream regions. In Section 4.2, the nested-grid circulation model is described. In Section 4.3, the model performance is assessed by comparing against various observations. In Section 4.4, the nested-grid model is used in a process study to examine the effect of tidal-mixing and wind-driven coastal upwelling on the cold surface water formation along the Nova Scotia coast in summer. In Section 4.5, an in-depth

study of the coastal upwelling is presented. In Section 4.6, the implications for salmon migration are discussed. A summary is presented in the last section.

4.2 Numerical Modelling System

The nested-grid ocean circulation modelling system used here consists of four submodels, with progressively smaller model domains and finer horizontal resolutions zooming from the northwest Atlantic into the central SS. The two outermost submodels, L1 and L2, are based on the Princeton Ocean Model (POM, *Mellor*, 2004). Submodel L1 is a 2D barotropic storm surge model covering the eastern Canadian shelf from the Labrador Shelf to the GoM with a horizontal resolution of 1/12°. Submodel L2 is a 3D baroclinic model covering the GSL, the SS, and the GoM with a horizontal resolution of 1/16° and 40 σ-layers in the vertical. Submodels L3 and L4 are also 3D and baroclinic with a horizontal resolution of $\sim$2 km and $\sim$500 m, respectively. Submodels L3 and L4 are based on the free-surface version of CANDIE (*Sheng et al.*, 1998), which is a 3D primitive-equation ocean circulation model that uses the A-grid, z-levels in the vertical and a fourth-order advection scheme. There are 47 z-levels in the vertical in L3 and L4, with relatively fine vertical resolutions of 3 m in the first layer, and 4 m between 3 m and 103 m, and 8 m in the deep water. The one arc-minute interval gridded bathymetry data from GEBCO (General Bathymetric Chart of the Oceans, `www.gebco.net`) is used for the model bathymetry. This version of DalCoast is called as DalCoast-CSS. A detailed description of the modelling system is presented in appendix A. It should be noted that the wind, pressure and other variables related to heat fluxes used in DalCoast-CSS are updated from NCEP reanalysis to NARR (North American Regional Reanalysis) for a better spatial and temporal coverage (32 km, 3-hourly). The temperature and salinity in the model are spectrally nudged toward the seasonal-mean climatologies at depths greater than 40 m in L2 and L3 using the spectral nudging method (*Thompson et al.*, 2007). Hence, the model temperature and salinity in the top 40 m evolve freely under the influence of external forcing. In addition, the semi-prognostic method (*Sheng et al.*, 2001) is used to further reduce the seasonal drift in the simulated circulation in L2. In this method, the simulated density in the hydrostatic equation is expressed as a linear combination of the simulated density and the climatological density, which is equivalent to adding a correction term to the horizontal pressure gradient terms in the momentum equation (*Sheng et al.*, 2001).

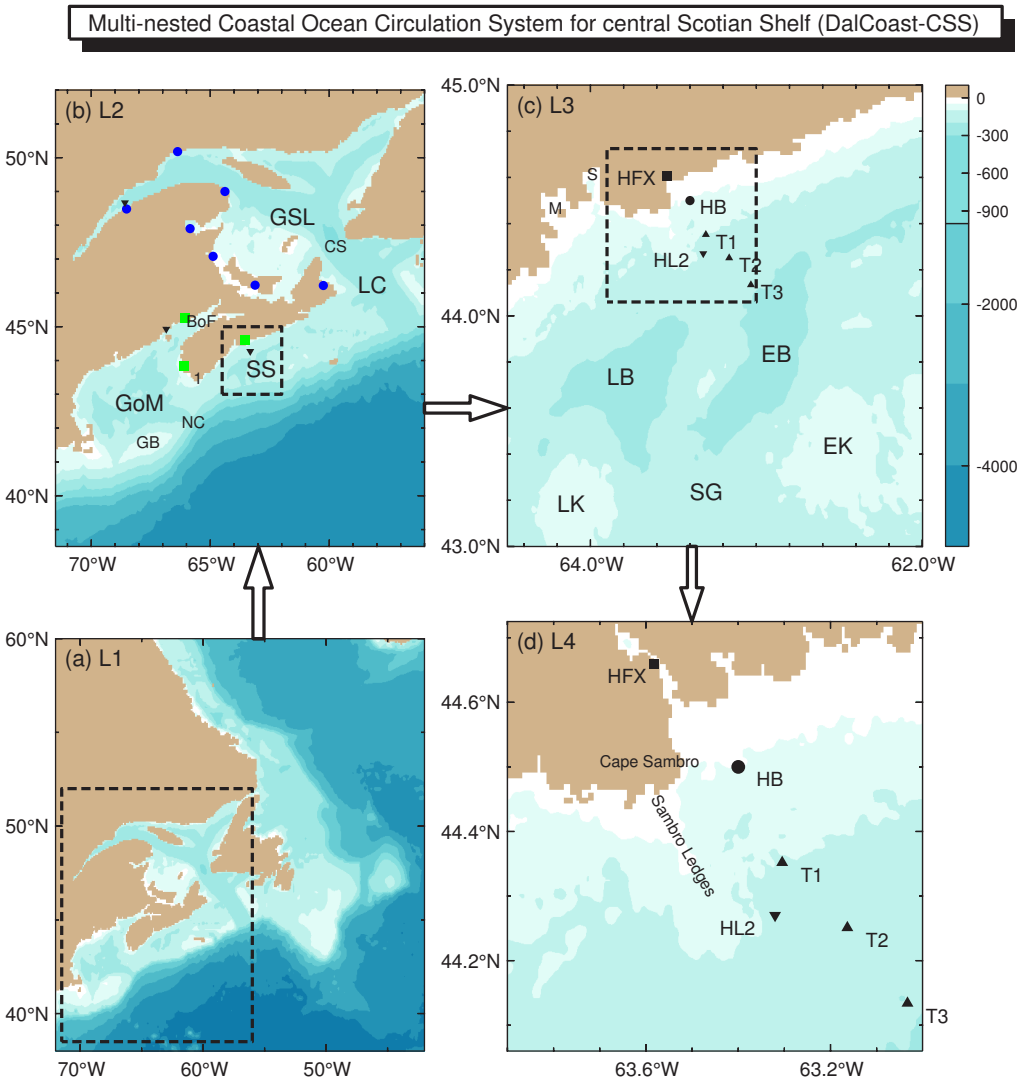

Figure 4.2: Domains and major bathymetric features of the four submodels of the nested-grid ocean circulation model. In (b), the blue solid circles and green solid squares indicate the tide gauge locations; the downward-pointing triangles indicate the position of hydrographic stations: Rimouski in the GSL, Station 2 on the SS, and Prince 5 in the BoF. In (c) and (d), the black solid circle indicates the position of the marine buoy outside Halifax Harbour (HB); the black solid square indicates the position of the tide gauge in Halifax Harbour (HFX); the black upward-pointing triangles indicate positions of three current moorings: T1, T2 and T3; the black downward-pointing triangle indicates the position of Station 2 (HL2). Land is masked by the tan color. The Gulf of Maine (GoM), Scotian Shelf (SS), Gulf of St. Lawrence (GSL), Bay of Fundy (BoF), Northeast Channel (NC), Laurentian Channel (LC), Cabot Strait (CS) and Georges Bank (GB) are labelled in (b). In (b), "1" represents Cape Sable. LaHave Basin (LB), LaHave Bank (LK), Emerald Basin (EB), Emerald Bank (EK) and Scotian Gulf (SG) are labelled in (c). The following geographical names are used in the discussion of coastal upwelling and labelled in (c) and (d): Mahone Bay (M), St. Margarets Bay (S), Halifax Harbour (HFX), Cape Sambro and Sambro Ledges.

4.3 Model Validation

DalCoast-CSS is initialized from the January mean hydrographic climatology and integrated from a state of rest for two years from January, 2011 to the end of 2012 using the configuration described in Section 4.2. In the model assessment, we mainly focus on the model results for 2012. The oceanographic measurements used for the assessment include satellite remote sensing data from GHRSST and Aquarius, and *in-situ* oceanographic observations made by tide gauges, a marine buoy, ADCPs and CTDs.

4.3.1 Sea Level

Sea level observations have been made by tide gauges at several locations in the study region (Fig. 4.2b). A MATLAB® package known as T_TIDE (*Pawlowicz et al.*, 2002) was used to conduct harmonic analysis of observed and simulated sea levels. *Ohashi and Sheng* (2015) recently assessed the performance of submodel L2 in simulating tides in the GSL. In this study, we assess the model performance in simulating tides in GSL-SS-GoM region. Figure 4.3 shows scatterplots between the observed and simulated amplitudes and phases of tidal elevation for the M_2 and K_1 constituents for 2012 at 10 tide gauge locations. Here we use a statistical quantity γ^2, which is similar to the one introduced in Chapter 3 Eq. (3.6), to provide a quantitative measure of the model performance:

$$\gamma^2 = \frac{Var\,(O - M)}{Var\,(O)} \tag{4.1}$$

where Var represents the variance operator, and O and M denote the observed and model simulated variables respectively. The smaller γ^2 is, the better the performance of the model is. Empirically, the threshold value of γ^2 is chosen to be 1. The calculated γ^2 is relatively small (< 0.1) and similar to the values discussed in *Ohashi and Sheng* (2015), indicating the submodel L2 is able to capturing the tides in the GSL-SS-GoM region.

We next assess the performance of the innermost submodel L4 in simulating the tidal and non-tidal components of sea levels in Halifax Harbour. Sea level observations have been made at a tide gauge in Halifax Harbour for almost a century (see the position marked by a black square in Fig. 4.2d). Observations of sea levels in a 2-month period (November 1 to December 31, 2012) in Halifax Harbour demonstrate that sea levels are strongly affected by tides which are predominantly semi-diurnal (Fig. 4.4a). A pronounced spring and neap variation is also evident in the sea level observations due mainly to the beating of the M_2

and S_2 tidal constituents. From the neap to spring tide, the observed tidal range increases from about 0.6 to 2.0 m. The non-tidal component of observed sea levels (Fig. 4.4b), which include the storm surge and inverse barometer effect ($\eta_a = -\tilde{P}_a/\rho g$, where $\tilde{P}_a$ is atmospheric pressure perturbation, ρ is density of seawater and g is acceleration of gravity), also contributes to the total sea level variations. Several peaks in the observed non-tidal component (Fig. 4.4b) can be seen in the fall and winter associated with storm events. The non-tidal observed sea levels are relatively small in summer due mainly to less severe weather conditions over the study region in summer than in other three seasons.

Overall, submodel L4 reproduces very well the sea level observations (Fig. 4.4a and b). The simulated tidal component is in good agreement with observations both in amplitudes and phases with $\gamma^2 = 0.03$. The simulated non-tidal component also has reasonable agreement with observations with $\gamma^2 = 0.34$. These low values of γ^2, which are similar to those discussed in previous study (*Shan et al.*, 2011), indicate that DalCoast-CSS performs well in simulating sea level variability in Halifax Harbour at timescales of hours to seasons. It should be noted that large mismatches during several occasions in the non-tidal component are due mainly to the less accurate atmospheric forcing during strong storm events used in driving the model.

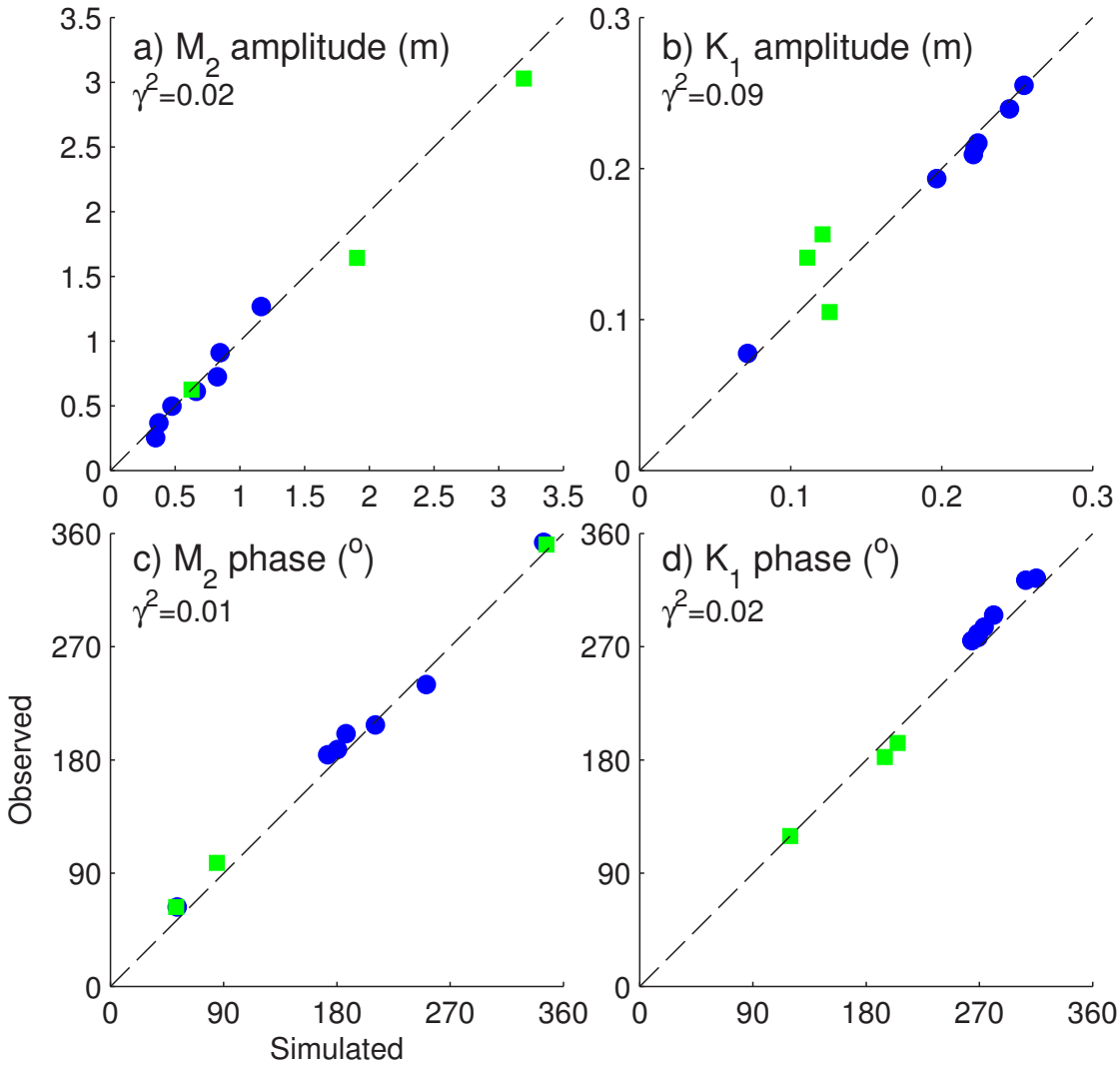

Figure 4.3: Scatterplots between observed and simulated amplitudes and phases of tidal elevations for the M_2 and K_1 tidal constituents for 2012 at 10 tide gauge locations shown in Fig. 4.2b. Stations in the Gulf of St. Lawrence are shown in circles. Outside the Gulf, the stations are shown in squares.

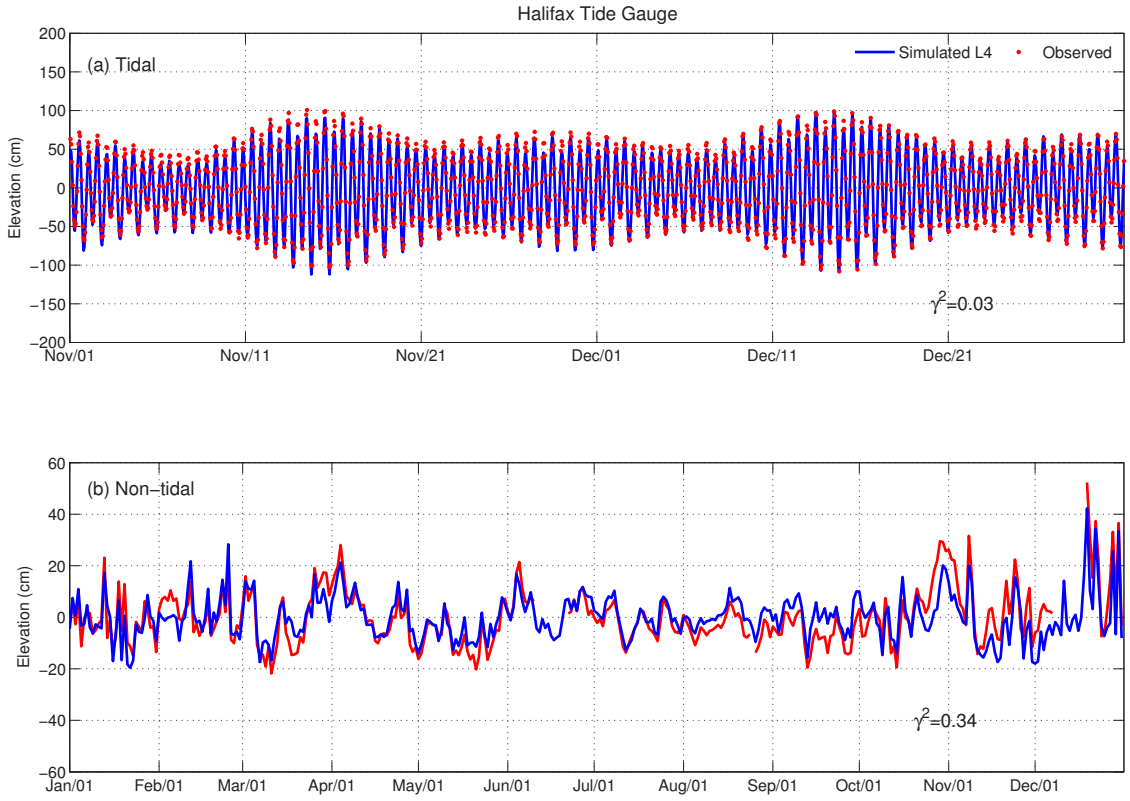

Figure 4.4: Time series of observed (red) and simulated (blue) (a) tidal and (b) non-tidal sea surface elevations at a tide gauge in Halifax Harbour (CHS 490). The simulated results are produced by submodel L4. The observed and simulated sea surface elevations are decomposed into tidal and non-tidal components using the MATLAB package T_TIDE.

4.3.2 Hydrography

We next evaluate the performance of DalCoast-CSS in simulating the 3D, time-varying hydrography. The temporal evolution of hydrography produced by the model is affected by both internal dynamics of the model and external forcing at the sea surface and along model open boundaries. The focus of this section is on the assessment of the model performance in simulating hydrography in the upper water column, where the spectral nudging method was not applied in the model.

4.3.2.1 Satellite Remote Sensing Observations

SEA SURFACE TEMPERATURE (SST): The simulated SST produced by submodel L2 of DalCoast-CSS has significant seasonal variations (Fig. 4.5a). In February, the SST is relatively cold ($\sim$0°C) in the shelf water region, including the GSL, SS and GoM; and relatively warm ($\sim$15°C) in the Slope Water region and adjacent deep waters. In May, the SST on the shelf starts to warm up to $\sim$5°C. In August, the SST further increases to $\sim$20°C in the shelf water region and $\sim$25°C in the deep water region, mainly due to the positive surface heat flux from the overlying atmosphere to the ocean. It should be noted that submodel L2 generates relatively cold surface waters in the Georges Bank, BoF and off Cape Sable due to the strong tidal mixing over the shallow banks. In November, the simulated SST decreases to $\sim$15°C on the shelf water region and $\sim$20°C in the deep water region.

The satellite remote sensing data of SST (Fig. 4.5b) produced by the GHRSST (Group for High Resolution Sea Surface Temperature) Multiscale Ultrahigh Resolution (MUR) project (`http://dx.doi.org/10.5067/GHGMR-4FJ01`) are used to assess the model performance in simulating the temporal and spatial variability of SST in the study region. The global Level 4 (i.e., gridded and with gaps filled) GHRSST MUR SST has a horizontal resolution of 1-2 km, which is based upon nighttime GHRSST L2P skin and subskin SST observations from several instruments such as the NASA Advanced Microwave Scanning Radiometer-EOS (AMSRE), and the MODIS on the NASA Aqua and Terra platforms.

Figure 4.5c presents the seasonal model biases in the SST, which are represented by differences between the simulated and observed monthly-mean SST. The seasonal biases of submodel L2 are relatively small and less than 2°C on the SS, indicating that DalCoast-CSS performs reasonably well in simulating the SST over this region. In the GoM, the

model underestimates the SST in February by $\sim$2°C and overestimates the SST in August and November by $\sim$2°C. In the GSL, relatively large model biases occur over the western side in August and eastern side in November. In addition, the model has a deficiency in simulating the warm core ring detachment observed in the Slope Water region (Fig. 4.5b-2). We speculate that the major reason for the model biases on the shelf (e.g., GoM and GSL) is due to the vertical mixing parameterization in the model. The major reason for the model deficiency in the Slope Water region is that the current, temperature and salinity at the open boundaries of submodel L2 are climatological five-day means produced by a coarse-resolution model for the northwest Atlantic Ocean (*Urrego-Blanco and Sheng*, 2012). As a result, without data assimilation, it is very difficult for DalCoast-CSS to reproduce realistically the timing and location of detachment of warm core rings in the Slope Water region.

SEA SURFACE SALINITY (SSS): The simulated SSS produced by submodel L2 of DalCoast-CSS is presented in Figure 4.6a. The model generates a sharp shelf-slope salinity front (marked by the 34 psu contour in Fig. 4.6a) over the Slope Water region off the SS and GoM in February, May, August and November. Another noticeable feature in the simulated SSS is the low-salinity surface waters in the western GSL, along the south shore of Nova Scotia, and over the northeastern GoM (Fig. 4.6a). These low-salinity waters have significant seasonal variations due to the time-varying freshwater discharge from the St. Lawrence River (SLR). In spring, the SLR runoff specified in the model increases significantly due to the melting of ice and snow. As a consequence, the simulated SSS decreases in the northwestern GSL in May. In August, the simulated SSS in the western GSL decreases further and the low-salinity surface water extends offshore along the Laurentian Channel to reach the shelf break. In November, the simulated SSS decreases along the south shore of Nova Scotia. In February, the simulated SSS decreases in the western SS and the eastern GoM. The equatorward propagation of a spring freshwater pulse of the SLR can be estimated from time series shown in Fig. 4.7. A discharge peak is followed by the downstream reduction of the amplitude and phase propagation of a low-salinity signal. The travel times of the simulated freshwater pulse in spring 2011 from Québec City are about 7 months and about 8 months to reach Halifax and Cape Sable, respectively. These estimated travel times are consistent with the values of 6 months and 8-9 months discussed in previous studies (*Sutcliffe et al.*, 1976; *Smith*, 1989). It should be

noted that the late arrival of the simulated freshwater pulse to Halifax could be attributed to the strong interannual variability of the SLR spring discharge (Fig. 4.7a). The seasonal variations of SSS outside the mouth of the Saint John River (SJR) are also captured by the model in the BoF. A low-salinity plume outside the mouth of the SJR is evident in May due to the large freshwater discharge. The SJR plume decays in the following months due to the decrease in the freshwater discharge of the SJR and strong tidal mixing in this region.

The satellite Aquarius SSS product (*NASA Aquarius project*, 2015) is used to assess the model performance in simulating the temporal and spatial variability of SSS in the study region. The Aquarius SSS was inferred from brightness temperatures at the sea surface measured by three satellite radiometers and can be considered approximately as the observed SSS in the top 1 mm of the ocean water. The Aquarius SSS data were available from August 2011 to June 2015, and not available after this period due to an unrecoverable hardware failure, which caused the termination of the mission. The latest (version 4) Aquarius Level 3 SSS product contains globally gridded 1 degree spatial resolution SSS. It should be noted that the Aquarius SSS are not available near the coast due to land contamination. The Aquarius SSS features large-scale patterns of seasonal variations in SSS over the GSL and on the SS (Fig. 4.6b). In the interior of the GSL, the Aquarius SSS is relatively low in August. Over the shelf break adjacent to the Sable Island, the Aquarius SSS is relatively high in May. A salinity front can be seen from the Aquarius SSS in Fig. 4.6b between the shelf water and the Slope Water in the four months. It should be noted that the spatial resolution of the Aquarius SSS is too coarse to resolve the salinity features near the coast. By comparison, the horizontal resolution of submodel L2 is about 1/16°, which is capable of resolving more fine-scale horizontal features of the SSS than the Aquarius product.

The seasonal model biases in the SSS, which are represented by differences between the simulated and Aquarius monthly-mean SSS, are small on the eastern SS in the four months, particularly in May (Fig. 4.6c-2). Submodel L2 however underestimates the monthly-mean SSS over the southwestern part of the model domain throughout the year by $\sim$2 psu and overestimates the SSS in the interior of GSL in August and November by $\sim$2 psu. The model deficiency in simulating the SSS could be explained by the lack of precipitation and evaporation processes at the sea surface in the model. It should be noted that the spectral

nudging method was only applied at depths greater than 40 m in the model. Hence, the model temperature and salinity in the top 40 m can evolve freely under the influence of internal dynamics of the model and external forcing. In this study, the simulated variability in SSS is due mainly to the low-salinity water from the GSL and high-salinity water from the Slope Water region. In addition, as mentioned above, the current, temperature and salinity at the open boundaries of submodel L2 are climatological five-day means produced by a coarse-resolution model for the northwest Atlantic Ocean (*Urrego-Blanco and Sheng*, 2012).

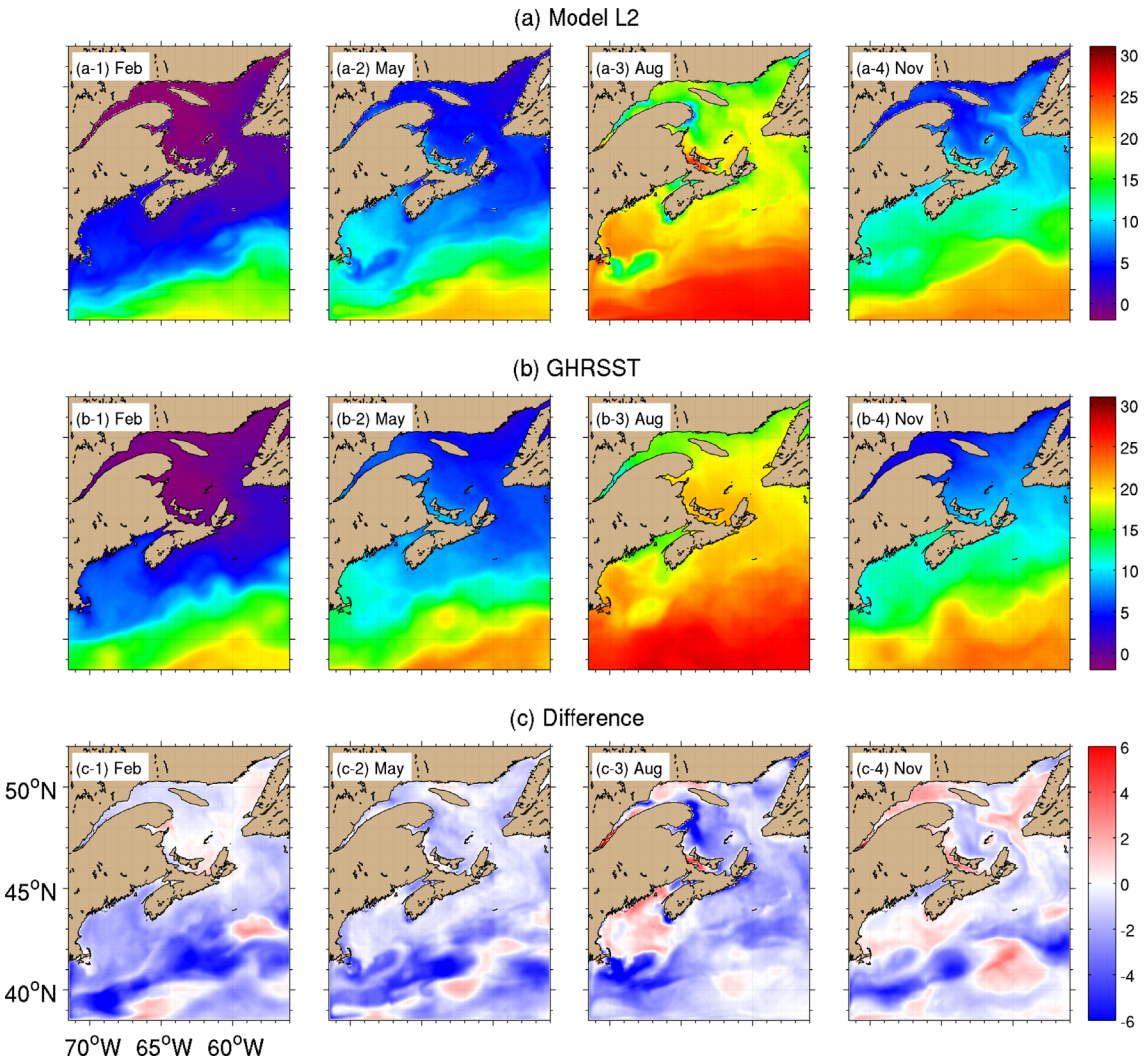

Figure 4.5: Simulated (upper panels) and observed (middle) monthly-mean sea surface temperature (SST) fields (in °C) in February, May, August and November 2012. Lower panels present the model biases represented by differences between the simulated and observed monthly-mean SST in each month. The simulated results are produced by submodel L2. The observations are extracted from the GHRSST MUR Level 4 product (`http://dx.doi.org/10.5067/GHGMR-4FJ01`).

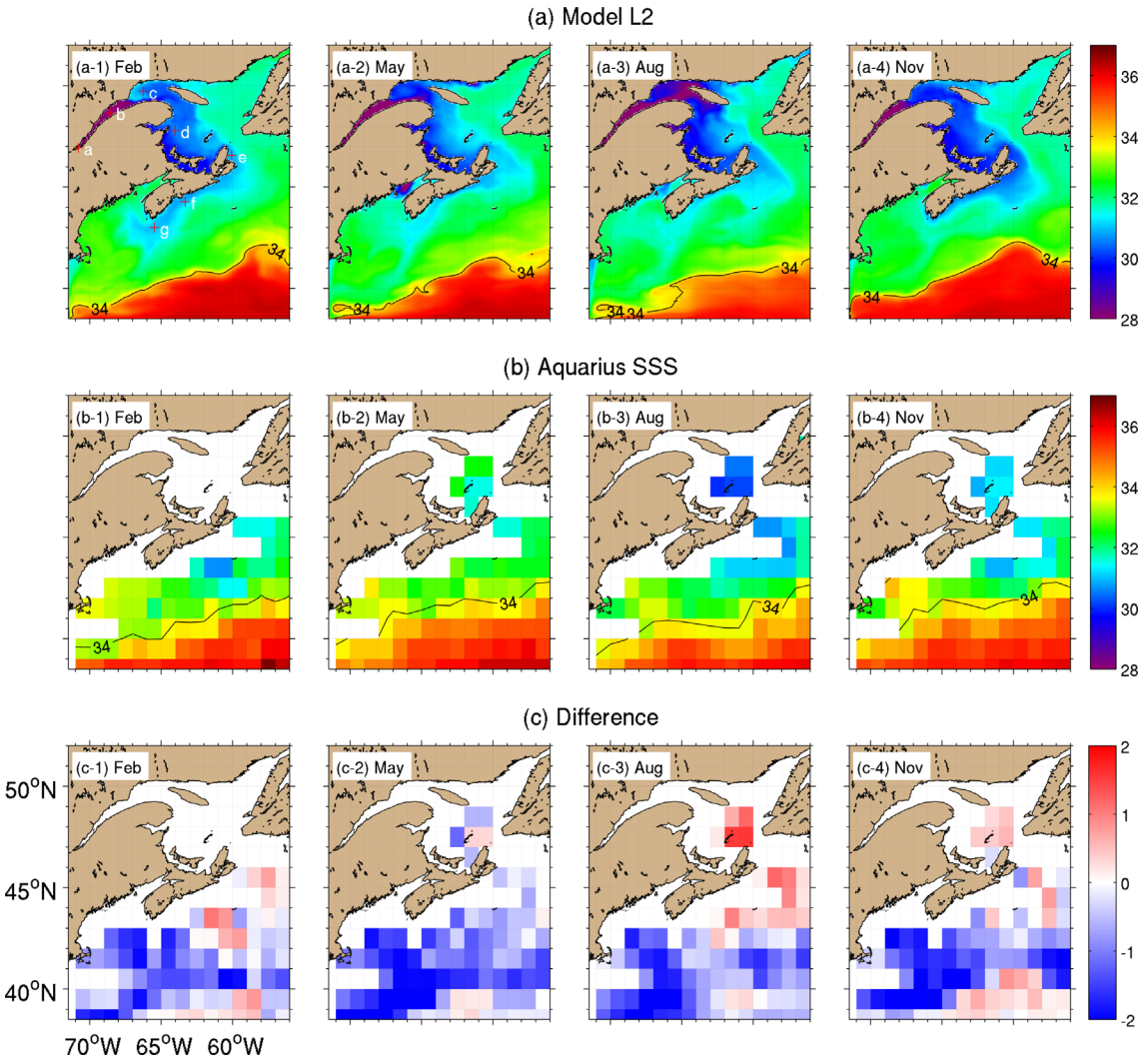

Figure 4.6: Simulated (upper panels) and observed (middle) monthly-mean sea surface salinity (SSS) fields in February, May, August and November 2012. Lower panels present the model biases represented by differences between the simulated and observed monthly-mean SSS in each month. The simulated results are produced by submodel L2. The observations are extracted from the Aquarius Level 3 sea surface salinity version 4 product. The locations marked by "+" in (a-1) are used in the discussion of freshwater pulse.

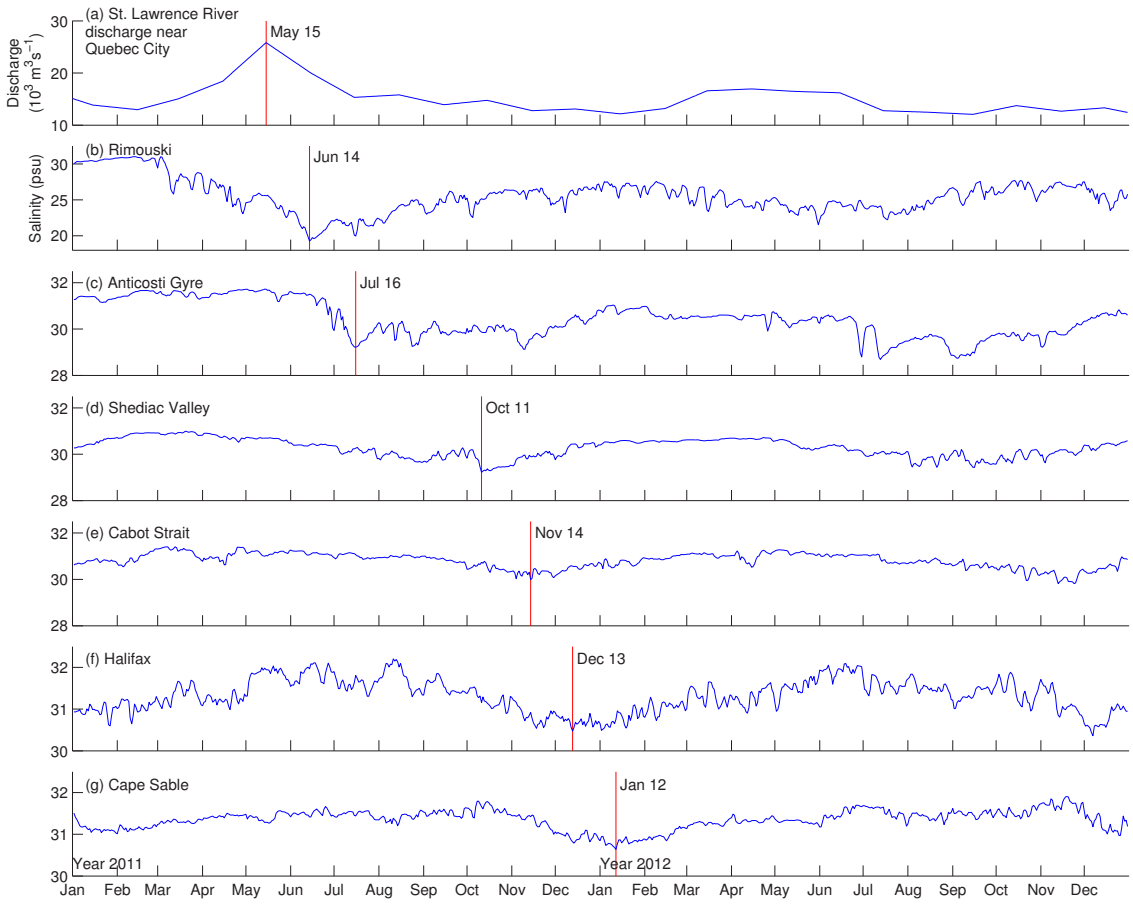

Figure 4.7: Time series of (a) the St. Lawrence River discharge near Québec City specified in the submodel L2 and (b-g) simulated sea surface salinity at selected downstream locations produced by submodel L2. The locations are marked by "+" in Fig. 4.6 (a-1). The St. Lawrence River discharge maximum in 2011 is indicated by the red vertical line in (a) and the subsequent sea surface salinity minimum at selected downstream locations is also indicated by the red vertical line in (b-g).

4.3.2.2 *In-situ* Observations

We next assess the model performance using the *in-situ* hydrographic observations. Sea surface temperatures have been measured at a marine buoy located outside Halifax Harbour since 2000 (black solid circle marked by HB in Fig. 4.2c). The depth of the water temperature sensor on this buoy is $\sim$0.67 m below the calm water line. The observed daily-mean SST (Fig. 4.8) has significant temporal variability on various timescales, with the seasonal cycle being the dominant. The observed SST time series also exhibit several rapid cooling in mid-July, near the end of August and mid-October in 2012. These SST cooling events are strongly correlated with upwelling-favorable alongshore winds. In comparison with the SST monthly climatology constructed from the entire 14-year observations (March 2000-March 2014, the black line with open circles in Fig. 4.8), the SST in 2012 is warmer than in the normal year. This is consistent with the previous finding by *Hebert et al.* (2013), who reported that the annual-mean ocean temperature at discrete depths from surface to bottom over the SS and GoM in 2012 was the warmest between 1970 and 2012.

The observed seasonal cycle of SST and some of the synoptic variations in 2012 are well captured by submodel L4 with γ^2=0.04 (Fig. 4.8). The simulated SST in August increases with time, which is in good agreement with the observations, due mainly to the downward surface heat flux from the atmosphere to the ocean in summer months. The observed timing of the subsequent rapid cooling event at the end of August is well captured by the model, although the magnitude of the cooling is underestimated. It should be noted that the simulated SST is $\sim$2°C cooler than the observed SST at the beginning of August and this model bias persists throughout the month of August, for which the exact reason is unknown. One plausible explanation is the accuracy of the net heat flux at the sea surface in the model. The net heat flux at the sea surface is a function of atmospheric variables and SST (*Gill*, 1982). The atmospheric variables include the air temperature, relative humidity, cloud cover, wind speed and air pressure. In this study, the atmospheric variables are taken from the NARR reanalysis and there is no feedback from the ocean to the atmosphere. Figure 4.9 shows that the heat fluxes at the buoy location in the model are in the same order of magnitude as the heat fluxes provided by the NCEP Climate Forecast System Version 2 (CFSv2) products (*Saha S, et al. 2011, updated monthly*, 2016) with noticeable differences at high frequencies. Another possible explanation is the crude vertical mixing parameterization used in the model.

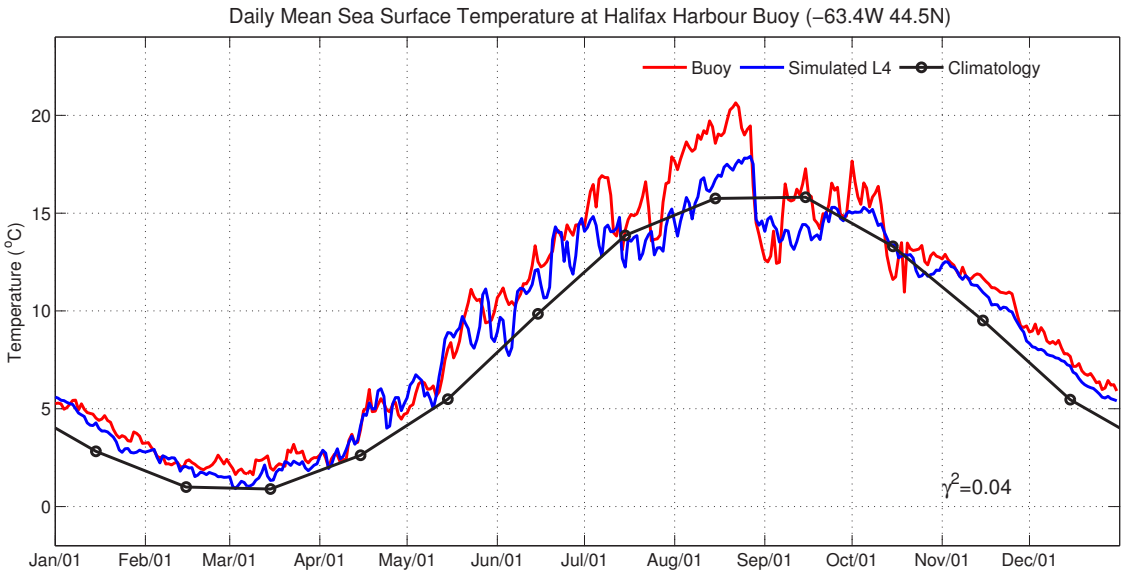

Figure 4.8: Time series of observed (red) and simulated (blue) sea surface temperature in 2012 at the Halifax Harbour buoy. The simulated results are produced by submodel L4.

The model performance in simulating the temperature and salinity in the water column is further assessed by comparing model results with CTD observations of temperature and salinity made by the Atlantic Zone Monitoring Program of Fisheries and Oceans Canada (*Therriault et al.*, 1998). *Ohashi and Sheng* (2015) recently validated the simulated temperature and salinity only in the GSL produced by a similar submodel L2. Here we mainly focus on the validation by including observations made on the SS and in the BoF. Figure 4.10 shows scatterplots between temperature and salinity values simulated by the submodel L2 for 2012 and their observed counterparts at Rimouski (in the GSL), Station 2 (on the SS) and Prince 5 (in the BoF). The calculated γ^2 values are about 0.09-0.42, which are similar to the values discussed in the literature by *Ohashi and Sheng* (2013, 2015), indicating that the current version of submodel L2 has a same level of performance in simulating the temperature and salinity in the study region.

The model performance in simulating the vertical distribution of temperature and salinity is assessed by comparing the innermost submodel L4 results with CTD observations of temperature and salinity made at Station 2 (downward-pointing triangle in Fig. 4.2d) on the Halifax Line. Figure 4.11 presents a comparison between the simulated time-depth distribution of temperature and salinity produced by submodel L4 of DalCoast-CSS and the CTD observations at Station 2.

Submodel L4 is able to capture many of observed features in the vertical temperature profiles at Station 2, including vertically uniform distributions in the top 60 m in late fall and winter and the development of thermal stratification in summer (Fig. 4.11a). The other important feature in summer reproduced by the model is the cold intermediate layer (CIL). The formation of the CIL is mainly due to winter convection, wind-induced mixing in the previous winter and equatorward advection of cold water by the Nova Scotia Current. The model is able to capture the three-layer vertical structure in temperature with a CIL in the middle of the water column in summer. However the model overestimates the temperature in the CIL and underestimates the temperature in the top 20 m in comparison with the observed profiles in summer. We also compared the simulated heat fluxes at Station 2 with the heat fluxes provided by the NCEP Climate Forecast System Version 2 (CFSv2) products and found no major differences. We speculate that model deficiency may be due to the crude vertical mixing parameterization used in the model. An enhanced version of the K profile parameterization (KPP) scheme of *Durski et al.* (2004) is used in submodel L3 to L5. A sensitivity study using different vertical parameterization schemes over this region will be conducted in a future study.

The nested-grid circulation model is also able to capture the general vertical structure in salinity at Station 2 (Fig. 4.11b). The low salinity in the upper layer of $\sim$40 m in late fall and winter at Station 2 of Halifax Line is associated with the arrival of the low-salinity water from the GSL. The model is also able to reproduce a bottom layer with relatively high salinity. The simulated layer thickness increases from $\sim$20 m in winter to $\sim$60 m in summer. The model however overestimates the salinity in the top 60 m in spring and underestimates the salinity in the bottom layer in summer. This model deficiency, as mentioned above, may be due to the lack of precipitation and evaporation processes at the sea surface in the model. In addition the warm and salty Slope Water intrusions at the shelf break may not be well represented in the model.

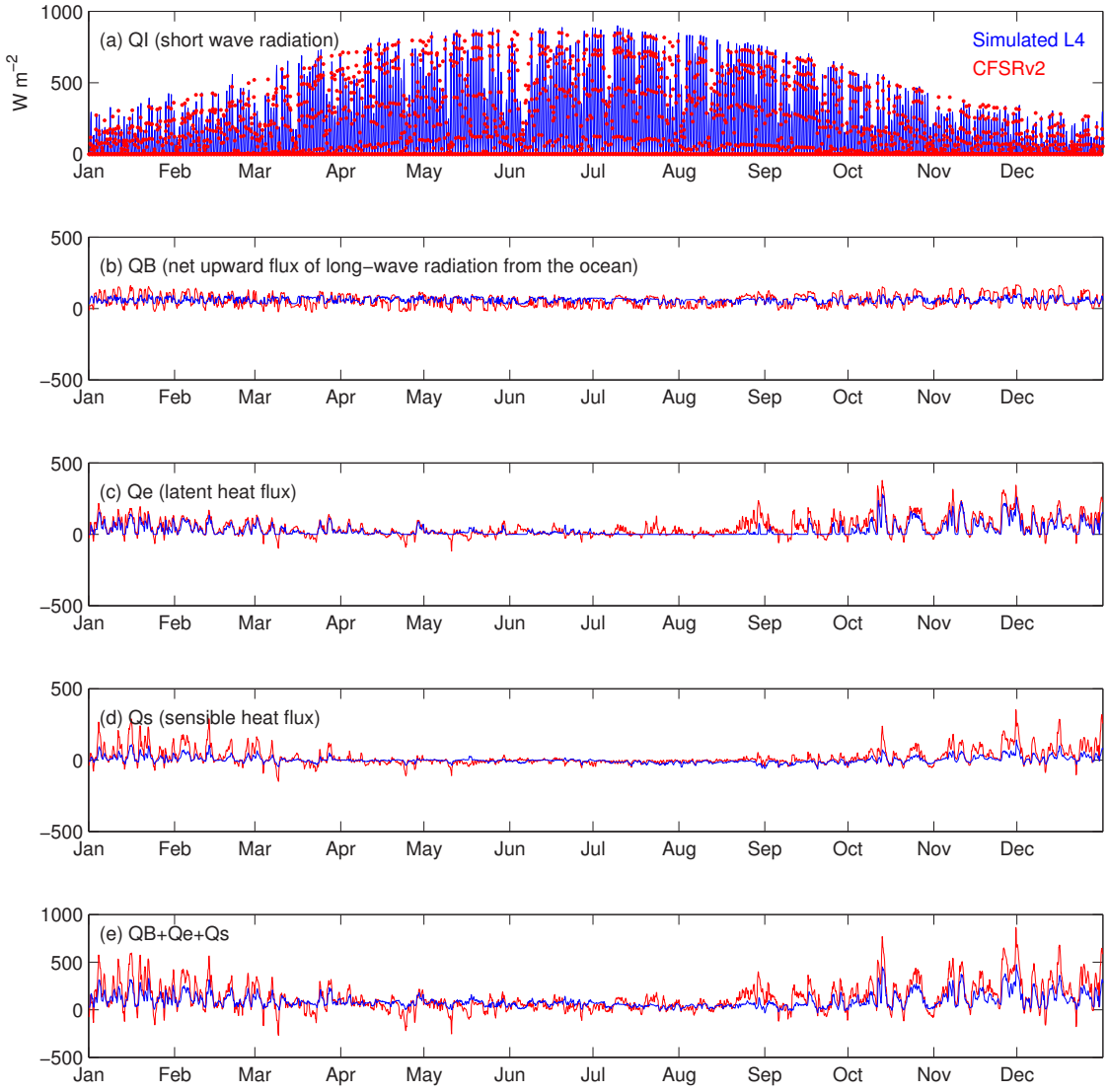

Figure 4.9: Time series of heat fluxes in 2012 produced by submodel L4 (blue) and CFSv2 products (red) at the marine buoy outside Halifax Harbour.

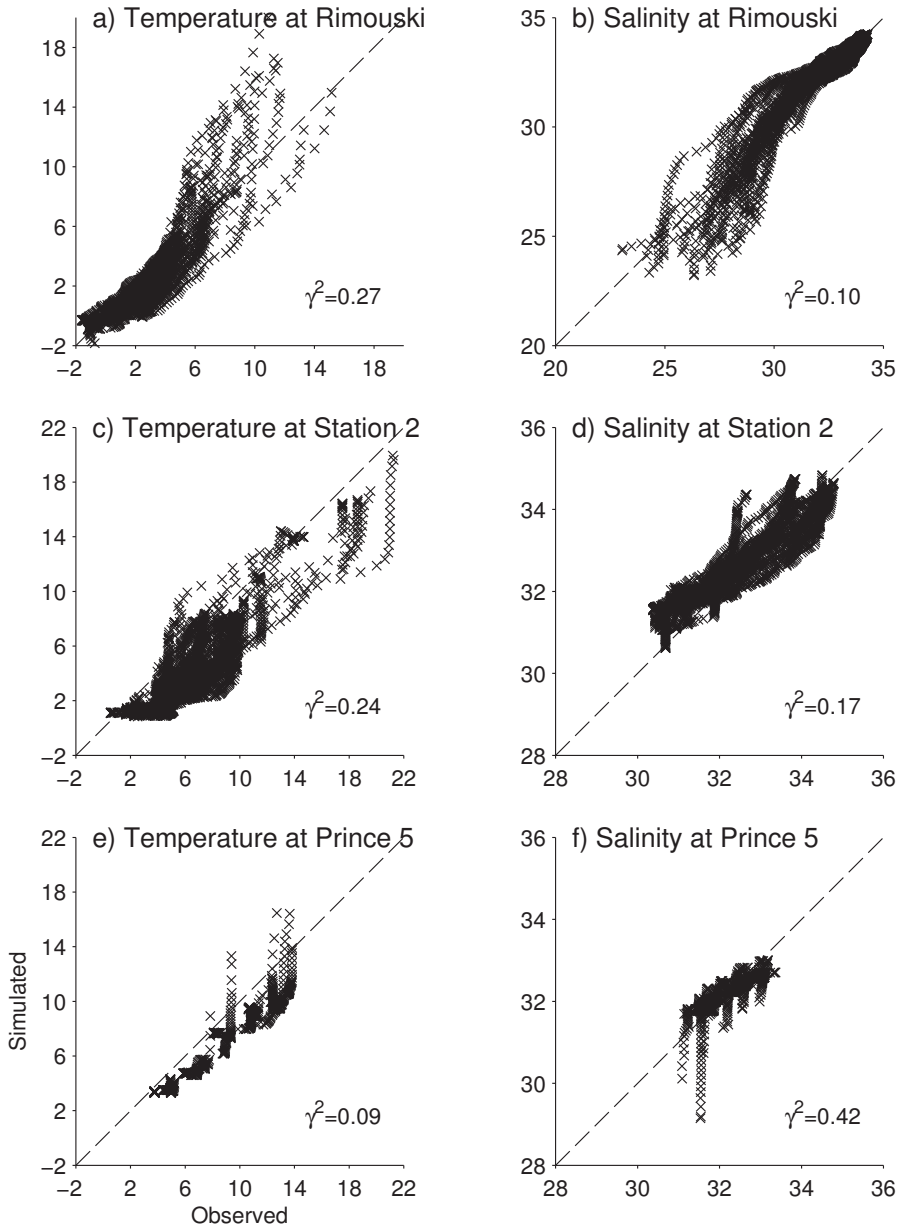

Figure 4.10: Scatterplots between observed and simulated temperature and salinity for 2012 at three hydrographic stations shown in Fig. 4.2b: Rimouski in the GSL, Station 2 on the SS, and Prince 5 in the BoF.

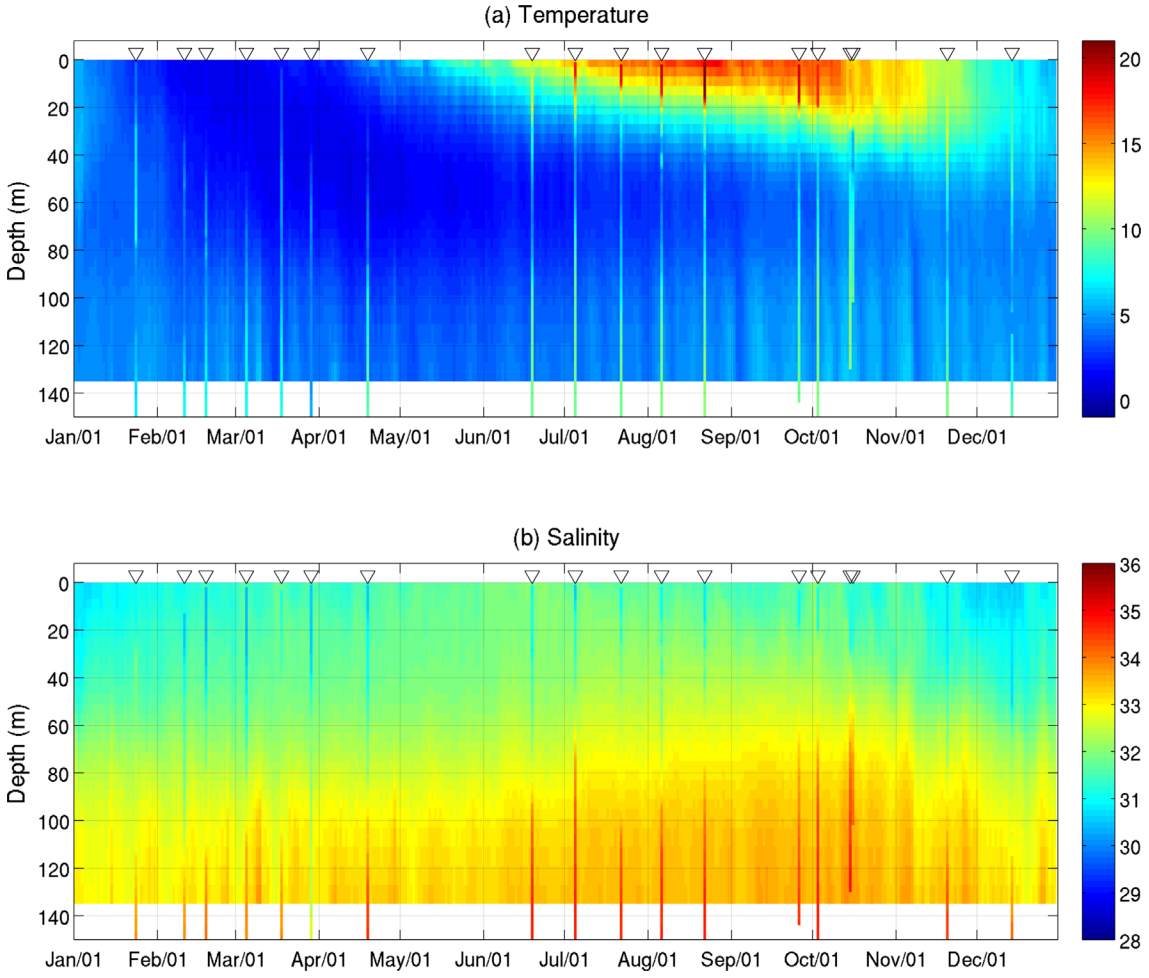

Figure 4.11: Time-depth distributions of simulated (a) temperature and (b) salinity at Station 2 in 2012. The simulated results are produced by submodel L4. The observed temperature and salinity profiles based on CTD casts are shown with 1-day width in the plots. The times of CTD casts are indicated by open triangles.

4.3.3 The Nova Scotia Current

We next assess the model performance in simulating the Nova Scotia Current (NSC) using *in-situ* current observations. Figure 4.12 presents the depth-integrated monthly-mean current produced by submodel L3 of DalCoast-CSS in February 2012, when the NSC transport is at its annual peak (*Loder et al.*, 2003). The main circulation feature as shown in Fig. 4.12 is that the simulated NSC flows southwestward following approximately the 150 m isobath along the coast. There are two small branches that separate from the main branch of the NSC. The first branch flows southward over the Emerald Basin to the Scotia Gulf and the second branch also flows southward over the LaHave Basin towards the LaHave Bank. The model also produces a westward shelfbreak jet over the area to the south of the Emerald Bank. The flow pattern described above is consistent with the density-driven currents calculated from historical hydrographic profiles (*Sheng and Thompson*, 1996) and seasonal circulation in winter diagnosed numerically from the seasonal-mean climatologies of temperature and salinity (*Hannah et al.*, 2001).

The NSC has been observed since 2008 using bottom-mounted ADCPs deployed by the Ocean Tracking Network (OTN) (`http://oceantrackingnetwork.org`) at three locations along a transect from the outside of Halifax Harbour (100 m isobath) to the edge of Emerald Basin (200 m isobath) (upward-pointing solid triangles in Fig. 4.2c). A visual comparison between the monthly-mean current observations (red arrows in Fig. 4.12) and monthly-mean model results suggests that the model is able to capture the magnitude and direction of the NSC in February 2012.

We next assess the model performance in simulating the temporal variability of the NSC transport. For simplicity, the NSC transport is defined as the alongshore transport passing through the transect occupied by the three ADCP stations, and the positive direction of the alongshore transport is toward northeast (58°T, degrees from true north in a clockwise direction). Figure 4.13 presents the NSC transport in 2011 and 2012 calculated from currents observed by ADCPs and simulated by submodel L3 of DalCoast-CSS at three locations. The observed time-mean (2008-2014) NSC transport is about -0.4 Sv (Sv $\equiv 10^6$ m^3 s^{-1}) to the southwest. The seasonal variation in the transport is evident in the observed monthly-mean climatology (2008-2014, the black line with open circles in Fig. 4.13a), with relatively stronger transport in winter and weaker in summer. The observed daily NSC transport has significant synoptic variability. It should be noted that

the observed transport in summer 2011 (2012) is stronger (weaker) than the climatology. The simulated NSC transport demonstrates a similar seasonal cycle in comparison with the observed transport. However the model overestimates the transport in summer 2012. We speculate that the weakening of the observed NSC in summer 2012 is related to the intrusion of abnormally warm Slope Water (*Hebert et al.*, 2013). As mentioned earlier, the model has deficiencies in simulating the circulation and associated variability over the Slope Water region. The seasonal transport anomaly (Fig. 4.13b) is then calculated by subtracting the seasonal cycle from the total transport. The observed transport anomaly fluctuates between -0.4 and $+0.4$ Sv in fall and winter, and the observed amplitudes of the fluctuations are damped in spring and summer. The transport anomalies, including the seasonality in the fluctuations, are captured reasonably well by submodel L3 with $\gamma^2 = 0.7$ in this two-year period. It should be noted that the model underestimates the transport anomaly during strong storm events in winter due most likely to the under-representation of the storm intensity by the regional reanalysis atmospheric forcing used in the model. In addition, power spectral analysis was conducted on the observed and simulated transport anomalies (Fig. 4.14). The power spectra of simulated transport anomalies are in good agreement with the observations for periods shorter than about two weeks (Fig. 4.14b). The coherence between the simulated and observed anomalies are significant and about 0.7 (Fig. 4.14c). The simulated anomalies are also in phase with the observed anomalies (Fig. 4.14d). However, the large variabilities at periods of $\sim$30- and $\sim$90 days in the observations are not simulated by the model. We speculate that these relatively long-term variabilities are related to the low-salinity pulses in the Nova Scotia Current.

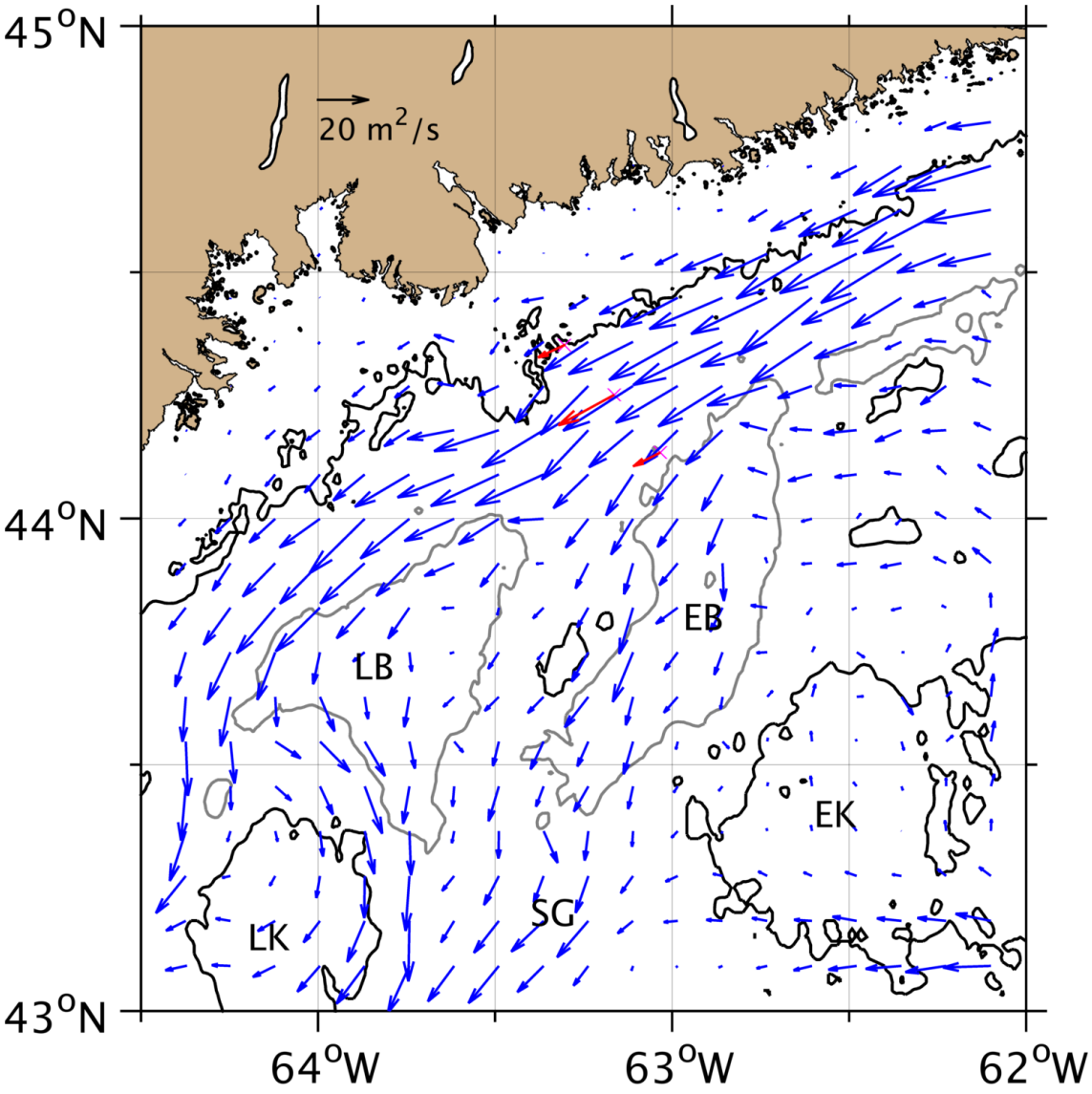

Figure 4.12: Horizontal distributions of monthly-mean vertically integrated currents in February 2012 in the central SS produced by submodel L3. For clarity, current vectors are plotted at every fifth model grid point. Red arrows show the observed vertically integrated current. The 100 m and 200 m isobaths are shown by the black and gray contours, respectively. The magenta "×" indicates positions of three current moorings. Abbreviations are used for the LaHave Basin (LB), Emerald Basin (EB), LaHave Bank (LK) and Emerald Bank (EK).

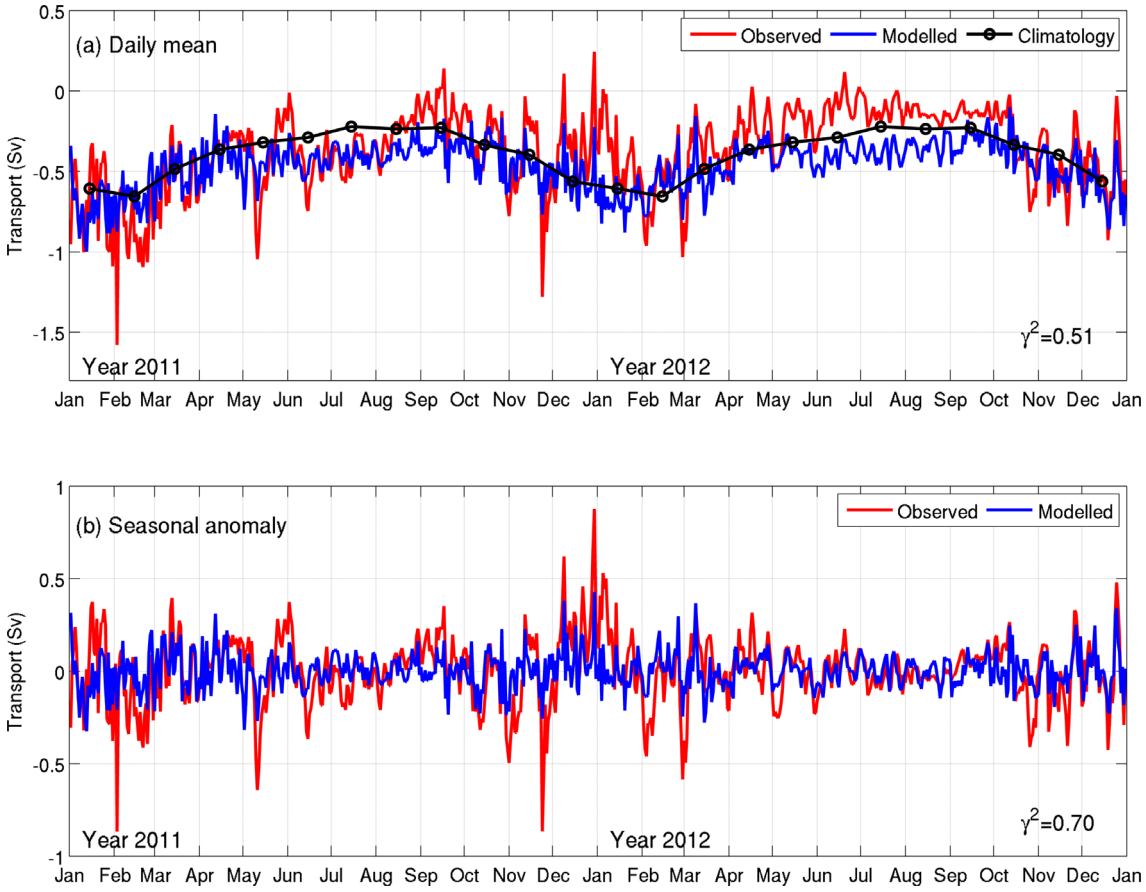

Figure 4.13: Time series of observed and simulated Nova Scotia Current transport in 2011 and 2012: (a) daily-mean values and (b) seasonal anomalies (calculated by subtracting the seasonal cycle). The simulated results are produced by submodel L3. The black curve in (a) is the monthly-mean transport calculated from the current observations from 2008 to 2014. The Nova Scotia Current transport is calculated using the observed and simulated currents at stations T1, T2 and T3 (Fig. 4.2). Positive values indicate northeastward transport.

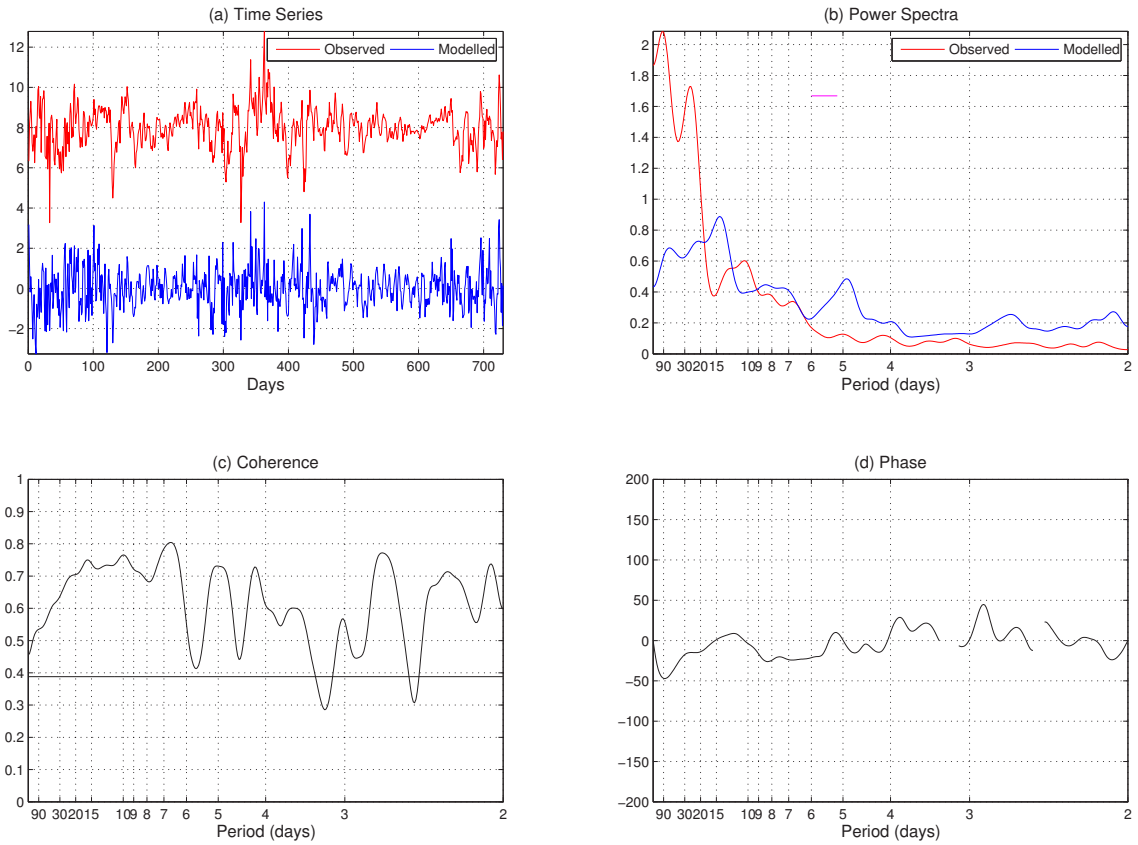

Figure 4.14: Power spectral analysis of observed and simulated seasonal anomalies of Nova Scotia Current transport in 2011 and 2012. A typical time lag window of 10% of record length is used. Time series in (a) are normalized to zero mean and unit variance. The normalized observed seasonal anomalies have been offset by 8 in (a). The bandwidth is marked by the magenta line in (b). The horizontal line in (c) represents the 5% significance level for zero coherence.

4.4 Physics Controlling Surface Temperature Variability in Summer

DalCoast-CSS is used to examine the effect of tidal-mixing and wind-driven coastal upwelling in the formation of cold surface coastal waters around Nova Scotia in summer as shown in Fig. 4.1. As suggested by previous studies, cold coastal waters are affected by various forcing mechanisms including tidal mixing (*Garrett et al.*, 1978; *Loder and Greenberg*, 1986) and wind-driven coastal upwelling (*Petrie et al.*, 1987). Three numerical experiments using different configurations of the submodel L2 are conducted as described below:

1. CONTROL RUN (*CR*): The DalCoast-CSS in this experiment is driven by the suite of forcing functions discussed in section 2, including tides, river discharges, atmospheric forcing and open boundary forcing to hindcast the ocean conditions.

2. NO WIND RUN (*NW*): Same as *CR*, except that the local wind stress is set to zero in submodel L2.

3. NO TIDE RUN (*NT*): Same as *CR*, except that the tides are turned off in this experiment. Specifically, the tidal elevations (η_t) and tidal currents (u_t) are set to zero along the open boundaries of submodel L2 (see Eq. A.1).

In experiments *NW* and *NT*, submodel L2 is initialized from the 3D circulation and hydrography on August 1, 2012 produced by the model in *CR* and integrated for one month. The model results of SST and SSS on September 1, 2012 from the above three experiments (Fig. 4.15) are examined to determine the main processes affecting the formation of the cold surface waters along the Nova Scotia coast.

The simulated SST in *CR* on September 1, 2012 has significant spatial variations in the study region (Fig. 4.15a-1). The simulated SST less than $\sim$12°C occurs mainly over three coastal areas: the BoF and adjacent waters, off Cape Sable, and along the southeastern shore of Nova Scotia. The simulated SST is relatively cold and about 16°C on the eastern Scotian Shelf. The simulated SST is relatively warm and about 20°C on the edge of central and western Scotian Shelf and adjacent Slope Water region. The simulated SST is also relatively warm and about 22°C in the Northumberland Strait ("2" in Fig. 4.15a-1) where the water depth is relatively shallow. In comparison with the observed SST on September

1, 2012 (Fig. 4.1), the simulated SST in *CR* (Fig. 4.15a-1) has similar spatial variations as observed. The observed cold coastal waters in the BoF and adjacent waters, off Cape Sable and along the southeastern shore of Nova Scotia are reproduced reasonably well by the model.

The simulated SSS in *CR* also has significant spatial variations (Fig. 4.15a-2). The simulated SSS around Prince Edward Island is less than 30.5 psu. The simulated SSS over the coastal waters of the eastern SS is relatively high and up to 31 psu. Two bands of low SSS can be seen on the SS. One band is along the inner shelf with the lowest SSS along the 100 m isobath. The width of this band increases significantly over the western SS. The other band is along the shelf break and only extended to about 64°W. Between the two low SSS bands, there is a pool of relatively high SSS ($>$32 psu) waters trapped in the middle- and outer- central SS. Beyond the SS, the simulated SSS is relatively high and greater than 32 psu in the Slope Water region. The simulated SSS in the southwest coast of Nova Scotia is also relatively high and greater than 32 psu. The low-salinity waters from the SJR can be seen in the vicinity of the River mouth (red dot in Fig. 4.15a-2). In the middle of BoF, a pool of relatively high SSS ($\approx$31.7 psu) waters is located off Cape Chignecto ("3" in Fig. 4.15a-2).

The simulated SST in the case of *NW* (Fig. 4.15b-1), in which the wind forcing is excluded, shows several distinct features in comparison with the SST in the case of *CR*. The SST in *NW* is relatively uniform and warm ($>$ 26°C) on the SS and adjacent Slope Water region. The cold water band along the southeastern shore of Nova Scotia does not appear in *NW*, which confirms that the formation of this cold water band near the coast is due mostly to the wind forcing. Specifically, the upwelling-favorable wind (Fig. 4.15a-1) pushes the surface water offshore and the cold deep water wells up to the surface near the coast. The SST in the case of *NW* on the SS and in the Slope Water region is warmer than the SST in the case of *CR*, due mainly to the zero simulated latent heat loss from the ocean under the no wind condition. It should also be noted that wind-induced vertical mixing also plays a role in affecting the SST. The cold surface water off Cape Sable is reduced in *NW* in comparison with the results in *CR*, which suggests that latent heat flux and wind-induced vertical mixing enhance the surface cooling in summer in this region. In the BoF, the SSTs in the cases of *NW* and *CR* are highly similar, indicating that physical processes other than the wind forcing play an important role in affecting the SST in this

region. The SSS in *NW* (Fig. 4.15b-2) also has several distinct features in comparison with the SSS in *CR*. The low SSS band is narrower than the one in *CR* and tightly trapped along the south shore of Nova Scotia with the lowest SSS near the coast. The displacement of the lowest SSS from the coast in *NW* to the $\sim$100 m isobath in *CR* can also be explained by the fact that the upwelling-favorable wind pushes the surface low SSS water offshore and the salty deep water wells up to the surface along the coast. The SSS in *NW* over the Slope Water is higher than the SSS in *CR*. The simulated SSS in the southwest coast of Nova Scotia is reduced significantly in comparison with the results in *CR*. Without the wind forcing (*NW*), the freshwater plume of the SJR is more clearly defined and the BoF is covered by a larger pool of higher SSS waters in comparison with the results in *CR*.

The SST in the case of *NT* (Fig. 4.15c-1), in which the tides are turned off in the model, differs from the SST in the case of *CR* over several coastal areas. The relatively cold waters in the BoF and off Cape Sable do not appear in *NT*. This confirms that tidal mixing plays a very important role in sustaining the well-mixed water over these regions even in summer when the heat flux from the atmosphere is high (*Garrett et al.*, 1978; *Loder and Greenberg*, 1986). In addition to tidal mixing, topographic upwelling due to the interaction between tides and bottom topography also contributes to the formation of cold surface waters off Cape Sable (*Tee et al.*, 1993). On the eastern and central SS and in the Slope Water region, by comparison, both the SST and SSS in the case of *NT* are similar to the SST and SSS in the case of *CR*, which indicates that tides play a minor role in affecting the SST and SSS over these regions. The simulated SSS along the southwest coast of Nova Scotia in the case of *NT* is lower than the SSS in the case of *CR*, indicating that tidal mixing also brings high salinity subsurface waters to the surface in this region. Without tides (*NT*), the freshwater plume of the SJR is also well defined. In addition, the pool of high SSS waters off Cape Chignecto is not evident in *NT*, indicating that tides play an important role in the formation of high SSS water in the BoF.

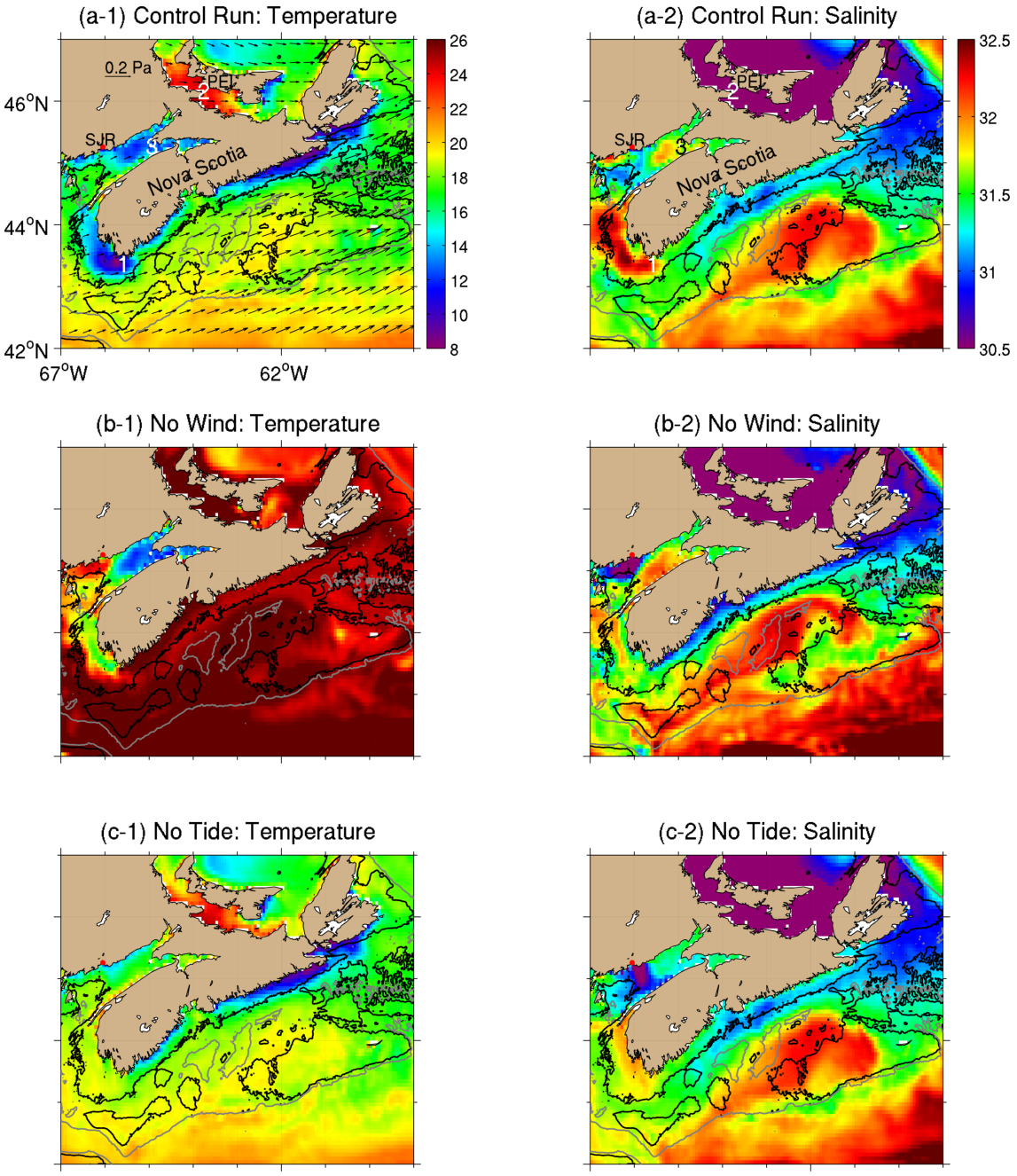

Figure 4.15: Distributions of sea surface temperature (left) and sea surface salinity (right) in September 1, 2012 in numerical experiments of (a) control run (*CR*), (b) no wind (*NW*) and (c) no tide (*NT*). The time-averaged wind stress vectors used in the model over the previous 48-hours are plotted in (a-1, black arrows). In (a-1) and (a-2), abbreviation is used for the Prince Edward Island (PEI) and "1" represents Cape Sable, "2" indicates Northumberland Strait and "3" marks Cape Chignecto. The red dot indicates the mouth of Saint John River (SJR). The 100 m and 200 m isobaths are shown by the black and gray contours, respectively.

4.5 Coastal Upwelling on the Scotian Shelf

As discussed in the previous section, coastal upwelling occurs on the Scotian Shelf when the region is experiencing winds from the southwest which blow parallel to the coast of Nova Scotia (Fig. 4.15a-1). The surface water flows offshore, due to the classic Ekman theory (1963), and is replaced by the cool, nutrient rich water which rises up into the coastal area from below, resulting in the upwelling phenomena.

Coastal upwelling on the Scotian Shelf has been the subject of several studies in the past. The first report of coastal upwelling on the Scotian Shelf goes back to *Hachey* (1937). He found that strong winds from the southwest were correlated with lower-than-normal sea surface temperatures near the coast. Satellite images of SST presented in *Petrie et al.* (1987) demonstrated the development of a band of cool surface waters near the coast of the Scotian Shelf during a month-long period of upwelling-favorable winds in 1984. *Donohue* (2001) simulated the upwelling event in 1984 by using the Princeton Ocean Model forced by spatially uniform wind and his results demonstrated that the realistic topography is required in order to produce the observed upwelling plume. Recently, *Laurent* (2011) examined the biological response to the upwelling in Lunenburg Bay, a coastal bay (60 km to the southwest of Halifax) on the coast of Nova Scotia. The observed chlorophyll concentration in the Bay was 1.1 ± 0.6 mg m^{-3} during mixed upwelling and downwelling events in summer, which is small compared to the typical value (> 5 mg m^{-3}) in other well-studied upwelling systems. *Laurent* (2011) attributed this limited response of phytoplankton variability in the Bay to the rapid wind-induced flushing and the low nitrate concentration in the Scotian Shelf water. In this section, the coastal upwelling over the Scotian Shelf is further investigated based on the latest observations made by various instruments and simulations from the recently developed DalCoast-CSS. In addition, a process study is conducted by using DalCoast-CSS to examine the role of irregular coastline and topography on the evolution of the coastal upwelling plume. The geographical names used in the following discussion are labelled in Fig. 4.2c and d.

4.5.1 Observed Coastal Upwelling

Two major upwelling events in the summer of 2012 were identified from satellite remote sensing data of SSTs (Fig. 4.16). One event was peaked on July 22 and the other was peaked on September 1, 2012. The observed SSTs in both events show similar spatial patterns of

the upwelling plume (Fig. 4.16a and c), which features a relatively cold water band ($<$ 16°C) along the coast and filaments extending offshore. Chlorophyll concentration is an important index of phytoplankton productivity. The observed chlorophyll concentrations in both events are relatively high in the upwelling plume region (marked by the 18.5°C isotherm in Fig. 4.16b and d).

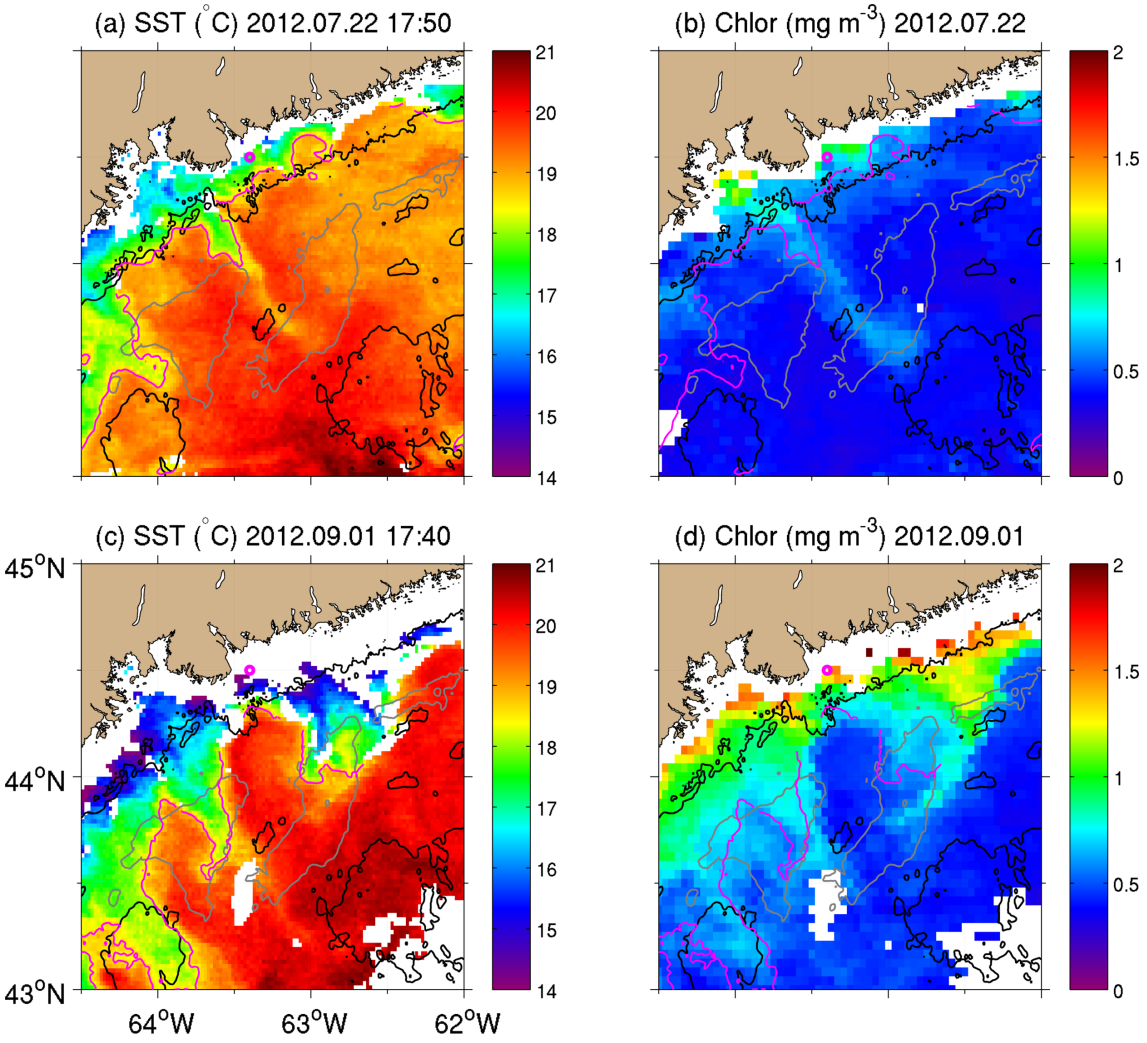

Figure 4.16: MODIS satellite remote sensing data of sea surface temperature (SST) and Chlorophyll concentration over the central Scotia Shelf and adjacent waters on July 22 and September 1, 2012. Data were extracted from the Ocean Color Website (`http://oceancolor.gsfc.nasa.gov`). The "o" indicates the positions of Halifax Harbour buoy. The 18.5°C isotherm is shown by the magenta contours. The 100 m and 200 m isobaths are shown by the black and gray contours, respectively.

In addition to the MODIS satellite remote sensing data of SSTs, the SSTs are also observed by a marine buoy outside Halifax Harbour (Fig. 4.17a). This independent *in-situ* SSTs allow us to check the quality of the satellite remote sensing data of SSTs. It should be noted that the depth of the water temperature sensor on this buoy is $\sim$0.67 m below the calm water line. While the MODIS SST represents the skin SST, which is a temperature measured by a radiometer at depth within a thin layer (500 μm) at the water side of the air-sea interface (*Donlon et al.*, 2002). In summer, the satellite remote sensing data of SSTs are in good agreement with the buoy measurements. In winter, most of the remote sensing data of SSTs are 1-2°C colder than observations at the buoy. The exact reason for the mismatch in winter is unknown since we expect the ocean in the top few meters is well mixed and has a uniform temperature profile in the well-mixed surface layer in winter.

The seasonal cycle and seasonal anomaly of SSTs are extracted from the observed time series at the buoy outside Halifax Harbour (Fig. 4.17). The observed SSTs at the buoy site had a strong seasonal cycle (Fig. 4.17a), which decreased to about 2°C in March and rose to about 22°C in August. The seasonal anomaly of SST (Fig. 4.17b) is then calculated by subtracting the seasonal cycle from the observed SSTs. The large seasonal SST anomalies in July and August were related to the coastal upwelling events. In July of 2012, there were two consecutive major coastal upwelling events. The first coastal upwelling event peaked on July 12 with about 5°C cooling in SST near the coast. The second coastal upwelling event peaked about 10 days later on July 22 (Fig. 4.16a) with a similar magnitude of SST cooling over coastal waters. After the coastal upwelling events, the SSTs gradually increased from 16°C to 22°C in August due to the positive heat flux from the atmosphere to the ocean. At the end of August, another major upwelling event occurred (Fig. 4.16c) with an about 10°C cooling in SST. A slightly elevated chlorophyll concentration is evident following these upwelling events (Fig. 4.17b). It should be noted that the magnitude of upwelling-induced chlorophyll concentrations increased to about 1-2 mg m^{-3}, which is less than the typical chlorophyll concentration change during the spring bloom in late March (up to $\sim$5 mg m^{-3}).

The wind conditions outside Halifax Harbour are presented in Fig. 4.18 in terms of (1) the magnitude and direction, and (2) along-shore and cross-shore components of wind stress. Wind stress is estimated from wind velocities measured at the marine buoy outside Halifax Harbour using the bulk formula from *Large and Pond* (1981). The wind stress

vectors (Figure 4.18a) in July, August and September of 2012 were mainly from southwest. The mean magnitude of wind stress is $\sim$0.04 Pa and the direction of wind stress is mainly along the coast. Based on the general orientation of the coastline, the wind stress vectors are projected to the along-shore (65°T) and cross-shore (155°T) components. As expected, the values of along-shore wind stress in these three months are mostly positive (upwelling-favorable) with a mean of 0.02 Pa. To further illustrate the relationship between the winds and upwelling events, we follow *Cushman-Roisin and Beckers* (2011) and define the wind impulse as the integration of the along-shore wind stress over time:

$$I = \int_0^T \tau_a \, dt \tag{4.2}$$

where τ_a is the along-shore wind stress and T the wind duration. Here we set T to be 5 days. Figure 4.18c shows the time series of wind impulse and the SST anomaly. It is evident that the negative SST anomaly peaks are coincident with positive wind impulse anomaly peaks. A scatterplot between the wind impulse anomaly and SST anomaly (Fig. 4.19) shows a negative relationship between the two variables with a correlation coefficient of -0.46. The associated linear regression between the wind impulse anomaly and SST anomaly has a slope of -1.25.

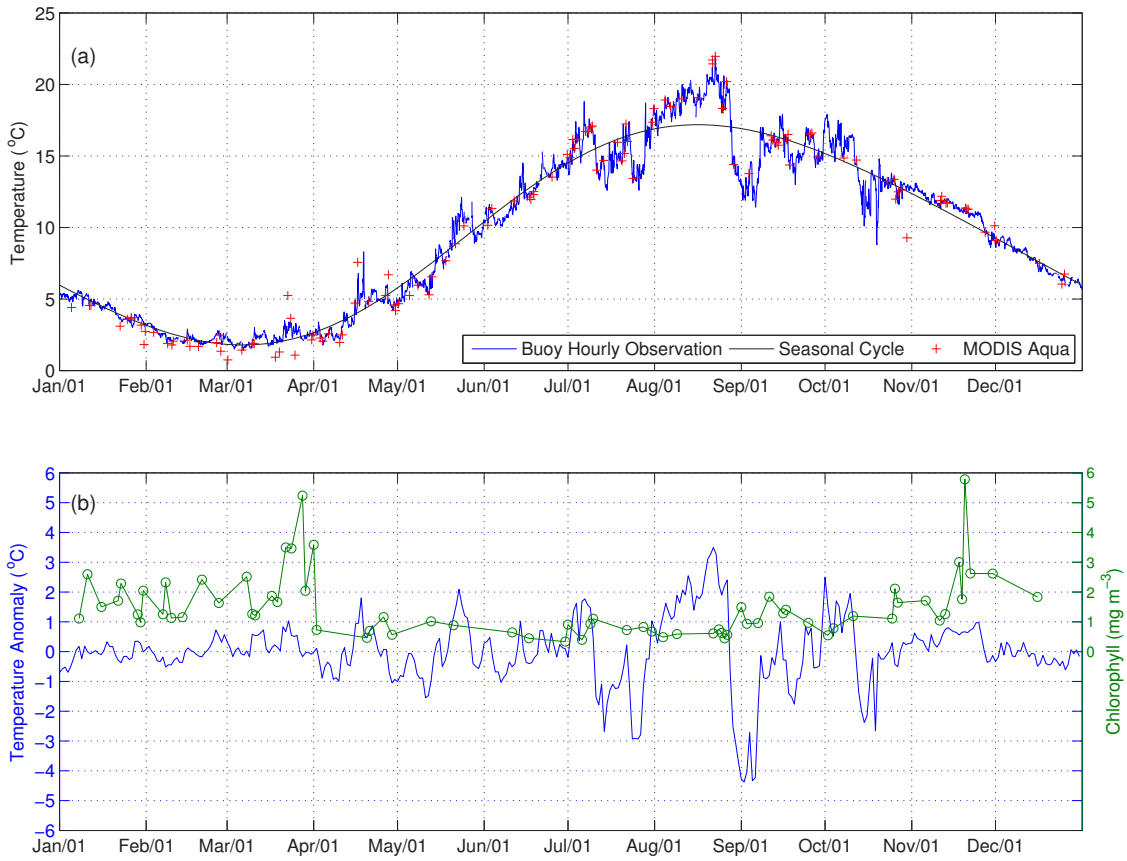

Figure 4.17: (a) Hourly time series of observed sea surface temperatures (blue) in 2012 and the fitted seasonal cycle (black) at the Halifax Harbour buoy. MODIS-aqua satellite remote sensing data of sea surface temperature (SST) at the buoy site were plotted as red "+". MODIS data were extracted from the Ocean Color Website (`http://oceancolor.gsfc.nasa.gov`). (b) Daily mean SST anomaly (blue) and chlorophyll concentration (green) of 2012. SST anomaly was calculated from the hourly observations. Chlorophyll concentration was extracted from the dataset provided by the Ocean Color Climate Change Initiative project (`http://www.oceancolour.org`). Note upwelling events occurred in July and the end of August 2012.

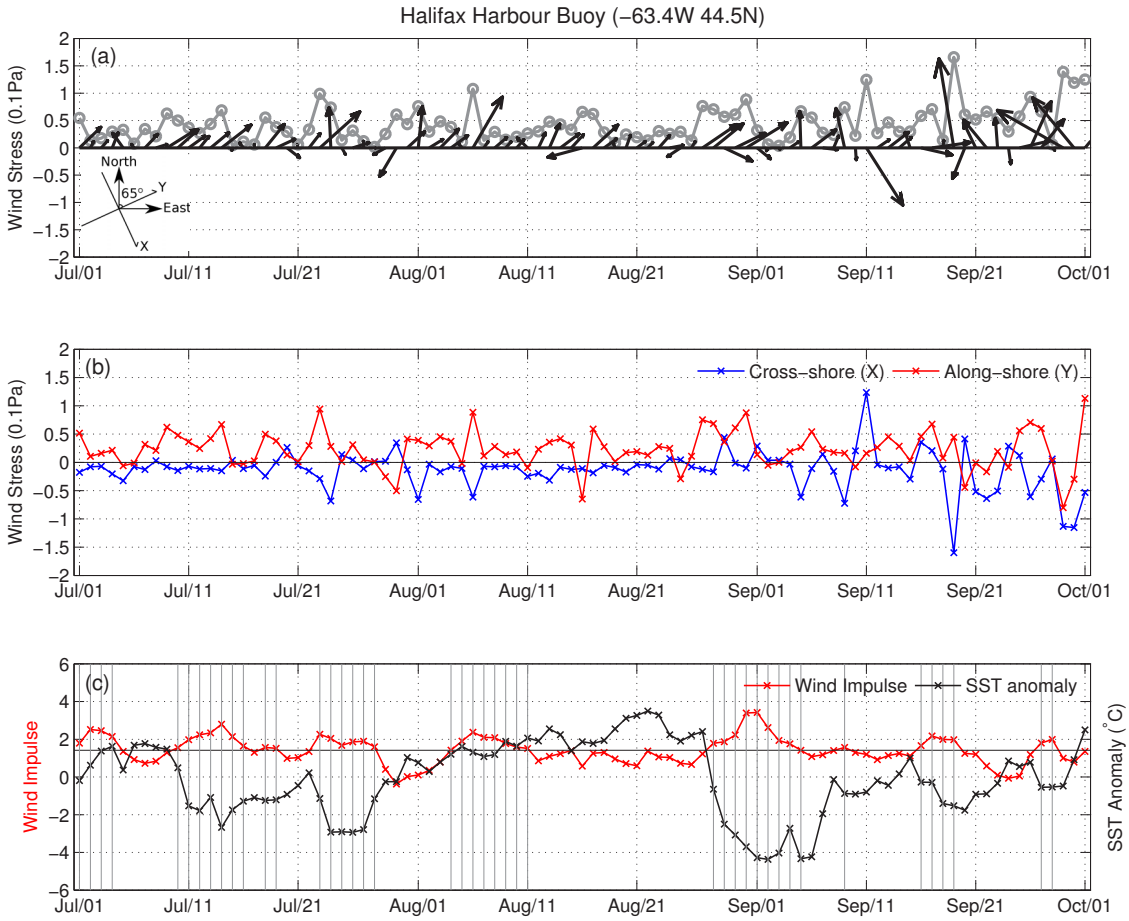

Figure 4.18: (a) Daily mean wind stress and the magnitude of wind stress is shown by the gray line, (b) along-shore (65°T) and cross-shore components, and (c) wind impulse and SST anomaly in July, August and September, 2012 at the Halifax Harbour buoy. In (c), the days with positive wind impulse anomaly are highlighted by vertical gray lines.

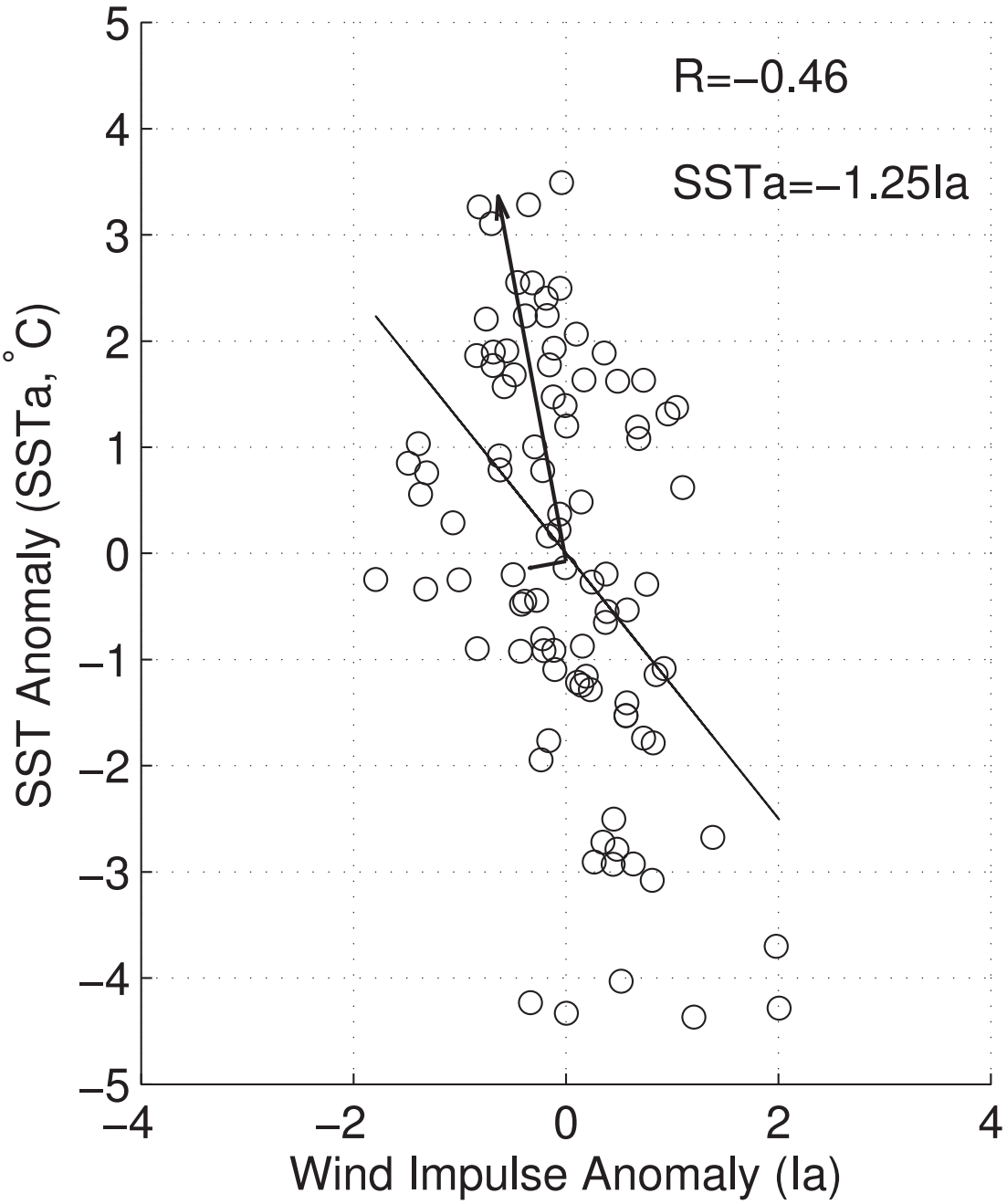

Figure 4.19: Scatterplot between wind impulse anomaly and SST anomaly in July, August and September, 2012 at the Halifax Harbour buoy. The correlation coefficient, R is equal to -0.46. The linear regression line is shown. The vectors shown by black arrows are the eigenvectors of the covariance matrix of the data, whereas the length of the vectors corresponds to the eigenvalues.

4.5.2 Simulated Coastal Upwelling

The coastal upwelling events in 2012 are reconstructed by using DalCoast-CSS described in Section 4.2. Figure 4.20 presents 12 instantaneous snapshots of the simulated SSTs produced by the submodel L3 of DalCoast-CSS to demonstrate the spatial distributions of SSTs at various stages of the coastal upwelling in the central Scotian Shelf adjacent to Halifax.

The snapshots from July 8 to July 11 depict the onset of coastal upwelling. The alongshore winds during this period were upwelling-favorable. The SSTs on the middle and outer shelf (beyond the 100 m isobath along the coastline) during this period were relatively uniform and increased from about 15°C to 18°C due to the positive heat flux from the atmosphere to the ocean. On July 8, the SSTs near the coast (from coastline to the 100 m isobath) were relatively uniform and about 15°C, which is similar to the SSTs on the shelf. On July 9, two coastal areas with relatively low SST appeared: one is to the west of Halifax Harbour and the other to the west of Mahone Bay. In the next two days (July 10 and 11), the SSTs in these two coastal areas further decreased to less than 10°C. In addition, a third coastal area with relatively low SST developed to the northeast of Halifax Harbour. It should be noted that the coastal upwelling plumes are not evident in Mahone and St. Margarets Bays. The snapshots from July 12 to July 15 represent the further development of the coastal upwelling. The winds during this period were mainly from southwest. (upwelling-favorable). The wind impulse was peaked on July 14 (Fig. 4.18c), leading to a significant offshore expansion of the low SST areas. In addition to the coastal upwelling event, the snapshots from July 28 to July 31 illustrate a coastal downwelling event. The winds on July 30 were mainly from northeast (downwelling-favorable). The low SST areas near the coast from the previous upwelling event are decreased under downwelling-favorable winds and the SSTs near the coast were relatively uniform on July 31.

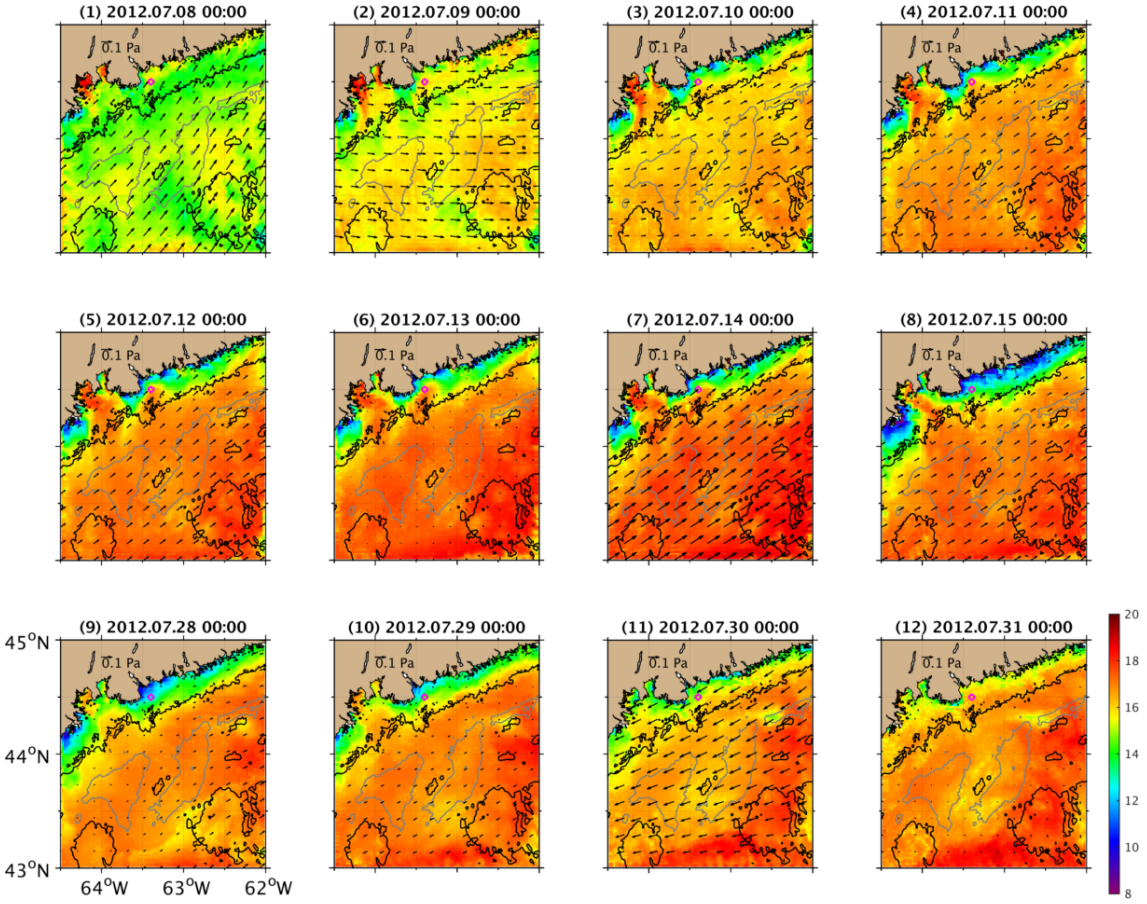

Figure 4.20: 12 instantaneous snapshots of simulated sea surface temperature (SST) over the central Scotia Shelf in July, 2012. The instantaneous wind stress vectors used in the model are plotted as black arrows. The "○" indicates the positions of Halifax Harbour buoy. The 100 m and 200 m isobaths are shown by the black and dark gray contours, respectively.

The simulated coastal upwelling events produced by the submodel L3 of DalCoast-CSS are now compared with the observations made by the Halifax Harbour buoy, gliders and satellite remote sensing. The model performance in simulating the temporal evolution of upwelling events is assessed by comparing the simulated SSTs produced by the submodel L3 with observations made at the Halifax Harbour buoy (Fig. 4.21). It should be noted that the comparison between the simulated SSTs produced by the submodel L4 and observations was presented in the previous model validation section (Fig. 4.8). The simulated SSTs produced by the submodel L3 are very similar to ones produced by the submodel L4. The simulated seasonal cycle of SST agrees with the observations as shown in Fig. 4.21a. The seasonal SST anomaly (Fig. 4.21b) is calculated by subtracting the seasonal cycle from the observed SST. The model is able to capture the SST anomaly during the upwelling events in July. The model also performs reasonably well in capturing the onset of the upwelling at the end of August. However, the model underestimates the sharp decrease in the SST anomaly of this upwelling event.

The horizontal spatial pattern of the simulated coastal upwelling plume is next compared with satellite remote sensing data of SST (Fig. 4.22). Two snapshots were selected with relatively cloud-free conditions and glider observations concurrently close to the coast: one is on July 13 and the other is on September 1, 2012. On July 13, the observed SST was relatively uniform and warm offshore ($>$15°C) and relative cold ($<$15°C) near the coast (Fig. 4.22a). The simulated SST has a similar pattern as the observed SST with a low SST area near the coast. On September 1, the observed SST is also relative uniform offshore but warmer ($>$20°C) than the SST observed on July 13. The observed upwelling plume near the coast on September 1 is well developed with filaments extending $\sim$100 km offshore. The model performs well in capturing the intensified upwelling cold water band along the coast. However, the model performs less well in simulating the observed filaments. Only small filaments develop along the 100 m isobath in the model. We speculate that the large vertical and horizontal mixing in the model erode the upwelling front and prevent the further growth of filaments.

The vertical structure of simulated temperature, salinity and density along two cross-shelf transects during two coastal upwelling events on July 13 and September 1, respectively, are compared with observations made by glider (Figs. 4.23and4.24). In the temperature transect, the model is able to capture the three layer structure in the vertical in comparison

with the observations. However, the simulated warm surface layer is too thin and the cold intermediate layer is too thick in comparison with the observations. The thick cold intermediate layer in the model could be related to the less warm Slope Water intrusion at the shelf break in the model. The thick cold intermediate layer in turn reduces the thickness of warm surface layer in the model through vertical mixing. In the salinity transect, the model is able to capture the relatively low salinity water in the top 100 m and the relatively high salinity ($>$34.5 psu) water in the deep layer ($>$100 m) of the Emerald Basin. However, the model overestimates the salinity in the top 50 m, which could be explained by the lack of precipitation and evaporation processes at the sea surface in the model. In the density transect, the simulated isopycnals tilted upward towards the coast (Fig. 4.23c-2) which is similar to the observations (Fig. 4.23c-1) for the upwelling events in July. The upward tilted isopycnals are a direct result of upwelling secondary circulation, bringing deeper denser water masses up to shallower regions. It should be noted that the observed less dense water masses in the top 20 m on the shelf are not captured by the model.

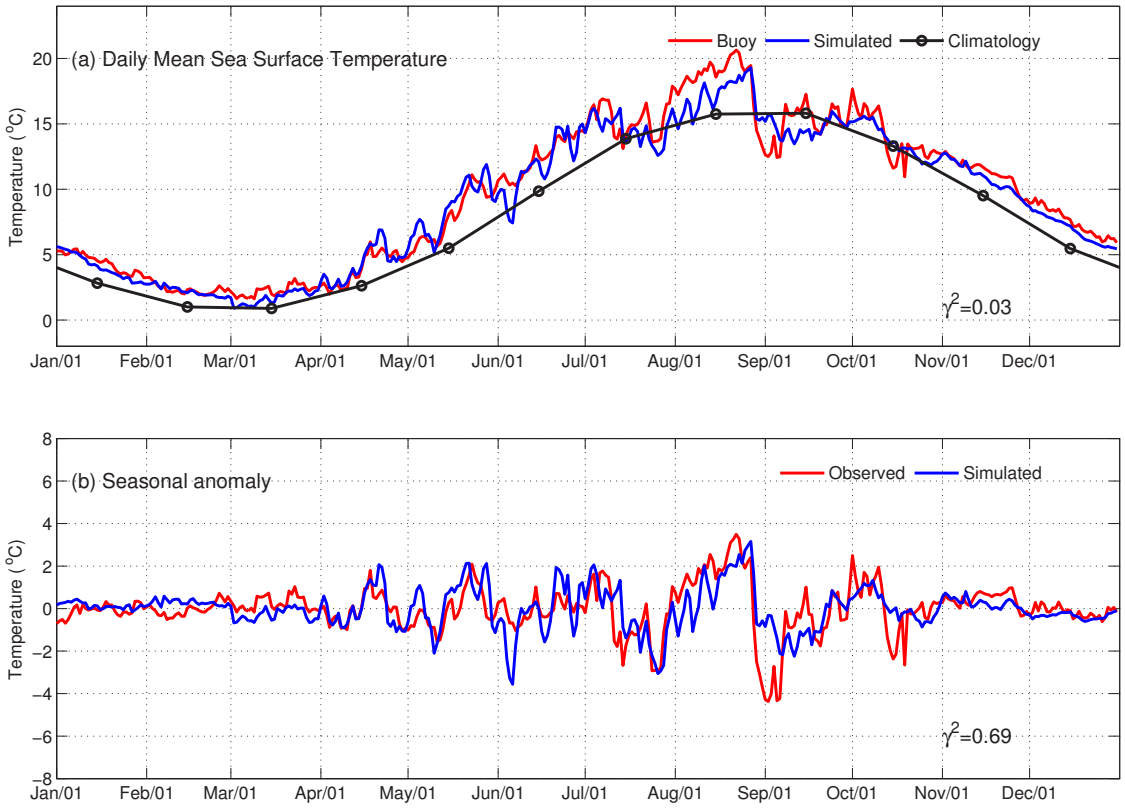

Figure 4.21: Time series of (a) observed and simulated sea surface temperature (SST) in 2012 at the Halifax Harbour buoy; (b) SST seasonal anomaly. The simulated results are produced by submodel L3. Note the upwelling events in July and the end of August 2012.

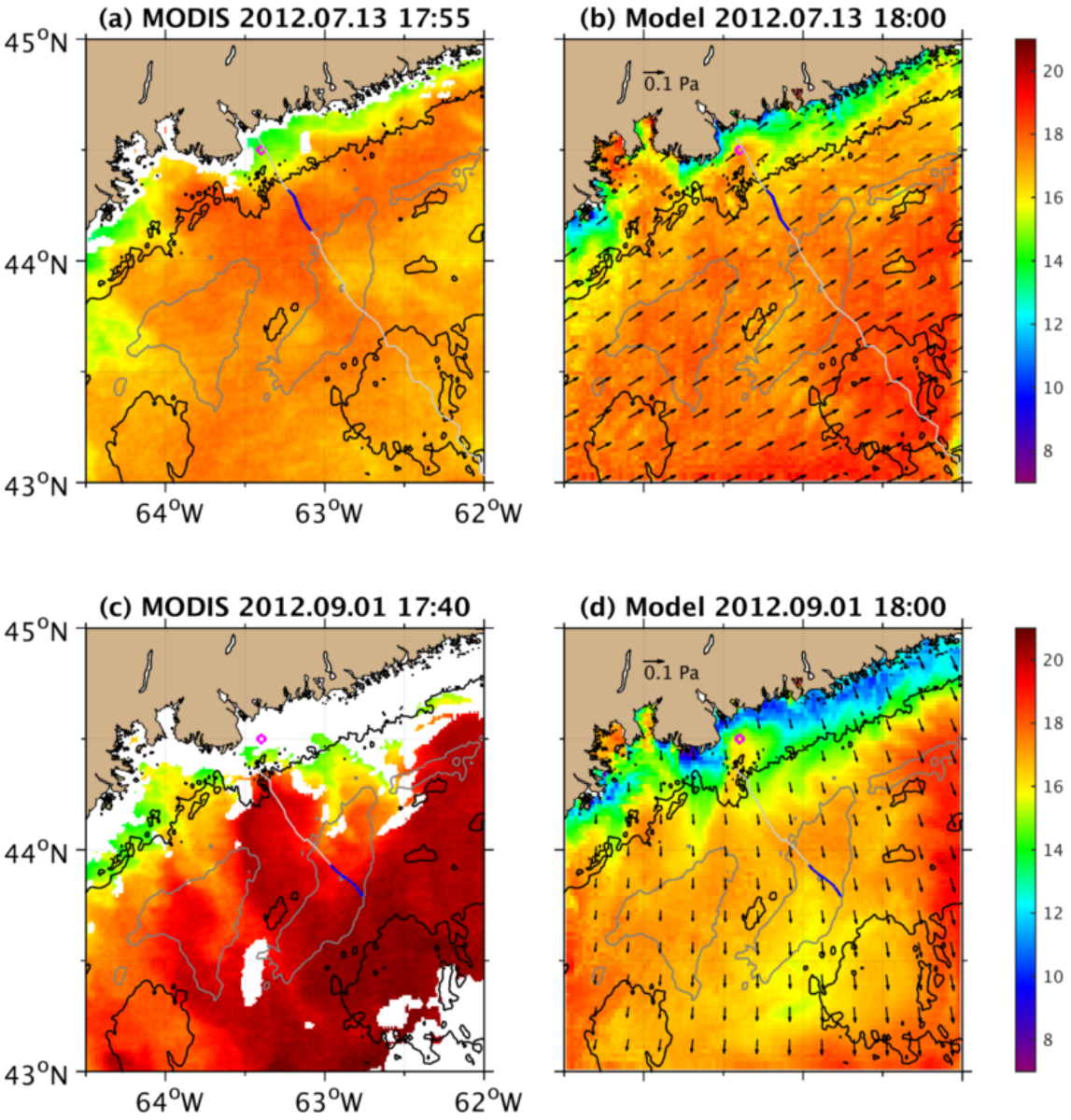

Figure 4.22: Observed and simulated sea surface temperature (SST) over the central Scotia Shelf on (a) July 13 and (b) September 1, 2012. The instantaneous wind stress vectors used in the model are plotted as black arrows. In each panel, the light gray line indicates the glider track. The blue portion on the glider track highlights the path during the corresponding day. The "○" indicates the positions of Halifax Harbour buoy. The 100 m and 200 m isobaths are shown by the black and dark gray contours, respectively.

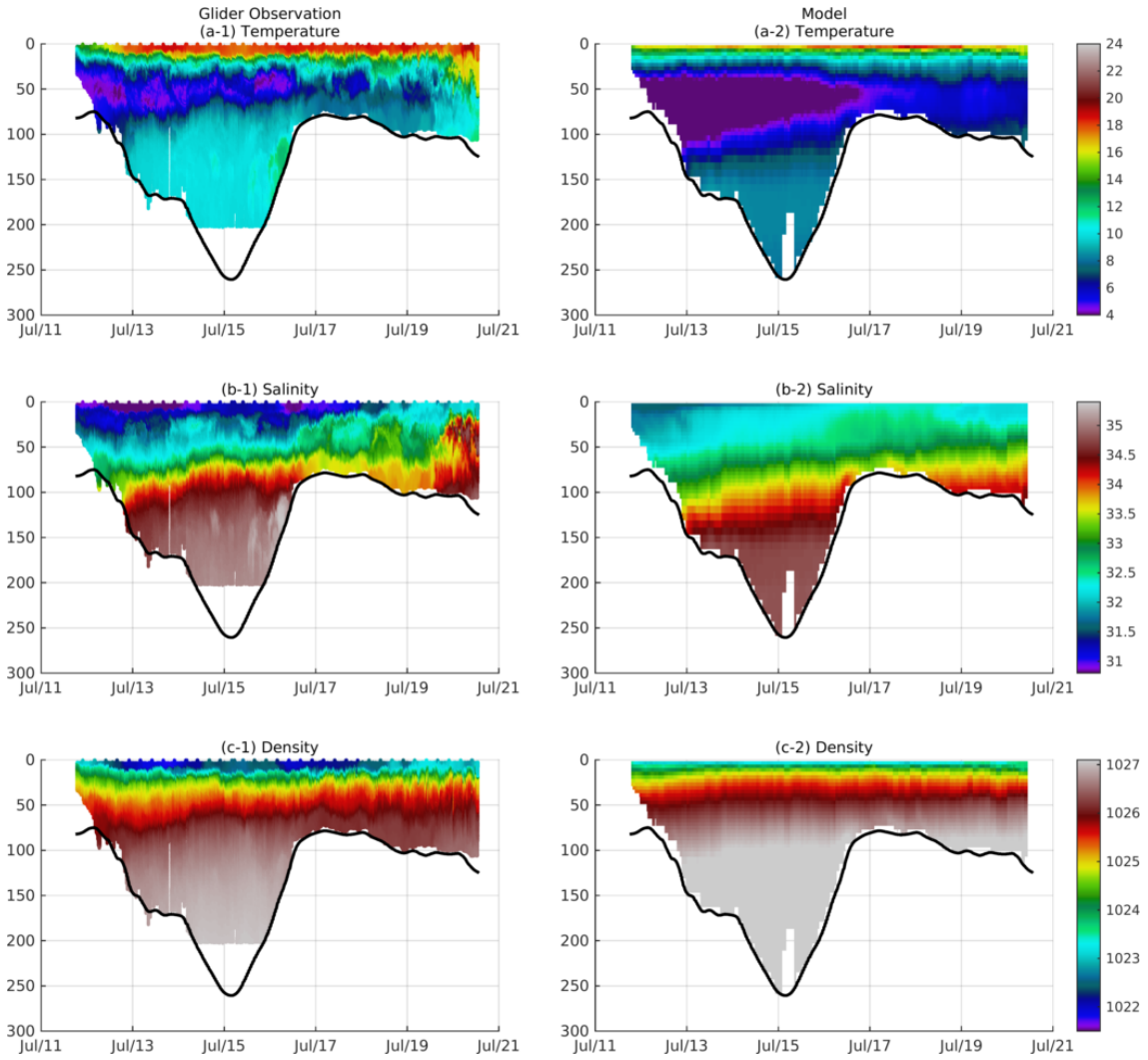

Figure 4.23: Cross-shelf transects of temperature, salinity and density from (Left panel) glider observations and (right panel) model simulations in July 2012. The glider trajectories are shown in Figure 4.22. The glider observations were provided by the glider research group from Dalhousie University (`http://gliders.oceantrack.org/`). Surveys were conducted at the Halifax Line, from Halifax Harbour to shelf break. Data were collected from temperature, conductivity and pressure sensors onboard the gliders.

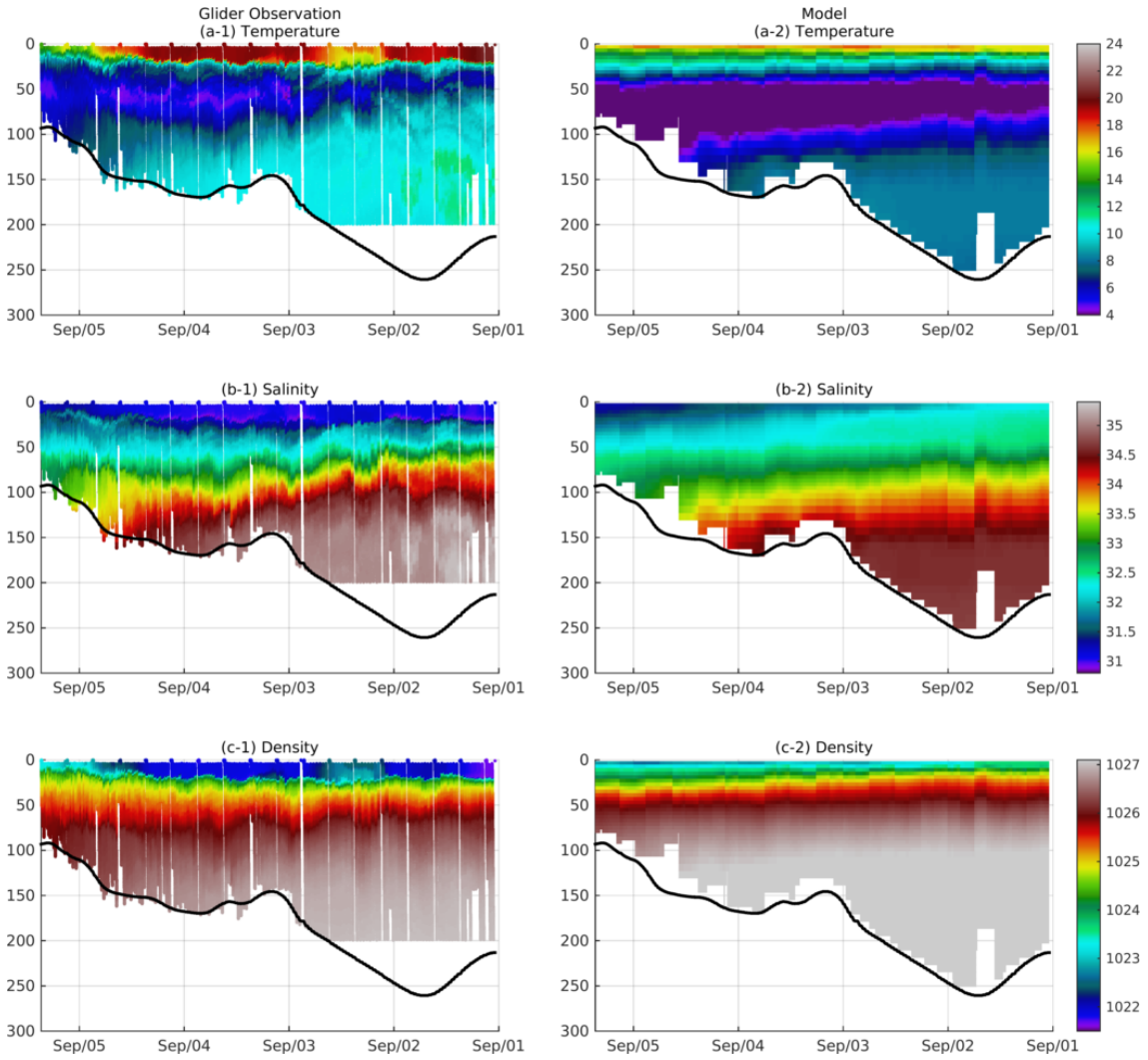

Figure 4.24: Cross-shelf transects of temperature, salinity and density from (Left panel) glider observations and (right panel) model simulations in September 2012. The glider trajectories are shown in Figure 4.22.

4.5.3 Role of Irregular Coastline and Topography in Coastal Upwelling: A Process Study

The SSTs in Mahone and St. Margarets Bays were warmer than the adjacent coastal area during coastal upwelling events in July 2012 as shown in simulated SSTs (Fig. 4.20). To identify the main physical processes affecting the spatial variability over coastal waters during upwelling events, a correlation analysis on the remote sensing data of SSTs over this region is conducted. The MODIS Aqua SSTs from 2002 to 2014 for this region are used for the analysis. The correlation coefficients between the SSTs time series at the marine buoy outside Halifax Harbour and other locations in the region are calculated for the summer (July, August and September) and winter (January, February and March). The maps of correlation coefficients in summer and winter demonstrate (Fig. 4.25) that the SSTs are more correlated in the along-shore direction than in the cross-shore direction. In the along-shore direction, the correlation decays much faster in the downstream direction (southwestward, in term of coastal trapped wave propagation) than in the upstream direction (northeastward) in summer, while the asymmetry in the downstream and upstream is not observed in winter. We speculate that the asymmetry in summer is related to Cape Sambro, where the correlation decreases significantly to the west of Cape Sambro. Thus, a process study using DalCoast-CSS is conducted to quantify the role of the irregular coastline and topography in the coastal upwelling on the central Scotian Shelf. Three numerical experiments using various specifications of coastline and topography of the submodel L3 are conducted as described below:

1. CONSTANT WIND RUN (*UPwind*): The DalCoast-CSS in this experiment is driven by the suite of forcing functions discussed in section 2, including tides, river discharges, atmospheric forcing and open boundary forcing, except that a typical upwelling-favorable wind stress (0.05 Pa and 65°T) is specified in submodel L2 and L3.

2. STRAIGHT COASTLINE RUN (*UPline*): Same as *UPwind*, except that the realistic irregular coastline in submodel L3 is replaced by a straight one.

3. SMOOTHED TOPOGRAPHY RUN (*UPtopo*): Same as *UPwind*, except that the realistic irregular topography near the coast (e.g., Sambro Ledges, a submerged bank associated with Cape Sambro) in submodel L3 is replaced by a smoothed

topography, in which the isobaths from 50 to 100 m adjacent to the coast are parallel to each other and have an angle of 65°T.

In experiments *UPwind*, *UPline* and *UPtopo*, submodel L2 and L3 are initialized from the 3D circulation and hydrography conditions on July 1, 2012 produced by the realistic hindcast run and integrated for three months. The model results of SSTs after 3, 5, 10, and 30 days relative to July 1, 2012 from the three experiments (Fig. 4.26) are examined to determine the role of irregular coastline and topography in the coastal upwelling on the central Scotian Shelf adjacent to Halifax.

A coastal upwelling plume develops under the constant upwelling-favorable wind condition in *UPwind*. After 3 days from the onset of the uniform wind (Fig. 4.26a-1), three filaments with relatively low SST near the coast developed, which are located to the west of Mahone Bay (Filament A), off the Cape Sambro (Filament B), and about 80 km to the northeast of Cape Sambro (Filament C). These filaments extend about 50 km offshore. The SSTs to the northeast and southwest of Filament A are relatively warm and about 15°C. The SSTs on the shelf are relatively uniform and about 15°C. After 5 days (Fig. 4.26a-2), the three filaments are further extended offshore. After 10 days (Fig. 4.26a-3), Filament A is further extended offshore. Filaments B and C are merged into a cold water band near the coast. St. Margarets Bay is covered by relatively cold surface water associated with the upwelling plume. The SST in Mahone Bay is warmer than the SST in the upwelling plume but colder than the SST on the shelf. The SST on the middle and outer shelf increased from about 15°C to 18°C due to the positive surface heat flux from the overlying atmosphere to the ocean. After 30 days (Fig. 4.26a-4), Filament A is extended to LaHave Bank and Mahone Bay is fully covered by relatively cold surface water associated with the upwelling plume. Backward breaking waves associated with the instability at the plume front are developed along the 100 m isobath to the northeast of the Sambro Ledges.

The coastal upwelling plume in the case of *UPline*, in which a straight coastline is specified, shows several distinct features in comparison with the plume in the case of *UPwind*. After 3 days, three filaments are also evident along the straight coastline. In comparison with the filaments in *UPwind*, the filaments in *UPline* extend further offshore. The filament close to Cape Sambro (Filament B) in *UPline* is located further southwest in comparison with the one in *UPwind*. After 5 days, the filaments extend further offshore. Filament B moves closer to Filament A, which is located to the west of Mahone Bay. After

10 days, Filament B is merged with Filament A to form a larger filament. Another filament is evident off Cape Sambro. After 30 days, the upwelling plume is very similar to the plume in *UPwind*. Backward breaking waves associated with the instability at the plume front are also developed along the 100 m isobath to the northeast of the Sambro Ledges. The southwestward propagation of the filament from Cape Sambro in the straight coastline is not evident in the results of *UPwind*, which indicates that the cape has a scattering effect for the along-shore wave propagation of the filaments.

The coastal upwelling plume in the case of *UPtopo*, in which the Sambro Ledges are removed, has similar features close to the coast but distinct features offshore in comparison with the plume in the case of *UPwind*. After 3, 5 and 10 days relative to July 1, the coastal upwelling plume from the coast to the 50 m isobath in *UPtopo* is very similar to the plume in *UPwind*, indicating that the presence of Sambro Ledges has little impact to the initial development of the filaments near the coast. However, the presence of Sambro Ledges can influence the further offshore development of filaments by affecting the circulation field. After 10 days, the filaments in *UPtopo* are advected southwestward by the Nova Scotia Current in the pathway between the 50 and 150 m isobaths. After 30 days, backward breaking waves associated with the instability at the plume front are developed along the 150 m isobath from northeast to southwest in *UPtopo*, while the instability waves are disrupted by the presence of Sambro Ledges in *UPwind*. The small-scale bathymetric spur off Sambro (i.e., Sambro Ledges) has a major influence on the downstream evolution of temperature after about 30 days.

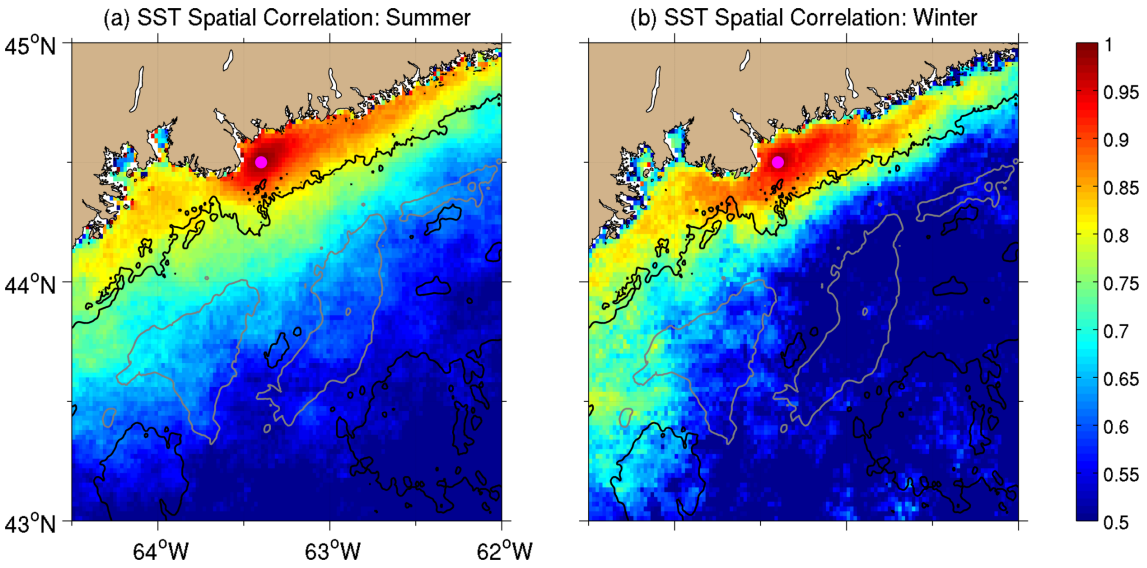

Figure 4.25: Distributions of correlation coefficients for time series of MODIS Aqua SSTs at any location with respect to the reference point at the marine buoy outside Halifax Harbour in summer and winter. MODIS Aqua SSTs over the central Scotia Shelf from 2002 to 2014 were gridded to a regular grid (0.02°) and the annual and semiannual cycles were removed. Then, the correlation coefficient between each grid point and the reference point ("•") was calculated for the summer (July, August, September) and winter (January, February, March) months. The 100 m and 200 m isobaths are shown by the black and gray contours, respectively.

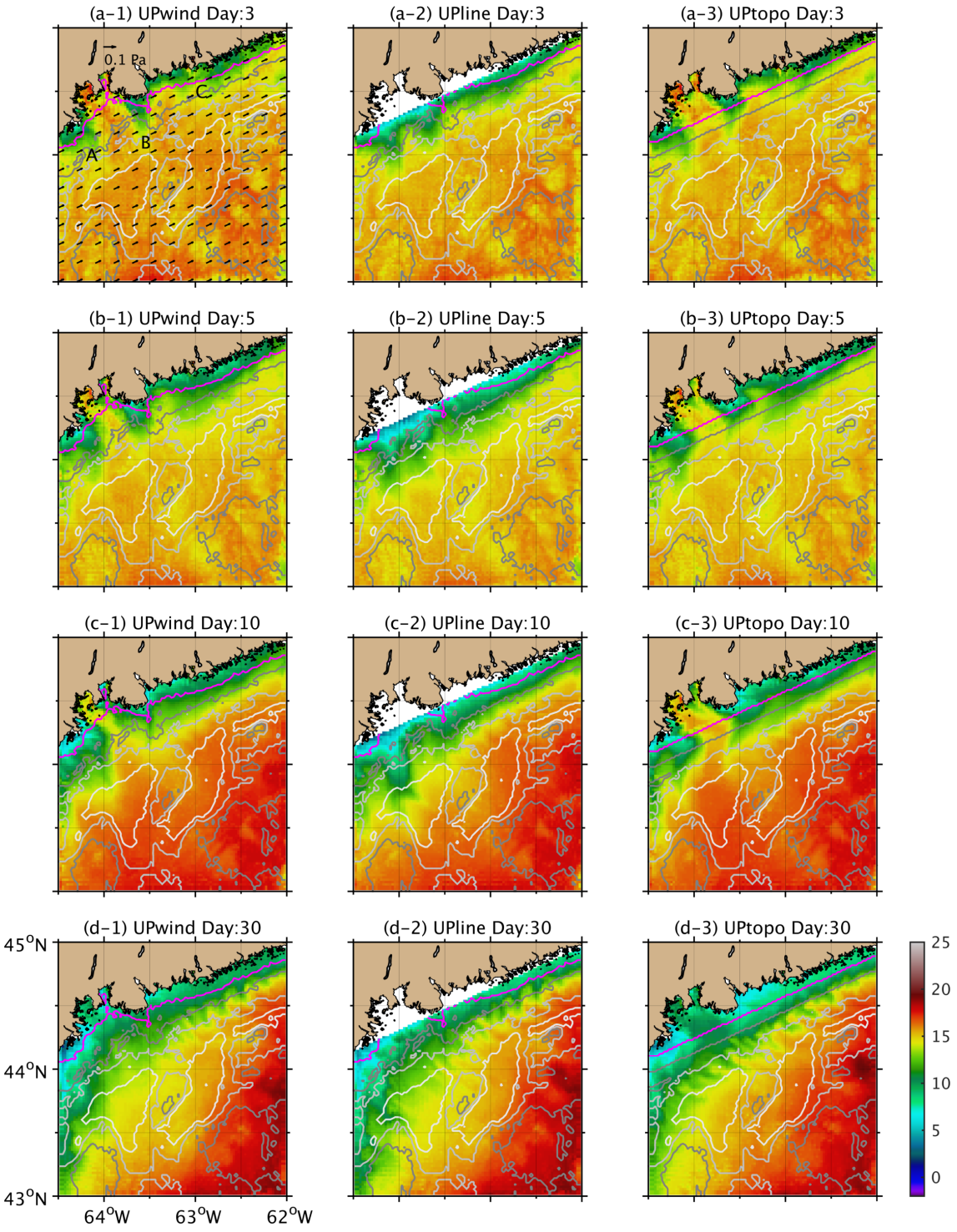

Figure 4.26: Sea surface temperatures in numerical experiments by using constant wind (*UPwind*), straight coastline (*UPline*) and smoothed topography (*UPtopo*). The model are initialized from the 3D circulation and hydrography conditions on July 1, 2012 produced by the realistic hindcast run. The model results after 5, 10, 15 and 30 days, relative to July 1, are shown. The constant wind stress vectors used in the model are plotted in (a-1, black arrows). A, B and C in (a-1) indicate three filaments. The 50 m isobath is shown by the magenta contours. The 100, 150 and 200 m isobaths are shown by colored contours from dark to light gray.

4.6 Implications for Salmon Migration

Atlantic salmon are widely distributed along the North Atlantic coast. Most Atlantic salmon populations, particularly those in the southern range of their distribution, have declined throughout the last century (*Parrish et al.*, 1998). Improved understanding of how physical changes in the ocean impact salmon survival is critical for managing these stocks, especially in light of the rapid changes in the marine environment.

As an anadromous species, Atlantic salmon migrate through the Gulf of Maine and Scotian Shelf to the Labrador Sea then crossing the Atlantic to feed inshore and in fjords of West Greenland (Fig. 4.27, *Hayes and Kocik*, 2014). Salmon enter the Gulf of Maine annually in May (*Kocik et al.*, 2009) and are observed off the coast of Halifax, Nova Scotia in June (*USASAC*, 2010; *Dever et al.*, 2016). Most salmon take two sea winters to complete their entire ocean migration, however, some fish do it in one sea winter (*USASAC*, 2010). Atlantic salmon adults return to their natal rivers to spawn in highly directed homeward migration, ranging from June to November. Recent studies by *Putman et al.* (2013, 2014) supported the idea of salmon using the Earth's magnetic field to guide their seaward and homeward migration. Depth monitoring acoustic tags data demonstrated that postsmolts reside in the top 1 m of the surface waters over 80% of the time and in the top 5 m 95% of the time (*Renkawitz et al.*, 2012). Water temperature plays an important role in both behavior and physiology of salmon. The onset of seaward salmon migration seems related to a 10°C threshold water temperature (*Zydlewski et al.*, 2005). *Handeland et al.* (2003) suggested that saltwater salmon has strong growth above 10°C with optima often around 13°C . However, growth rates of salmon rapidly decline above 14°C.

Two implications can be inferred from the above key observed factors of salmon migrating from the Gulf of Maine to the Halifax Line. First, (near) sea surface temperature may play a major role in affecting the salmon migration. The annual-mean ocean temperature at discrete depths from surface to bottom over the SS and GoM in 2012 was the warmest between 1970 and 2012 (*Hebert et al.*, 2013). The observed surface temperature at the marine buoy outside Halifax Harbour reached 10°C about half-month earlier in 2012 than climatology (Fig. 4.8) This abnormal warm sea surface temperature could force the postsmolts to have an earlier migration and similar issues may be encountered in the return migration for adults. Second, the surface current on the Scotian Shelf may play an adverse role during the postsmolts migration. The Nova Scotia Current on the Scotian Shelf flows

southwestward with significant seasonal and interannual variability (Figs.4.12 and 4.13). The seaward migrating postsmolts have to swim against this prevailing current, which increases their energy expenditure. In addition, the interannual variability in the Nova Scotia Current could affect the migration duration by reducing (increasing) the ground migration speed under stronger (weaker) Nova Scotia Current conditions, for postsmolts migrating at a given speed. As shown in the sensitivity study with idealized bathymetry discussed in the previous section, the small-scale bathymetric features (e.g., Cape Sambro and Sambro Ledges) have to be resolved in the circulation model in order to realistically simulate the SST and current. Thus high-resolution models are required to simulate the movement of salmon in the coastal region.

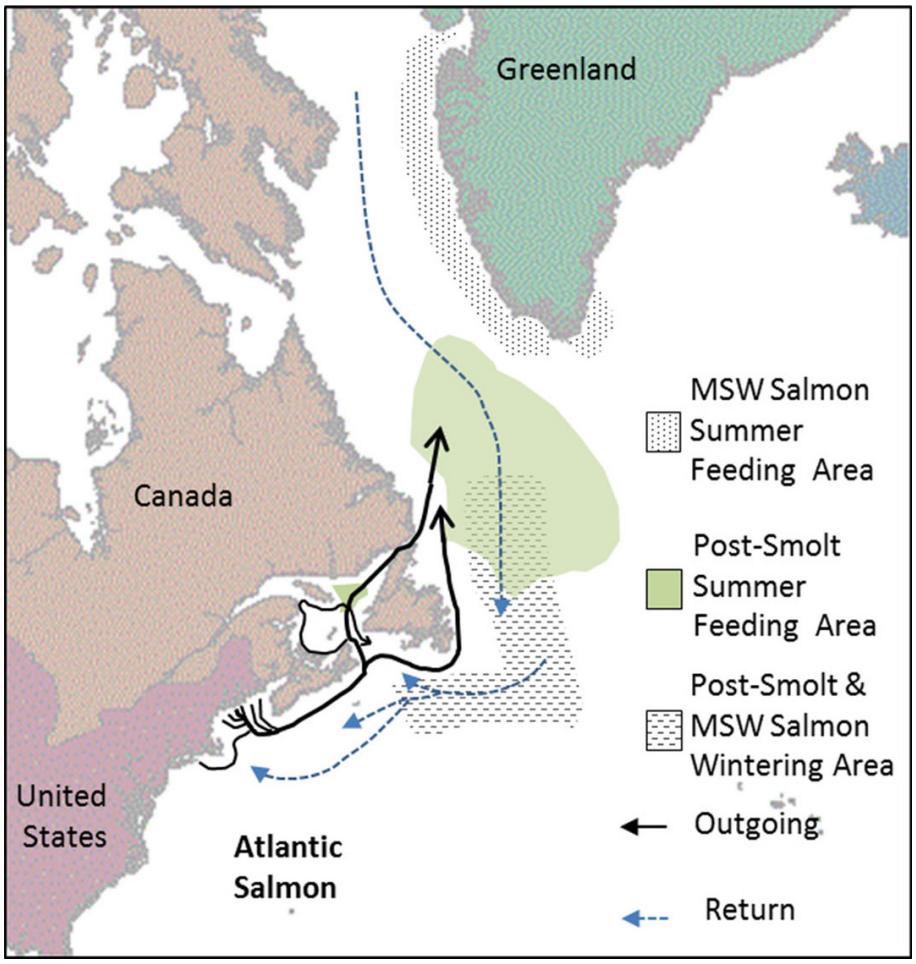

Figure 4.27: Distribution and migratory pathways of Atlantic salmon in Atlantic basins. (Adapted from *Hayes and Kocik*, 2014)

4.7 Summary

A multi-nested shelf circulation model (DalCoast-CSS) was used for simulating the variability of circulation and hydrography over the coastal and shelf waters of Nova Scotia. The nested-grid model consists of four submodels downscaling from the eastern Canadian Shelf to the central Scotian Shelf. The nested-grid model was driven by tides, river discharges, and atmospheric forcing. The model performance was assessed by using satellite remote sensing data and *in-situ* observations. The simulated tidal and non-tidal sea levels were in good agreement with tide gauge observations; the simulated monthly-mean sea surface temperature and salinity were in fair agreement with satellite remote sensing observations; and the simulated daily-mean sea surface temperature outside Halifax Harbour reproduced the observed daily to seasonal variations. The nested-grid model was also able to capture the synoptic variability of the Nova Scotia Current (NSC) transport. However, the model had some deficiencies in simulating the thermocline intensity in summer, the intrusion of warm and salty Slope Water, and the seasonal cycle of the NSC. We speculate that these model deficiencies may be due to the crude vertical mixing parameterization used in the model. A sensitivity study using different vertical parameterization schemes over this region will be conducted in a future study.

The satellite-observed sea surface temperature revealed that the Atlantic side of Nova Scotia is occasionally surrounded by cold surface waters along the coast in summer, which is due to tidal mixing and wind-driven coastal upwelling. In this study, these physical processes contributing to the formation of these cold surface waters were investigated based on model results in three numerical experiments using DalCoast-CSS. The model results confirmed that the formation of cold water in the Bay of Fundy and off Cape Sable is due mainly to tidal mixing and topographical upwelling. The model results also demonstrated that the cold water along the south shore of Nova Scotia is a result of wind-driven coastal upwelling. In addition, the temporal and spatial evolution of coastal upwelling in the central Scotian Shelf adjacent to Halifax was discussed by using various observations and DalCoast-CSS. The roles of irregular coastline and topography in coastal upwelling were investigated by contrasting the results from a suite of model runs differing only in the specification of coastline and topography. This process study demonstrated that irregular coastline (e.g., cape) has a scattering effect for the along-shore wave propagation of the filaments and irregular topography (e.g., submerged bank) can

influence the further offshore development of filaments. The implications of circulation and hydrography on the Scotian Shelf for the Atlantic salmon migration were also discussed. The abnormal warm (cold) sea surface temperature on the Scotian Shelf and adjacent waters could force an earlier (later) migration of the Atlantic salmon. The Nova Scotia Current and associated seasonal and interannual variability may play an adverse role during the postsmolts migration by influencing their energy expenditure and migration duration. The role of small-scale bathymetric features (e.g., Cape Sambro and Sambro Ledges) in realistically simulating the SST and current suggests that high-resolution models are required to simulate the movement of salmon in the coastal region.

CHAPTER 5

NORTH ATLANTIC [1]

5.1 Introduction

American and European eels (*Anguilla rostrata* and *Anguilla anguilla*) are widely distributed along the eastern coast of North America and the coast of Europe, respectively. According to *Bertin* (1956), their life cycle is a remarkable example of response to environment (e.g., temperature, salinity, light and current) and can be divided into eight phases: (1) birth in the Sargasso Sea and existence as a transparent larva or *leptocephalus*; (2) migration under the influence of ocean currents towards the continental shelf waters; (3) metamorphosis of the leptocephali into minute transparent eels or *elvers*; (4) upstream migration by these elvers to the continental fresh waters; (5) metamorphosis of the elvers into yellow eels; (6) growth of these in rivers and lakes; (7) final metamorphosis into silver eels, and the development of male or female sexual maturity; and (8) seaward migration of the sliver eels from the fresh waters to the Sargasso Sea where they breed and die.

The spawning of eel in the sea was first speculated by Aristotle in 350 BC (*Bertin*, 1956). After more than two centuries, a milestone discovery was made by the Danish scientist *Johannes Schmidt* in 1922. He deduced the spawning area of the European eel in the Sargasso Sea, according to the location where the smallest eel larvae were found. After nearly another century, our knowledge is still limited in terms of the long-distance oceanic migration of silver eel from the North Atlantic coastal waters to the Sargasso Sea. For

[1] This chapter was modified from a paper entitled "Exploring the role of the physical marine environment in silver eel migrations using a biophysical particle tracking model" by Béguer-Pon, M., S. Shan, K. R. Thompson, M. Castonguay, J. Sheng and J. Dodson published in *ICES Journal of Marine Science* in 2016. This is a collaborative work. As the second author of the article, I was the principal contributor for the model implementation and simulation, and associated description and discussion in this paper.

example, the migration routes eels take, the navigation cues they use and the environmental conditions they experience are not well understood.

Over the past decade, collective efforts have been made to observe the eel's seaward migration from the coast using pop-up archival satellite tags. European eels were tracked off the coast of Ireland (*Aarestrup et al.*, 2009). In another study, European eels were tracked for up to 2300 km from the Swedish coast to the north of Ireland (*Westerberg et al.*, 2014). A recent tracking study showed that European eels from the Mediterranean can cross the Strait of Gibraltar and continue their migration into the Atlantic Ocean (*Amilhat et al.*, 2016). American eels have also been tagged and released on the Scotian Shelf annually since 2012 and one individual was tracked migrating 2400 km to the northern limit of the spawning site in the Sargasso Sea (*Béguer-Pon et al.*, 2015). These observed eel migratory tracks revealed that eels perform diel vertical migrations (DVMs)[2] during their spawning migration in the open ocean. Although these experiments represent important steps forward in understanding the eel's seaward migration, limitations in our understanding remain. For example, experiments using tagged eels usually suffered from unknown early tag detachments and high predation rate of eels. As to the reason for this, it is shown in laboratory studies that the eel's swimming performance is impaired by the attached tag (e.g., *Methling et al.*, 2011), which may lead to the high predation rate of tagged eels at sea (e.g., *Béguer-Pon et al.*, 2012).

In addition to observational studies, a particle tracking model is very useful for investigating the migration of eels given the paucity of biological observations using satellite tags discussed above. In ecology, particle tracking models are called individual-based models, which simulate populations as being composed of discrete individual organisms. Unlike traditional differential equation population models, which are described in terms of imposed top-down population parameters (such as birth and death rates), individual-based models are bottom-up models in which population-level behaviors emerge from the interactions among autonomous individuals with each other and their abiotic environment (*DeAngelis and Grimm*, 2014). As demonstrated in Chapter 3, particle tracking models can be used to track the movement of individual passive particles and investigate the transport pathway and residence time in the ocean. In fact, several studies on eel larvae dispersal (e.g., *Bonhommeau et al.*, 2009a,b, 2010; *Rypina et al.*, 2014) tracked eel larvae

[2]Eels swim in the shallow warm water during the night and make a steep dive at dawn to deep water and stay there for the day before ascending again at dusk.

as passive particles due to their limited swimming ability. However, the active swimming of adult eels adds a layer of complexity to the particle tracking model. Thus, it comes as no surprise that only one published paper (*Fricke and Kaese*, 1995) was found in the literature concerning the spawning migration of eels from coast to the Sargasso Sea that employs a particle tracking model. In their study, *Fricke and Kaese* (1995) simulated the migration of European eels by releasing particles off the European coasts swimming at around 200 m depth without DVM and at a constant heading to the southwest, but other key parameters of the tracking experiment were not well explained. At this point, it could be argued that a better particle tracking model for simulating eel's seaward migration is needed to complement the relevant field observations.

In this study, a newly developed biophysical particle tracking model is used to examine the impact of circulation on the seaward migration of American and European eels from the coastal waters of North Atlantic to the Sargasso Sea. In Section 5.2, the ocean circulation model of the North Atlantic used in this study is introduced. In Section 5.3, the biophysical particle tracking model is described. In Section 5.4, the particle tracking results are presented to assess the effect of the flow field on the resulting migratory patterns, including migration route and duration, environmental conditions experienced along the migration route, and energy expenditure. In Section 5.5, the implication of physical oceanic environment for eel migration are discussed. A summary is presented in the last section.

5.2 Circulation of the North Atlantic

In this study, the three-dimensional time-varying circulation over the North Atlantic produced by an ocean general circulation model is used for tracking the movement of eels. The circulation model was developed during the GOAPP project (Global Ocean-Atmosphere Prediction and Predictability, http://www.goapp.ca) and used to study the circulation of the North Atlantic (*Higginson et al.*, 2011; *Higginson*, 2012). The model is based on version 2.3 of NEMO (Nucleus for European Models of the Ocean) with the OPA (Océan PArallélisé) as the ocean circulation component and LIM2 (Louvain-la-Neuve sea Ice Model, version 2) as the sea-ice component (*Madec*, 2008). The model domain covers the North Atlantic (5-68°N, 100°W-34°E, Fig. 5.1) with a nominal 1/4° horizontal resolution and a maximum of 46 levels in the vertical. The model forcing at the sea surface, including wind stress, net heat fluxes, and freshwaters, is specified using the CORE (Common Ocean-ice Reference Experiments) normal-year dataset. The lateral open boundary conditions are specified using temperature, salinity, and transport obtained from a global 1/4° model. To suppress drift and bias, the model is spectrally nudged (*Thompson et al.*, 2006) to a monthly temperature and salinity climatology constructed from a blend between the Yashayaev climatology (http://www2.mar.dfo-mpo.gc.ca/science/ocean/woce/climatology/naclimatology.htm) and the PHC (Polar science center Hydrographic Climatology)/Levitus climatology (*Steele et al.*, 2001). The model is integrated for 16 years from January 1990 to December 2005, and model simulations of three-dimensional currents, temperature and salinity are stored every 5 d.

The ocean circulation in the North Atlantic (Fig. 5.1a) has been the subject of many studies over the past century (see *Schmitz and McCartney*, 1993 for a review). The subtropical and subpolar gyres were identified and studied in the past (e.g., *Reid*, 1994; *Talley et al.*, 2011). In the rest of this paragraph, a brief summary of the circulation system in the North Atlantic is provided. The major upper ocean circulation pattern in the North Atlantic consists of the subtropical and subpolar gyres (Fig. 5.1b and c). One of the dominant features in the upper layer of the North Atlantic is the Gulf Stream (GS). The current is energetic, exceeding 1 m s^{-1} in places, and the water in the GS is relatively warm and saline. Near Cape Hatteras, the GS moves offshore into deeper waters and the path becomes more variable with meanders and eddies. Beyond the tail of the Grand Banks, the GS becomes the North Atlantic Current (NAC). Part of the NAC separates to form the

Azores Current. The latter flows eastward and feeds recirculations to the south and west, such as the Canaries Current and the North Equatorial Current, completing the circulation that is the subtropical gyre. The remainder of the NAC continues northeastwards, either towards the Norwegian Sea or into the subpolar gyre. This gyre comprises the Irminger Current towards Iceland, with return flow equatorward via the East and West Greenland and Labrador currents.

The three-dimensional currents simulated by the NEMO model reproduce reasonably well the subtropical and subpolar circulation, in terms of both the long-term mean and temporal variability (Fig. 5.2). The GS extension is one of the energetic regions in the North Atlantic. The modelled temperature field features warm and cold core rings near the confluence regime of GS and Labrador Current (Fig. 5.1b). The circulation model also captures the separation of the GS and the relatively strong mesoscale variability in the GS extension region (Fig. 5.2).

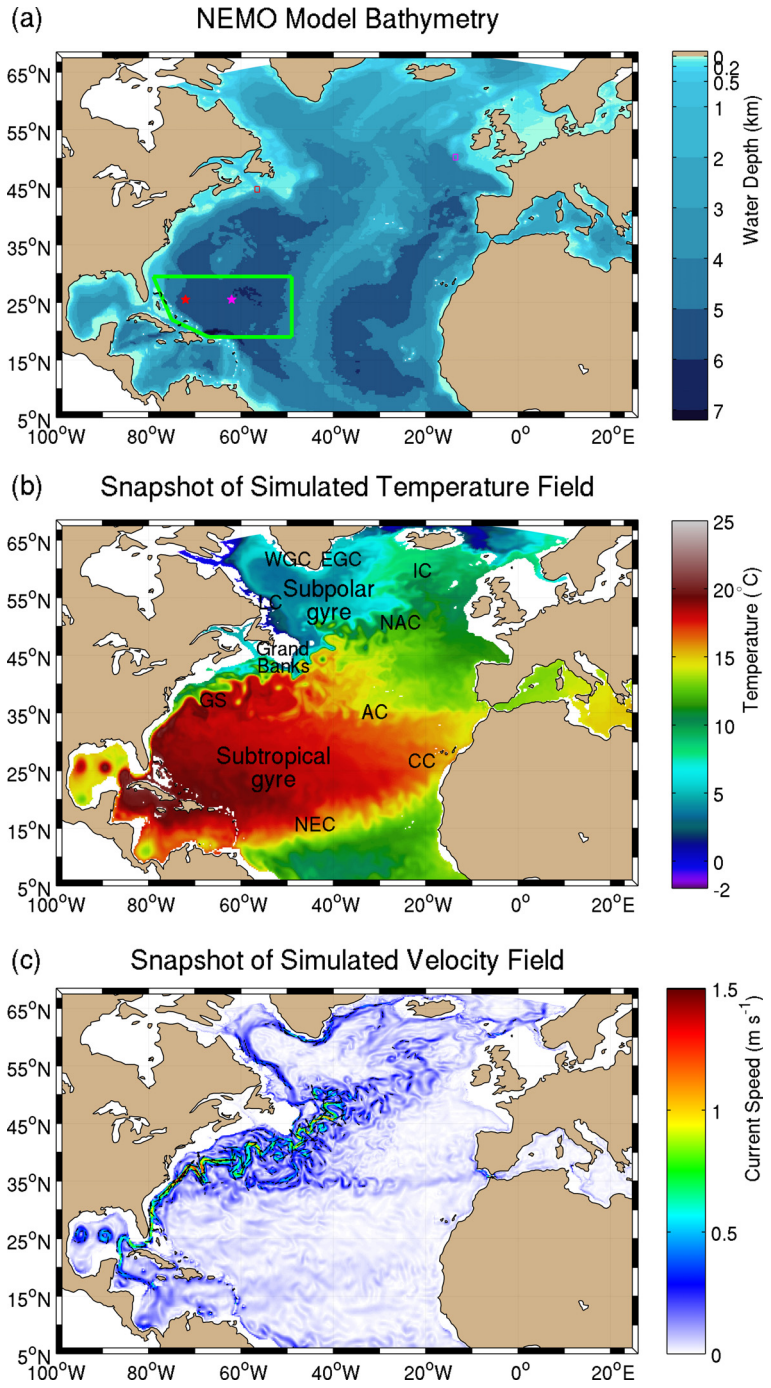

Figure 5.1: The North Atlantic Ocean model (a) bathymetry and snapshots of simulated (b) temperature (°C) and (c) velocity (m s^{-1}) fields at 200 m at the end of October 2004. In (a), areas marked by the red and magenta boxes indicate the initial release locations of the American and European eels, respectively. The area marked by the green polygon indicates the assumed spawning area. The red (72°W, 25.5°N) and magenta (62°W, 25.5°N) stars indicate the locations where the smallest American and European eel larvae were found, respectively. In (b), the currents that are labelled are the Gulf Stream (GS), the North Atlantic Current (NAC), the Azores Current (AC), the Canaries Current (CC), the North Equatorial Current (NEC), the Irminger Current (IC), the East Greenland Current (EGC), the West Greenland Current (WGC), and the Labrador Current (LC). In (c), the current direction for the current speed > 0.2 m s^{-1} is indicated by the black arrows.

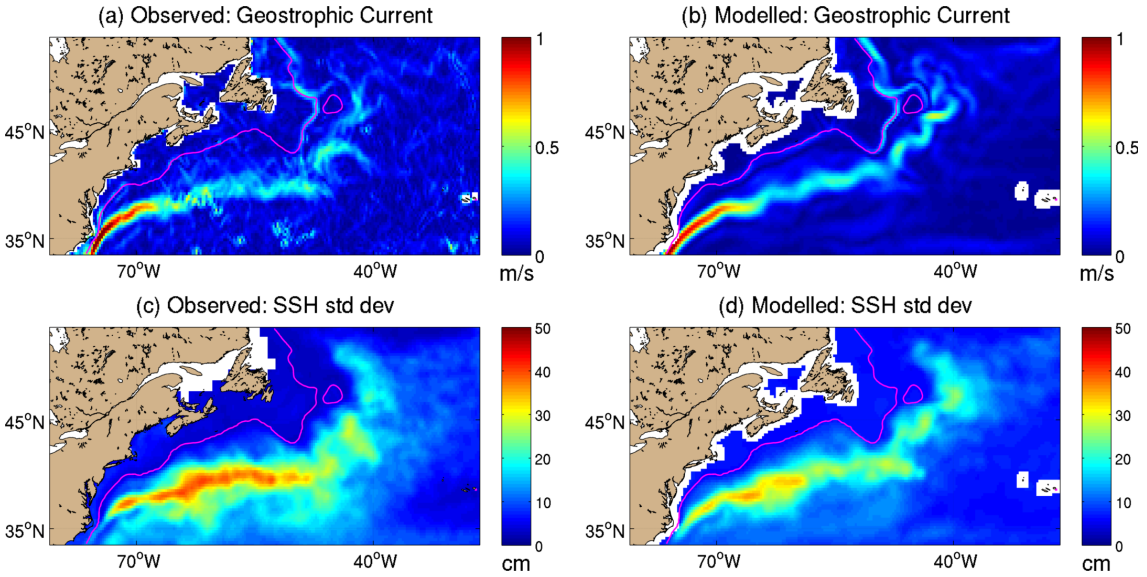

Figure 5.2: Speeds of time mean surface geostrophic currents derived from (a) altimetry and gravity observations (*Higginson et al.*, 2011) and (b) 10-year mean NEMO modelled sea surface height from 1996 to 2005. Standard deviation of sea level anomaly calculated from (c) AVISO product of gridded daily sea level anomaly and (d) NEMO modelled sea surface height. The 500 m isobath is plotted in magenta indicating the shelf break. The AVISO altimeter products were produced by Ssalto/Duacs and distributed by AVISO with support from CNES.

5.3 Biophysical Particle Tracking Model

5.3.1 Horizontal Movement

In the particle tracking model, each particle is considered as a virtual eel (v-eel) carried by ocean currents. The horizontal movement of v-eels is expressed in terms of the physical and biological components:

$$\frac{d\vec{x}}{dt} = \vec{u}_P(\vec{x}, t) + \vec{u}_B(\vec{x}, t) \tag{5.1}$$

where $\vec{x}$ is the eel's horizontal position at time t, $\vec{u}_P$ and $\vec{u}_B$ are the components of flow associated with passive drift by ocean currents and active migratory swimming, respectively. Both $\vec{u}_P$ and $\vec{u}_B$ are functions of space and time. A forward Euler time-stepping scheme is used to solve Eq. (5.1) in this study. The novelty of this study is the addition of the migratory behaviors to the passive drift.

5.3.1.1 Physical component ($\vec{u}_P$)

The results produced by the North Atlantic circulation model for the years of 2004 and 2005 are used to provide three-dimensional time-varying ocean currents and hydrographic fields for the biophysical particle tracking model. A nearest-neighbor-based scheme is used to interpolate the modelled currents, temperature, and salinity to the particle location.

A random walk process, which is similar to the one introduced in Chapter 3, is included in the particle tracking model to account for the particle movement associated with subgrid-scale turbulence and other local processes which are not resolved by the circulation model. The horizontal random displacement at each time-step of the model is defined by $\xi\sqrt{2K_h\Delta t}$ where ξ is a Gaussian random variable with zero mean and unit variance, K_h is the horizontal eddy diffusivity coefficient, and Δt is the time-step (*Taylor*, 1922). Based on sensitivity studies, K_h is set to be homogeneous and isotropic with a value of 10 m^2 s^{-1} (*Riddle and Lewis*, 2000).

5.3.1.2 Biological component ($\vec{u}_B$)

The movement of eels is influenced by local environmental conditions, such as the Earth's magnetic field, light intensity, temperature, salinity and so on. A statistical model was developed to probabilistically simulate the $\vec{u}_B$. The idea is to express the probability density of the swimming velocity at a given time as a mixture distribution:

$$p(\vec{u}_B) = \sum_{i=1}^{m} \alpha_i p_i(\vec{u}_B) \tag{5.2}$$

where p_i is the biological velocity probability distribution for the i^{th} behavior preference. The weighting factors (α_i) determine the relative importance of the i^{th} swimming response at a given time. Thus this statistical model is named as the Multiple Response Movement Model. It should be noted the probability density function $p(\vec{u}_B)$ is a weighted sum of the individual components with $\sum_{i=1}^{m} \alpha_i = 1$ and $0 \leq \alpha_i \leq 1$. In this study, two responses ($m = 2$) of swimming behaviors are implemented: random swimming ($i = 1$) and directed swimming ($i = 2$). A detailed description of the preferred directed swimming is given in the following section.

5.3.1.3 Simulated horizontal swimming behaviors

Several horizontal swimming behaviors are considered to explore their associated pathways in the North Atlantic and listed in Table 5.1. A passive drift is first considered (Exp$_{Drift}$, Table 5.1) in which the v-eels are transported by horizontal ocean currents without active horizontal swimming behaviors. Three active swimming behaviors are evaluated (Table 5.1): (i) random swimming (Exp$_{Rand}$), (ii) true navigation towards a target (core spawning area) in the Sargasso Sea (Exp$_{Navi}$), and (iii) innate compass orientation towards the boundaries of the spawning area in the Sargasso Sea (Exp$_{Ori}$). In Exp$_{Rand}$ ($\alpha_1 = 1$, i.e., 100% of the swimming effort is directed towards random swimming), each v-eel randomly selects a direction at each time-step regardless of the oceanic current direction or the eels position. Mathematically, the distribution of swimming direction [$p(\theta)$] follows a uniform distribution from 0° to 360° [$p(\theta) = \mathrm{U}(0°, 360°)$]. The other two active behaviors have preferred swimming directions (θ_0). The swimming direction at each time-step is sampled from a weighted sum of two uniform distributions with 90% ($\alpha_2 = 0.9$) effort drawn from a preferred directed swimming centred on θ_0 and 10% ($\alpha_1 = 0.1$) effort associated with random searching:

$$p(\theta) = \alpha_1 \mathrm{U}(0°, 360°) + \alpha_2 \mathrm{U}(\theta_0 - \Delta\theta, \theta_0 + \Delta\theta) \tag{5.3}$$

where $\Delta\theta$ represents the spread around the preferred direction. In this study, we set $\Delta\theta = 22.5°$, $\alpha_1 = 0.1$ and $\alpha_2 = 0.9$. The main purpose for implementing some random swimming and a spread is to account for other unresolved biological behaviors and environmental distractions during the eel's migration.

For the true navigation (Exp$_{Navi}$), the preferred swimming direction (θ_0) is directed towards the spawning site and θ_0 is adjusted at each time-step according to the v-eels

current position and the spawning site. This swimming behavior assumes that eels possess an internal map of the Earth's geomagnetic field and have knowledge of the location of the general spawning area. For the compass orientation behavior towards the Sargasso Sea (Exp_{Ori}), the preferred swimming direction (θ_0) is fixed and not adjusted at each time-step. The heading is fixed at 180°T (i.e., to the south) and 217.7°T (southwest) for American eel and European eel, respectively. In this latter behavior, eels migrate towards the boundaries of the spawning area using an innate compass direction. Other orientation mechanism(s) that would allow them to reach the exact location of the spawning site within the Sargasso Sea are not simulated. Therefore, only the success in reaching the boundaries of the spawning area is calculated for this behavior (see below).

5.3.2 Vertical Movement (Diel Vertical Migration)

The DVMs have been observed for both American and European eel species at sea (*Aarestrup et al.*, 2009; *Béguer-Pon et al.*, 2015), in which eels remain in relatively shallow waters at night, while at dawn they make a steep dive to deep waters (up to 1200 m) where they remain for the day before ascending again at dusk. The DVM is implemented in the particle tracking model by considering four vertical specific layers: 50 and 200 m as "surface" layers experienced at night, and 600 and 1000 m as "deep" layers experienced during the day. Thus four combinations of vertical migrations are considered: 50–600, 200–600, 50–1000, and 200–1000 m. In this study, an equal duration of night and day is assumed, which means that a 12 h alternation between surface and deep layers was achieved in the particle tracking model by shifting v-eels vertical position from one layer to the other layer instantaneously. In reality, however, the duration of night and day is not equal, and changes as the eels migrate to the Sargasso Sea by way of seasonal daylight changes and local effects on day length. We also assume v-eels perform horizontal swimming continuously day and night.

Table 5.1: List of horizontal swimming behaviors considered in this study.

Experiments	Migratory behaviors	Description
Exp_{Drift}	Passive drift	No swimming. Carried by ocean currents
Exp_{Rand}	Random direction	Swimming in random direction
Exp_{Navi}	True navigation	Constantly adjust to the spawning area
Exp_{Ori}	Compass orientation towards the Sargasso Sea	South (180°T) for American eel, southwest (217.7°T) for European eel

The heading units are degrees from true north in a clockwise direction (North is 0°T and south is 180°T).

5.3.3 Key Biological Parameters of Eels used in the Model

In this study, three different body lengths of American and European eels are considered, which correspond to the smallest (∼40 cm), the mean size (∼64 cm), and the largest (∼101 cm) silver eels that are usually caught during their downstream migration in Europe and in North America at latitudes that cover the departure locations chosen for our simulations (*Vøllestad*, 1992; *Jessop*, 2010). The largest eels correspond to females (*Krueger and Oliveira*, 1997). Four swimming speeds are also considered in simulations, ranging from a low value (0.5 BL s^{-1}) to a high value (1.5 BL s^{-1}) (Table 5.2). These speed values were previously used in swim tunnel experiments on male and female European eels, and the optimal speed at 18°C was estimated at between 0.7 and 1.0 BL s^{-1} (*van den Thillart et al.*, 2007; *Burgerhout et al.*, 2013a,b).

5.3.4 Energy Expenditure

Silver eels do not feed while migrating and rely on the stored lipids as the main source of energy to accomplish their long spawning migration (*Tesch*, 2003). Based on the field observations and laboratory experiments, the energy expenditure of eel migration can be described as a function of body mass, swimming speed, and a coefficient related to ocean temperature (*Béguer-Pon et al.*, 2016):

$$\Delta E_t = 0.7 \times 10^{-3}(96.62 \times V_t^{2.51} + 0.140256 \times C_T \times MR_t^{0.79}) \times \Delta t \times 18.89 \quad (5.4)$$

where ΔE_t is the energy expenditure (in J g^{-1}) from time t to $t + \Delta t$, V_t is the swimming speed (in BL s^{-1}) at time t, MR_t the remaining body mass (in g) at time t, Δt is the time-step, and C_T a coefficient that takes into account the effect of water temperature on the oxygen consumption rate. The coefficient C_T has three values: 0.5, 1, and 1.6 for temperature below 7.5°C, between 7.6 and 15°C and above 15°C, respectively. Details about the procedure to obtain the above formula for calculating the energy expenditure can be found in *Béguer-Pon et al.* (2016).

5.3.5 Design of Particle Tracking Experiments

The v-eels are released over two 1°×1° areas. One release area is over the Scotian Shelf off the Laurentian Channel in Canada for the American eel, and the other is over the Irish continental shelf for the European eel (Fig. 5.1a). The Scotian Shelf is chosen because of

Table 5.2: Number of scenarios (numerical experiments) conducted with different combinations of parameters.

Values	Ocean currents (NEMO 2004-2005)		(α_1, α_2)		Body length (BL, mm)			Swimming speed (BL s^{-1})				DVM (Top/bottom, m)				Total runs for both species
	On	Off	(1.0,0.0)	(0.1,0.9)	404	637	1016	0.5	0.8	1.0	1.5	50/600	50/1000	200/600	200/1000	
Exp_{Drift}	✓				✓									✓		2
Exp_{Rand}	✓		✓		✓				✓					✓		2
Exp_{Navi}	✓	✓		✓	✓	✓	✓	✓	✓	✓	✓	✓	✓	✓	✓	192
Exp_{Ori}	✓	✓		✓	✓	✓	✓	✓	✓	✓	✓	✓	✓	✓	✓	192
Total number of scenarios																388

Here α_1 is the weighting factor of the random swimming response, while α_2 is the weighting factor of the preferred direction swimming response [Eq. (5.3)].

the potential importance of migrating silver eels from the St. Lawrence system (largest individuals, majority of females, *Jessop*, 2010) and the Irish continental shelf corresponds to areas where satellite tracking studies of eels started or ended (*Aarestrup et al.*, 2009; *Westerberg et al.*, 2014). The spawning area is defined according to *Miller et al.* (2015). In Exp_{Navi}, a target inside the spawning area is assigned for each species (Figs. 5.1 and 5.4). Each target represents the most probable site according to empirical distribution data for the smallest larvae (*Kleckner and McCleave*, 1985; *Miller et al.*, 2015) and supported by the recent modelling work of *Rypina et al.* (2014) for the American eel. For each particle tracking experiment, six successive releases of a patch of 500 particles are performed at a time interval of 5 days, over a period of the migration-departure time window (the month of November for American eels and December for European eels; 6 releases; Fig. 5.1a). This suppresses the dependence of numerical results on the initial release time. The positions of 3000 v-eels (500 particles $\times$ 6 releases) are updated using Eq. (5.1) and tracked for a period of 250 d with a time-step of 3 h for each species. A total of 388 scenarios are considered with a different combination of parameters (Table 5.2). Success is defined as the percentage of particles reaching the boundaries of the global spawning area (all behaviors) and also reaching the specific target within spawning areas (most probable or core spawning site; Exp_{Navi} only). The great-circle distance between the northern boundary of the global spawning area and the specific target within it is $\sim$630 km for American eels and 520 km for European eels. The success rate is calculated at the beginning and end of the spawning season, which are after 107 and 180 d of tracking, respectively, for American eels (mid-February/March and late May), or after 150 and 250 d of tracking, respectively, for European eels (March and late July; *Miller et al.*, 2015). At each model time-step (i.e., every 3 h), the following four key variables are calculated and stored: the oceanic currents, the water temperature, the salinity, and the eels energy expenditure. For each eel species, the ensemble means of these variables from the 3000 particles are calculated for each scenario.

It is known that the tracking results could be sensitive to the number of particles released. A sensitivity study is thus conducted on the number of particles required to achieve statistically stable results. The results suggest that the estimation of success rate is not reliable for the number of particles < 100 and converges for the number of particles $>$ 400 (Fig. 5.3). In consideration of the computational time required for running the 388

scenarios and the disk space needed to store the results, we choose to seed 500 particles for each release in this study (for six different times, i.e., 3000 particles for each scenario).

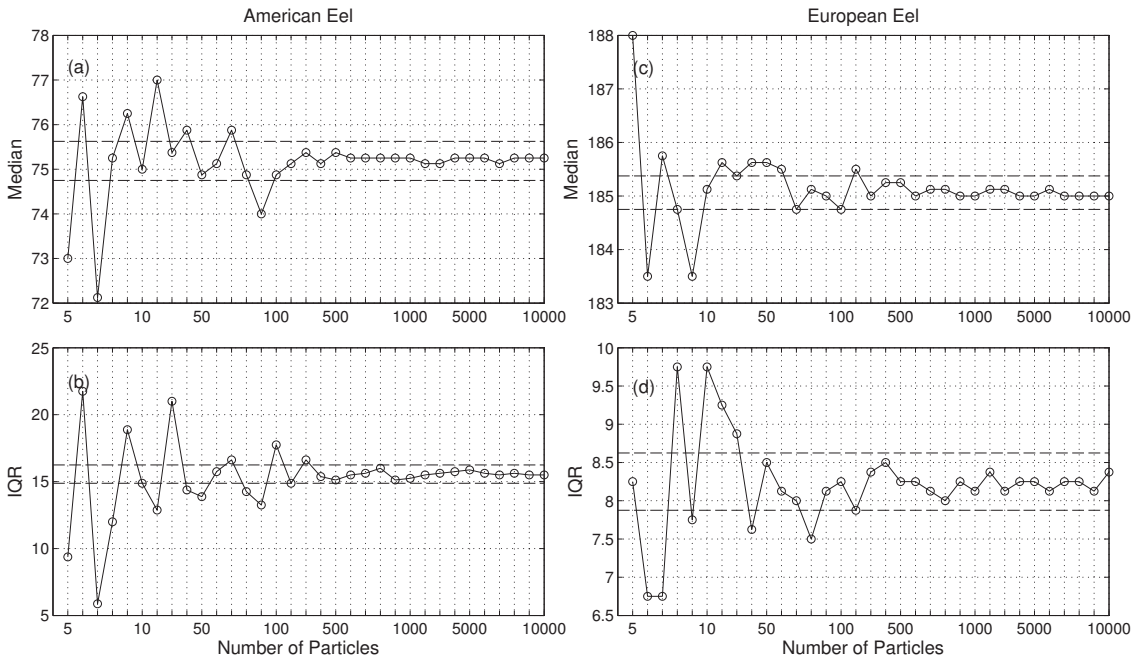

Figure 5.3: Sensitivity of the median and IQR to the number of particles for the American (a, b) and European (c, d) eels. Median is a measure of the time (days since release) when 50% of particles reached the target. IQR (interquartile range) is a measure of the time range (in days) for the percentage of particles that reached the target increasing from 25 to 75. The horizontal dashed-lines in (a) and (c) indicate the times when 48% and 52% of particles reached the target with 10^4 particles initially released. The horizontal dash-lines in (b) and (d) indicate time ranges for the percentage of particles that reached the target increasing from 26 to 74 and 24 to 76, respectively, with 10^4 particles initially released. The medium-size v-eels (BL=637 mm) swimming at 0.5 BL s^{-1} are used in the sensitivity study.

The particle tracking results are quantified by analyzing the v-eel trajectories, success and duration of migration, energy expenditure, and environmental conditions experienced along the migration route. The effect of the flow field on the spawning migration is assessed by comparing the mean success, duration of migration, total distance travelled, and the energy expenditure of scenarios in the presence of the oceanic background current with those scenarios performed in the absence of the oceanic background current independently for the two directed swimming behaviors.

5.4 Particle Tracking Results

5.4.1 Success and duration of Migration

5.4.1.1 Passive drift ($\vec{u}_P$ only)

Figure 5.4a shows v-eel trajectories in the passive drift experiment (Exp$_{Drift}$). Passive v-eels released over the Scotian Shelf are first advected by currents over the shelf break. Some particles spread onto the Shelf. Some particles drift into the open ocean then are advected by the GS to the east. After passing 50°W, some particles drift northeastward with the NAC and some particles move southeastward with the Azores Current. Passive v-eels released off the Irish continental shelf are advected to the northeast by the NAC ($\sim$0.3 m s^{-1} at 200 m, Fig. 5.1c). The results in Exp$_{Drift}$ suggest that none of the passive v-eels released either over the Scotian Shelf or the Irish continental shelf reach the Sargasso Sea after 250 d of tracking (i.e., at the end of the spawning period for European eel) for the four tested ranges of DVM (50/600, 50/1000, 200/600, 200/1000 m).

5.4.1.2 Active swimming behavior ($\vec{u}_P + \vec{u}_B$)

Random swimming (Exp$_{Rand}$):
The trajectories of v-eels with random swimming (Fig. 5.4b) are mainly advected by the oceanic background flow ($\vec{u}_P$), resulting in a general pattern similar to the results of Exp$_{Drift}$ (Fig. 5.4a). The stochastic nature of random swimming ($\vec{u}_B$) is reflected in the fuzziness of each individual trajectory. For the American v-eels, a few are able to escape from the GS and move towards to the northern boundary of the spawning site after 250 d. The v-eels released off Ireland are mainly trapped in the NAC and the Irminger Current. After 250 d, they are far away from the spawning site. The results in Exp$_{Rand}$ suggest that without a preferred swimming direction, the v-eels could not reach the spawning sites in a realistic time window.

Preferred directed swimming (Exp$_{Navi}$ and Exp$_{Ori}$):
The v-eels with directed swimming are able to reach the spawning area (Fig. 5.4c and d). All the v-eels swimming faster than 0.5 and 0.8 m s^{-1} reach target before the beginning of the spawning season for American and European eels, respectively (Figs. 5.5 and 5.6). At the slowest swimming speed tested, 49.1% of the American v-eels reach the target before the end of spawning season, while none for the European eel. On average and at the optimal swimming speed of 0.8 BL s^{-1} (*van den Thillart et al.*, 2007; *Palstra et al.*, 2008), small

American v-eels reach the target within 103 d (range: 77-242 d), medium ones within 64 d (range: 54-162 d), and large ones within 40 d (range: 35-58 d) (Exp_{Navi}), before or at the beginning of the spawning season (Fig. 5.5). For the same scenarios, small European v-eels reach the target at the end of their spawning season (within 206 d; range 191-224 d), the medium v-eels at the beginning of the spawning season (within 129 d; range 121-137 d) and the largest before the spawning season (within 81 d; range: 76-86 d) (Fig. 5.6).

The success and duration of migration are affected by the type of swimming behaviors. For both species, v-eels reach the boundaries of the spawning area earlier on average in Exp_{Ori} than in Exp_{Navi} (Figs. 5.5 and 5.6, Table 5.3). This is mainly due to the travelled distance which is on average greater by 20.5% for American v-eels and by 12.2% for European v-eels in Exp_{Navi} (2346 km compared with 1947 km and 4960 compared with 4422 km).

The success and duration of migration are also affected by the ocean currents, especially for eels migrating at speed ≤ 0.5 m s^{-1} (Tables 5.4, Figs. 5.5 and 5.6). For both species, ocean currents increase the average duration of migration. For instance, the duration of migration of American v-eels swimming at 0.2 m s^{-1} is increased by 11 d on average, reaching 78 d (Table 5.4). However, for American v-eels in both directed swimming experiments, the duration of migration is reduced for a certain proportion of v-eels by 1.2-39 d according to different swimming speeds, indicating that ocean currents could be favorable at some locations (Table 5.4). The ocean currents (e.g., the Gulf Stream) increase the spatio-temporal variability of v-eels in comparison with the scenarios with no background ocean circulation, thus a long tail is evident in the distribution of the number of particles that reach the spawning area for American v-eels swimming at speed ≤ 0.5 m s^{-1} (see the violin plots[3] in Figs. 5.5 and 5.6).

[3] A violin plot is a combination of a box plot and a kernel density plot. Specifically, it starts with a box plot. Then a rotated kernel density plot is added to each side of the box plot (*Hintze and Nelson*, 1998).

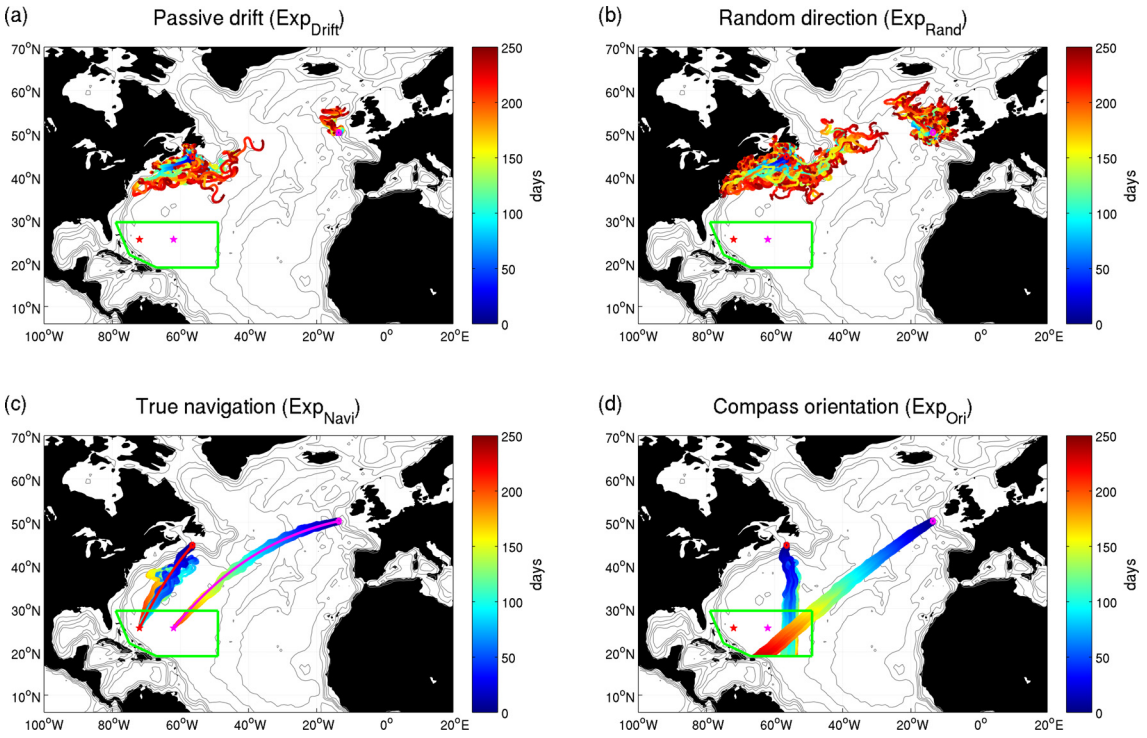

Figure 5.4: Selected v-eel trajectories from four particle tracking experiments (Table 5.1): (a) Passive drift, (b) Random direction, (c) True navigation and (d) Compass Orientation. The v-eels had a body length of 404 mm, a swimming speed of 0.8 BL s^{-1}, and made DVMs between 200 and 600 m. In each tracking experiment, 3000 virtual eels were tracked for each species. For clarity, 1200 v-eel trajectories were randomly selected for each species and plotted. The red and magenta squares indicate the initial release areas for American and European eels, respectively. The green polygon is the spawning area in the Sargasso Sea. The red and magenta stars indicate locations where the smallest American and European eel larvae were found, respectively. The red and magenta lines connecting the squares and starts in (c) indicate v-eel trajectories without background oceanic currents, which are the great-circle (shortest) lines.

Table 5.3: Overall success of the tested scenarios (taking into account the oceanic circulation). (Adapted from *Béguer-Pon et al.*, 2016)

		Behavior		
		Ture navigation		Orientation towards Sargasso Sea
	Species	To target inside spawning area	To limits of spawning area	To limits of spawning area
Success[a] at the beginning of the spawning season	American v-eel	87.1 (0-100)	90.2 (7.4-100)	99 (90.6-100)
	European v-eel	33.3 (0-100)	34.6 (0-100)	50 (0-100)
Success[a] at the end of the spawning season	American v-eel	94.9 (49.8-100)	96.8 (69.5-100)	100 (99.7-100)
	European v-eel	91.7 (0-100)	91.7 (0-100)	93.1 (17.6-100)
Duration of migration (d)	American v-eel	97 (19-250)	86 (15-250)	68 (15-250)
	European v-eel	119 (40-225)	106 (35-203)	99 (35-175)
Distance travelled (km)	American v-eel	3886 (2752-7160)	3391 (2294-6640)	2472 (1942-3447)
	European v-eel	5838 (5012-6949)	5028 (4420-6243)	4619 (4131-5151)
Percentage of energy spent for transportation	American v-eel	24.5 (15.5-47.7)	20.5 (12.9-40.2)	17.6 (9-35.8)
	European v-eel	44.6 (27.6-81.3)	40.4 (24.7-75.1)	34.7 (21-67.8)

Means with ranges (min-max) are reported.

[a]Percentage of particles reaching the limits of the spawning area or the target inside the spawning area.

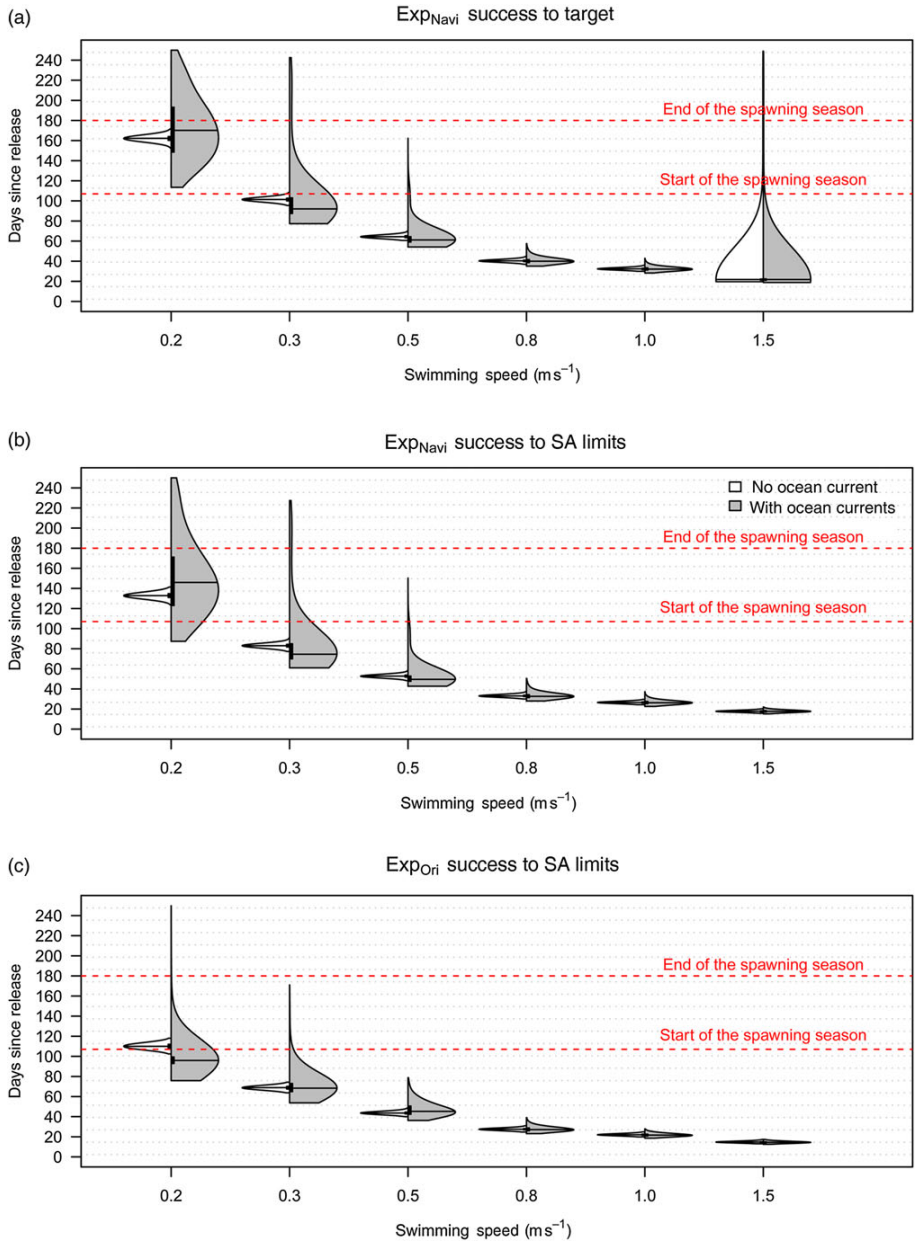

Figure 5.5: Distribution of the transit time of American v-eels travelling from the release site to the target inside the spawning area (SA) (a) or to the boundaries of the spawning area (b) and (c). Results according to two active behaviors and various swimming speed values are shown. Violin plots are a combination of a box plot and kernel density plot which reveals important information about the distribution of data. Horizontal expansions of the violin plots are relative to the percentage of particles that reach the spawning area. (Adapted from *Béguer-Pon et al.*, 2016)

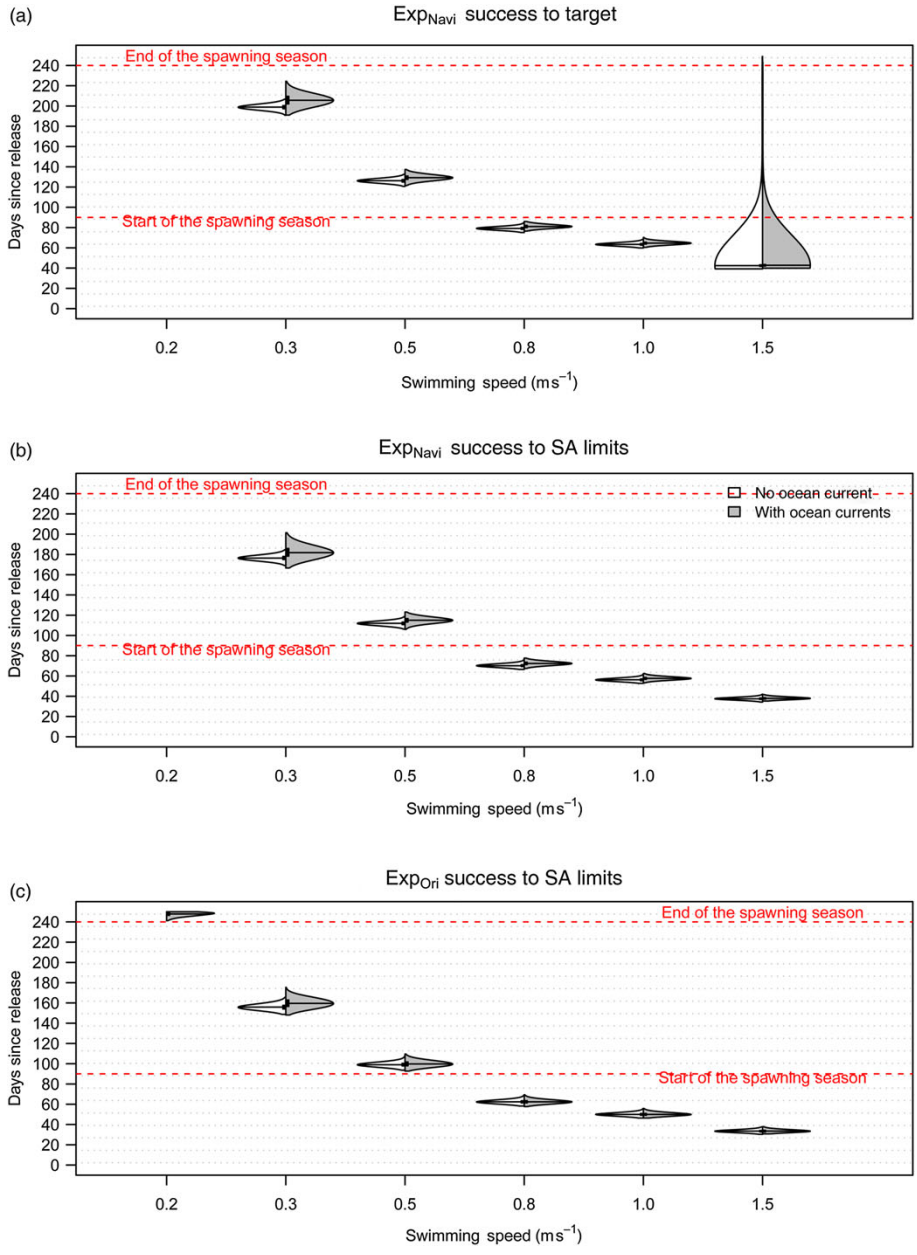

Figure 5.6: Distribution of the transit time of European v-eels travelling from the release site to the target inside the spawning area (SA) (a) or to the boundaries of the spawning area (b) and (c) according to two active behaviors and various swimming speed values. Otherwise as in Fig. 5.5. (Adapted from *Béguer-Pon et al.*, 2016)

Table 5.4: Summary of effects of ocean currents on the simulated spawning migration of v-eels from North America and Western Europe. (Adapted from *Béguer-Pon et al.*, 2016)

		Sws in true navigation (to target) (m s^{-1})			Sws in orientation towards Sargasso Sea (to limits of spawning area) (m s^{-1})		
Effect on	Species	0.2[a]	0.5	1.0	0.2[a]	0.5	1.0
Duration of migration	American	+11 d (-39,+78 d)	+3.2 d (-6.5,+92 d)	+0.25 d (-1.8,+7.0 d)	+14 d (-26.6,+131.8 d)	+1.7 d (-3.8,+30 d)	+0.38 d (-1.2,+3.0 d)
	European	+6.8 d (-0.1,+17.8 d)	+3.0 d (-0.8,+4.8 d)	+1.2 d (-0.6,+2 d)	+3.8 d (-0.6,+9.8 d)	+0.8 d (-0.9,+1.9 d)	NS
Mean total travelled distance	American	+40.9% (-16.6,+135%)	+7.3% (-33.1,+154%)	+1.5% (-15,+21.9%)	+15.2% (-4.6,+79.6%)	+7.8% (-31.4,+59.2%)	+0.7% (-13.6,+16.6%)
	European	+2.9% (-3.3,+8.7%)	+1.4% (-1.7,+3.5%)	+0.7% (-0.9,+2%)	+1.6% (-10.4,+4.4%)	+0.8% (-0.2,+2.5%)	NS
Total energy cost	American	+6.3% (-24.6,+43.8%)	-0.9% (-9.8,+11.1%)	NS	-11.2% (-23.9,+103%)	+7.8% (-8.2,+71.7%)	NS
	European	+2.8% (0,+7.1%)	+1.6% (+0.4,+2.2%)	NS	NS	NS	NS

Differences between average values for scenarios with ocean circulation and for those without ocean circulation are reported if statistically significant (otherwise NS is reported). Ranges are also reported: they are the difference between maximal or minimal values calculated for scenarios with and without ocean circulation. For instance: America v-eels swimming at 0.2 m s^{-1} travel on average 11 more days because of the ocean circulation, but this delay of migration can be reduced by 39 d or increased by 78 d.

[a] 0.3 m s^{-1} for European eels since no v-eels were able to reach the spawning area before the end of the tracking period (250 d).

5.4.2 Energy Expenditure

Table 5.3 listed the energy expenditure of v-eels successfully reaching the limits of the spawning area or the target inside the spawning area. The percentages of energy expenditure are all less than 100%, indicating that the v-eels have enough energy reserve to spend on migration. The American v-eels spend an average of 24.5% (max of 47.7%) of energy to reach the spawning site (target, Exp_{Navi}) while the European v-eels require 44.6% (max of 81.3%). The swimming behavior affects the energy spent for reaching the boundaries of the spawning area. For American v-eels, 20.5% of energy is spent in true navigation behavior experiments (Exp_{Navi}) while 17.6% in compass orientation behavior experiments (Exp_{Ori}). For European v-eels, 40.4% of energy is spent for Exp_{Navi} while 34.7% for Exp_{Ori}. The effects of ocean currents on the energy expenditure are also listed in Table 5.4. For American v-eels, the ocean currents have significant effect on their energy expenditure only for swimming speed at 0.5 m s^{-1} or less. For example, the energy expenditure for reaching the boundaries of the spawning area in compass orientation behavior experiments is reduced 11.2%, increased 7.8% and no significant changes for swimming speed at 0.2, 0.5 and 1.0 m s^{-1}, respectively. For European v-eels, the ocean currents have relatively small effect on the energy expenditure. Even for the v-eels swimming at the lowest speed (i.e., 0.2 m s^{-1}), the additional energy expenditure due to ocean currents is only about 2.8%.

5.4.3 Environmental Conditions Experienced along the Migration Route

5.4.3.1 Oceanic currents

The oceanic currents experienced by the American eels and European eels reaching the spawning area are significantly different as illustrated in Figs. 5.7 and 5.8. American v-eels encounter the strongest currents during the first half of their journey (up to 0.7 m s^{-1}) as they cross the Gulf Stream (GS). For individual American v-eels, the effect of the GS leads to significantly different trajectories. The v-eel can be trapped in the GS rings (Fig. 5.7b) and the v-eel could also take advantage of the strong meandering current in the GS moving towards the Sargasso Sea (Fig. 5.7c). European v-eels experience weak currents ($<$0.1 m s^{-1}) during the first 1500 km of their journey and strong flow in the Azores Current. For individual European v-eels, the oceanic currents experienced are relatively weak, resulting in similar migratory trajectories (Fig. 5.8).

5.4.3.2 Temperature

The temperature experienced by v-eels varies as they perform DVM at different depths vertically and migrate from the coast to the Sargasso Sea horizontally (Fig. 5.9). Four DVM ranges are considered in the particle tracking model: 50–600, 200–600, 50–1000, and 200–1000 m. As expected, the temperature experienced by v-eels is colder at deeper DVM depth. For American v-eels, the sharp Gulf Stream front can be seen about 500 km from the release site. Beyond the Gulf Stream, the temperature at all DVM layers remained nearly constant. For European v-eels, the temperature gradually increases throughout the migration path at 50 and 200 m depths. A subsurface front can be seen about 3000 km from the release site at 600 m depth. For both species, the temperature at 50 m depth increases more rapidly at the end of the journey, due to the development of the seasonal thermocline in summer in the Sargasso Sea.

5.4.3.3 Salinity

The salinity experienced by v-eels also varies as they perform DVM at different depths vertically and migrate from the coast to the Sargasso Sea horizontally (Figs. 5.10 and 5.11). For American v-eels, two regions with different vertical salinity profiles are evident: one is on the continental shelf, the other is in the open ocean. The salinity increased with DVM depth on the shelf due to the freshwater inputs from the coast, while the salinity decreased with DVM depth in the Sargasso Sea and adjacent open ocean due to excessive evaporation. The salinity has a sharp increase of $\sim$2 psu at 500 km from the release site in the Gulf Stream. The salinity is almost constant beyond Gulf Stream. For European v-eels, the salinity decreases with DVM depth. The salinity at 50 and 200 m depths increases from about 35.5 psu to about 37 psu as the v-eels approaching to the Sargasso Sea. While the salinity at 1000 m is almost constant in the Sargasso Sea and adjacent open ocean.

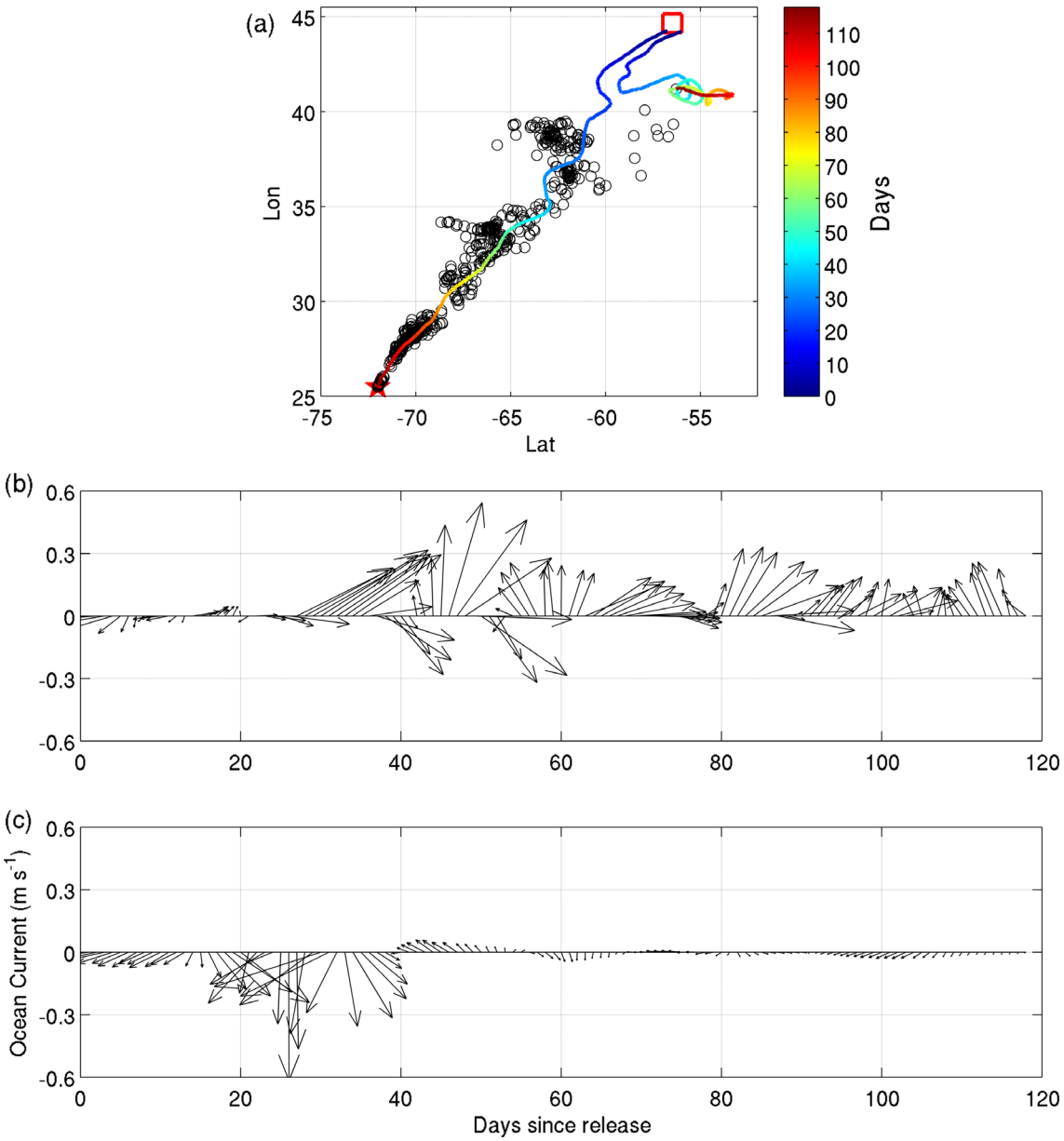

Figure 5.7: Trajectories (a) and ocean currents experienced by American v-eels farthest (b) and closest (c) to the target location (red star). The v-eels (BL = 404 mm, Sws = 0.5 BL s^{-1}) were released on 1 November. On day 118 since release, the first v-eel reached the target location. The locations of v-eels on day 118 are plotted as black circles along with the farthest and closest trajectories in (a).

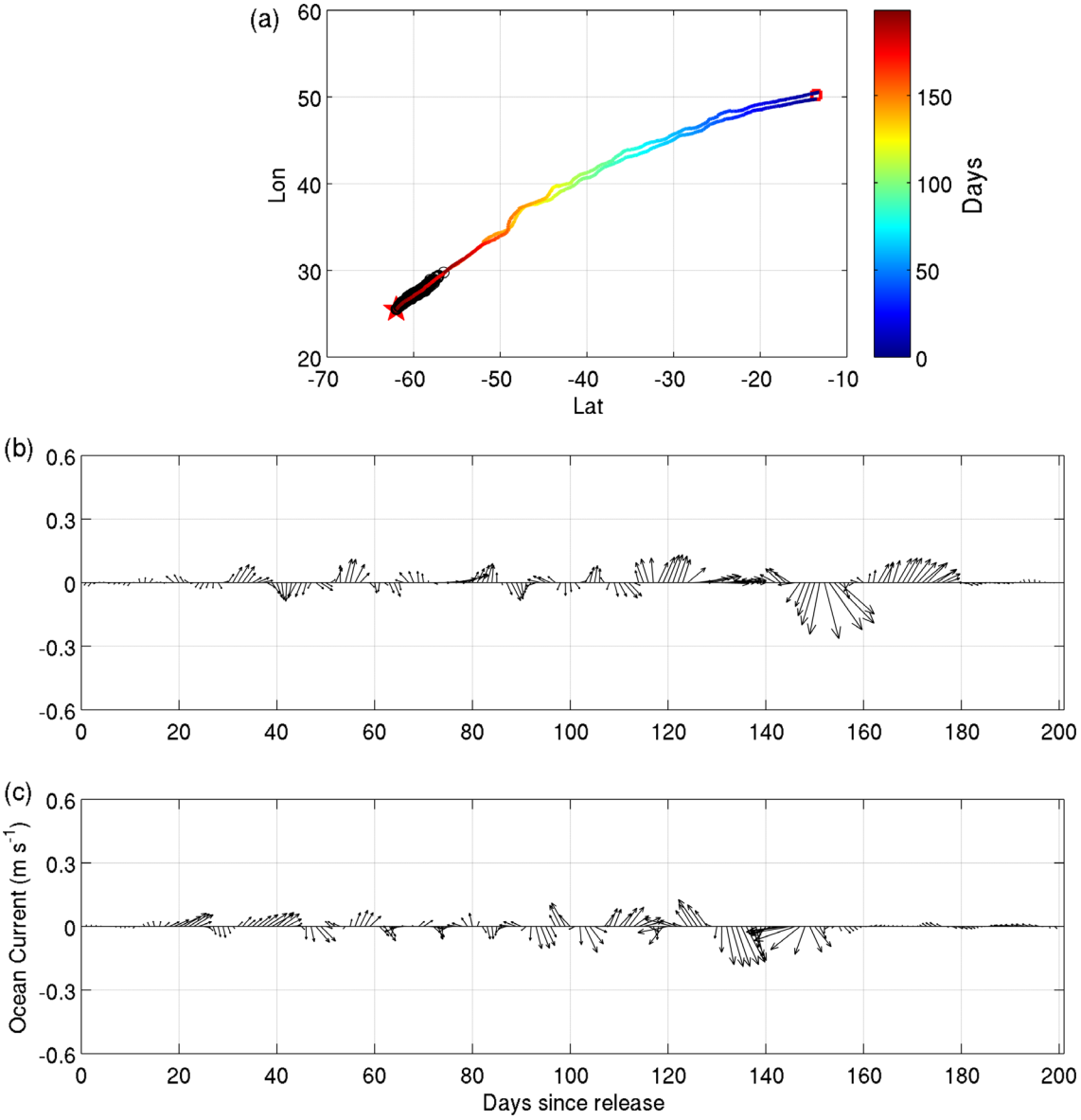

Figure 5.8: Trajectories (a) and ocean currents experienced by European v-eels farthest (b) and closest (c) to the target location (red star). The v-eels (BL = 637 mm, Sws = 0.5 BL s^{-1}) were released on 1 December. On day 199 since release, the first v-eel reached the target location. The locations of v-eels on day 199 are plotted as black circles along with the farthest and closest trajectories in (a).

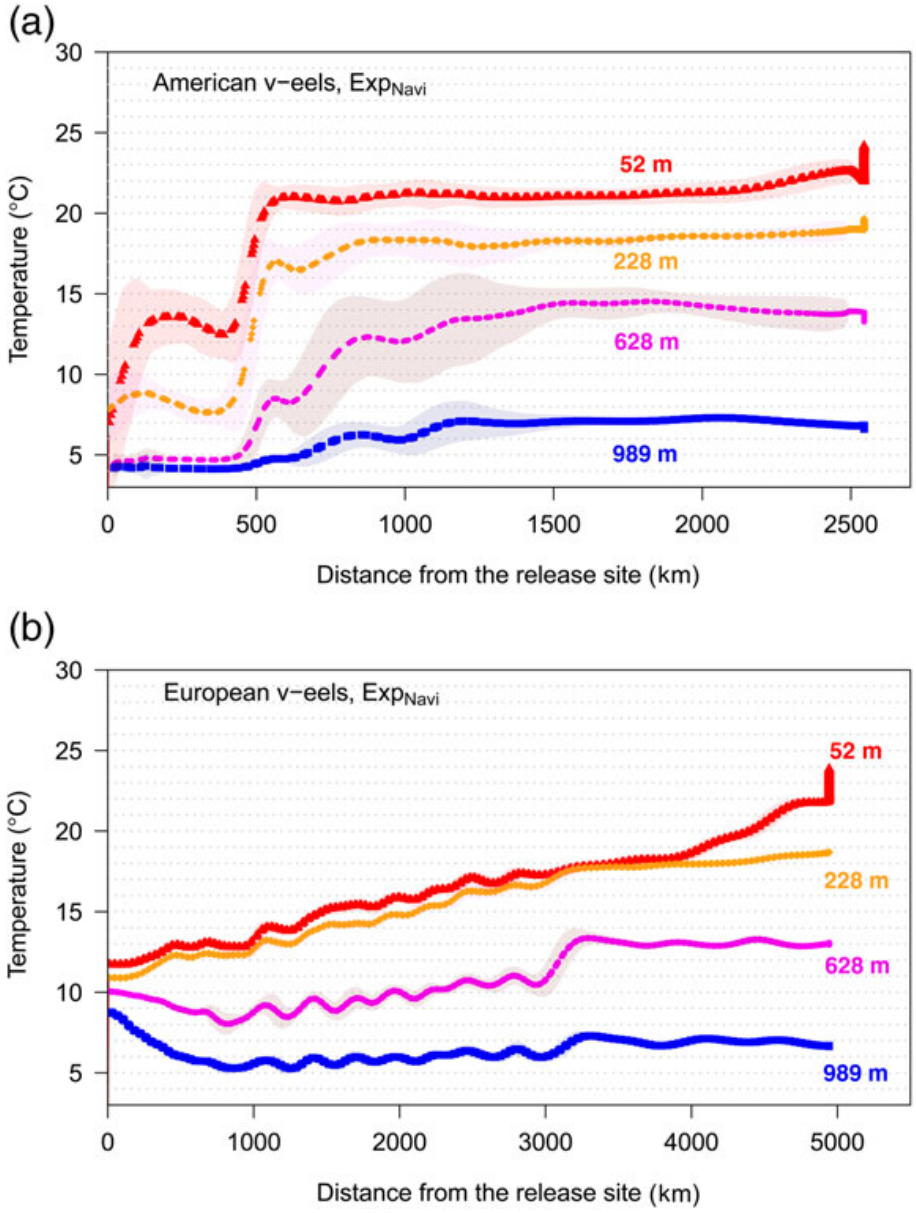

Figure 5.9: Mean water temperature experienced by v-eels during their migration routes with true navigation from the North American coast (a) or from the Northwestern European coast (b) to the Sargasso Sea at various depths. The shaded areas represent the standard deviation around the mean. The sharp decrease or increase at the end of the tracking was due mainly to the local change of temperature, particularly for the depth (52 m) close to the surface. (Adapted from *Béguer-Pon et al.*, 2016)

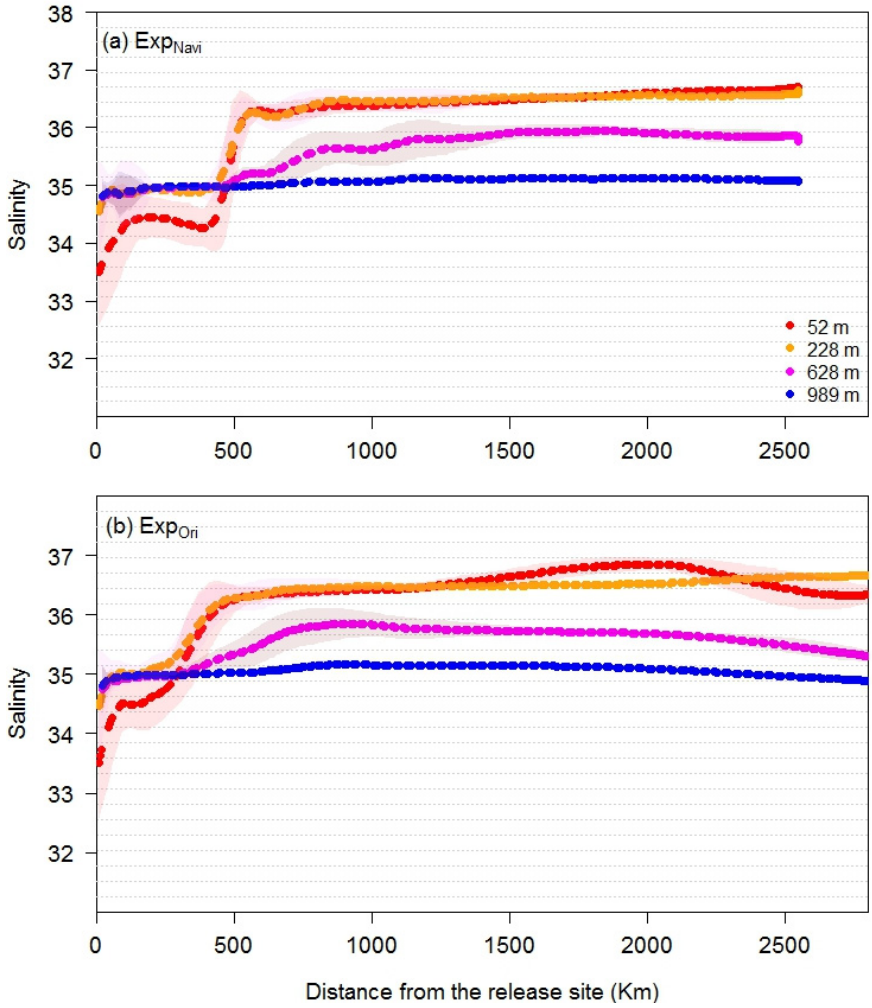

Figure 5.10: Mean salinity experienced by v-eels migrating from the North American coast to the spawning area in the Sargasso Sea according to two horizontal behaviors and at various depths. The shaded areas represent the standard deviation around the mean. (Adapted from *Béguer-Pon et al.*, 2016)

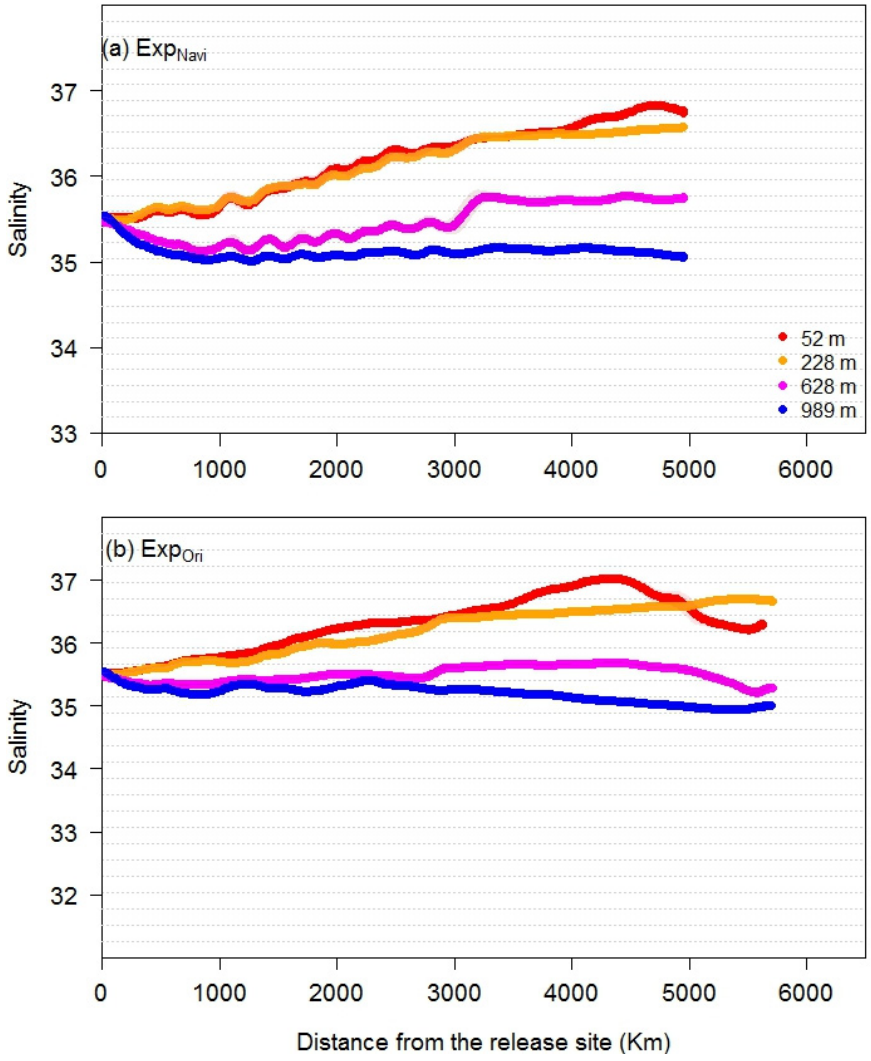

Figure 5.11: Mean salinity experienced by v-eels migrating from the Northwestern European coast to the spawning area in the Sargasso Sea according to two horizontal behaviors and at various depths. The shaded areas represent the standard deviation around the mean. (Adapted from *Béguer-Pon et al.*, 2016)

5.5 Implications for Eel Migration

The numerical particle tracking experiments presented in this chapter demonstrated that orientated swimming behavior is required for the eels to reach the spawning area. The v-eels drifting with oceanic currents or swimming in random directions are not able to reach the spawning area in time for spawning, while v-eels with orientated swimming behaviors are able to reach the spawning area in time. The two orientated swimming behaviors explored in this study can be considered as simple parameterizations of eel sensing the Earth's magnetic field. Further laboratory and field studies will be required to provide new insights on how silver eels use the Earth's magnetic field during their seaward migration in the open ocean. The Multiple Response Movement Model (Eq. (5.2)) proposed in this study can be revised accordingly to accommodate more complex swimming behaviors.

Based on the various body lengths and swimming speeds examined in this study, we identified that only the smallest (40 cm) European v-eels swimming at the lowest swimming speed (0.5 BL s^{-1}) are unable to reach the spawning area in time. Nearly 50% of the smallest American v-eels swimming at the lowest swimming speed reach the spawning area before the end of the spawning season (Exp_{Navi}), whereas none of the European v-eels navigating at this minimum speed complete their migration before the end of the spawning season (Figs 5.5 and 5.6).

The results of particle tracking experiments with and without ocean current ($\vec{u}_P$) demonstrated that the ocean circulation affects the eel migration, particularly for the American v-eels at lowest swimming speeds (Table 5.4). The presence of strong ocean currents (e.g., Gulf Stream) can deflect or even temporarily trap v-eels at low swimming speed, which would in turn increase the duration of migration and total travelled distance.

Both the current and temperature experienced along the migration paths revealed in this study have implications for eel's DVM. Four vertical specific layers were considered in this study: 50 and 200 m as "surface" layers experienced at night, and 600 and 1000 m as "deep" layers experienced during the day. The ocean currents at 600 and 1000 m are weaker than at 50 or 200 m in general over the North Atlantic. Thus a deeper swimming depth would be favorable to the eel migration. As expected, additional tracking experiments demonstrated 100% of American v-eels without DVM swimming at 0.5 m s^{-1} at 1000 m depth reaching the spawning sites within 70 d and 163 d if swimming at 200 m depth. However, the temperatures at 1000 m are below 10°C, which would be too cold to complete

maturation. As suggested by laboratory experiments, temperature < 10°C can postpone the maturation process (*Boëtius and Boëtius*, 1980; *van Ginneken and Maes*, 2005) and the final thermal preferendum of sexually mature American eel has been established at around 17.5°C (*Haro*, 1991; *van Ginneken and Maes*, 2005). It should be noted that the 17.5°C corresponds to the temperature at about 200 m depth in the spawning area, which implies that eels are likely to spawn at 200 m depth at night.

The results of particle tracking experiments indicated that energy is not a limiting factor for eel's seaward migration. The maximum energy expenditure is 48 and 82% for American and European v-eels, respectively (Table 5.3). The energy expenditure of eel migration is calculated as a function of body mass, swimming speed, coefficient related to the sea water temperature. The energetic cost associated with DVM is complicated and difficult to estimate, thus is not considered in this study.

5.6 Summary

A biophysical particle tracking model was used in this chapter to simulate the oceanic migration of American and European silver eels from two release areas: off the Scotian Shelf (Canada) and off the Irish continental shelf. In this collaborative work, I was the principal contributor for the model implementation and simulation, and associated description and discussion in the joint paper entitled "Exploring the role of the physical marine environment in silver eel migrations using a biophysical particle tracking model". Several swimming behaviors were considered including: passive drift, random swimming, true navigation to specific spawning sites and innate compass orientation towards the spawning area in the Sargasso Sea. I developed the statistical model to probabilistically simulate the eel's swimming behaviors by expressing the probability density of the swimming velocity at a given time as a mixture distribution. Several combinations of swimming speeds and depths were also examined. The effects of ocean circulation on resulting migratory pathways of virtual eels (v-eels), environmental conditions experienced along their oceanic migration, and energy consumption were assessed. Simulations show that orientated swimming behavior is required for the eels to reach spawning area in time. The presence of ocean currents increases the duration of migration and travelled distances, particularly for American v-eels at low swimming speed. The current, temperature and salinity experienced along the migration paths were revealed. Model results also suggest

that energy would not be a limiting factor.

CHAPTER 6

CONCLUSIONS

My doctoral research combined the Eulerian and Lagrangian models to study the circulation and hydrography on the Scotian Shelf and adjacent deep waters of the North Atlantic with biological implications on wide spatial scales ranging from small scale (10 km) to basin scale (10^3 km). For the Sable Gully, the model results suggest that the circulation is significantly affected by the tide-topography interaction, wind-driven circulation, and shelfbreak jet. The knowledge gained about the three-dimensional (3D) circulation in the Gully can be used in developing an effective management plan for the Gully Marine Protected Area. The role of small-scale bathymetric features (e.g., Cape Sambro and Sambro Ledges) in realistically simulating the sea surface temperature (SST) and current suggests that high-resolution models are required to simulate the movement of marine animals (e.g., Atlantic salmon) in the coastal region. The coupled biophysical particle tracking model developed for tracking eel's migration is a useful tool that can complement ongoing field tracking experiments and help lead to a better understanding of the eels seaward migration. A statistical model was also developed to probabilistically simulate the eel's swimming behaviors by expressing the probability density of the swimming velocity at a given time as a mixture distribution. The expertise gathered in the present work can be used to develop similar models for other regions and species. The biological behavior could vary significantly among different species, the need for collaborations between researchers in physical oceanography and marine biology continues to grow.

6.1 Main Results and their Significance

This thesis studied the circulation and hydrography on the Scotian Shelf and adjacent deep waters of the North Atlantic and examined their implications for the marine animal distribution and migration. Three geographic regions with different spatial scales and three representative species were selected and investigated: (1) Sable Gully and northern bottlenose whale (Chapter 3), (2) central Scotian Shelf adjacent to Halifax and Atlantic salmon (Chapter 4), (3) North Atlantic and American and European eels (Chapter 5). The main results for the above three research subjects are summarized below.

The numerical ocean circulation models developed in this study, DalCoast-Gully and DalCoast-CSS, represent the latest advancement of the multi-nested version of DalCoast, which is state-of-the-art nested-grid modelling systems for the Scotian Shelf and adjacent deep waters. To date, the relocatability of DalCoast, by using a one-way nesting technique, allowed us to achieve high-resolution simulation of circulation and hydrography over four scientifically and socio-economically important marine areas of Nova Scotia: Lunenburg Bay (DalCoast-LB, *Yang and Sheng* (2008)), Halifax Harbour (DalCoast-HFX, *Shan et al.* (2011)), Sable Gully (DalCoast-Gully, Chapter 3), and central Scotian Shelf adjacent to Halifax (DalCoast-CSS, Chapter 4).

The time-dependent, spatially varying physical environment of the Sable Gully was constructed by employing a nested-grid ocean circulation model and a particle tracking model in Chapter 3. Circulation and hydrography over the Sable Gully and adjacent waters in the year of 2006 were reconstructed using a newly developed ocean circulation model (DalCoast-Gully). Based on the 3D current field produced by DalCoast-Gully, particle tracking experiments were conducted both forward and backward in time to examine the particle pathway, upstream and downstream areas, and residence time of the Sable Gully. The modelled circulation and hydrography in the Sable Gully and adjacent waters were shown to have significant temporal and spatial variability. An analysis of the along-canyon volume transport suggested that on the annual mean timescale, tidal residual is the primary contributor to the on-shelf transport of the slope water into the Gully. The e-folding residence time is about 7 and 13 days in February and August 2006, respectively, estimated from the movements of particles released at the depth of the Gully rim and tracked forward in time. The particle movements from tracking experiments with and without tides suggested that tidal circulation reduces the residence time in the

Gully, particularly along the Gully flanks. The implications of oceanic circulation for the distribution and migration of northern bottlenose whale in the Gully and adjacent canyons were discussed. Although 3D circulation in the Gully discussed in this study may not have direct impact on the distribution and migration of northern bottlenose whale, the circulation could play an important role in advecting whale's prey (e.g., squid) into the Gully.

Circulation and hydrography on the central Scotian Shelf adjacent to Halifax were discussed in Chapter 4. Similar to Chapter 3, a nested-grid ocean circulation model (DalCoast-CSS) was used. The model performance was assessed extensively against observations, including satellite remote sensing data from GHRSST and Aquarius and *in-situ* measurements taken by tide gauges, a marine buoy, ADCPs and CTDs. It was shown that the simulated tidal and non-tidal sea levels were in good agreement with tide gauge observations, the simulated monthly-mean sea surface temperature and salinity were in fair agreement with satellite remote sensing observations, and the simulated daily-mean sea surface temperature outside Halifax Harbour were similar to the observed daily to seasonal variations. The nested-grid model was also able to capture the synoptic variability of the Nova Scotia Current transport. The satellite remote sensing data of sea surface temperatures revealed that the Atlantic side of Nova Scotia is occasionally surrounded by cold surface waters in summer, which is due to tidal mixing and wind-driven coastal upwelling. In this study, these physical processes contributing to the formation of those cold water regions were investigated based on model results in three numerical experiments using DalCoast-CSS. The model results confirmed that the formation of cold water in the Bay of Fundy and off Cape Sable is due mainly to tidal mixing and topographical upwelling. The model results also indicated that the cold water along the south shore of Nova Scotia is a result of wind-driven coastal upwelling as expected. In addition, the temporal and spatial evolution of coastal upwelling in the central Scotian Shelf adjacent to Halifax was discussed by using various observations and DalCoast-CSS. The roles of irregular coastline and topography in coastal upwelling were investigated by contrasting the results from a suite of model runs differing only in the specification of coastline and topography. This process study demonstrated that irregular coastline (e.g., cape) has a scattering effect to the along-shore wave propagation of the filaments and irregular topography (e.g., submerged bank) can influence the further offshore development of

filaments. The implications of circulation and hydrography on the Scotian Shelf for the Atlantic salmon migration were also discussed. The abnormal warm (cold) sea surface temperature on the Scotian Shelf and adjacent waters could force an earlier (later) migration of the Atlantic salmon. The Nova Scotia Current and associated seasonal and interannual variability may play an adverse role during the postsmolts migration by influencing their energy expenditure and migration duration. The role of small-scale bathymetric features (e.g., Cape Sambro and Sambro Ledges) in realistically simulating the SST and current suggests that high-resolution models are required to simulate the movement of salmon in the coastal region.

The effect of the general oceanic circulation on the seaward migration of American and European eels from coastal waters to the Sargasso Sea was quantified by employing a biophysical particle tracking model in Chapter 5. This newly developed model tracks virtual eels (v-eels) in a quasi 3D fashion to include background ocean currents, various swimming behaviors and diel vertical migration (DVM). The oceanic currents, temperature, salinity and energy expenditure are also recorded along the eel's migration route. The effects of ocean circulation on migratory pathways of v-eels, environmental conditions experienced along their oceanic migration, and energy consumption were assessed. Simulations show that orientated swimming behavior is required for the eels to reach the spawning area in time. The presence of ocean currents increases the duration of migration and travelled distances, particularly for American v-eels at low swimming speed. The current, temperature and salinity experienced along the migration paths are revealed. Model results also suggest that energy would not be a limiting factor.

6.2 Future Work

With the observational database growing and computational technologies improving, the following improvements and breakthroughs could be expected.

The modelling system for the Sable Gully (DalCoast-Gully) presented in Chapter 3 is ready to be further developed to run operationally in supporting the Marine Protected Area management, oil-gas operation in the adjacent waters, and the field observations of marine animals (e.g., whales in the Gully and seals around the Sable Island). DalCoast-Gully shares a similar modelling framework of the operational circulation model for the Halifax Harbour (DalCoast-HFX, `http://extrememarine.ocean.dal.ca/dalcoast`).

The experiences and tools gained in developing DalCoast-HFX are applicable to DalCoast-Gully. There are still many important scientific questions related to the physical processes in the Gully that require further observational and modelling studies. For example, more work is needed to improve the model skill in capturing the amplification of tidal current ellipses towards bottom (*Swart et al.*, 2011). The near bottom amplifications of M_2 and K_1 are most likely due to the bottom trapped internal tides and internal waves, which could not be simulated well by the model due mostly to the model horizontal and vertical resolution. A future research direction is to nest a high-resolution non-hydrostatic circulation submodel in DalCoast-Gully in order to explicitly resolve internal waves and internal tides in the regioin. In addition, the simulated cold intermediate layer (CIL) and warm intermediate layer (WIL) were too diffusive for which the exact reasons are unknown. Possible explanations include the coarse horizontal resolution of the NCEP reanalysis dataset used in calculating the net heat flux in the model, the seasonal climatology used in the large-scale northwest Atlantic submodel, and the vertical mixing parameterization used in the model.

The modelling system for the central Scotian Shelf adjacent to Halifax (DalCoast-CSS) presented in Chapter 4 has many potential applications for future studies concerning the physical environmental conditions over coastal and shelf waters of Nova Scotia. Firstly, the results produced by the DalCoast-CSS can be used in specifying better open boundary conditions for the operational circulation forecast system for Halifax Harbour, which is supported by MEOPAR (`http://meopar.ca`) as a part of an integrated ocean observation and prediction system. Secondly, DalCoast-CSS can be used to provide detailed physical oceanic environmental conditions for the studies of marine animal migration and distribution on the Scotian Shelf.

For both DalCoast-Gully and DalCoast-CSS, two-way nesting, coupling with atmosphere/wave/ice models, and assimilating observations are three important research directions in the future. Firstly, two-way nesting is a more advanced nesting technique than the one-way nesting used in this thesis. In one-way nesting, the results of the coarse-resolution larger domain submodel (LM) are used in specifying the open boundary conditions of the fine-resolution smaller domain submodel (SM) without any feedback from the SM to LM. In two-way nesting, the SM results are also fed back to the LM, which could lead to

performance improvements in both LM and SM. Secondly, coupling DalCoast with atmosphere/wave/ice models can simulate more accurately the physical processes in the upper ocean including the atmospheric conditions during storms, the wave-induced mixing, and heat and salt fluxes. Thirdly, assimilating observations into DalCoast can further improve the model performance. In this thesis, *in-situ* and satellite remote sensing observations on the Scotian Shelf and adjacent deep waters were used to assess the performance of DalCoast. Recently, a CODAR (Coastal Ocean Dynamics Applications Radar) system was constructed and came into operation as a part of the MEOPAR project. The CODAR system is centred to the shelf waters off Halifax and provides real-time surface ocean currents up to 200 km off the coast, which is the similar area covered by the submodel L3 of DalCoast-CSS. Assimilating the real-time CODAR currents could be a key component to forecast ocean conditions operationally in this region by using DalCoast-CSS in the future.

The biophysical particle tracking model used to simulate the seaward migration of eels in Chapter 5 can be refined in both its physical and biological components. Firstly, the physical circulation model used in the study is able to capture the mean and variation of the flow field (*Higginson et al.*, 2011). However, the models horizontal resolution is relatively coarse. The flow fields from a finer horizontal resolution model could have stronger mean currents and more small-scale features (e.g., eddies), which can lead to faster transit time and more complicated trajectories (*Blanke et al.*, 2012). The physical component will benefit from the improved 3D circulation and hydrography fields provided by the global operational circulation models (e.g., NEMO, `http://marine.copernicus.eu` and HYCOM (HYbrid Coordinate Ocean Model), `http://hycom.org`). The increased spatial resolution and extended temporal coverage of these oceanic fields would empower us to conduct simulation on a longer time scale to assess the climate change impact on the eel migration. Secondly, the biological component modelling the swimming behavior will benefit from the growing observations of eel migration. Ongoing satellite telemetry studies are currently refining our limited understanding of the spawning migration of American and European eels. For instance, recently one American eel was tracked to the edge of its spawning area (i.e., Sargasso Sea) (*Béguer-Pon et al.*, 2015) and European eels were tracked from Mediterranean Sea through Gibraltar Strait to the Atlantic Ocean (*Amilhat et al.*, 2016). The migratory behaviors extracted from these new observations

can be incorporated into the biological component. The biophysical particle tracking model with a more realistic biological component will provide a better estimates of energy expenditure and migratory success, and potentially be used to test hypotheses about the observed population decline in both eel species.

APPENDIX A

CIRCULATION MODEL

The ocean circulation modelling system used in my doctoral research was modified from the circulation modelling system developed previously for two coastal waters along the Nova Scotia coast: Lunenburg Bay (DalCoast-LB, *Yang and Sheng*, 2008) and Halifax Harbour (DalCoast-HFX, *Shan et al.*, 2011). Both DalCoast-LB and DalCoast-HFX were extensively validated against observations. In my doctoral research, the modelling system of DalCoast-HFX is relocated to two study areas: the Sable Gully and the central Scotian Shelf adjacent to Halifax. As a result, the latest model setups are named as the DalCoast-Gully and DalCoast-CSS, respectively. The main advantage of the multi-nested model is that small-scale circulation features can be resolved by the finest-resolution submodel driven by dynamically consistent open boundary conditions provided by larger domain, coarser resolution submodels.

A.1 DalCoast-Gully

The circulation model used for Chapter 3 is DalCoast-Gully, which has five submodels with progressively smaller model domains and finer horizontal resolutions covering from the northwest Atlantic to the Sable Gully. The two outer-most submodels, L1 and L2, are based on DalCoast (*Thompson et al.*, 2007) and constructed from the Princeton Ocean Model (POM, *Mellor*, 2004). Submodels L3 to L5 are based on the free-surface version of CANDIE (*Sheng et al.*, 1998), which is a three-dimensional (3D), primitive equation ocean circulation model that uses an A-grid, z-level and fourth-order advection scheme. The outer-most submodel L1 is a 2D barotropic storm surge model covering the eastern Canadian shelf from the Labrador Shelf to the Gulf of Maine with a horizontal resolution

of 1/12°. Submodel L2 is a 3D prognostic model with horizontal resolutions of 1/16° and 30 σ-levels in the vertical. Submodels L3 to L5 are also 3D and prognostic with horizontal resolutions of $\sim$2 km, $\sim$1 km and $\sim$500 m, respectively.

The modelling system is driven by tides, atmospheric forcing and lateral open boundary conditions. The atmospheric forcing includes three-hourly sea level pressure (SLP) and surface wind fields taken from the regional GEM (Global Environmental Multiscale) forecast products produced by the Meteorological Service of Canada (MSC). The atmospheric fields provided by the MSC have a horizontal resolution of 1/4°. The bulk formula of *Large and Pond* (1981) is used to convert the wind speed to wind stress. The MSC wind stress and SLP fields are linearly interpolated to every model timestep and mapped to each model grid.

The heat fluxes at the sea surface used to drive submodels L2 to L5 include solar radiation, long-wave radiation, latent heat flux and sensible heat flux. The six-hourly NCEP (National Centers for Environmental Prediction) reanalysis fields (*Kalnay et al.*, 1996) of the air temperature, relative humidity and cloud cover, and the MSC wind speed and air pressure are used to compute the net heat fluxes at every model timestep on each model grid.

For submodel L1, a *Sommerfeld* (1949) radiation condition is used for the sea surface elevations and the depth-mean currents at the open boundaries. For submodel L2, the lateral open boundary conditions include the specification of surface elevations and depth-averaged currents at the open boundaries of submodel L2. At the eastern open boundary, for example, the modelled normal flow (u_e) and surface elevation (η_e) take the following relationship (*Flather and Davies*, 1976):

$$u_e = u_c + u_w + u_t + \frac{c}{h}(\eta_e - \eta_w - \eta_t) \tag{A.1}$$

where η_w is the wind-driven surface elevations calculated by submodel L1 and η_t is the hourly tidal sea surface elevations calculated using harmonic constants extracted from WebTide dataset (*Dupont et al.*, 2002) for five major tidal constituents M_2, K_1, N_2, S_2 and O_1. In Eq. (A.1), u_w and u_t are the depth-averaged wind-driven and tidal currents from submodel L1 and WebTide, respectively, u_c is the climatological monthly mean baroclinic currents produced by a coarse resolution northwest Atlantic Ocean model (*Sheng et al.*, 2001), c is the phase speed of the external gravity wave, and h is the local water depth.

The conventional one-way nesting technique is used in specifying lateral open boundary

conditions of other submodels of DalCoast-Gully, in which the coarser-resolution, upper-level submodel provides boundary conditions for the finer-resolution, lower-level submodel and the solution of the finer-resolution domain does not feed back to the coarser-resolution domain. For submodels L3 to L5, the *Orlanski* (1976) radiation condition is first used to determine whether the propagation direction at the open boundary is inward or outward. For inward propagations, the model variables (i.e., temperature, salinity, and normal flow) at the open boundary are restored to the model results produced by the larger domain upper-level submodels. For outward propagations, the model variables at the open boundary are radiated outward.

The horizontal subgrid-scale mixing parameterization in the DalCoast-Gully (L1 to L5) is based on the shear and grid size dependent scheme of *Smagorinsky* (1963). The vertical subgrid-scale mixing parameterization in submodels L1 and L2 is based on the *Mellor and Yamada* (1982) level-2.5 turbulent closure scheme. An enhanced version of the K profile parameterization (KPP) scheme of *Durski et al.* (2004) is used in submodels L3 to L5.

Monthly mean temperature and salinity climatology of *Geshelin et al.* (1999) with a horizontal resolution of 1/6° over the northwest Atlantic is used in initializing submodels L2 to L5. To reduce the model drift, the sea surface temperature and salinity in the model are restored to the monthly mean climatology of *Geshelin et al.* (1999) with a timescale of 15 days.

A.2 DalCoast-CSS

The circulation model used for Chapter 4 is DalCoast-CSS, which has four submodels with progressively smaller model domains and finer horizontal resolutions covering from the northwest Atlantic to the inner Scotian Shelf adjacent to Halifax. The two outer-most submodels are similar to DalCoast-Gully. Submodels L3 to L4 are based on CANDIE with horizontal resolutions of $\sim$2 km and $\sim$500 m, respectively.

The nested-grid modelling system is driven by atmospheric forcing, heat fluxes, freshwater input and lateral open boundary conditions. The wind, pressure and other variables related to heat fluxes used in DalCoast-CSS are updated from NCEP reanalysis and MSC products to NARR (North American Regional Reanalysis) for a better spatial and temporal coverage (32 km, 3-hourly). Freshwater inputs from major rivers in the region are implemented in submodel L2 using idealized channels cut into the model's coastline. A

simple numerical scheme based on the salt and volume conservation is used in the model to specify the salinity and surface elevation at the head of each idealized channel (see *Ohashi and Sheng* (2013) for details).

The lateral open boundary conditions used in submodel L2 are similar to those in DalCoast-Gully (Eq. A.1) except for tides and large scale currents. The hourly tidal sea surface elevation and currents are calculated by using harmonic constants extracted from the OSU (Oregon State University) tidal model (*Egbert and Erofeeva*, 2002) for the eastern continental shelf of North America for eight major tidal constituents (M_2, S_2, N_2, K_2, K_1, O_1, P_1 and Q_1). A detailed description of the OSU tidal model and extraction method can be found at `http://volkov.oce.orst.edu/tides/EC.html`. The large scale currents are specified by using the climatological daily-mean baroclinic currents (temporally interpolated from five-day means) produced by a coarse-resolution circulation model for the northwest Atlantic Ocean (*Urrego-Blanco and Sheng*, 2012).

APPENDIX B

LIST OF PUBLICATIONS

1. Shan, S., J. Sheng, and B. J. W. Greenan, 2014. Physical processes affecting circulation and hydrography in the Sable Gully of Nova Scotia. *Deep Sea Research Part II: Topical Studies in Oceanography*, **104**: 35-50
2. Shan, S., J. Sheng, and B. J. W. Greenan, 2014. Modelling study of three-dimensional circulation and particle movement over the Sable Gully of Nova Scotia. *Ocean Dynamics*, **64**: 117-142
3. Béguer-Pon, M., S. Shan, K. R. Thompson, M. Castonguay, J. Sheng and J. Dodson, 2016. Exploring the role of the physical marine environment in silver eel migrations using a biophysical particle tracking model. *ICES Journal of Marine Science*, **73**: 57-74.
4. Shan, S., J. Sheng, K. Ohashi and M. Dever, 2016. Assessing the performance of a multi-nested ocean circulation model using satellite remote sensing and *in-situ* observations. *Satellite Oceanography and Meteorology*, DOI:10.18063/SOM.2016.01.004.
5. Béguer-Pon, M., M. Castonguay, S. Shan, J. Benchetrit, and J. J. Dodson, 2015. Direct observations of American eels migrating across the continental shelf to the Sargasso Sea. *Nature Communication*, **6**: 8705.
6. Shan, S. and J. Sheng, 2016. A modelling study of coastal upwelling on the Scotian Shelf. *Journal of Geophysical Research*, in preparation.

APPENDIX C

COPYRIGHT PERMISSION

Copyright Clearance Center RightsLink®

Home | Account Info | Help | Live Chat

Title: Physical processes affecting circulation and hydrography in the Sable Gully of Nova Scotia

Author: Shiliang Shan,Jinyu Sheng,Blair J.W. Greenan

Publication: Deep Sea Research Part II: Topical Studies in Oceanography

Publisher: Elsevier

Date: June 2014

Logged in as:
Shiliang Shan
Account #:
3000590801

LOGOUT

Order Completed

Thank you very much for your order.

This is a License Agreement between Shiliang Shan ("You") and Elsevier ("Elsevier"). The license consists of your order details, the terms and conditions provided by Elsevier, and the payment terms and conditions.

Get the printable license.

License Number	3870970074954
License date	May 16, 2016
Licensed content publisher	Elsevier
Licensed content publication	Deep Sea Research Part II: Topical Studies in Oceanography
Licensed content title	Physical processes affecting circulation and hydrography in the Sable Gully of Nova Scotia
Licensed content author	Shiliang Shan,Jinyu Sheng,Blair J.W. Greenan
Licensed content date	June 2014
Licensed content volume number	104
Licensed content issue number	n/a
Number of pages	16
Type of Use	reuse in a thesis/dissertation
Portion	full article
Format	both print and electronic
Are you the author of this Elsevier article?	Yes
Will you be translating?	No
Title of your thesis/dissertation	EULERIAN AND LAGRANGIAN STUDIES OF CIRCULATION ON THE SCOTIAN SHELF AND ADJACENT DEEP WATERS OF THE NORTH ATLANTIC WITH BIOLOGICAL IMPLICATIONS
Expected completion date	Aug 2016
Estimated size (number of pages)	200
Elsevier VAT number	GB 494 6272 12
Permissions price	0.00 CAD
VAT/Local Sales Tax	0.00 CAD / 0.00 GBP
Total	0.00 CAD

ORDER MORE... | CLOSE WINDOW

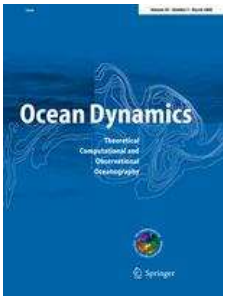

Title: Modelling study of three-dimensional circulation and particle movement over the Sable Gully of Nova Scotia
Author: Shiliang Shan
Publication: Ocean Dynamics
Publisher: Springer
Date: Jan 1, 2013

Order Completed

Thank you for your order.

This Agreement between Shiliang Shan ("You") and Springer ("Springer") consists of your license details and the terms and conditions provided by Springer and Copyright Clearance Center.

Your confirmation email will contain your order number for future reference.

Get the printable license.

License Number	3870951415866
License date	May 16, 2016
Licensed Content Publisher	Springer
Licensed Content Publication	Ocean Dynamics
Licensed Content Title	Modelling study of three-dimensional circulation and particle movement over the Sable Gully of Nova Scotia
Licensed Content Author	Shiliang Shan
Licensed Content Date	Jan 1, 2013
Licensed Content Volume	64
Licensed Content Issue	1
Type of Use	Thesis/Dissertation
Portion	Full text
Number of copies	100
Author of this Springer article	Yes and you are a contributor of the new work
Order reference number	None
Title of your thesis / dissertation	EULERIAN AND LAGRANGIAN STUDIES OF CIRCULATION ON THE SCOTIAN SHELF AND ADJACENT DEEP WATERS OF THE NORTH ATLANTIC WITH BIOLOGICAL IMPLICATIONS
Expected completion date	Aug 2016
Estimated size(pages)	200
Requestor Location	Shiliang Shan Dept. of Oceanography 1355 Oxford Street POB 15000 Halifax, NS B3H4R2 Canada Attn: Shiliang Shan
Billing Type	Invoice
Billing address	Shiliang Shan Dept. of Oceanography 1355 Oxford Street POB 15000 Halifax, NS B3H4R2 Canada Attn: Shiliang Shan
Total	0.00 CAD

Order Completed

Thank you very much for your order.

This is a License Agreement between Shiliang Shan ("You") and Oxford University Press ("Oxford University Press"). The license consists of your order details, the terms and conditions provided by Oxford University Press, and the payment terms and conditions.

Get the printable license.

License Number	3870970687764
License date	May 16, 2016
Licensed content publisher	Oxford University Press
Licensed content publication	ICES Journal of Marine Science
Licensed content title	Exploring the role of the physical marine environment in silver eel migrations using a biophysical particle tracking model:
Licensed content author	Mélanie Béguer-Pon, Shiliang Shan, Keith R. Thompson, Martin Castonguay, Jinyu Sheng, Julian J. Dodson
Licensed content date	01/01/2016
Volume number	73
Issue number	1
Type of Use	Thesis/Dissertation
Requestor type	Academic/Educational institute
Format	Print and electronic
Portion	Figure/table
Number of figures/tables	15
Will you be translating?	No
Author of this OUP article	Yes
Order reference number	None
Title of your thesis / dissertation	EULERIAN AND LAGRANGIAN STUDIES OF CIRCULATION ON THE SCOTIAN SHELF AND ADJACENT DEEP WATERS OF THE NORTH ATLANTIC WITH BIOLOGICAL IMPLICATIONS
Expected completion date	Aug 2016
Estimated size(pages)	200
Publisher VAT ID	GB 125 5067 30
Total	0.00 USD

BIBLIOGRAPHY

Aarestrup, K., F. Ø kland, M. M. Hansen, D. Righton, P. Gargan, M. Castonguay, L. Bernatchez, P. Howey, H. Sparholt, M. I. Pedersen, and R. S. McKinley, Oceanic Spawning Migration of the European Eel (*Anguilla anguilla*), *Science*, *325*, 1660, 2009.

Allen, S. E., and X. Durrieu De Madron, A review of the role of submarine canyons in deep-ocean exchange with the shelf, *Ocean Science Discussions*, *6*, 1369–1406, 2009.

Amilhat, E., K. Aarestrup, E. Faliex, G. Simon, H. Westerberg, and D. Righton, First evidence of European eels exiting the Mediterranean Sea during their spawning migration, *Scientific Reports*, *6*, 21817, 2016.

Awaji, T., Water mixing in a tidal current and the effect of turbulence on tidal exchange through a strait, *Journal of Physical Oceanography*, *12*, 501–514, 1982.

Batchelor, G. K., *An Introduction to Fluid Dynamics*, Cambridge Mathematical Library, Cambridge University Press, 2000.

Béguer-Pon, M., J. Benchetrit, M. Castonguay, K. Aarestrup, S. E. Campana, M. J. Stokesbury, and J. J. Dodson, Shark predation on migrating adult American eels (*Anguilla rostrata*) in the Gulf of St. Lawrence, *PloS one*, *7*, e46830, 2012.

Béguer-Pon, M., M. Castonguay, S. Shan, J. Benchetrit, and J. J. Dodson, Direct observations of American eels migrating across the continental shelf to the Sargasso Sea, *Nature Communication*, *6*, 8705, 2015.

Béguer-Pon, M., S. Shan, K. R. Thompson, M. Castonguay, J. Sheng, and J. J. Dodson, Exploring the role of the physical marine environment in silver eel migrations using a biophysical particle tracking model, *ICES Journal of Marine Science*, *73*, 57–74, 2016.

Bertin, L., *Eels: A Biological Study*, Cleaver-Hume Press Ltd, London, 1956.

Bilgili, A., J. A. Proehl, D. R. Lynch, K. W. Smith, and M. R. Swift, Estuary/ocean exchange and tidal mixing in a Gulf of Maine Estuary: A Lagrangian modeling study, *Estuarine, Coastal and Shelf Science*, *65*, 607–624, 2005.

Blanke, B., S. Bonhommeau, N. Grima, and Y. Drillet, Sensitivity of advective transfer times across the North Atlantic Ocean to the temporal and spatial resolution of model velocity data: Implication for European eel larval transport, *Dynamics of Atmospheres and Oceans*, *55*, 22–44, 2012.

Bobanovic, J., Barotropic circulation variability on Canadian Atlantic Shelves, Ph.D. thesis, Dalhousie University, 1997.

Boëtius, I., and J. Boëtius, Experimental maturation of female silver eels, *Anguilla anguilla*: estimates of fecundity and energy reserves for migration and spawning, *Dana (Denmark)*, *1*, 1–28, 1980.

Bonhommeau, S., B. Blanke, A.-M. Tréguier, N. Grima, E. Rivot, Y. Vermard, E. Greiner, and O. Le Pape, How fast can the European eel (*Anguilla anguilla*) larvae cross the Atlantic Ocean?, *Fisheries Oceanography*, *18*, 371–385, 2009a.

Bonhommeau, S., O. Le Pape, D. Gascuel, B. Blanke, a M Tréguier, N. Grima, Y. Vermard, M. Castonguay, and E. Rivot, Estimates of the mortality and the duration of the trans-Atlantic migration of European eel *Anguilla anguilla* leptocephali using a particle tracking model., *Journal of Fish Biology*, *74*, 1891–1914, 2009b.

Bonhommeau, S., M. Castonguay, E. Rivot, R. Sabatié, and O. Le Pape, The duration of migration of Atlantic *Anguilla* larvae, *Fish and Fisheries*, *11*, 289–306, 2010.

Brennan, C. E., L. Bianucci, and K. Fennel, Sensitivity of northwest North Atlantic shelf circulation to surface and boundary forcing: a regional model assessment, *Atmosphere-Ocean*, *DOI: 10.1080/07055900.2016.1147416*, 2016.

Burgerhout, E., S. A. Brittijn, C. Tudorache, D. L. de Wijze, R. P. Dirks, and G. E. E. J. M. van den Thillart, Male European eels are highly efficient long distance swimmers: Effects of endurance swimming on maturation, *Comparative Biochemistry and Physiology Part A: Molecular & Integrative Physiology*, *166*, 522–527, 2013a.

Burgerhout, E., C. Tudorache, S. A. Brittijn, A. P. Palstra, R. P. Dirks, and G. E. E. J. M. van den Thillart, Schooling reduces energy consumption in swimming male European eels, *Anguilla anguilla* L., *Journal of Experimental Marine Biology and Ecology*, *448*, 66–71, 2013b.

Carter, G. S., Barotropic and baroclinic M2 tides in the Monterey Bay region, *Journal of Physical Oceanography*, *40*, 1766–1783, 2010.

Carter, G. S., O. B. Fringer, and E. D. Zaron, Regional models of internal tides, *Oceanography*, *25*, 56, 2012.

Cong, L., J. Sheng, and K. R. Thompson, A retrospective study of particle retention on the outer banks of the Scotian Shelf. *Canadian Technical Report of Hydrography and Ocean Sciences 170*: viii + 132p, 1996.

Csanady, G., and P. Hamilton, Circulation of slopewater, *Continental Shelf Research*, *8*, 565–624, 1988.

Cummins, P. F., and L.-Y. Oey, Simulation of barotropic and baroclinic tides off northern british columbia, *Journal of Physical Oceanography*, *27*, 762–781, 1997.

Cushman-Roisin, B., and J.-M. Beckers, *Introduction to Geophysical Fluid Dynamics: Physical and Numerical Aspects*, vol. 101, Academic Press, 2011.

De Leo, F. C., C. R. Smith, A. A. Rowden, D. A. Bowden, and M. R. Clark, Submarine canyons: hotspots of benthic biomass and productivity in the deep sea, *Proceedings of the Royal Society B: Biological Sciences*, *277*, 2783–2792, 2010.

de Margerie, S., and K. Lank, Tidal circulation of the Scotian Shelf and Grand Banks. Contractor Report for the Department of Fisheries and Oceans, NO. 08SC.FP901-5-X515, Dartmouth, NS. http://publications.gc.ca/pub?id=430773&sl=0, Accessed 30 October 2012. 49p, 1986.

DeAngelis, D. L., and V. Grimm, Individual-based models in ecology after four decades, *F1000Prime Reports*, *6*, 39, 2014.

Dever, M., J. F. Kocik, D. Hebert, J. Zydlewski, J. P. Hawkes, and D. Stich, Linkage between coastal conditions, detection patterns and migratory behavior of Atlantic salmon postsmolts along the Halifax Line, in preparation, 2016.

Donlon, C. J., P. J. Minnett, C. Gentemann, T. J. Nightingale, I. J. Barton, B. Ward, and M. J. Murray, Toward improved validation of satellite sea surface skin temperature measurements for climate research, *Journal of Climate*, *15*, 353–369, 2002.

Donohue, S. M., A numerical model of an upwelling event off the coast of Nova Scotia, MSc Thesis, Royal Military College of Canada, 2001.

Drinkwater, K., B. Petrie, and W. H. Sutcliffe, Seasonal geostrophic volume transports along the Scotian Shelf, *Estuarine and Coastal Marine Science*, *9*, 17–27, 1979.

Dupont, F., C. G. Hannah, D. A. Greenberg, J. Y. Cherniawsky, and C. E. Naimie, Modelling system for tides for the Northwest Atlantic coastal ocean. *Canadian Technical Report of Hydrography and Ocean Sciences 221*: vii + 72p, 2002.

Durski, S. M., S. M. Glenn, and D. B. Haidvogel, Vertical mixing schemes in the coastal ocean: Comparison of the level 2.5 Mellor-Yamada scheme with an enhanced version of the K profile parameterization, *Journal of Geophysical Research*, *109*, C01015, 2004.

Egbert, G. D., and S. Y. Erofeeva, Efficient inverse modeling of barotropic ocean tides, *Journal of Atmospheric and Oceanic Technology*, *19*, 183–204, 2002.

Egbert, G. D., A. F. Bennett, and M. G. G. Foreman, Topex/poseidon tides estimated using a global inverse model, *Journal of Geophysical Research*, *99*, 24821–24852, 1994.

Ekman, V. W., *On the influence of the earth's rotation on ocean-currents*, ALMQVIST & WIKSELLS BOKTRYCKERI AB UPPSALA, 1963, reprinted from Arkiv för matematik, astronomi, och fysik. Band 2: No. 11. 1905.

Flather, R. A., and A. M. Davies, Note on a preliminary scheme for storm surge prediction using numerical models, *Quarterly Journal of the Royal Meteorological Society*, *102*, 123–132, 1976.

Franklin, J. L., and D. P. Brown, Atlantic hurricane season of 2006, *Monthly Weather Review*, *136*, 1174–1200, 2008.

Fricke, H., and R. Kaese, Tracking of artificially matured eels (*Anguilla anguilla*) in the Sargasso Sea and the problem of the eel's spawning site, *Naturwissenschaften*, *82*, 32–36, 1995.

Garrett, C., Tidal resonance in the Bay of Fundy and Gulf of Maine, *Nature*, *238*, 441–443, 1972.

Garrett, C., J. Keeley, and D. Greenberg, Tidal mixing versus thermal stratification in the Bay of Fundy and Gulf of Maine, *Atmosphere-Ocean*, *16*, 403–423, 1978.

Geshelin, Y., J. Sheng, and R. J. Greatbatch, Monthly mean climatologies of temperature and salinity in the western North Atlantic. *Canadian Data Report of Hydrography and Ocean Sciences 153*: vi + 62p, 1999.

Gill, A. E., *Atmosphere-ocean dynamics*, Academic Press, New York, NY, 1982.

Gordon, R. L., and N. F. Marshall, Submarine canyons: Internal wave traps?, *Geophysical Research Letters*, *3*, 622–624, 1976.

Greenan, B. J. W., B. Petrie, W. G. Harrison, and P. M. Strain, The onset and evolution of a spring bloom on the Scotian Shelf, *Limnology and Oceanography*, *53*, 1759, 2008.

Greenan, B. J. W., B. D. Petrie, and D. A. Cardoso, Mean circulation and high-frequency flow amplification in the Sable Gully, *Deep Sea Research Part II: Topical Studies in Oceanography*, *104*, 20–34, 2014.

Greenberg, D. A., J. W. Loder, Y. Shen, D. R. Lynch, and C. E. Naimie, Spatial and temporal structure of the barotropic response of the Scotian Shelf and Gulf of Maine to surface wind stress: A model-based study, *Journal of Geophysical Research*, *102*, 20897–20915, 1997.

Gully Marine Protected Area Regulations, Last amended on 3 April 2008. SOR/2004-112. `http://laws-lois.justice.gc.ca/PDF/SOR-2004-112.pdf`. Accessed 1 August 2013, 2004.

Hachey, H., Ekmans theory applied to water replacements on the Scotian shelf, *Proceedings of the Nova Scotian Institute of Science*, *19*, 264–276, 1937.

Hachey, H. B., A winter incursion of Slope Water on the Scotian Shelf, *Journal of the Fisheries Research Board of Canada*, *10*, 148–153, 1953.

Hall, R. A., and G. S. Carter, Internal tides in Monterey Submarine Canyon, *Journal of Physical Oceanography*, *41*, 186–204, 2010.

Hall, R. A., J. M. Huthnance, and R. G. Williams, Internal tides, nonlinear internal wave trains, and mixing in the faroe-shetland channel, *Journal of Geophysical Research: Oceans*, *116*, 2011.

Hall, R. A., M. H. Alford, G. S. Carter, M. C. Gregg, R.-C. Lien, D. J. Wain, and Z. Zhao, Transition from partly standing to progressive internal tides in Monterey Submarine Canyon, *Deep Sea Research Part II: Topical Studies in Oceanography*, *104*, 164–173, 2014.

Han, G., and J. W. Loder, Three-dimensional seasonal-mean circulation and hydrography on the eastern Scotian Shelf, *Journal of Geophysical Research: Oceans*, *108*, 2003.

Han, G., C. G. Hannah, J. W. Loder, and P. C. Smith, Seasonal variation of the three-dimensional mean circulation over the Scotian Shelf, *Journal of Geophysical Research*, *102*, 1011–1025, 1997.

Han, G., P. Roussel, and J. W. Loder, Modeling tidal currents and seasonal-mean circulation in the Sable Gully region, in *Estuarine and Coastal Modeling: Proceedings of the Seventh International ASCE Conference*, edited by M. L. Spaulding, pp. 22–34, 2001.

Handeland, S., Bjrnsson, A. Arnesen, and S. Stefansson, Seawater adaptation and growth of post-smolt Atlantic salmon (*Salmo salar*) of wild and farmed strains, *Aquaculture*, *220*, 367–384, 2003.

Hannah, C. G., J. A. Shore, J. W. Loder, and C. E. Naimie, Seasonal circulation on the western and central Scotian Shelf, *Journal of Physical Oceanography*, *31*, 591–615, 2001.

Haro, A. J., Thermal preferenda and behavior of Atlantic eels (genus *Anguilla*) in relation to their spawning migration, *Environmental biology of fishes*, *31*, 171–184, 1991.

Hayes, S. A., and J. F. Kocik, Comparative estuarine and marine migration ecology of Atlantic salmon and steelhead: Blue highways and open plains, *Reviews in Fish Biology and Fisheries*, *24*, 757–780, 2014.

Hebert, D., R. Pettipas, D. Brickman, and M. Dever, Meteorological, sea ice and physical oceanographic conditions on the Scotian Shelf and in the Gulf of Maine during 2012. *Canadian Science Advisory Secretariat Research Document 058*: v + 46p, 2013.

Hickey, B., Coastal submarine canyons, in *Topographic effects in the ocean, Proceedings Hawaiian Winter Workshop, University of Hawaii at Manoa*, pp. 95–110, 1995.

Hickey, B. M., The response of a steep-sided, narrow canyon to time-variable wind forcing, *Journal of Physical Oceanography*, *27*, 697–726, 1997.

Higginson, S., Mapping and understanding the mean surface circulation of the North Atlantic: insights from new geodetic and oceanographic measurements, Ph.D. thesis, Dalhousie University, 2012.

Higginson, S., K. Thompson, J. Huang, M. Véronneau, and D. Wright, The mean surface circulation of the North Atlantic subpolar gyre: A comparison of estimates derived from new gravity and oceanographic measurements, *Journal of Geophysical Research: Oceans*, *116*, 2011.

Hintze, J. L., and R. D. Nelson, Violin plots: A box plot-density trace synergism, *The American Statistician*, *52*, 181–184, 1998.

Hooker, S. K., H. Whitehead, and S. Gowans, Ecosystem consideration in conservation planning: energy demand of foraging bottlenose whales (*Hyperoodon ampullatus*) in a marine protected area, *Biological Conservation*, *104*, 51–58, 2002.

Hunkins, K., Mean and tidal currents in Baltimore Canyon, *Journal of Geophysical Research*, *93*, 6917–6929, 1988.

Jessop, B. M., Geographic effects on American eel (*Anguilla rostrata*) life history characteristics and strategies, *Canadian Journal of Fisheries and Aquatic Sciences*, *67*, 326–346, 2010.

Kalnay, E. C., M. Kanamitsu, R. Kistler, W. Collins, D. Deaven, L. Gandin, M. Iredell, S. Saha, G. White, J. Woollen, et al., The NCEP/NCAR 40-year reanalysis project, *Bulletin of the American Meteorological Society*, *77*, 437–471, 1996.

Katavouta, A., Non-linear coupling of scales of ocean variability and implications for downscaling, Ph.D. thesis, Dalhousie University, 2015.

Kepkay, P. E., W. G. Harrison, J. B. C. Bugden, and C. J. Porter, Seasonal plankton production in The Gully ecosystem, in *Advances in Understanding The Gully Ecosystem: A Summary of Research Projects Conducted at the Bedford Institute of Oceanography (1999-2001)*, edited by F. D. G. Gordon D C, vol. 2377, pp. 65–72, 2002.

Kinsella, E. D., A. E. Hay, and W. W. Denner, Wind and topographic effects on the Labrador current at Carson Canyon, *Journal of Geophysical Research*, *92*, 10853–10869, 1987.

Kleckner, R., and J. McCleave, Spatial and temporal distribution of American eel larvae in relation to North Atlantic Ocean current systems, *Dana*, *4*, 67–92, 1985.

Klinck, J., Circulation near submarine canyons: A modeling study, *Journal of Geophysical Research*, *101*, 1211–1223, 1996.

Kocik, J. F., J. P. Hawkes, T. F. Sheehan, P. A. Music, and K. F. Beland, Asessing estuarine and coastal migration and survival of wild Atlanic salmon smolts from the Narraguagus River Maine using ultrasonic telemetry, *American Fisheries Society Symposium*, *69*, 293–310, 2009.

Kolmogorov, A. N., *Kolmogorov in Perspective*, vol. 20 of *History of Mathematics*, American Mathematical Societly, Providence, Rhode Island, 2000.

Krueger, W. H., and K. Oliveira, Sex, size, and gonad morphology of silver American eels *Anguilla rostrata*, *Copeia*, *1997*, 415–420, 1997.

Large, W. G., and S. Pond, Open ocean momentum flux measurements in moderate to strong winds, *Journal of Physical Oceanography*, *11*, 324–336, 1981.

Laurent, A., Examining the influence of meteorological events on plankton dynamics in a coastal ecosystem (Lunenburg Bay, Canada), Ph.D. thesis, Dalhousie University, 2011.

Loder, J. W., and D. A. Greenberg, Predicted positions of tidal fronts in the gulf of maine region, *Continental Shelf Research*, *6*, 397–414, 1986.

Loder, J. W., B. Petrie, and G. Gawarkiewicz, The coastal ocean off northeastern North America: A large-scale view, in *The Sea*, edited by A. R. Robinson and K. H. Brink, vol. 11, pp. 105–133, 1998.

Loder, J. W., C. G. Hannah, B. D. Petrie, and E. A. Gonzalez, Hydrographic and transport variability on the Halifax section, *Journal of Geophysical Research*, *108*, C11, 2003.

Lynch, D. R., D. A. Greenberg, A. Bilgili, D. J. McGillicuddy Jr, J. P. Manning, and A. L. Aretxabaleta, *Particles in the Coastal Ocean: Theory and Applications*, Cambridge University Press, 2015.

Madec, G., *NEMO ocean engine*, Note du Pole de modélisation, Institut Pierre-Simon Laplace (IPSL), France, No 27 ISSN No 1288-1619., 2008.

Marshall, J., and R. A. Plumb, *Atmosphere, ocean and climate dynamics: an introductory text*, Elsevier Academic Press, 2008.

Martin, P. J., S. R. Smith, P. G. Posey, G. M. Dawson, and S. H. Riedlinger, Use of the Oregon State University Tidal Inversion Software (OTIS) to generate improved tidal prediction in the East-Asian seas. No. NRL/MR/7320-09-9176. Naval Research Laboratory, Oceanography Division, Stennis Space Center, MS 39529-5004, 2009.

McLellan, H. J., L. Lauzier, and W. B. Bailey, The Slope Water off the Scotian Shelf, *Journal of the Fisheries Research Board of Canada*, *10*, 155–176, 1953.

Mellor, G. L., *Users guide for a three dimensional, primitive equation, numerical ocean model*, Atmospheric and Oceanic Sciences Program, Princeton University, 2004.

Mellor, G. L., and T. Yamada, Development of a turbulence closure model for geophysical fluid problems, *Reviews of Geophysics and Space Physics*, *20*, 851–875, 1982.

Methling, C., C. Tudorache, P. V. Skov, and J. F. Steffensen, Pop up satellite tags impair swimming performance and energetics of the European eel (*Anguilla anguilla*), *PLoS one*, *6*, e20797, 2011.

Miller, M. J., S. Bonhommeau, P. Munk, M. Castonguay, R. Hanel, and J. D. McCleave, A century of research on the larval distributions of the Atlantic eels: a re-examination of the data, *Biological Reviews*, *90*, 1035–1064, 2015.

Moors-Murphy, H. B., Submarine canyons as important habitat for cetaceans, with special reference to the Gully: A review, *Deep-Sea Research Part II: Topical Studies in Oceanography*, *104*, 6–19, 2014.

NASA Aquarius project, Aquarius Official Release Level 3 Sea Surface Salinity Standard Mapped Image Monthly Data V4.0. Ver. 4.0. PO.DAAC, CA, USA. Dataset accessed [2015-07-24], 2015.

Ohashi, K., and J. Sheng, Influence of St. Lawrence River discharge on the circulation and hydrography in Canadian Atlantic waters, *Continental Shelf Research*, *58*, 32–49, 2013.

Ohashi, K., and J. Sheng, Investigating the effect of oceanographic conditions and swimming behaviours on the movement of particles in the Gulf of St. Lawrence using an individual-based numerical model, *Atmosphere-Ocean*, *DOI: 10.1080/07055900.2015.1090390*, 2015.

Ohashi, K., J. Sheng, K. R. Thompson, C. Hannah, and H. Ritchie, Effect of stratification on tidal circulation over the Scotian Shelf and Gulf of St. Lawrence: a numerical study using a three-dimensional shelf circulation model, *Ocean Dynamics*, *59*, 809–825, 2009.

Orlanski, I., A simple boundary condition for unbounded hyperbolic flows, *Journal of Computational Physics*, *21*, 251–269, 1976.

Palstra, A., V. J. T. van Ginneken, and G. E. E. J. M. van den Thillart, Cost of transport and optimal swimming speed in farmed and wild European silver eels (*Anguilla anguilla*), *Comparative Biochemistry and Physiology Part A: Molecular & Integrative Physiology*, *151*, 37–44, 2008.

Parker, B. B., The relative importance of the various nonlinear mechanisms in a wide range of tidal interactions (review), in *Tidal Hydrodynamics*, edited by B. B. Parker, pp. 237–268, John Wiley & Sons, Hoboken, New Jersey, 1991.

Parrish, D. L., R. J. Behnke, S. R. Gephard, S. D. McCormick, and G. H. Reeves, Why aren't there more Atlantic salmon (*Salmo salar*)?, *Canadian Journal of Fisheries and Aquatic Sciences*, *55*, 281–287, 1998.

Pawlowicz, R., B. Beardsley, and S. Lentz, Classical tidal harmonic analysis including error estimates in MATLAB using T_TIDE, *Computers & Geosciences*, *28*, 929–937, 2002.

Petrie, B. D., and K. F. Drinkwater, Temperature and salinity variability on the Scotian Shelf and in the Gulf of Maine 1945-1990, *Journal of Geophysical Research*, *98*, 20079–20089, 1993.

Petrie, B. D., B. Topliss, and D. G. Wright, Coastal upwelling and eddy development off Nova Scotia, *Journal of Geophysical Research*, *92*, 12979–12991, 1987.

Petrie, B. D., J. A. Shore, C. G. Hannah, and J. Loder, Physical oceanography, in *The Gully: A scientific review of its environment and ecosystem*, edited by W. G. Harrison and D. G. Fenton, pp. 20–57, Canadian Stock Assessment Secretariat Research Document 98/83, Department of Fisheries and Oceans, Dartmouth, NS, Canada, 1998.

Press, W. H., S. A. Teukolsky, W. T. Vetterling, and B. P. Flannery, *Numerical Recipes in FORTRAN: The Art of Scientific Computing*, Second Edition. Cambridge University Press, New York, 1992.

Putman, N., K. Lohmann, E. Putman, T. Quinn, A. Klimley, and D. Noakes, Evidence for geomagnetic imprinting as a homing mechanism in Pacific salmon, *Current Biology*, *23*, 312–316, 2013.

Putman, N. F., M. M. Scanlan, E. J. Billman, J. P. ONeil, R. B. Couture, T. P. Quinn, K. J. Lohmann, and D. L. Noakes, An inherited magnetic map guides ocean navigation in juvenile Pacific salmon, *Current Biology*, *24*, 446–450, 2014.

Reid, J. L., On the total geostrophic circulation of the North Atlantic Ocean: Flow patterns, tracers, and transports, *Progress in Oceanography*, *33*, 1–92, 1994.

Renkawitz, M. D., T. F. Sheehan, and G. S. Goulette, Swimming depth, behavior, and survival of Atlantic salmon postsmolts in Penobscot Bay, Maine, *Transactions of the American Fisheries Society*, *141*, 1219–1229, 2012.

Ridderinkhof, H., and J. T. F. Zimmerman, Mixing processes in a numerical model of the Western Dutch Wadden Sea, in *Residual Currents and Long-term Transport*, edited by R. T. Chang, pp. 194–209, Springer-Verlag, New York, 1990.

Riddle, A. M., and R. E. Lewis, Dispersion experiments in U.K. coastal waters, *Estuarine, Coastal and Shelf Science*, *51*, 243–254, 2000.

Rudnick, D. L., Ocean research enabled by underwater gliders, *Annual Review of Marine Science*, *8*, 519–541, 2016.

Rutherford, R. J., H. Breeze, and N. S. By, The Gully Ecosystem. *Canadian Manuscript Report of Fisheries and Aquatic Sciences 2615*: vi + 28p., 2002.

Rypina, I. I., J. K. Llopiz, L. J. Pratt, and M. S. Lozier, Dispersal pathways of American eel larvae from the Sargasso Sea, *Limnology and Oceanography*, *59*, 1704–1714, 2014.

Saha S, et al. 2011, updated monthly, NCEP Climate Forecast System Version 2 (CFSv2) Selected Hourly Time-Series Products. Research Data Archive at the National Center for Atmospheric Research, Computational and Information Systems Laboratory. http://dx.doi.org/10.5065/D6N877VB. Dataset accessed [2016-01-04], 2016.

Sandstrom, H., and J. A. Elliott, Internal tide and solitons on the Scotian Shelf: A nutrient pump at work, *Journal of Geophysical Research*, *89*, 6415–6426, 1984.

Sandstrom, H., and J. A. Elliott, Production, transformation, and dissipation of energy in internal tides near the continental shelf edge, *Journal of Geophysical Research*, *116*, 1–16, 2011.

Schmidt, J., The breeding places of the eel, *Philosophical Transactions of the Royal Society of London B: Biological Sciences*, *211*, 179–208, 1923.

Schmitz, W. J., and M. S. McCartney, On the north Atlantic circulation, *Reviews of Geophysics*, *31*, 29–49, 1993.

Schwing, F. B., Subtidal response of Scotian Shelf circulation to local and remote forcing. Part II: Barotropic model, *Journal of Physical Oceanography*, *22*, 542–563, 1992.

Shan, S., and J. Sheng, Examination of circulation, flushing time and dispersion in Halifax Harbour of Nova Scotia, *Water Quality Research Journal of Canada*, *47*, 353–374, 2012.

Shan, S., J. Sheng, K. R. Thompson, and D. A. Greenberg, Simulating the three-dimensional circulation and hydrography of Halifax Harbour using a multi-nested coastal ocean circulation model, *Ocean Dynamics*, *61*, 951–976, 2011.

Shan, S., J. Sheng, and B. J. Greenan, Physical processes affecting circulation and hydrography in the Sable Gully of Nova Scotia, *Deep Sea Research Part II: Topical Studies in Oceanography*, *104*, 35–50, 2014.

Sheng, J., and K. R. Thompson, A robust method for diagnosing regional shelf circulation from scattered density profiles, *Journal of Geophysical Research*, *101*, 25647–25659, 1996.

Sheng, J., D. G. Wright, R. J. Greatbatch, and D. E. Dietrich, CANDIE: A new version of the DieCAST ocean circulation model, *Journal of Atmospheric and Oceanic Technology*, *15*, 1414–1432, 1998.

Sheng, J., R. J. Greatbatch, and D. G. Wright, Improving the utility of ocean circulation models through adjustment of the momentum balance, *Journal of Geophysical Research*, *106*, 16711–16728, 2001.

Sheng, J., X. Zhai, and R. J. Greatbatch, Numerical study of the storm-induced circulation on the Scotian Shelf during Hurricane Juan using a nested-grid ocean model, *Progress in Oceanography*, *70*, 233–254, 2006.

Sheng, J., J. Zhao, and L. Zhai, Examination of circulation, dispersion, and connectivity in Lunenburg Bay of Nova Scotia using a nested-grid circulation model, *Journal of Marine Systems*, *77*, 350–365, 2009.

Shepard, F., N. Marshall, and P. McLoughlin, Currents in submarine canyons, in *Deep Sea Research and Oceanographic Abstracts*, vol. 21, pp. 691–706, Elsevier, 1974.

Shepard, F. P., and R. F. Dill, *Submarine canyons and other types of sea valleys*, Second Printing. Rand McNally & Company, Chicago, 1969.

Smagorinsky, J., General circulation experiments with the primitive equations, *Monthly Weather Review*, *91*, 99–164, 1963.

Smith, P. C., Seasonal and interannual variability of current, temperature and salinity off southwest Nova Scotia, *Canadian Journal of Fisheries and Aquatic Sciences*, *46*, s4–s20, 1989.

Smith, P. C., and F. B. Schwing, Mean circulation and variability on the eastern Canadian continental shelf, *Continental Shelf Research*, *11*, 977–1012, 1991.

Smith, P. C., R. W. Houghton, R. G. Fairbanks, and D. G. Mountain, Interannual variability of boundary fluxes and water mass properties in the Gulf of Maine and on Georges Bank: 19931997, *Deep Sea Research Part II: Topical Studies in Oceanography*, *48*, 37–70, 2001.

Smith, W. H. F., and D. T. Sandwell, Global sea floor topography from satellite altimetry and ship depth soundings, *Science*, *277*, 1956–1962, 1997.

Sommerfeld, A., *Partial differential equations.*, 1949, Lectures on Theoretical Physics, vol 6, Academic Press, San Diego, CA.

Steele, M., R. Morley, and W. Ermold, PHC: A global ocean hydrography with a high-quality Arctic Ocean, *Journal of Climate*, *14*, 2079–2087, 2001.

Sutcliffe, W. H., Jr., R. H. Loucks, and K. F. Drinkwater, Coastal circulation and physical oceanography of the Scotian Shelf and the Gulf of Maine, *Journal of the Fisheries Research Board of Canada*, *33*, 98–115, 1976.

Swart, N. C., S. E. Allen, and B. J. W. Greenan, Resonant amplification of subinertial tides in a submarine canyon, *Journal of Geophysical Research*, *116*, 1–14, 2011.

Talley, L. D., G. L. Pickard, W. J. Emery, and J. H. Swift, *Introduction to Descriptive Physical Oceanography.*, Academic Press, Boston. 471 pp., 2011.

Tang, L., J. Sheng, B. G. Hatcher, and P. F. Sale, Numerical study of circulation, dispersion, and hydrodynamic connectivity of surface waters on the Belize shelf. *Journal of Geophysical Research*, **111**: C01003., 2006.

Taylor, G. I., Diffusion by continuous movements, *Proceedings of the London Mathematical Society*, *2*, 196–212, 1922.

Tee, K. T., P. C. Smith, and D. Lefaivre, Topographic upwelling off southwest Nova Scotia, *Journal of Physical Oceanography*, *23*, 1703–1726, 1993.

Tesch, F. W., *The Eel*, Blackwell Publishing, Oxford, UK. 408 pp, 2003.

Therriault, J. C., B. D. Petrie, P. Pepin, J. Gagnon, D. Gregory, J. Helbig, A. Herman, D. Lefaivre, M. Mitchell, B. Pelchat, J. Runge, and D. Sameoto, Proposal for a northwest Atlantic zonal monitoring program. *Canadian Technical Report of Hydrography and Ocean Sciences 194*: vii + 57p, 1998.

Thompson, K. R., and J. Sheng, Subtidal circulation on the Scotian Shelf: Assessing the hindcast skill of a linear, barotropic model, *Journal of Geophysical Research*, *102*, 24987–25003, 1997.

Thompson, K. R., R. H. Loucks, and R. W. Trites, Sea surface temperature variability in the shelf-slope region of the Northwest Atlantic, *Atmosphere-Ocean*, *26*, 282–299, 1988.

Thompson, K. R., D. G. Wright, Y. Lu, and E. Demirov, A simple method for reducing seasonal bias and drift in eddy resolving ocean models, *Ocean Modelling*, *13*, 109–125, 2006.

Thompson, K. R., K. Ohashi, J. Sheng, J. Bobanovic, and J. Ou, Suppressing bias and drift of coastal circulation models through the assimilation of seasonal climatologies of temperature and salinity, *Continental Shelf Research*, *27*, 1303–1316, 2007.

Thygesen, U. H., How to reverse time in stochastic particle tracking models, *Journal of Marine Systems*, *88*, 159–168, 2011.

Urrego-Blanco, J., and J. Sheng, Interannual variability of the circulation over the eastern Canadian shelf, *Atmosphere-Ocean*, *50*, 277–300, 2012.

Urrego-Blanco, J., and J. Sheng, Study on subtidal circulation and variability in the Gulf of St. Lawrence, Scotian Shelf, and Gulf of Maine using a nested-grid shelf circulation model, *Ocean Dynamics*, *64*, 385–412, 2014.

USASAC, USASAC (2010) Annual report of the U.S. Atlantic Salmon Assessment Committee. Prepared for U.S. Section to NASCO. Annual report 2009/22. Vol 22, 124 pp., 2010.

van den Thillart, G. E. E. J. M., A. Palstra, and V. J. T. van Ginneken, Simulated migration of European silver eel; swim capacity and cost of transport, *Journal of Marine Science and Technology*, *15*, 1–16, 2007.

van Ginneken, V. J. T., and G. E. Maes, The European eel (*Anguilla anguilla*, Linnaeus), its lifecycle, evolution and reproduction: a literature review, *Reviews in Fish Biology and Fisheries*, *15*, 367–398, 2005.

Vøllestad, L. A., Geographic variation in age and length at metamorphosis of maturing European eel: environmental effects and phenotypic plasticity, *Journal of Animal Ecology*, pp. 41–48, 1992.

Westerberg, H., N. Sjöberg, I. Lagenfelt, K. Aarestrup, and D. Righton, Behaviour of stocked and naturally recruited European eels during migration, *Marine Ecology Progress Series*, *496*, 145–157, 2014.

Wimmer, T., and H. Whitehead, Movements and distribution of northern bottlenose whales, *Hyperoodon ampullatus*, on the Scotian Slope and in adjacent waters, *Canadian Journal of Zoology*, *82*, 1782–1794, 2004.

Wu, Y., C. L. Tang, and C. G. Hannah, The circulation of eastern Canadian seas, *Progress in Oceanography*, *106*, 28–48, 2012.

Yang, B., and J. Sheng, Process study of coastal circulation over the inner Scotian Shelf using a nested-grid ocean circulation model, with a special emphasis on the storm-induced circulation during tropical storm Alberto in 2006, *Ocean Dynamics*, *58*, 375–396, 2008.

Zydlewski, G. B., A. Haro, and S. D. McCormick, Evidence for cumulative temperature as an initiating and terminating factor in downstream migratory behavior of Atlantic salmon (*Salmo salar*) smolts, *Canadian Journal of Fisheries and Aquatic Sciences*, *62*, 68–78, 2005.